Novel Materials and Processing Routes Using Alkali-activated Systems

by

Hussam Suhail G Alghamdi

A Dissertation Presented in Partial Fulfillment
of the Requirements for the Degree
Doctor of Philosophy

Approved July 2019 by the
Graduate Supervisory Committee:

Narayanan Neithalath, Chair
Subramaniam Rajan
Barzin Mobasher
Morteza Abbaszadegan
Dhruv Bhate

ARIZONA STATE UNIVERSITY

August 2019

ABSTRACT

This dissertation aims at developing novel materials and processing routes using alkali activated aluminosilicate binders for porous (lightweight) geopolymer matrices and 3D-printing concrete applications. The major research objectives are executed in different stages. Stage 1 includes developing synthesis routes, microstructural characterization, and performance characterization of a family of economical, multifunctional porous ceramics developed through geopolymerization of an abundant volcanic tuff (aluminosilicate mineral) as the primary source material. Metakaolin, silica fume, alumina powder, and pure silicon powder are also used as additional ingredients when necessary and activated by potassium-based alkaline agents. In Stage 2, a processing route was developed to synthesize lightweight geopolymer matrices from fly ash through carbonate-based activation. Sodium carbonate (Na_2CO_3) was used in this study to produce controlled pores through the release of CO_2 during the low-temperature decomposition of Na_2CO_3. Stage 3 focuses on 3D printing of binders using geopolymeric binders along with several OPC-based 3D printable binders. In Stage 4, synthesis and characterization of 3D-printable foamed fly ash-based geopolymer matrices for thermal insulation is the focus. A surfactant-based foaming process, multi-step mixing that ensures foam jamming transition and thus a dry foam, and microstructural packing to ensure adequate skeletal density are implemented to develop foamed suspensions amenable to 3D-printing. The last stage of this research develops 3D-printable alkali-activated ground granulated blast furnace slag mixture. Slag is used as the source of aluminosilicate and shows excellent mechanical properties when activated by highly alkaline activator (NaOH + sodium silicate solution). However, alkali activated slag sets and hardens rapidly which is undesirable for 3D printing. Thus, a novel

mixing procedure is developed to significantly extend the setting time of slag activated with an alkaline activator to suit 3D printing applications without the use of any retarding admixtures. This dissertation, thus advances the field of sustainable and 3D-printable matrices and opens up a new avenue for faster and economical construction using specialized materials.

DEDICATION

I would like to dedicate my dissertation to my parents, my brothers, my sister, my wife, and my beautiful daughters.

ACKNOWLEDGMENTS

I would like to express my sincere gratitude to my advisor and committee chair, Professor Narayanan Neithalath, for his undivided attention, guidance, encouragement and motivation throughout my research. Without his encouragement and enthusiasm this dissertation would not have been possible. I would like to extend my regards to my committee members: Professors Subramaniam Rajan, Barzin Mobasher, Morteza Abbaszadegan, and Dhruv Bhate for their guidance and taking the time to examine this work.

I want to thank Dr. Akash Dakhane for teaching and supporting in the beginning of my research work. I extend my thanks to my current research group Aashay, Sooraj, Matthew, Naman, Pu, Anand, Emily and every other student (past and present) in our structures and materials group for all their help and guidance during completion of my dissertation.

I would like to thank the laboratory support staff: Peter Goguen, Jeff Long, and Kenneth Witczak for all their assistance throughout this research.

Finally, I would like to thank Arizona State University and the Ira A. Fulton Schools of Engineering for providing me with the resources which enabled the completion of this PhD.

TABLE OF CONTENTS

Page

CHAPTER Page

CHAPTER Page

CHAPTER Page

LIST OF TABLES

Table Page

Table Page

LIST OF FIGURES

Figure Page

Figure Page

Figure Page

Figure Page

Figure Page

Figure Page

CHAPTER 1

INTRODUCTION

1.1. Background

Concrete is the most widely used man-made material on the planet and Ordinary Portland Cement (OPC) is the most significant component of concrete. The immense use of OPC is associated with almost 5-7% of the global greenhouse gas production. Cement is also among the most energy intensive construction materials after aluminum and steel and therefore it becomes imperative to find a suitable substitute for OPC. Over the last few years, the development of binder systems using alkali activated aluminosilicate materials has emerged as a possible substitute for OPC based binders. The worldwide availability of by-product aluminosilicate materials such as ground granulated blast furnace slag, or fly ash provides an opportunity to consume these industrial waste materials, as an alternative to OPC based concrete [1,2]. These aluminosilicate materials may also be obtained in nature, for instance, natural pozzolan, or kaolin. Alkali-activated cementitious materials have been documented to exhibit several advantages over traditional cement based materials including fire resistance, high compressive strength, freeze-thaw resistance, low thermal conductivity, low shrinkage, rapid setting and hardening, high durability, and resistance to alkali aggregate reaction [3–7].

The activation process is key to taking advantage of the remarkable properties of these aluminosilicate materials. Strong alkaline activators are needed to initiate the activation of aluminosilicates and form an amorphous-to-semi crystalline aluminosilicate inorganic polymer (geopolymer) [8,9]. The geopolymer-based porous ceramics can be produced at lower temperatures as compared to conventional ceramic sintering by partly replacing the

sintering process with alkaline activation and consolidation [10,11]. The high pH of the alkaline activators breaks down the Si-O-Si and Al-O-Al covalent bonds [12] to produce a strong and durable gel network during the geopolymerization process. The most common alkali activation agents used to activate aluminosilicate materials are sodium hydroxide (NaOH) and potassium hydroxide (KOH). The mechanism of the geopolymerization is somewhat complicated [13]. However, these mechanisms can be simplified into few steps which are dissolution (water consumption), equilibrium of speciation, gelation, re-arrangement, polymerization, and hardening [14–16].

Several studies have reported the use of geopolymer concrete mixes for 3D printing from a sustainability stand point [17,18]. The optimum concentration of activators to have a workable mix within the printability window for these mixes can ensure desired pre-print performance and post-print mechanical properties. Hence, there is a need for developing and characterizing novel geopolymer based binders for three-dimensional (3D) printing applications. Alkali activated slag as a sustainable alternative to OPC has the potential to be used in 3D printing applications. However, there is a need for a novel processing technique to extend its setting time, which is possible with the use of a highly alkaline activator ($NaOH + Na_2SiO_3$) and is explored in this study.

1.2. Research Approach

This dissertation is a multi-faceted research effort to realize the potential of alkali-activation of binders. As such, the entire dissertation has five major focus areas. The research began with utilizing the chemistry of alkali-activation to create and characterize porous ceramics. Porous materials with tunable pore structure (sizes, volume, connectivity, and shapes) are widely used in environmental applications (water filtration, membranes)

[19–23], energy conversion [24,25], building insulation (thermal and acoustic) [26–32], and vibration mitigation [32–34]. The major emphasis was to get an understanding of the synthesis routes, microstructural properties, and performance characterization of a family of economical and multifunctional porous ceramics developed through geopolymerization of an abundant volcanic tuff (aluminosilicate mineral) as the primary source material. Mineral additives including metakaolin, silica fume, alumina powder, and pure silicon powder were used as additional ingredients when necessary and activated by potassium-based alkaline agents. The composition and heat treatment regimens were modified to provide the desired pore structure features for percolation, contaminant retention, and thermal conductivity. The treatment temperatures used were lower than those used in conventional porous ceramic synthesis.

The synthesized matrices were extensively characterized for a variety of physical properties and evaluated for the desired performance features. Mercury intrusion porosimetry was used to determine the porosity and characteristic pore sizes of the matrices and ascertain the efficiency of the geopolymerization and foaming processes. Electrical impedance spectroscopy was used to determine the connectivity of the pore network in the matrices while guarded hot-plate method was used to determine the thermal conductivity of the porous ceramics. The influence of pore structure for filtration applications as well as the thermal performance of the porous matrices were evaluated. The porous ceramic matrices developed in this study using abundant aluminosilicate materials as the major component are shown to have the potential to be used for multifunctional applications and can be processed at a fraction of the cost of commercially available porous matrices with similar features. The synthesis routes are also more energy efficient than many available

technologies. It has been shown that the synthesis parameters including the composition and treatment regimens can be tailored to achieve the desired thermal and fluid transport, and contaminant capture characteristics. Moreover, the abundance of the source materials in nature, the ease with which these systems can be manufactured, and the range of tunable microstructure and mechanical properties enables them to be used in large volume applications such as building insulation and low volume applications such as water filtration.

The next stage of the research focused on synthesizing fly ash based geopolymer matrices through carbonate-based activation. The most common alkali activators used to activate aluminosilicates are NaOH and KOH. However, their high alkalinity (pH = 13-14) poses potential problems [2,3] in their widespread utilization. Therefore, Na_2CO_3 as a mild alkali activator was used in this study to initiate the dissolution of aluminosilicate particles to form a geopolymer network, and to examine the influence of carbonate anions on the process of geopolymerization. Na_2CO_3 when mixed with water produces sodium hydrogen carbonate that decomposes at low temperatures during heating and release CO_2 that help form more pores. While the release of CO_2 in the manufacturing of a building material is not particularly attractive as far as global warming is concerned, the quantity is rather small to warrant any special concern. Consequently, a processing route was developed to synthesize lightweight geopolymer matrices from fly ash through carbonate-based activation. Two different curing temperatures (85 and 100°C) were used to produce two sets of samples (non-foamed and foamed). Sodium silicate solution was used along with Na_2CO_3 to improve the mechanical properties of the synthesized geopolymer samples. Various Na_2O-to-binder (n) and SiO_2-to-Na_2O (M_s) ratios were adopted to find the

optimum n and M_s ratios. Several experiments were carried out to ensure the performance of synthesized geopolymer matrices. The pore-forming process was tuned in such a way that the resulting matrices have adequate mechanical and insulation properties, but it is possible to tailor the composition and processing to obtain requisite properties, enabling microstructural design of materials for performance. The synthesized matrices were subjected to microstructure and reaction product characterization using several techniques. The critical pore sizes were found to be lower (albeit at similar porosities) when the matrices were synthesized using a combination of carbonates and silicates rather than carbonates alone, indicating the influence of silicates and their polymerization on refining the pore structure. Thermal analysis, FTIR spectroscopy and SEM studies revealed the presence of sodium bicarbonate and sodium carbonate in the matrices, along with the alkali aluminosilicate gel.

The third stage of this study focusses on 3D printing of geopolymer-based binders along with several OPC based 3D printable binders. Recent studies have established the used of concrete in three-dimensional printing applications in the construction industry [18,35–41]. In fact, 3D-printing technique dates back to 1980 and is gaining more significance in many production processes during the last decades [42]. Complex and multi-scale structures can be fabricated by 3D-printing techniques through computer-aided design (CAD) [43,44]. Recently, 3D-printing has been employed in the construction industry because it enables to speed up the construction process and build complex architectural shapes without formwork leading to labor and energy reductions [40,41]. In other words, many challenges such as cost, time, and shape complexity can be overcome through 3D-printing technology. The main objective of this study is to understand the effect of alkali activators on

rheological characteristics and determine the printability limit of these mixtures. The major areas of this stage include determination of: (a) initial setting time, (b) flowability of mixtures, (c) rheological characterization to identify the parameters affecting extrudability (during printing) and shape stability (after printing), (d) pore and microstructural features to understand the effect of squeeze and overburden pressure, and (e) compressive and flexural strength characteristics. 3D printable alkali activated binders based on class F fly ash and ultra-fine limestone were successfully designed. The fine limestone powder was essential to obtain cohesion and shape stability immediately after printing. Sodium hydroxide, sodium silicate, and sodium sulfate (Na_2SO_3) were utilized as alkali activators. Furthermore, 30% of OPC and slag were added to fly ash to improve the mechanical properties.

The designed mixes were subjected to rheological, extrusion, and mechanical tests to understand the effect of the alkali activators and the additives on the binder performance. The printability of these mixes was qualified based on the extrudability and shape stability of the mixes. The designed printable mixes subjected to parallel plate rheology showed a reduction in the yield stress by the action of the alkali activators favoring extrudability and the cohesiveness of the activators favored the shape stability retention. Hence, the design printable mixes qualified the printability criterion and gave satisfactory performance in extrusion. Moreover, the extensional yield stress and wall slip shear stresses were predicted using the Benbow Bridgewater model and showed a direct correlation with the parallel plate and tack test rheology. Mini slump tests and setting times were evaluated to correlate the fresh properties with the retention characteristics. A printability zone was established based on the correlation of yield stress and mini slump values. This helps to decide whether

a mix is printable or not since it decides on the fresh properties, its evolution, and the retention characteristics.

Slag and OPC were used to replace the fly ash for improved mechanical properties. However, the heat treatment curing showed shrinkage cracks in slag mixes which resulted in a reduction in the compressive and flexural strengths. The binder performance and printability criterion required to establish alkali activated fly ash mixes as a suitable and sustainable alternative for conventional cementitious binders in 3D printing are brought out.

The fourth stage of this study focused on synthesizing 3D-printable geopolymeric foams for specific building functions – in this case, thermal insulation. Surfactant as a direct foaming agent and bubbles stabilizer was used in this study. Past studies have reported the use of 3D-printing to fabricate porous materials from different starting materials for many applications such as water filtration, catalysis, biomedical scaffolds, and lightweight structural elements [23,32,34,45–49]. Extensive applications in building insulation need porous materials. Synthesized 3D-printable foamed suspensions in this study have high potential of replacing the conventional building insulation materials such as extruded polystyrene, mineral wool etc. that can be placed in between the concrete layers of a typical insulated precast concrete wall panel (sandwich wall panel). The fire resistance and environmental sustainability of many of the commonly used insulation materials are questionable [50–52], which can be overcome by the proposed approach.

Mini-slump and single printed filaments were the techniques that were used in this study to indicate the shape stability and shape retention factor. Also, the viscosity recovery (buildability test) was used to evaluate the buildability of the foamed suspensions which

showed better buildability with most of the initial viscosity recovered after extrusion effect. Moreover, lower thermal conductivity were targeted and the obtained values ranged between 0.15 and 0.25 W/m-K, for porosities ranging from 55-75% which already lower than those of conventional cement pastes (~0.8 W/m-K), but not lower than those of commonly used insulation materials including polystyrene and mineral wool (~0.05 W/m-K). Hence, composite structure was printed including large voids to be used in sandwich wall panels. 60-70% was the optimum air volume fraction which accomplish effective thermal conductivity based on the effective medium theory. Therefore, 3D-printing of geopolymeric foams has a potential to be employed in conjunction with precast wall manufacturing to develop economical and sustainable structural systems that compare with existing systems with respect to thermal insulation capacity.

The fifth and final area of focus of this study is on alkali activated slags in 3D printing of concrete. It has been documented that ground granulated blast furnace slag when used as the source of aluminosilicate, shows excellent mechanical properties when activated by alkali activators. Although, alkali-activated slag has many advantages in terms of high strength, and durability, all previous studies have not tried using slag as a sole binder to develop 3D-printable mixtures because it has a very rapid setting time leading to unfavorable effects in 3D-printing applications. Previous studies developed 3D-printable binders using a combination of slag and fly ash along with silica fume that provides a delayed setting time due to the presence of fly ash [53–55]. Other studies reported that the initial setting time of AAS can be extended to be about 3h by increasing mixing time till 30 min but this mixture was not amenable to be printable [56,57].

This study mainly focuses on solving this challenge and developing alkali-activated slag mixture as an alternative sustainable binder satisfying 3D-printing requirements. Consequently, a novel processing technique was established to significantly extend the setting time of slag activated with a highly alkaline activator (NaOH + sodium silicate). Besides the setting time, viscosity and cohesion which are essential fresh parameters for 3D printing applications are evaluated for 3D printable mixtures with slag as a sole binder, without using retarding admixtures. Moreover, no fine ingredients or thixotropic modifiers were added to the binder to improve the rheological characteristics of the mixture. A simple mixing method which depends on deflocculation and dispersion of early formed C-S-H is adopted to delay the initial setting time and obtain cohesive mixture at the same time. Fresh and hardened properties of the printable mixture are investigated and evaluated in this study.

1.3. Research Objectives

This research has focused on developing novel materials and processing routes using alkali activated aluminosilicate binders, particularly in synthesizing porous geopolymer matrices and 3D-printable geopolymer mixtures. The major objectives are listed below:

1. To synthesize and characterize economical and multi-functional porous ceramics based on geopolymerization of abundant aluminosilicates.
2. To synthesize lightweight geopolymer matrices from fly ash through a novel alkali carbonate-based activation method.
3. To develop insights into paste composition and extrusion rheology of 3D-printable fly ash-based alkali activated binders.

4. To synthesize and characterize 3D-printable geopolymeric foams for thermally efficient building envelope materials.
5. To develop a novel mixing procedure to extend the setting time of alkali activated slag for 3D-printing of concrete.

Experimental work was carried out using advanced microstructural characterization techniques such as thermo-gravimetric analysis (TGA), mercury intrusion porosimetry (MIP), dynamic shear rheology, isothermal calorimetry, thermal conductivity, X-ray diffraction etc.

1.4. Dissertation Outline

The dissertation consists of five research papers that have been published, submitted or being prepared for possible publication. These papers are presented in Chapters 3-7. The overall organization of the thesis is shown below.

Chapter 1 gives a brief introduction about the study and presents the background on alkali activated binders. The process of alkali activation is explained briefly along with the different focus areas pertinent to this study. The research objectives are identified, and a chapter outline is presented.

Chapter 2 presents an overview of the materials and methods used for characterization of the binders developed in this study and presents a thorough literature review on alkali activation and 3D printing of alkali activated composites.

Chapter 3 describes the synthesis routes and microstructural and performance characterization of a family of economical, multifunctional porous ceramics developed through geopolymerization of an abundant volcanic tuff (aluminosilicate mineral) as the primary source material. Extensive microstructural characterization using different

techniques to examine the morphology and to quantify the pore volumes, sizes, and connectivity, which are important in dictating the performance characteristics, are reported. Measurements of flow rates and thermal conductivity demonstrate the multifunctionality of the synthesized matrices, which demonstrate adequate strengths for a number of buildings-related applications.

Chapter 4 describes a novel synthesis route for porous geopolymers based on carbonate-based activation of fly ash as the primary source material. The aqueous dissolution of sodium carbonate supplies NaOH which provides the alkaline medium for fly ash geopolymerization (along with externally supplied sodium silicate also, if needed). The CO_2 released from the low temperature (~100 °C) decomposition of carbonates formed as reaction products, acts as the pore-forming agent. The dosage of the alkaline agents is tailored to obtain a porous material with large enough porosity (~50%), and sufficient mechanical strength (~15 MPa) and thermal conductivity (~0.3 W/m-K) so as to be used as structural/insulating elements in buildings. Detailed analysis of microstructure and reaction products reveals the presence of sodium carbonate crystals in the matrix, recrystallized from the initial carbonates added.

Chapter 5 discusses the material design of alkali activated fly ash-based binders for extrusion-based 3D printing and the rheological responses that are influential in ensuring printability. Fly ash is supplemented with fine limestone, slag, or portland cement to provide adequate microstructural packing required for printability. The alkaline activators help reduce the yield stress and enhance the cohesiveness of the mixtures. Based on the measured shear yield stress at different times and concurrent printing of a filament, the printability window and yield stress bounds for printability, applicable for the chosen

printing parameters, are established. This approach could be used for mixture qualification for extrusion-based printing. The Benbow-Bridgwater model is implemented on extrusion rheology results of pastes to determine the extrusion yield stress and wall slip shear stress, which are useful process-related parameters.

Chapter 6 presents a novel approach for the synthesis of 3D-printable geopolymeric foams for thermally efficient building envelope materials and their corresponding properties. A surfactant-based foaming process and multi-step mixing that ensures foam jamming transition and thus a dry foam, and microstructural packing to ensure adequate skeletal density are implemented to develop foamed suspensions amenable to 3D-printing. Further, it is shown that designed architectures that minimize heat transfer can be printed in between the concrete layers of a sandwich wall panel using foamed matrices to obtain composites with thermal insulation properties comparable to or better than those of currently available insulated concrete wall panels.

Chapter 7 discusses a simple modified mixing procedure to extend the initial setting time of alkali-activated slag mixtures and simultaneously create cohesive mixture for 3D-printing of concrete. The disintegration of the initially formed primary C-S-H (deflocculation) is the essential criteria adopted in this study to produce mixtures for 3D-printing requirements with sufficient initial setting time. Sodium hydroxide is used in combination with sodium silicate solution as the alkali activation agent. The procedure adopted in this study is successfully able to prolong the initial setting time to be around eight hours.

Chapter 8 summarizes the conclusions and recommends likely candidate topics for future research.

CHAPTER 2

LITERATURE REVIEW

2.1. INTRODUCTION

This chapter is divided into three main sections. The first section consists of the materials used in this study. These materials include ordinary portland cement (OPC) and cementitious binders such as fly ash and slag. Supplementary cementitious materials include limestone, pozzolans such as metakaolin, silica fume and volcanic tuff. Additional materials used in this study include foaming agents to create porous ceramics matrices as well as alkali activation agents such as alkali hydroxides and silicates, sodium carbonate, and sodium sulfate. The next section describes the sample preparation methods for mixtures in this study and provides detailed information about 3-D printing and the procedures employed to 3D print alkali activated mixtures and porous ceramics. This section also covers the material characterization techniques used to understand the rheology of fresh mixtures (mini-slump, vane-Shear, parallel plate, and extrusion), reaction kinetics (thermo-gravimetric analysis (TGA), calorimetry), Thermal conductivity, porosity (mercury intrusion porosimetry (MIP)),mechanical strength (compression, flexure) and microstructure characterization (x-ray diffraction (XRD), scanning electron microscopy (SEM), Fourier transform infrared spectroscopy (FTIR)).

2.2. MATERIALS USED

2.2.1. Fly Ash

Fly ash has been used in the construction industry for the past several years as a sustainable substitute for ordinary portland cement to reduce the overall carbon emissions. Being a

waste product from coal power plants, fly ash is available in abundance at a lower cost which also helps reduce the overall cost of production of concrete. At the same time, fly ash demonstrates pozzolanic properties and reacts to produce secondary hydration products. The spherical nature of fly ash particles helps aid the rheology of the binder. Fly ash is predominantly available in two forms – Class C Fly ash and Class F Fly ash. These two classes are differentiated by the level of calcium present in the powders. Class F Fly ash is the preferred material used in this study because of its low calcium content which enables workability and mitigates any setting times issues in geopolymer binders. The Class F Fly ash used in this study has a median particle size of 17.9 μm and a specific gravity of 2.34. Table 2-1 shows the chemical composition and Figures 2-1 (a-c) show the particle size distribution, XRD pattern and SEM image of Class F Fly Ash.

The X-ray diffraction (XRD) pattern of the fly ash is shown in Figure 2-1(b). The halo in the 2θ range of 20° to 40° is indicative of the amorphous nature of the fly ash, which enables better reactivity during the geopolymerization process. Quartz, hematite, and mullite are the major crystalline species as determined from the XRD pattern of the fly ash. Figure 2-1(c) shows the scanning electron microscope image of fly ash, showing the spherical particles.

Table 2-1: Chemical composition of Class F fly ash.

Oxide	SiO_2	Al_2O_3	Fe_2O_3	CaO	MgO	SO_3	LOI
% by mass	58.40	23.80	4.19	7.32	1.11	3.04	2.13

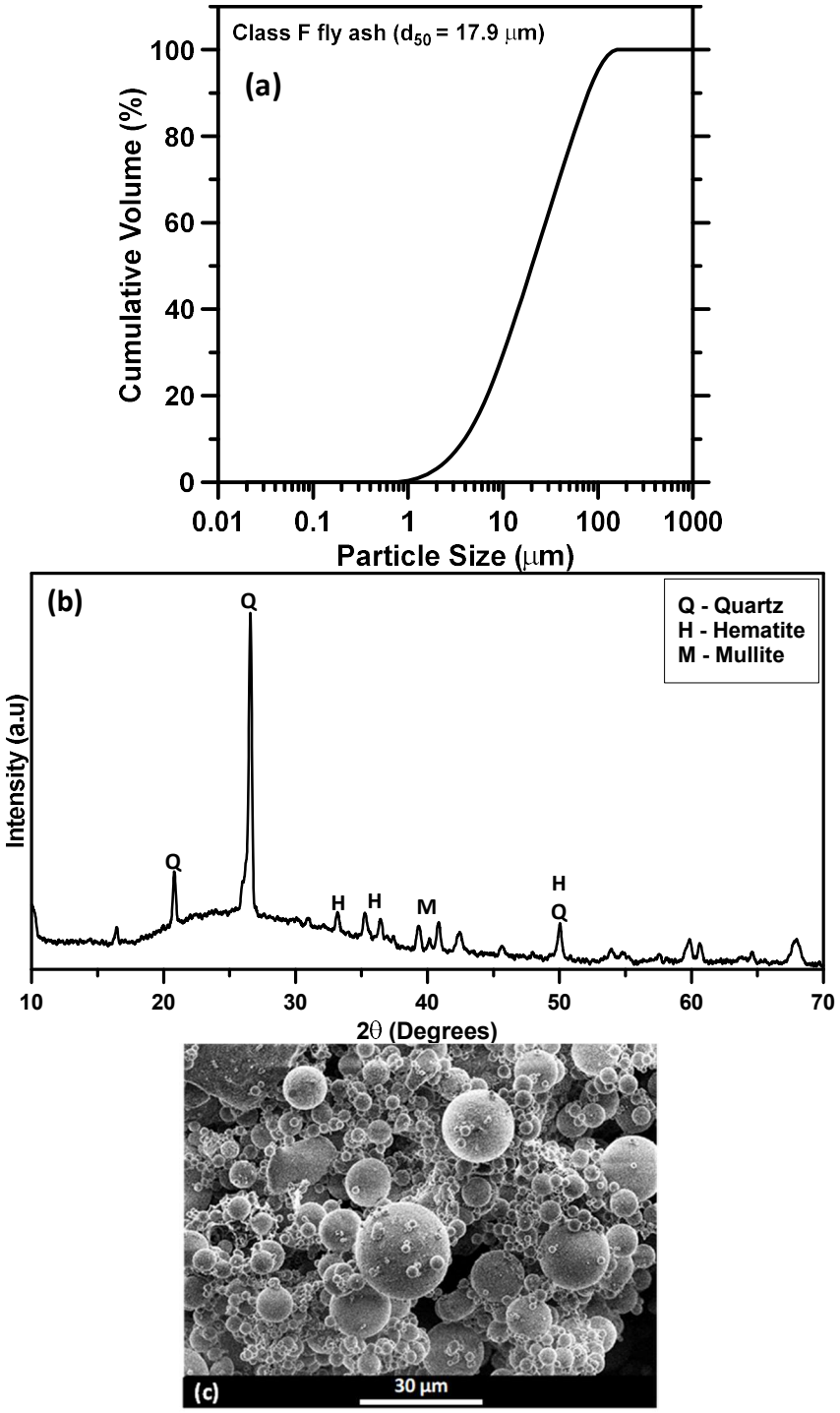

Figure 2-1: (a) Particle size distribution, (b) X-ray diffraction pattern, and (c) scanning electron microscope image of the class F fly ash.

2.2.2. Slag

Slag is a by-product of the iron and steel industry and is used as one of the primary cement replacement materials in the forms of blast furnace slag, granulated blast furnace slag and ground granulated blast furnace slag. Slag is a latent hydraulic material and reacts with water to form hydrates as well as with calcium hydroxide to form secondary hydration products. It produces C-A-S-H gel when activated by alkaline activators. The slag used in this study has a median size of 8.9 μm and a specific gravity of 2.9. Table 2-2 shows the chemical composition and Figures 2-2 (a and b) show the particle size distribution and SEM image of slag.

Table 2-2: Chemical composition of slag.

SiO_2	Al_2O_3	Fe_2O_3	CaO	MgO	SO_3	Na_2O	K_2O	LOI
36.0	10.5	0.67	39.8	7.93	2.10	0.27	0.80	3.01

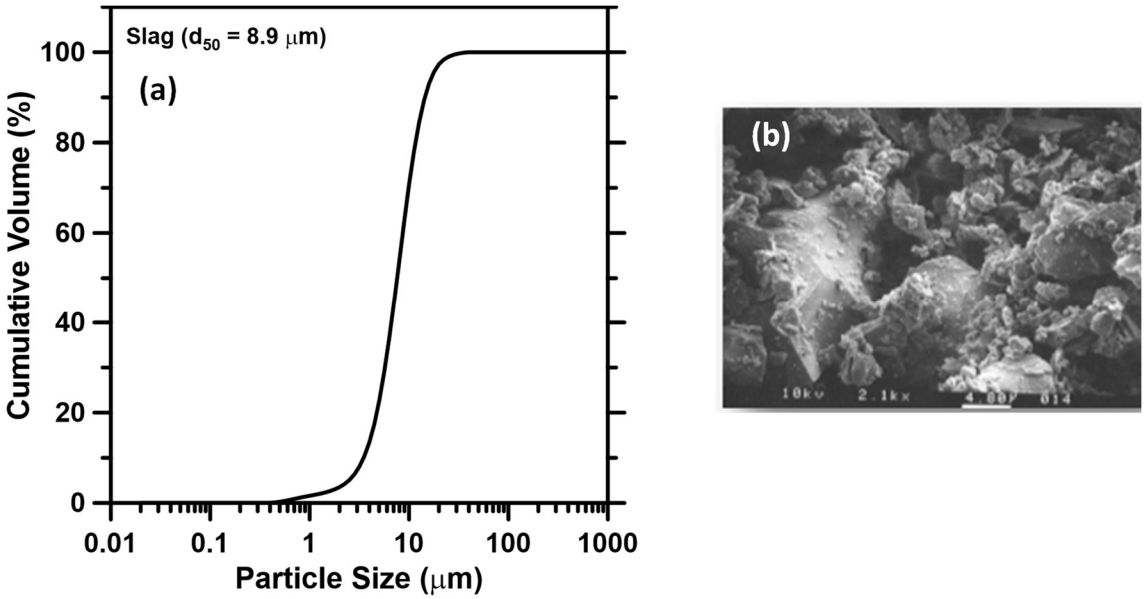

Figure 2-2: (a) Particle size distributions (PSD), and (b) SEM image of slag [58].

2.2.3. Limestone

Limestone is a naturally occurring mineral which contains more than 99% of $CaCO_3$. Limestone has been increasingly used in construction to replace OPC as an inert filler because of its abundance. The limestone used in this study had a median size of 1.5 µm and a specific gravity of 2.7. Because of its finer size, limestone improves the particle packing of the binder which makes it useful to create dimensionally stable 3D printed composites. Figures 2-3 (a-b) show the particle size distribution and strength results showing the influence of limestone. It is observed from Figure 2-3 (b) that OPC binder containing finer limestone has a higher compressive strength as compared to traditional OPC [59]. This is due to the increased particle packing in the presence of fine limestone, which results in lower porosity and consequently leads to higher value for strength. Further, it is also observed that higher limestone replacement may reduce the compressive strength of the binder [59].

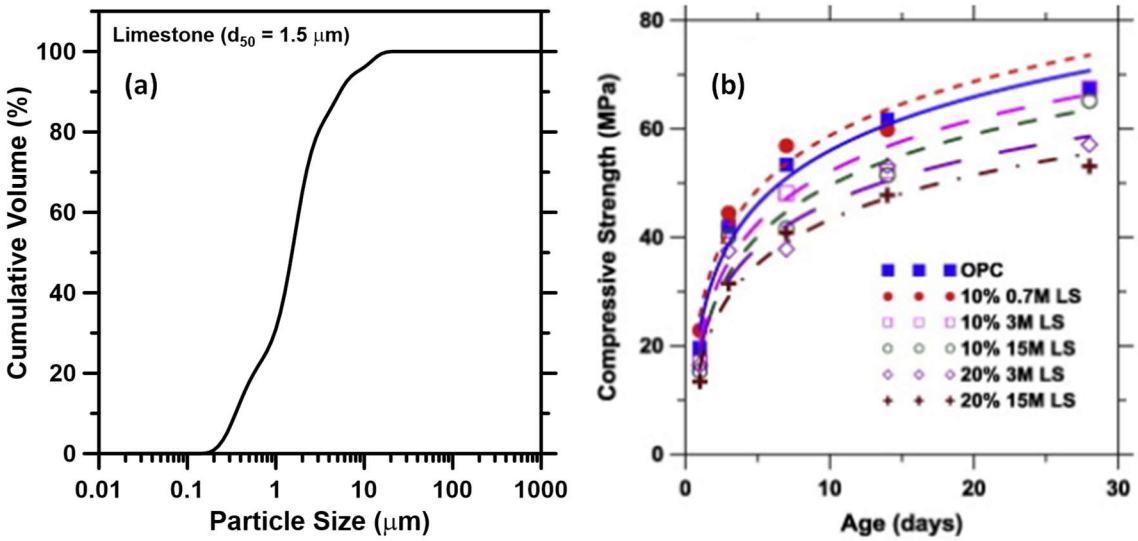

Figure 2-3: (a) Particle size distributions (PSD) of limestone, and (b) Compressive strength development of OPC- limestone pastes [59].

2.2.4. Metakaolin

Metakaolin is a pozzolanic material produced by calcination of clay mineral (kaolinite) at high temperatures ranging from 650 to 800 °C. It contains mainly alumina (40-45 %) and silica (50-55 %) but lacks ferrite. Metakaolin used in this study has a median size of 5.3 μm and a specific gravity of 2.5. Table 2-3 shows the chemical composition and Figures 2-4 (a-c) show the particle size distribution, XRD pattern and SEM images of metakaolin. Metakaolin has amorphous nature as noticed by the broad hump in the XRD spectra (see halo in the $2\theta = 15^{o}$ to 30^{o}).

Table 2-3: Chemical composition of metakaolin.

SiO_2	Al_2O_3	Fe_2O_3	CaO	MgO	SO_3	Na_2O	K_2O	LOI
51.7	43.2	0.5	---	---	---	---	---	0.16

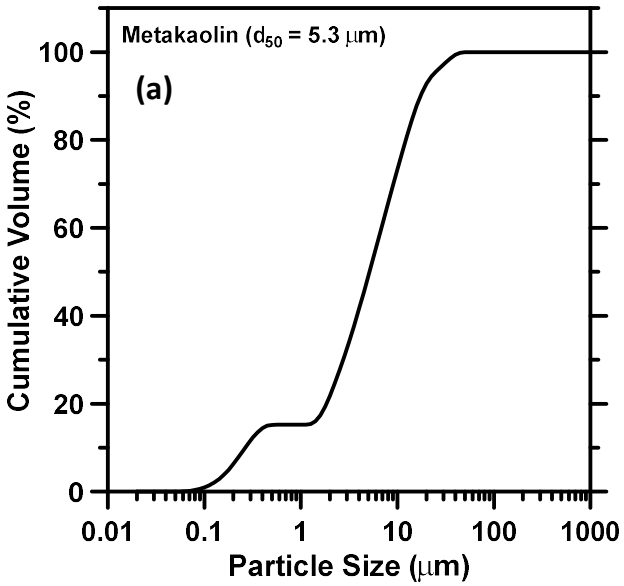

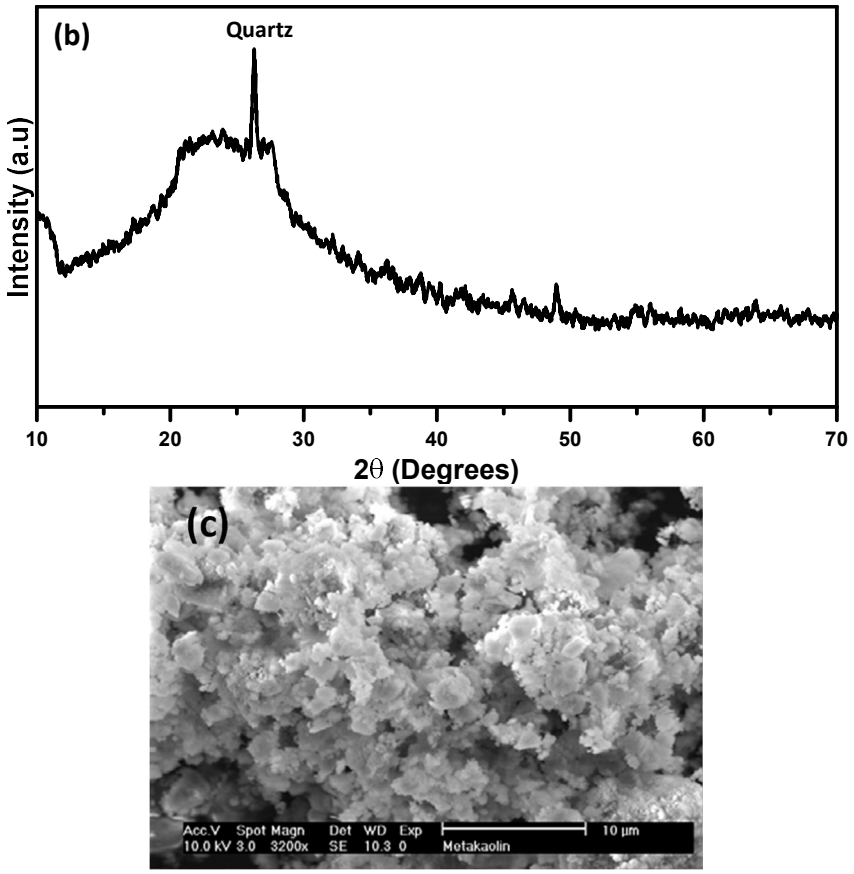

Figure 2-4: (a) Particle size distributions (PSD), (b) X-ray diffraction patterns, and (c) SEM image of metakaolin [60].

2.2.5. Silica Fume

Silica fume, also called microsilica, is produced as a by-product during the production of silicon metal or ferrosilicon alloys in electric arc furnaces. It is an extremely fine amorphous form of silica with typically spherical particles as shown in Figures 2-5. Two types of silica fume are commercially available in the market depending on the manufacturing process – densified and undensified. The densified silica fume is used in this study because of its higher bulk density. The median size of the silica fume used in this study was found to be 0.1 µm and a dry specific gravity of 2.2. Table 2-4 shows the chemical composition and Figures 2-5 (a-b) show the XRD pattern and SEM image of

silica fume. Silica fume has amorphous nature as noticed by the broad hump in the XRD spectra (see halo in the 2θ = 15º to 35º)

Table 2-4: Chemical composition of silica fume.

SiO_2	Al_2O_3	Fe_2O_3	CaO	MgO	SO_3	Na_2O	K_2O	LOI
93.4	0.42	0.52	1.91	---	0.34	0.25	0.79	2.3

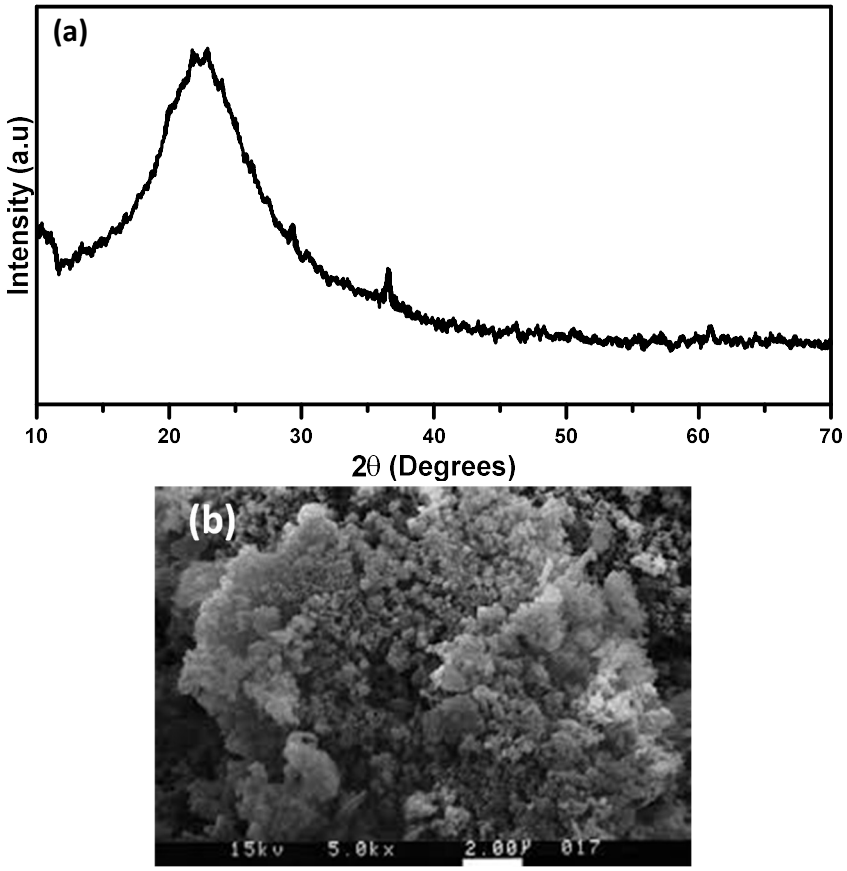

Figure 2-5: (a) X-ray diffraction patterns, and (b) SEM image of silica fume [58].

2.2.6. Volcanic Tuff

Volcanic tuff Natural Pozzolan is a type of crystalline clay ejected during volcanic eruption. It is a naturally occurring pozzolanic material and mildly reacts with the by-product of cement hydration to form secondary hydration products. However, the reactivity of volcanic tuff natural pozzolan is minimal due to its crystalline nature at room temperature and requires high temperature and high pH environment (alkaline activators)

to begin dissolution and participate in the reaction process. This material mainly consists of alumina and silica as shown in Table 2-5. The median size of particles is 6.0 μm and the specific gravity is 2.46. Figures 2-6 (a-b) show the particle size distribution and XRD pattern of the volcanic tuff natural pozzolan.

Figure 2-6(b) shows the X-ray diffraction (XRD) patterns of the volcanic tuff natural pozzolan material. Although the volcanic tuff natural pozzolan is mostly crystalline, it also contains glassy phases as noticed in the halo recorded in the 2θ range of 20° to 35°. The main peak in XRD pattern of the volcanic tuff natural pozzolan located at a 2θ of 28° is attributed to quartz. The other crystalline phases are attributed to minerals affiliated to the feldspar group {((K or Na) $AlSi_3O_8$)) or ((Ca, Na) $Al_2Si_2O_8$)}.

Table 2-5: Chemical composition of volcanic tuff.

SiO_2	Al_2O_3	Fe_2O_3	CaO	MgO	SO_3	Na_2O	K_2O	LOI
74.83	14.9	0.96	1.66	1.75	0.01	2.10	3.39	---

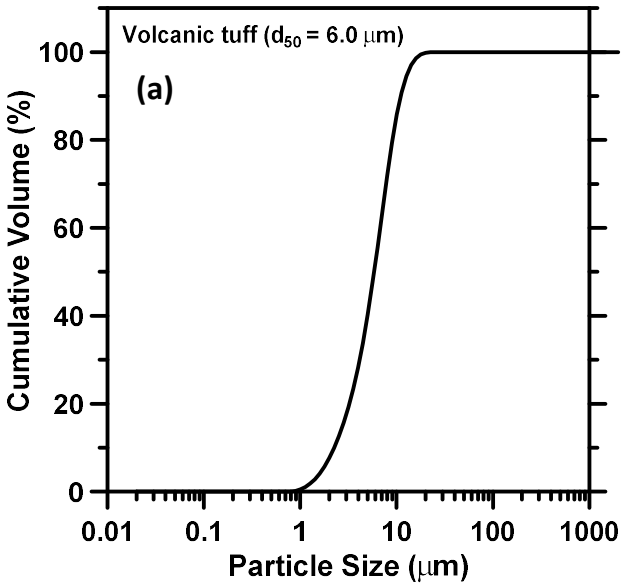

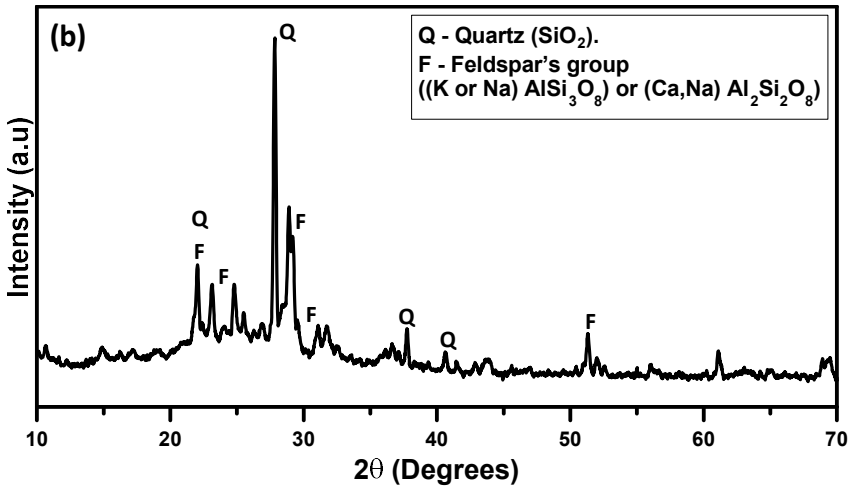

Figure 2-6 : (a) Particle size distributions (PSD), and (b) X-ray diffraction patterns of volcanic tuff.

2.2.7. Foaming Agents

Foaming agents are used to produce a special class of lightweight ceramic materials. These agents can be classified as physical or chemical foaming agents depending on the nature of the foaming process. Physical foaming agents such as surfactants create bubbles during mixing [61–63], while the chemical foaming agents react to release gases inside the mixture which is the reason for foaming. Metallic free silicon [11,64], alumina powder [61,65], and hydrogen peroxide [61,63] are generally used as chemical foaming agents to synthesize geopolymeric foam. The free metallic silicon redox reaction can induce porosity by formation of hydrogen gas as shown in Equation 2-1 [10]. Equations 2-2, 2-3, and 2-4 show the redox reactions for alumina powder and hydrogen peroxide [66,67]. The role of sodium carbonate as a foaming agent is also shown in Equations 2-5 and 2-6 after releasing CO_2 during the decomposition of hydrolysis of sodium carbonate at heat treatment [68].

$$4H_2O + Si^0 \rightarrow 2H_2 \uparrow + Si(OH)_4 \quad (2\text{-}1)$$

$$2Al + 6H_2O + 2KOH \rightarrow 2K[Al(OH)_4] + 3H_2 \uparrow \quad (2\text{-}2)$$

$$2Al + 6H_2O + 2NaOH \rightarrow 2Na[Al(OH)_4] + 3H_2 \uparrow \quad (2\text{-}3)$$

$$H_2O_2 \rightarrow 2H_2O + O_2 \uparrow \quad (2\text{-}4)$$

$$Na_2CO_3 + H_2O \rightarrow NaHCO_3 + NaOH \quad (2\text{-}5)$$

$$2NaHCO_3 \xrightarrow{\Delta} Na_2CO_3 + H_2O + CO_2 \uparrow \quad (2\text{-}6)$$

2.2.8. Alkali Activation Agents

Alkali-activation is a chemical process that is utilized to break the highly stable covalent bonds of alumina and silica present in aluminosilicate materials. There are several different alkali activators used in this study ranging from high pH activators such as sodium and potassium hydroxides all the way to neutral activators such as sodium sulphate. Other activators such as sodium carbonate, sodium and potassium silicates have also been used. While high pH activators are beneficial in terms of high strength and chemical reactivity, low pH alternatives have been also been considered in this study because of safety considerations in field applications. Figures 2-7(a-c) show the effect of the alkali cation (Na or K) and concentration of alkaline activators on the compressive strength of slag mortars [69].

In this study, sodium silicate solution (waterglass) supplied by PQ Corporation has a solids content of 36%, a silica modulus (molar ratio of SiO_2-to-Na_2O) (M_s) of 3.3, and specific gravity of 1.38 g/cm^3. Potassium silicate solution (KASIL) supplied by PQ Corporation has a solids content of 44%, a silica modulus (molar ratio of SiO_2-to-K_2O), (M_s) of 3.29, and density of 1.34 g/cc. The sodium hydroxide, potassium hydroxide, sodium carbonate and sodium sulfate powders were determined to have specific gravities of 2.13, 2.04, 2.54 and 2.66 g/cm^3 respectively.

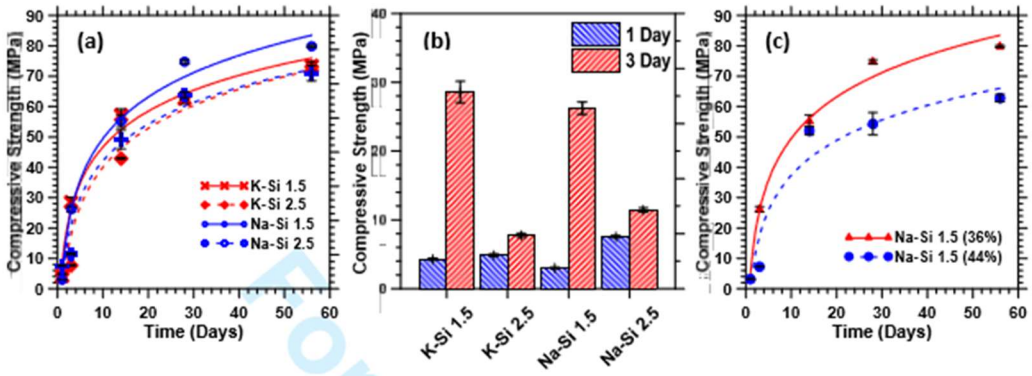

Figure 2-7: Compressive strength development of Na- and K-silicate (36% solids content) activated slag mortars, (b) compressive strength at early ages (1 and 3 days) for the Na- and K-silicate activated mortars, and (c) compressive strength development of Na silicate activated slag mortars as a function of the solids content in the Na silicate solution [69].

2.3. METHODS

2.3.1. Mini-Slump

A mini slump cone with a bottom diameter of 38 mm, top diameter of 19 mm, and a height of 57 mm is used to determine the shape stability of the binders for 3D-printing. The paste is loaded in the mini-slump cone and then slowly lifted to determine the slump value. The mini-slump cone used in this study is presented in Figure 2-8 .

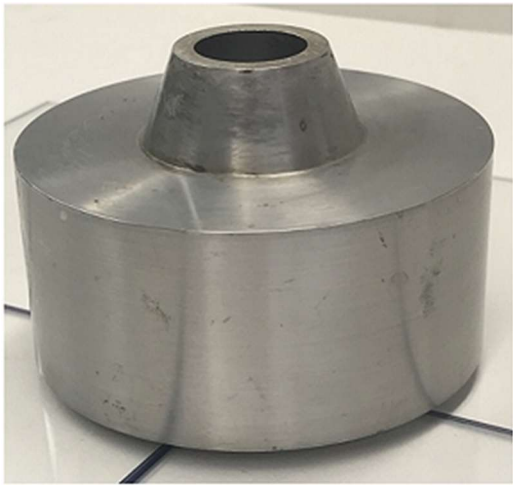

Figure 2-8: Mini-slump cone used in this study.

2.3.2. Rheology

A dynamic shear rheometer (TA Instruments AR 2000EX) was used in this study to carry out the rheological studies of fresh binders such as yield stress, plastic viscosity, tack force, and buildability of the mixtures, the instrument is shown in Figures 2-9(a and b). Two different geometries were employed in this study including the parallel plate and vane in cup geometry. The upper and lower plates of the parallel plate geometry were serrated at depths of 1 mm and 0.15 mm respectively to prevent paste slip on the shearing surface. The cup in vane shear geometry and the lower plate in parallel plate geometry were conditioned to a temperature of 25 ± 0.1 °C.

The sequence of steps employed in rotational rheology includes: (i) a stepped ramp up pre-shear phase for approximately 80 s to homogenize the paste, (ii) a stepped ramp-up, and (iii) a stepped ramp-down, as shown in Figure 2-9(c) [70,71]. The data was collected from only the down-ramp phase. Shear stress and shear rate data were extracted using TA Instruments' TRIOS software package. The range of the shear rate used in this test were from 5-to-100 s^{-1}, and the Bingham model was used to extract the apparent yield stress from the relationship between shear stress and shear strain rate. In addition to shear rheology, the parallel plate test set up was also used for the tack test. The tack test indicates the adhesive properties and cohesion of the paste mixtures. Figure 2-9(d) shows The experimental scheme of buildability test which was done in a sequence of steps that mimic extrusion-based 3D printing [53,54]. The steps employed include: (i) a stepped ramp-up pre-shear phase for approximately 80 s to homogenize the suspension, (ii) constant low shear rate of 0.01 s^{-1} for 60 s to determine the initial viscosity of fresh suspensions before printing, (iii) constant high shear rate of 100 s^{-1} for 30s which mimics the extrusion process,

and (iv) constant low shear rate of 0.01 s^{-1} for 60 s to determine the final viscosity of suspensions after extrusion printing.

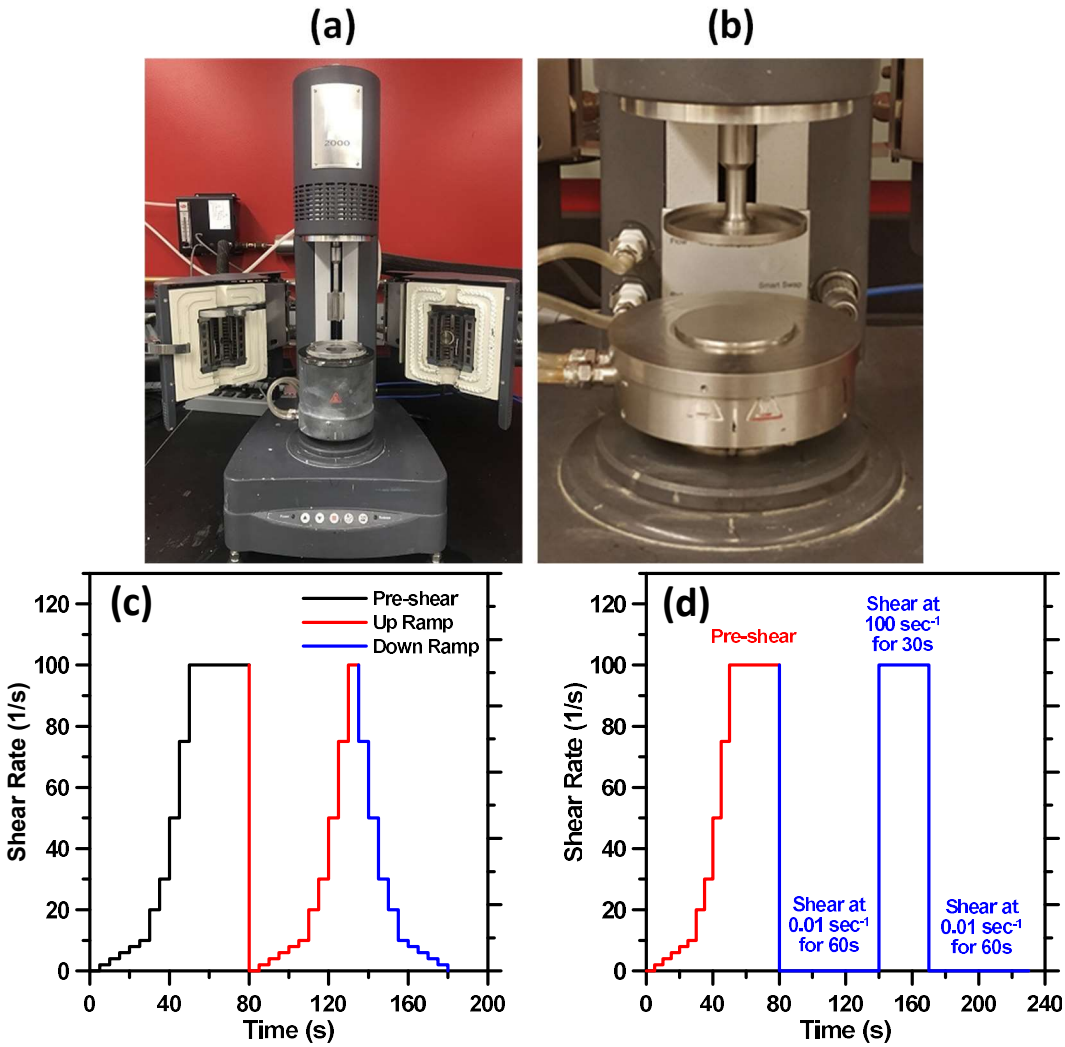

Figure 2-9: (a) TA Instruments AR 2000EX used in this study, showing the vane in cup, and (b) parallel plate configuration, (c) rheology test procedure to determine yield stress and plastic viscosity, and (d) plastic viscosity recovery of the mixtures for buildability.

2.3.3. Extrusion

A 4.45 kN servo-controlled MTS machine is used to carry out the extrusion rheology studies of alkali activated printable pastes. The paste sample is filled in the extruder immediately after mixing, ensuring that no air voids are entrapped in the paste. The plunger

is placed inside the barrel in direct contact with the compacted paste. The assembly is placed in a specially fabricated holder to allow the upper platen of the test machine to axially compress the plunger. A multi-speed extrusion test with ram velocities ranging from 150 mm/min to 10 mm/min is used (see Figure 2-10(c)). The nozzle (die) diameters used for the extrusion test are 4 mm and 6 mm, and the corresponding nozzle lengths are 35 mm and 20 mm respectively. The extrusion velocity is calculated from the ram velocity using flow equivalence, given as:

$$D_b^2 V_{ram} = D_d^2 V_{ext} \tag{2-7}$$

where V_{ram} is the ram velocity and V_{ext} is the extrusion velocity, and D_b and D_d are the barrel and die diameters respectively. The instrument, the extruder set up and the experimental procedure for extrusion test used in this study is shown in Figure 2-10.

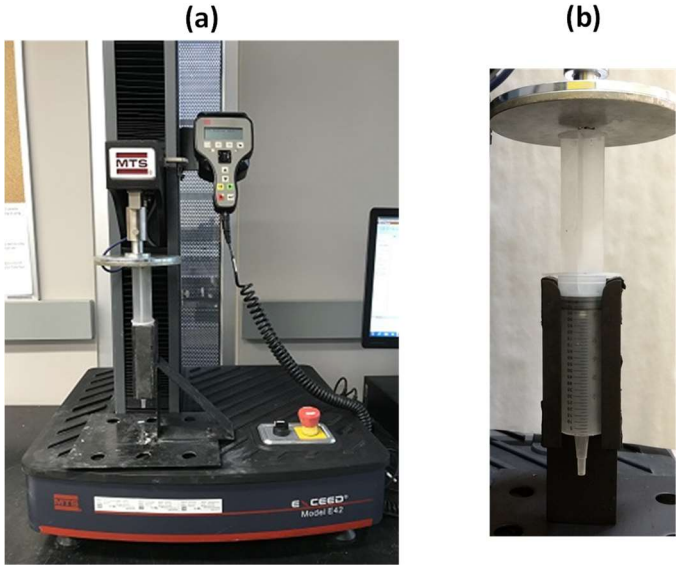

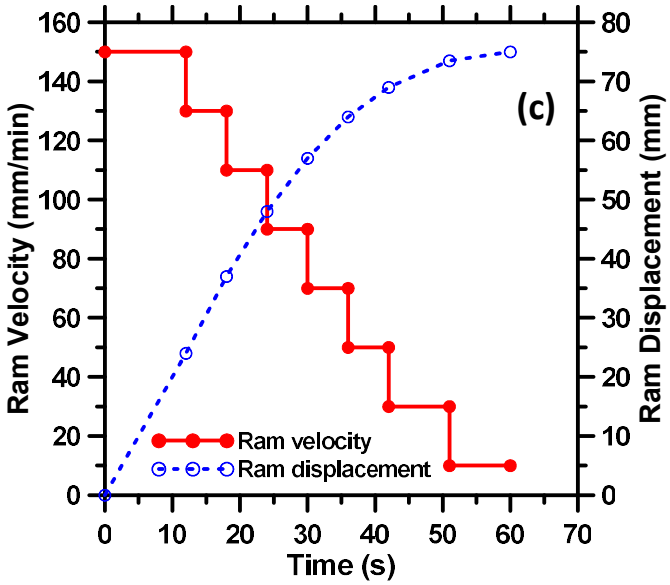

Figure 2-10: (a) A 4.45 kN servo-controlled MTS machine, (b) barrel-die extruder system, and (c) experimental procedure used for extrusion test.

2.3.4. Thermo-gravimetric Analysis (TGA)

Thermo-gravimetric analysis (TGA) is performed using a Perkin Elmer simultaneous thermal analyzer (STA 6000). In this study, TGA is performed to identify the reaction products. The instrument is capable of handling temperatures ranging from 15°C to 1000°C. Different reaction products in the sample decompose over different temperature ranges which is identified by the mass loss profile of the sample. The heat flow profile is used to identify the type of reaction products formed in the sample. The instrument used in this study is shown in Figure 2-11.

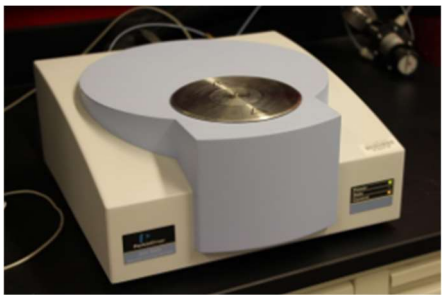

Figure 2-11: Perkin Elmer simultaneous thermal analyzer (STA 6000).

2.3.5. Isothermal Calorimetry

A TAM Air micro calorimeter 2700 Series is used to carry out isothermal calorimetry experiments in accordance with ASTM C 1702. Isothermal calorimetry is a useful technique to measure the heat evolution associated with exothermic or endothermic reactions and monitor the hydration reactions progression. The instrument used in this study is shown in Figure 2-12.

Figure 2-12: TAM Air instrument.

2.3.6. Thermal Conductivity

The thermal conductivity of porous ceramic samples is determined in accordance with ASTM C 177 using the guarded hot plate method. The applied power is measured in a central hot plate, which is surrounded by heat-isolating guards, ensuring 1D heat flow. Plate specimens (200 mm X 200 mm X 25 mm) are cast and tested. Fourier's equation is used to determine the thermal conductivity of the samples (λ) as shown in Equation 2-8:

$$\lambda = \frac{q\ L}{2\ A\ (T_{hot} - T_{cold})} \tag{2-8}$$

where q is the power input to the heater, L is the thickness of the plate, A is the surface area of the plate, T_{hot} is the temperature of the hot surface, and T_{cold} is the temperature of

the cold surface. The thermal conductivity set up used in this study is shown in Figures 2-13(a and b).

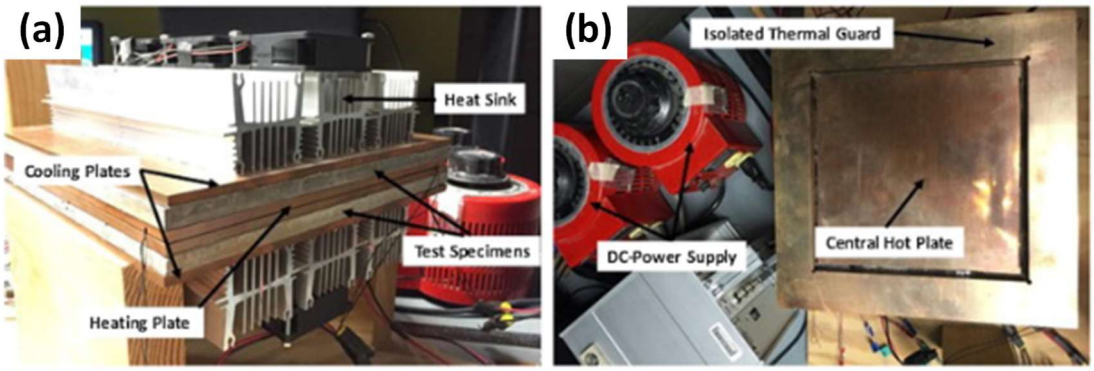

Figure 2-13: (a) Side profile of the guarded hot plate apparatus, and (b) aerial profile of the centralized metered section for determining thermal conductivity [72].

2.3.7. Mercury Intrusion Porosimetry (MIP)

Mercury intrusion porosimetry (MIP) is a useful method to investigate the pore structure of cementitious materials. Mercury porosimetry analyses the progressive intrusion of mercury into a porous structure under controlled pressures. From the pressure versus intrusion data, the instrument generates volume and size distributions using the Washburn equation. A Quantachrome Instruments Pore Master is the instrument used for intrusion measurement in this study as shown in Figure 2-14. The instrument is capable of handling a maximum pressure of approximately 415 MPa (60,000 psi).

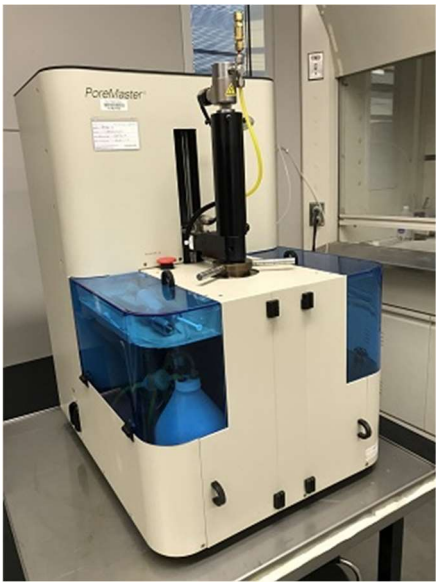

Figure 2-14: Quantachrome PoreMaster mercury intrusion porosimeter.

2.3.8. Mechanical Properties

Accu-Tek Touch 250 Series Compression Machine with electro-hydraulic pump is used in this study to determine the compressive strength of samples. This instrument is capable to handling up to 250,000 lbf. The compression test machine used in this study is presented in Figure 2-15(a).

The flexural strength of the beams specimens is determined using a three-point-bending test using a 4.45 kN servo-controlled MTS machine as shown in Figure 2-15(b). A displacement rate of 0.5 mm/min is used for the tests [73].

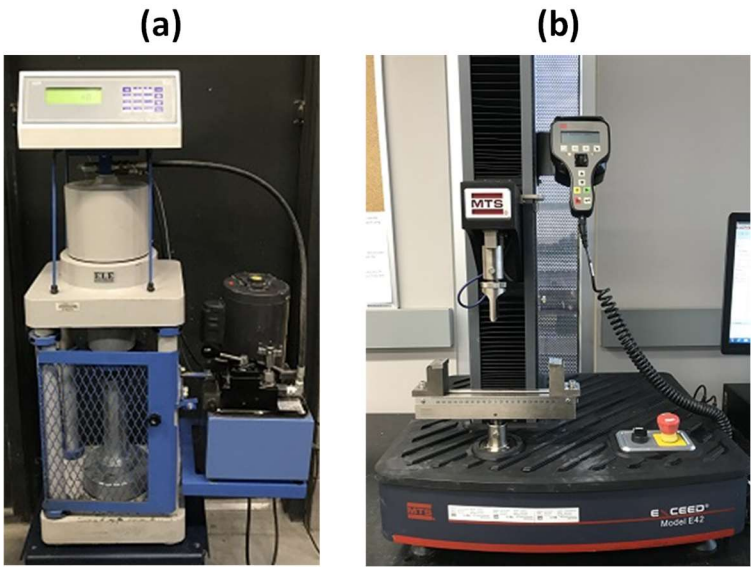

Figure 2-15: (a) Compression test machine, and (b) a 4.45 kN servo-controlled MTS machine showing three-point-bending test set up used in this study.

2.3.9. X-Ray Diffraction (XRD)

X-Ray diffraction (XRD) is performed on powdered samples using a high-resolution diffractometer (Siemens D 5000) in a θ-θ configuration using Cu-Kα radiation (λ=1.54 Å). X-Ray diffraction is rapid and useful analytical technique for phase identification in the materials by measuring the scattered X-ray intensity as a function of outgoing direction. In this study, the powder samples are prepared and tested between 2θ values of 10° and 70° with step size of 0.02° and step time of 1.0 s.

2.3.10. Scanning Electron Microscopy (SEM)

The microstructure and reaction product morphology of the samples are evaluated using a Nanoimages SNE-4500 Plus Table top SEM. The tabletop SEM operates at a significantly faster rate as compared to an XL-30 environmental SEM and at the same pixel resolution. The instrument is capable of operating in two imaging modes – SE and BSE. For this study, both imaging techniques are utilized to study the cured alkali activated samples. Small pieces of specimens cut from larger samples are polished to obtain a smooth surface for

electron microscopy. After polishing, the samples are ultrasonically cleaned and rinsed with alcohol to remove the debris from sectioning and handling and then placed on a stub with the help of carbon tape. The sample is then sputter-coated with Au-Pd coating to enhance the image quality. Sample is then placed in the chamber inside the instrument for imaging. In addition to the imaging, elemental analysis is also carried out using a Bruker XFlash 630 Energy dispersive X-ray spectroscope (EDS) built in the electron microscope. The instrument used in this study is presented in Figure 2-16.

Figure 2-16: Nanoimages SNE-4500 Plus Table top SEM.

2.3.11. Fourier Transform Infrared (FTIR)

Fourier transform Infrared (FTIR) spectra of the sample is acquired using an ATR Mattson Genesis FTIR spectroscope with an attenuated total reflectance (ATR) diamond crystal attachment. The spectra of the powdered samples are obtained in the wavenumber range of 4000 to 700 cm^{-1} at a resolution of 1 cm^{-1}. The instrument used in this study is shown in Figure 2-17.

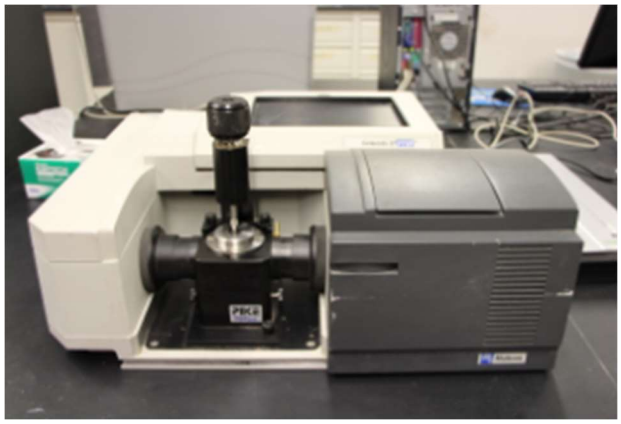

Figure 2-17: ATR Mattson Genesis FTIR spectroscope.

2.4. ALKALI-ACTIVATION OF ALUMINOSILICATES

The aluminosilicate constituents of the pozzolans are readily activated by strong alkali solutions to undergo geopolymerisation. The alkali activators include a mixture of alkali hydroxides and alkali silicates. Alkali hydroxides include potassium hydroxide (KOH), and sodium hydroxide (NaOH), while alkali silicates include potassium silicate (K_2SiO_3) and sodium silicate (Na_2SiO_3). Due to the availability of Na_2SiO_3 and NaOH, their mixtures are most commonly used as activators. The solid NaOH or KOH can be easily dissolved in water to produce aqueous NaOH or KOH of the desired concentration. Alternatively, a mixture of sodium carbonate (Na_2CO_3) and sodium sulphate (Na_2SO_4) have been used to achieve binding of slag mixtures [74].

The initial geopolymerization process involves alkaline-induced dissolution of Si and Al atoms in the aluminosilicate binders to form two tetrahedral anions, silicates $[SiO_4]^-$ and aluminates $[AlO_4]^-$ in the solution. The two tetrahedral anions undergo polymerization via shared oxygen atoms to form Si-O-Al-O bonds, thus, initiating the formation of aluminosilicate gel [15]. The reaction mechanism of alkali-activated aluminosilicates is shown in Figure 2-18.

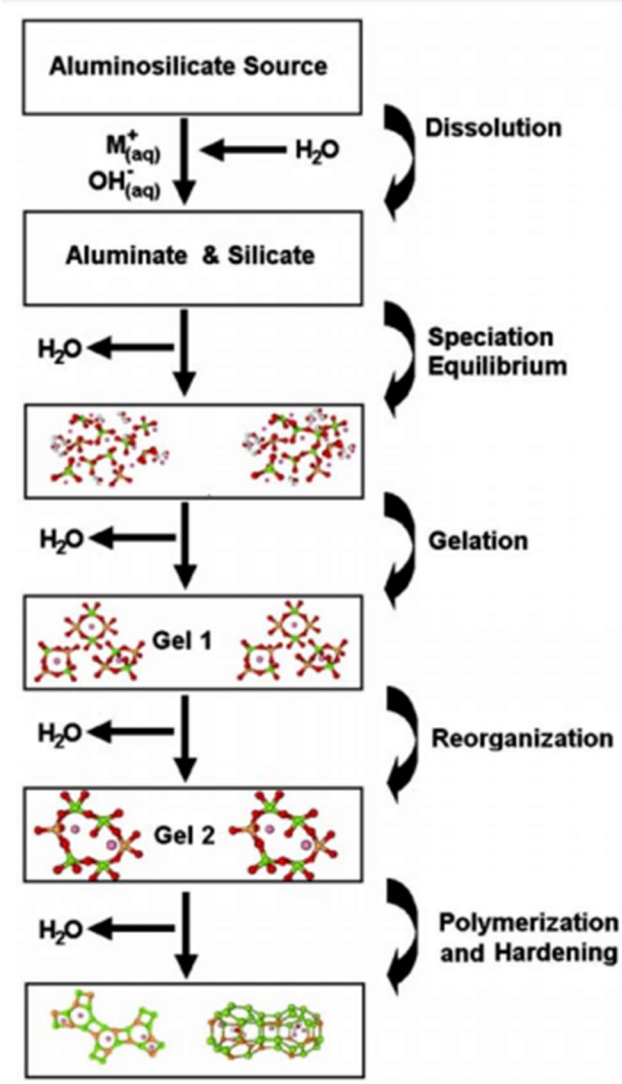

Figure 2-18: Reaction mechanism of alkali-activated aluminosilicates [15].

2.4.1. Application of Geopolymers – Porous Ceramics

The strength properties and foamability of geopolymers make it suitable for high-porous ceramics (foamed ceramics), which are potentially suitable for a variety of engineering applications such as filters [75], lightweight structural components [76], thermal insulators and acoustical materials for soundproofing [77,78]. Porous ceramic geopolymer-based materials have high water absorption and retention capacity due their unique pore morphology, pore size distribution, and pore connectivity. However, pore characteristics

in porous geopolymers are influenced by their chemical compositions and processing methods. Porous geopolymers synthesized with aluminosilicate binders containing higher H_2O/Al_2O_3 ratios (lower proportions of Al_2O_3) exhibit higher porosity and higher water absorption and retention capacities due to larger pore size and large pore volumes. However, the high porosity comes at the expense of the mechanical strength, which may have limitations in some applications, especially those requiring higher strengths. By contrast, porous ceramic-geopolymer based materials synthesized with lower H_2O/Al_2O_3 ratios (higher proportions of Al_2O_3) are denser, have smaller pore sizes, and smaller pore volumes, which results in a better water retention capacity without significant loss of mechanical strength. Such porous geopolymers may be useful for water retention applications requiring high-strength materials [79].

Highly porous geopolymers find applications in water and waste treatment due to their potentially unique properties especially as adsorbents/ion-exchangers, photocatalysts, high-pressure filtration membranes, filter media, anti-microbial materials, pH buffers, carrier or bioreactor surface and a media for solidification or stabilization of water treatment residues [80].

Closed porous geopolymer ceramics are useful for thermal-acoustic insulation applications. Closed cells in geopolymer foams (GFs) have low thermal and acoustic conductivities, thus suitable as heat-insulators and sound-proofing materials. Where fluid transport or filtration is not required in GFs, the suitable foaming agents include aluminum and silicon powder [63]. These foaming agents generate intense redox reaction due to high alkalinity of the system (see Equations 2-1 to 2-3).

2.4.2. Application of Geopolymers – Non-foamed Ceramics

Replacing OPC with geopolymer binders results in concrete products with better properties, particularly increased compressive and tensile strengths, low drying shrinkage, low heat of hydration, low water permeability, low chloride permeability, extreme acid resistance capacity, corrosion resistance, low thermal conductivity, and thermal/fire resistance [15,81].

Geopolymers also have the potential to offer economic benefits over OPC. Using low-cost pozzolanic materials as by-product such as fly-ash, GGBFS, and silica fume as well volcanic ash implies that the cost of producing geopolymeric composites is potentially more competitive than that of OPC. The cost of concrete products produced using OPC is 11% higher than geopolymeric composites of the same grade [82]. Geopolymeric composites have the potential to bring down environmental degradation costs by 7% compared to 39% higher for OPC concrete [83], even though more research on the exact environmental implications of geopolymers are warranted. Furthermore, the high strength and corrosion-resistant properties of geopolymeric composites offer cost-savings associated with maintenance or replacement of architectural structures or civil engineering projects as compared to normal-strength OPC concrete [82].

2.5. 3D-PRINTING OF CEMENTITIOUS COMPOSITES

Three-dimensional concrete printing (3DCP) of concrete structures is an innovative and challenging application in the construction industry. This process is also called additive manufacturing. It allows freedom of concrete product design, customization, automation and mass production, minimization of concrete waste, reduce labor, and use of low-cost construction materials [41,84–87]. Although a number of 3D printed concrete structures

are already being showcased worldwide (see Figure 2-19), multiple challenges remain at the technical and processing level. A suitable concrete for 3DCP should have a high workability (flow) for easy extraction, optimum open time and high early strength to support subsequent 3D-printed layers [55]. Suitability of the concrete material is a major challenge, with high-performance cement-based materials being non-3D printable due to poor rheological and stiffening properties [84,85]. A study reported in [88] evaluated the potential of extrudable foamed concrete to be 3D printable into multilayer insulating panels. It was noted that OPC-based foamed concrete was not 3D-printable as it lacked dimensional stability in the green state. The rheological properties of geopolymer concrete (smooth viscosity), controllable setting time and high strength makes geopolymers suitable candidate materials for digital fabrication through 3DCP.

Several geopolymer mix designs have been studied for optimization of rheological properties and controllable alkali activated geopolymerization for 3DCP. Two studies have developed mixture designs with a common goal to increase silica and alumina content in the 3D printable geopolymer pastes [54,55]. The study reported in [55] proposed a geopolymer mix design comprising ground granulated blast furnace slag, fly-ash, and silica fume with a mix ratio of 3:1:0.5. In the geopolymer mix design, silica fume contained 96.85 % silica, fly-ash contained >70% total Si-Al-Fe (42.09%, 25.13% and 13.16%) and slag contained > 50% total Si-Al-Fe (32.83%, 14% and 13.16%). The resultant mixture contained improved silica and alumina content, which are critical for geopolymerization. This geopolymer mixture design was activated using sodium meta-silicate powder (SiO_2: 50 wt.%, Na_2O: 46 wt.% and water: 4 wt.%); where it exhibited good rheology, shorter initial setting time, high compressive strength and printability. The good rheology of this

mixture included flowability and pumpability due to its low yield stress and viscosity, which requires low-to-moderate pumping pressure. These rheological properties were essential for extrusion of the geopolymer during 3DCP. Importantly, the yield stress, initial setting time and compressive strength were easily controlled by the amount of sodium silicate activator used [55]. The study reported in [54] used a mixture containing fly-ash, GGBS, and silica fume as the starting materials as well as river sand as a bulking material. Using Class F fly ash and silica fume implies high silica content was used. Addition of GGBS supplies free lime (CaO), which is useful in improving rheological properties of the geopolymer concrete mix, with respect to extrudability and open setting time (thixotropy open time), which is the time interval beyond which the material losses its extrudability property. However, incremental addition of GGBS in the mix design decreased the thixotropy and open time. Incremental addition of sand reduced the extrudability of the geopolymer mix [54].

A mortar mixture design comprising two parts of alkali-activated metakaolin and one part of OPC has also been evaluated for 3DCP suitability [89]. After 48-hr curing period, the printed mortar beams and cylinders exhibited significantly higher maximum compressive and flexural loads compared to those produced using OPC alone [89]. From the reviewed literature, individual geopolymer mortars lack the desired rheological properties for 3DCP, especially with respect to extrudability, printability and buildability. However, there is a dearth of experimental data on the optimization of mixture designs for geopolymer mortars for 3DCP.

Extrusion 3DCP is the most common technique and is already being used in large scale additive manufacturing processes for construction. Sufficiently viscous geopolymer with

adequate yield stress is extruded and placed layer-by layer in computer-controlled manner to produce physical objects. It is suitable for component manufacturing and placement of architectural walls for buildings, construction components (structural panels), in-situ castle, walls, and columns [85,87,90].

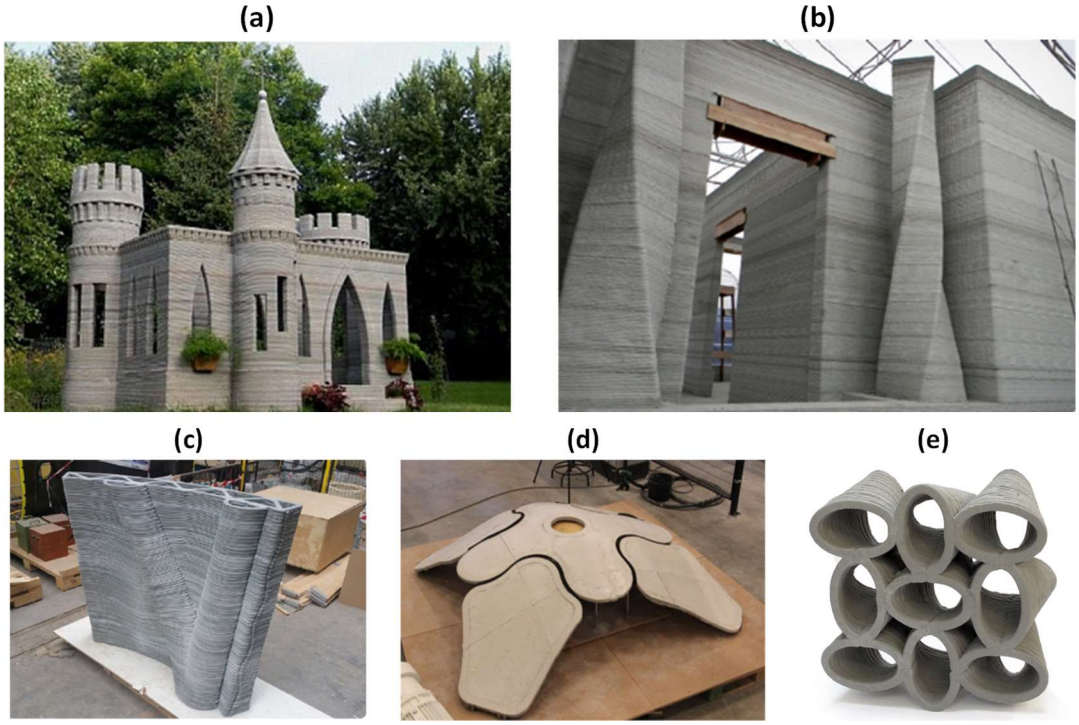

Figure 2-19: 3D printed (a and b) in situ castle and wall and columns [85,87], and (c-e) vertical and horizontal walls and panels [85,90]. Note that these are made using regular concrete and not geopolymers, but are shown here for demonstration of 3D printable concrete structured.

For this study a desktop printer based on Cartesian configuration [91] is customized with a 100 cm^3 barrel to print the paste and mortar mixtures. The printer used in this study is shown in Figure 2-20(a). The diameter of the barrel (D_b) used for paste printing is 35 mm. Two different die exit diameters are adopted in this study (4 mm and 6 mm) with lengths of 35 mm and 20 mm respectively (see Figure 2-20(b)) to maintain the die length-to-diameter ratios (L_d/D_d) of 9 and 3.33. The die entry diameter is 10 mm. The inner surface of barrel is lubricated to reduce the wall friction and ensure smooth and easy motion of the

piston. Slic3r software [92] is used to adjust the printing parameters including printing speed, layer width and height, and infill volume and pattern. The printing parameters used in this study are: layer height of 3mm, layer width of 6 mm, and printing speed of 20 mm/s.

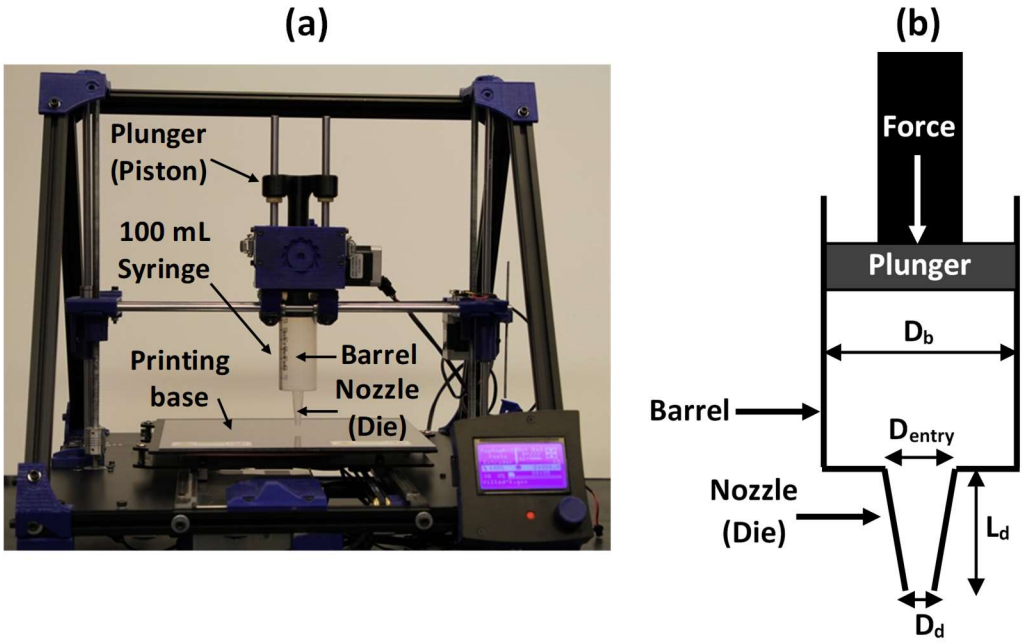

Figure 2-20: (a) The printer, (b) geometry of the syringe extruder used in this study.

CHAPTER 3[1]

SYNTHESIS AND CHARACTERIZATION OF ECONOMICAL, MULTI-FUNCTIONAL POROUS CERAMICS BASED ON ABUNDANT ALUMINOSILICATES

3.1. INTRODUCTION

Porous materials with tunable pore structure (sizes, volume, connectivity, and shapes) are widely used in environmental applications (water filtration, membranes) [19–23], energy conversion [24,25], building insulation (thermal and acoustic) [26–32], and vibration mitigation [32–34]. Porous materials with novel 3D architecture have also been developed to enhance electromagnetic absorption, with wide interest in military, aerospace, and electronic applications [93–95]. In general, the manufacturing routes for industrial porous ceramics are classified into: (i) partial sintering, (ii) ceramic suspensions, (iii) direct foaming, and (iv) sacrificial agents [96–98]. Porous ceramics are processed using extrusion, pressing or compaction, and casting methods. Recently, novel additive manufacturing-based techniques have been reported to fabricate microstructure-designed porous materials [23,32–34,45]. In general, many of the conventional porous ceramics are resistant to high pH solutions, acids, and organic solvents [99]. Furthermore, porous ceramics demonstrate efficient strength-to-weight ratio, high temperature resistance, and microbial or biological degradation resistance [99]. They are also more shock resistant, and demonstrate better corrosion and wear resistance, making them the material of choice for a wide variety of applications. Almost all the traditional methodologies to fabricate porous

[1] This chapter is derived from publication: H. Alghamdi, A. Dakhane, A. Alum, M. Abbaszadegan, B. Mobasher, N. Neithalath, Synthesis and characterization of economical, multi-functional porous ceramics based on abundant aluminosilicates, Materials & Design. 152 (2018) 10–21.

ceramics involve high temperature treatment (i.e., sintering) to complete the process [100]. The use of coarse powders in sintering or partially sintering a green ceramic hinders full densification. The use of a pore forming agent in the process and subsequently sintering the mixture results in the entrapment of pores in the matrix, leading to a porous ceramic. The use of high temperature treatment often results in better mechanical and thermal properties.

In this study, a geopolymerization process is implemented to develop an economical porous ceramic from an abundantly available aluminosilicate material. Geopolymers are amorphous three-dimensional aluminosilicate-based binders, which can be synthesized from natural minerals (such as the volcanic tuff used in this study), calcined clays (kaolin/metakaolin), or industrial wastes (fly ash). Strong alkaline activators are needed to initiate the activation of the aluminosilicates and the formation of an amorphous-to-semi crystalline aluminosilicate inorganic polymer (geopolymer) [8,9]. The high pH of the alkaline activators breaks down the Si-O-Si and Al-O-Al covalent bonds [12], and a strong and durable gel network is formed during the geopolymerization process. More details on the mechanisms and reactions in geopolymerization can be found in literature [14–16]. The advantage of geopolymer-based porous ceramic is that they can likely be produced at lower temperatures (than that is conventionally used for ceramic sintering) because the chemical reaction (alkaline activation) and consolidation can partly replace the sintering process [10,11]. The most common activators used in the geopolymerization reaction of aluminosilicates are alkaline hydroxide (Na or K as the cations) and/or their corresponding silicate solutions. Potassium-based geopolymers have been reported to provide better microstructure control and thermal properties [101–103].

Economical porous ceramics are synthesized in this study through the use of a volcanic tuff natural pozzolan as the primary source material. A potassium-based alkaline solution, comprising of a combination of hydroxides and silicates is used as the activating agent. Different precursor compositions, curing temperatures (lower than the sintering temperatures used in ceramic production), and the use of pore forming agents are used to obtain the desired pore characteristics. Two methodologies are outlined – in the first procedure, treatment temperatures up to 650^{o}C are employed whereas compositional changes effected in the second procedure reduces the required treatment temperature to 85^{o}C. The pore structure features (pore volume, sizes, connectivity), reaction products, and the selected performance characteristics (percolation, thermal conductivity, strength) are evaluated to ascertain the efficiency of the chosen geopolymerization process in producing porous ceramics. The study provides novel, economic (based on an abundant natural pozzolan), and energy-efficient (low processing temperatures) routes for synthesis of porous ceramic matrices for thermal and filtration applications. The combination of synthesis methods, microstructural characterization, and performance evaluation reported in this study is expected to help in the selection of these multi-functional matrices for desired applications. The fact that such a material can be produced in a facility that routinely deals with cement-based materials, makes the scale-up of production relatively easier, and thus high-volume applications such as building envelope systems can be easily realized, in addition to lower-volume applications such as filtration media.

3.2. EXPERIMENTAL PROGRAM

3.2.1. Materials

The source materials utilized in this study are: (i) a volcanic tuff natural pozzolan (NP), (ii) metakaolin (MK), (iii) silica fume (SF) and (iv) high purity-alumina powder (Al_2O_3). The chemical compositions of the source materials are shown in Table 3-1. The median particle sizes are 12.0 μm for NP, 0.1 μm for SF, 5.3 μm for MK, and 6.0 μm for the alumina powder, as determined using laser particle size analysis.

Table 3-1: Chemical composition and physical characteristics of the source materials.

Oxide	Amounts (% by mass)			
	Natural pozzolan (NP)	Metakaolin (MK)	Silica Fume (SF)	Alumina Powder (Al_2O_3)
Silicon Dioxide (SiO_2)	74.83	51.7	93.4	---
Aluminum Oxide (Al_2O_3)	14.9	43.2	0.42	> 99
Iron Oxide (Fe_2O_3)	0.96	0.5	0.52	---
Calcium Oxide (CaO)	1.66	---	1.91	---
Magnesium Oxide (MgO)	1.75	---	---	---
Sulfur Trioxide (SO_3)	0.01	---	0.34	---
Sodium Oxide (Na_2O)	2.10	---	0.25	---
Potassium Oxide(K_2O)	3.39	---	0.79	---
Loss on Ignition (L.O.I)	---	0.16	2.3	---
Density (g/cm^3)	2.46	2.5	2.2	---

Figure 3-1 shows the X-ray diffraction (XRD) patterns of the source materials. Although the natural pozzolan is mostly crystalline, it also contains glassy phases as noticed in the halo recorded in the 2θ range of 20° to 35°. The main peak in XRD pattern of the NP located at a 2θ of 28° is attributed to quartz. The other crystalline phases are attributed to minerals affiliated to the feldspar group {((K or Na) $AlSi_3O_8$)) or ((Ca, Na) $Al2Si_2O_8$)}. The other source materials, MK and SF are amorphous as noticed by the broad hump in the XRD spectra (see halo in the 2θ = 15° to 30° for MK and 2θ = 15° to 35° for SF).

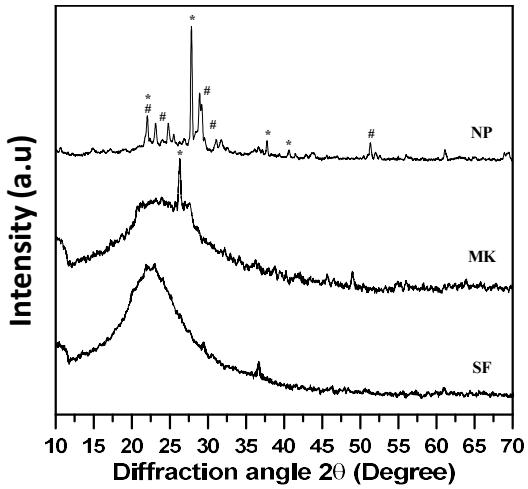

Figure 3-1: X-ray diffraction patterns of the natural pozzolan (NP), metakaolin (MK), and silica fume (SF) (*: quartz; #: Feldspar group {((K or Na) $AlSi_3O_8$)) or ((Ca, Na) $Al_2Si_2O_8$)}).

3.2.2. Sample Preparation

Two procedures were adopted in this study for the preparation of porous aluminosilicate-based ceramic systems. The first procedure (Procedure I) involves the use of the source materials listed earlier along with an activating solution prepared by dissolving KOH pellets into potassium silicate solution (KASIL). An alkaline cation such as K^+ can promote and stimulate condensation reactions to complete geopolymerization [104]. Additionally, the polycondensation of aluminate and silicate anions is influenced by the size of the cation; the larger the cation, the higher the extent of polycondensation [105]. Also, geopolymers based on potassium has been noted to show better elevated temperature performance than those based on sodium [106]. Thus, potassium-based activators are employed in this study to synthesize porous ceramic matrices.

KASIL, supplied by PQ Corporation has a solids content of 44%, a silica modulus (molar ratio of SiO_2-to-K_2O), M_s of 3.29, and density of 1.34 g/cc. For matrices prepared using this procedure, the NP content ranged from 50% to 100% by mass whereas the MK or SF

content ranged from 0 to 50% by mass. The proportions of the seven samples prepared using Procedure I are shown in Table 3-2. The amounts of potassium silicate and potassium hydroxide were adjusted to provide an activator with an M_s of 1.5. The ratio of K_2O-to-total powder was maintained as 0.05. The mass-based liquid-to-powder ratio (l/p) varied between 0.40 and 0.60; with a higher l/p required for blends with higher amounts of metakaolin or silica fume. This is because of the fine sizes and hydrophilicity of these particles. As is well known, water is essential during the reactions to help dissolve the starting solid aluminosilicates and hydrolyze alumina and silica ions, but the resulting dilution reduces the alkaline activity leading to slow reaction and polymerization. A high water content can hinder polycondensation when the intrinsic reaction changes from hydrolysis (water consumption) to polycondensation (water release) [107].

The activator solution was added to the powder mixture and mixed for at least 15 minutes until a homogeneous mixture was obtained. The mixture was then placed in cylindrical molds (25 mm diameter and 50 mm long) and immediately inserted into a laboratory oven for heat curing. In this procedure, all the samples were sequentially exposed to two different time-temperature combinations. First, the samples were subjected to 100ºC for 24 h to complete the polycondensation and polymerization process. Thereafter, the samples were heated to 650ºC for 3 h to ensure adequate property development. After heat treatment, the samples were cooled by exposing them to ambient temperature before testing.

Table 3-2: Compositions of seven matrices prepared using Procedure I.

Sample ID	NP (%)	MK (%)	SF (%)	K_2O-to-total powder (mass ratio)	SiO_2/K_2O (molar ratio)	Liquid/powder (mass-based)
GK100	100	---	---	0.05	1.5	0.4
GKM85	85	15	---	0.05	1.5	0.5
GKM75	75	25	---	0.05	1.5	0.5
GKM50	50	50	---	0.05	1.5	0.6
GKS85	85	---	15	0.05	1.5	0.5
GKS75	75	---	25	0.05	1.5	0.5
GKS50	50	---	50	0.05	1.5	0.6

(In this table, G stands for geopolymerized samples, K for the natural pozzolan, M for metakaolin, and S for silica fume).

In the second procedure, only NP and MK were used as the starting materials, along with alumina powder. Geopolymers with a molar SiO_2-to-Al_2O_3 ratio of 4.0 are reported to have high degrees of polymerization and smaller pore sizes [26,66]. In this case, the activator solution was prepared using potassium silicate and KOH solutions to obtain a molar composition of K_2O. $2SiO_2$. $18H_2O$. A combination of NP and MK were added along with the alumina powder to the activating solution. Alumina powder was used to maintain a molar ratio SiO_2-to-Al_2O_3 ratio of 4.0 because the NP did not have ample alumina as can be noted from Table 3-1. The NP content ranged from 0 to 35% by mass whereas the MK and alumina powder content ranged from 50% to 100% and 0% to 15% by mass respectively as shown in Table 3-3. The three mixtures thus prepared are denoted as G1, G2, and G3. In order to enhance the porosity of the binder systems, silicon powder of 99.9999% purity (supplied by Alfa Aesar) was used as a foaming agent (FA) along with the aforementioned binders (mixtures F1, F2, and F3 in Table 3-3). The free metallic silicon redox reaction could induce porosity by H_2 evolution as shown in Equation 3-1 [10,11]. Other materials such as hydrogen peroxide (H_2O_2), aluminum powder (Al) [61,66], and surfactants [61] have been used as pore formers in geopolymeric systems.

$$4H_2O + Si^0 \rightarrow 2H_2 \uparrow + Si(OH)_4 \quad (3\text{-}1)$$

The foamed samples were prepared by adding 0.02 wt% of silicon powder to the G series pastes, during mechanical mixing. The contents were mixed for at least 15 minutes until a homogeneous mixture was obtained. The mixture was placed in molds and transferred to an oven set to 85°C and treated for 24 h to complete the polycondensation reactions. Subsequently, the hardened samples were demolded and kept at room temperature to be cooled.

Table 3-3: Compositions of matrices prepared using Procedure II. The ratios listed are molar ratios.

Samples	Binder composition	Silicon Powder	SiO_2/K_2O	SiO_2/Al_2O_3	H_2O/K_2O
G1	100% MK	0%	2	4	18
G2	70% MK, 25% NP, 5% Al_2O_3	0%	2	4	18
G3	50% MK, 35% NP, 15% Al_2O_3	0%	2	4	18
F1	100% MK	0.02%	2	4	18
F2	70% MK, 25% NP, 5% Al_2O_3	0.02%	2	4	18
F3	50% MK, 35% NP, 15% Al_2O_3	0.02%	2	4	18

3.2.3. Test Methods

Mercury intrusion porosimetry (MIP) is a useful method to investigate the pore structure of cementitious materials. To determine the porosity and critical pore sizes, the samples were weighed and placed into the sample holder. The sample holder was carefully placed into the low-pressure chamber of the porosimeter (Quantachrome Instruments Pore Master). In this step, the applied pressure fills the sample with mercury from ambient pressure to 345 KPa (60 psi). The sample was then removed from the low-pressure chamber and placed in the high-pressure chamber. In this step, the mercury intrudes the sample through the application of pressure, up to 414 MPa (60,000 psi). The pore diameter (d) as

a function of the intrusion pressure is obtained from the Washburn equation (Equation 3-2).

$$d = \frac{-4\,\sigma\,cos\theta}{\Delta P} \quad (3\text{-}2)$$

where ΔP is the difference in the pressure between successive steps (MPa), θ is the contact angle between mercury and the cylindrical pore which was taken as 130° in this study [27,108,109], and (σ) is the surface tension between mercury and the pore walls (485 mN/m).

A gas pycnometer (Ultrapyc 1200e, Quantachrome Instruments) was used to determine the specific gravity and bulk density of the samples.

Thermo-gravimetric analysis (TGA) was performed by using a Perkin Elmer simultaneous thermal analyzer (STA 6000). In this study, TGA was performed to identify the reaction products. The sample was heated from room temperature to 50°C and then held for 1 min, and then heated to 800°C at a constant rate of 15°C/min in an inert (N_2) environment. The mass loss during the thermal treatment was recorded as a function of the temperature.

X-Ray diffraction (XRD) was performed on powdered samples using a high-resolution diffractometer (Siemens D 5000) in a θ-θ configuration using Cu-Kα radiation (λ=1.54 Å). The samples were tested between 2θ values of 10° and 70° with step size of 0.02° and step time of 1.0 s.

The microstructure and morphology of the porous samples were evaluated using a Philips XL30 Field Emission Environmental scanning electron microscope (FESEM) in the secondary mode. Prismatic pieces of specimens were prepared by sizing larger samples, and the surface polished using fine-grit sandpaper to obtain a smooth surface for secondary electron imaging.

Fourier transform Infrared (FTIR) spectra of the samples were obtained using an ATR Mattson Genesis FTIR spectroscope with a single reflection attenuated total reflectance diamond crystal attachment. The spectra of the powdered samples, was obtained in the wavenumber range of 4000 to 700 cm^{-1} at a resolution of 1 cm^{-1}.

Electrical impedance spectroscopy (EIS) was used to determine the effective electrical conductivity (σ_{eff}) of the samples, which in turn were used to determine the pore connectivity factor (β). A Solartron^{TM} 1260 frequency response analyzer operating in the 1 Hz to 1 MHz range, with a 250 mV AC signal, was employed. The impedance data was recorded at a rate of 10 steps per decade of frequency. The measurements were carried out on 25 mm diameter and 50 mm long cylindrical specimens. The specimens were soaked in 3% NaCl solution for 24 h to saturate the pores (σ_o of NaCl = 4.4 S/m). Two copper plates were placed at the ends of the specimen to be used as electrodes and attached to the impedance analyzer. From the Nyquist plot (the plot of real vs. imaginary impedance), the meeting point of the bulk arc and electrode arc is denoted as the bulk resistance of the specimen (R_b) [110]. The effective electrical conductivity (σ_{eff}) and the pore connectivity factor (β) were determined as shown in Equations 3-3 and 3-4:

$$\sigma_{eff} = \frac{L}{(R_b \cdot A)} \tag{3-3}$$

$$\beta = \frac{\sigma_{eff}}{(\sigma_o \cdot \phi_V)} \tag{3-4}$$

where, L is the length of the specimen, A is the cross-section area of the specimen, and ϕ_V is the volumetric porosity.

For the percolation test, 75 mm diameter x 150 mm long cylindrical foamed samples (F1, F2, and F3) were prepared. By using an electrical saw, three 10 mm thick discs were cut

from each sample. The external perimeters of the samples were coated with epoxy and the samples were carefully inserted into the tube. The contacts between the sample and the internal surface of the tube was sealed by silicon to ensure that no water leaked through the specimen sides. 30 ml of tap water was poured into the test pipe and the water was allowed to seep through the samples under gravity. The time taken to flow through the 10 mm thick disc was measured using a stopwatch, to determine the flow rate. Only the foamed samples for used for this test because the other samples did not have enough pore volume or connectivity to enable percolation without any applied pressure.

The thermal conductivity of porous ceramic samples was determined in accordance with ASTM C 177 using the guarded hot plate method. The applied power is measured in a central hot plate, which is surrounded by heat-isolating guards, ensuring 1D heat flow. Plate specimens (200 mm X 200 mm X 25 mm) were cast and tested after the corresponding curing regimes mentioned in the previous section. Fourier's equation was used to determine the thermal conductivity of the samples (λ) as shown in Equation 3-5:

$$\lambda = \frac{q\ L}{2\ A\ (T_{ho}\ - T_{cold})} \tag{3-5}$$

where q is the power input to the heater, L is the thickness of the plate, A is the surface area of the plate, T_{hot} is the temperature of the hot surface, and T_{cold} is the temperature of the cold surface.

The compressive strengths of the samples were determined in accordance with ASTM C 109. Cylindrical samples, 25 mm in diameter and 50 mm high were tested in a compression frame to determine the strength.

3.3. RESULTS AND DISCUSSIONS

3.3.1. Compressive Strength

The compressive strengths of cylindrical samples of the porous ceramic prepared using Procedures I and II (Tables 3-2 and 3-3) are shown in Figures 3-2(a) and (b). The matrices prepared using a combination of the natural pozzolan and metakaolin in accordance with Procedure-I does not show sufficient mechanical strength, as can be noticed from Figure 3-2(a). This can be attributed to the fact that the alkalinity of the activator is not high enough to enable the formation of sufficient amount of reaction products by breaking down the Si-O-Si and Al-O-Al bonds, especially given the fact that the NP lacks significant amorphous content (Figure 3-1). When silica fume is used along with NP, the matrices gain higher strengths, contributed both by the reactivity of fine silica fume, as well as the enhanced silicate polymerization at higher temperatures. Not surprisingly, the matrices synthesized at 650^{o}C show higher strengths. For the matrices proportioned using the second procedure, the strengths are lower for the foamed samples, because of their higher porosities (see Table 3-5). The compressive strengths of the non-foamed samples are around 10 MPa, while those for the foamed samples are around 4 MPa. Both these systems can be used as (non-heavy) load-bearing components in buildings, or as insulation. The strengths are in the range of typical aerated or foamed concrete blocks used as masonry elements or load-bearing or non-load bearing insulation in buildings.

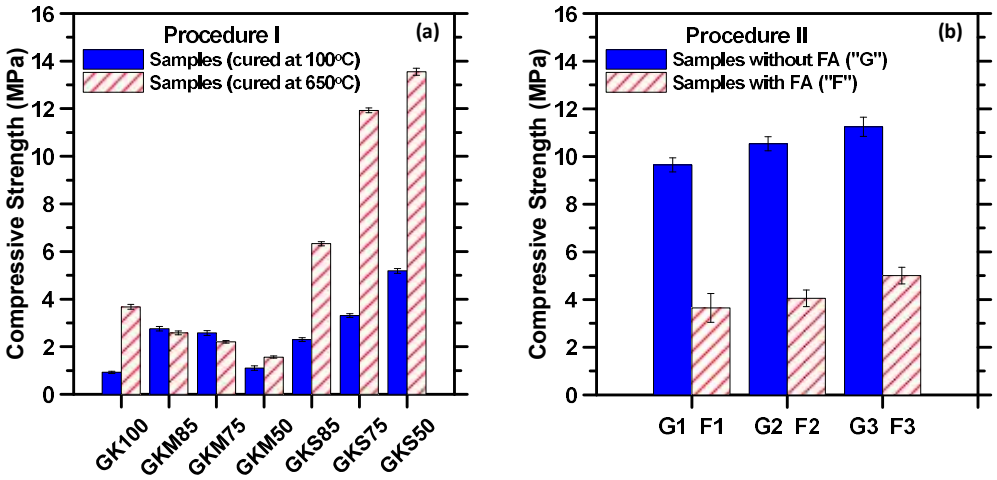

Figure 3-2: Compressive strength of all the matrices prepared using: (a) Procedure I, and (b) Procedure II.

3.3.2. Pore Structure

This section investigates the pore structure of the different porous ceramics synthesized as part of this study. The pore volumes and pore sizes are important in ensuring hydraulic and thermal performance of these porous materials, which are important potential avenues for use of these novel materials. The influence of material composition, the type of activation, and treatment conditions on the resultant pore structure are discussed.

Figure 3-3 shows the pore structure features for the blends proportioned using Procedure I (Table 3-2). Figures 3-3(a) and (b) depict the cumulative volume intruded and differential volume curves as a function of pore sizes for the activated NP-MK-SF blends treated at 100°C while Figures 3-3(c) and (d) shows the corresponding information for the blends treated at 650°C. Table 3-4 shows the porosities of these samples along with the critical pore sizes (corresponding to the peak in the differential volume curve, which is indicative of the percolating pore size in the material [111]). The specific gravities and bulk densities of the samples are also shown in this table. The porosities were calculated using the cumulative volume of mercury intruded, and the bulk densities. In general, all the

specimens have porosities in the range of 40% to 50%. The higher porosity in these mixtures can be attributed to the higher liquid-to-binder ratio used in these samples because the excess water that does not contribute to the geopolymeric reaction aids in pore formation during its removal due to heating [21,107]. The higher alumina content also could have acted as a pore forming agent in alkaline environments [61,66]. However, the concentration of alkalis used in this procedure is much lower than its concentration used in other previous studies [10,112], which could have impacted the pore formation. It can be noticed that the porosity is the highest for the NP-MK blend containing equal amounts of both, while the critical pore sizes are quite similar irrespective of the chosen compositions. With an increase in treatment temperature to 650^{o}C, the porosities and critical pore sizes are relatively unchanged, but the surface texture of the samples were found to be significantly improved, with no noticeable cracks and little to no powdering on scratching. The critical pore sizes of the SF containing samples were much lower than that of the MK containing samples, alluding to the increased degree of silica polymerization, especially when exposed to higher temperatures (these samples were also stronger than the rest, especially when treated at the higher temperature). Also note the bimodal pore size distribution in the specimens containing SF (Figure 3-3), where the smaller pores (< 0.1 μm) are attributed to those in the reaction product, and the larger ones due to the removal of water during the geopolymerization reaction. The specific gravities and bulk densities reported in Table 3-4 also are not significantly different from each other. Heat treatment also did not produce any significant changes even though the MK-containing blends show a slightly lower bulk density than the corresponding SF-containing blends. The blend

containing 50% NP and 50% MK showed the largest porosity and pore sizes and was chosen for further studies.

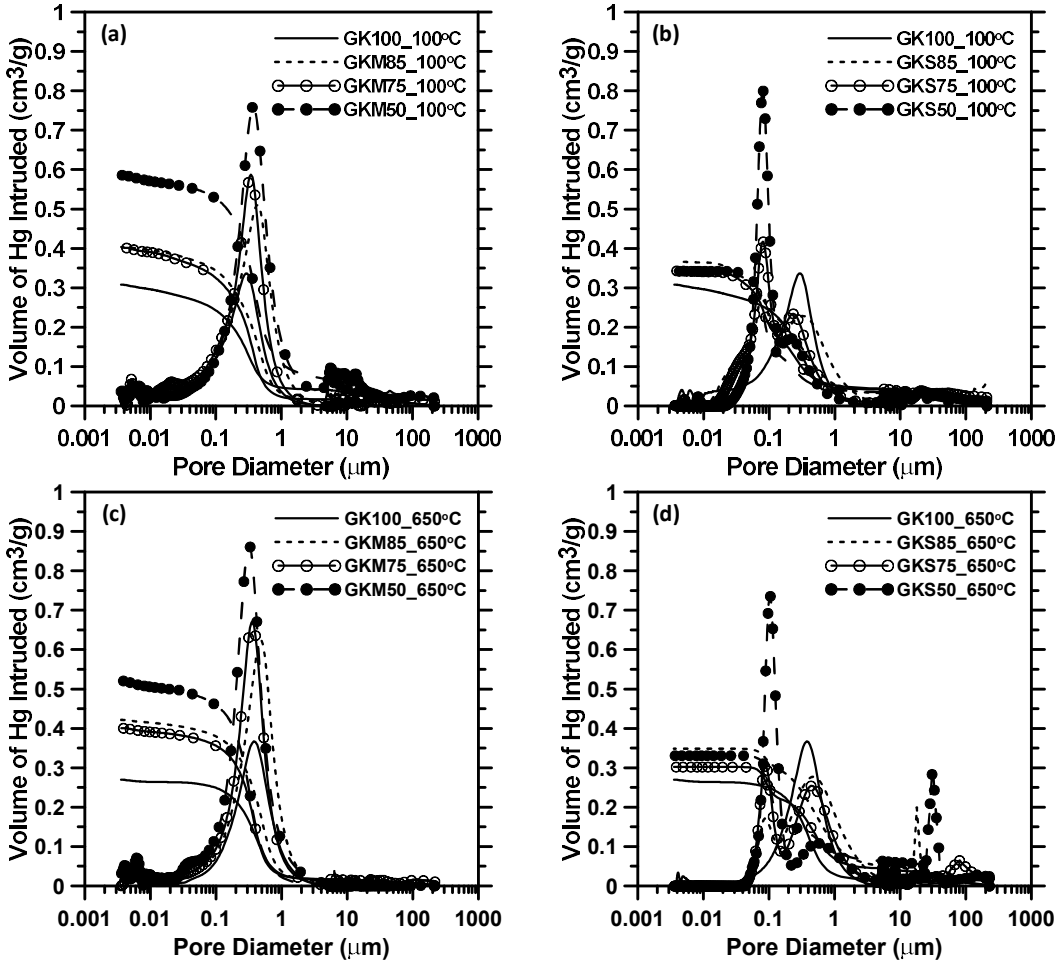

Figure 3-3: Cumulative pore volume and differential pore volume of samples proportioned using Procedure I: (a) and (b) treated at 100°C; (c) and (d) treated at 650°C. Note that (a) and (c) shows the specimens with metakaolin and (b) and (d) shows those with silica fume.

Table 3-4: Porosity and pore sizes of samples prepared using Procedure I.

Sample ID	Porosity (%)		Critical pore size (μm)		Specific gravity (g/cm^3)		Bulk density (g/cm^3)	
	100ºC	650ºC	100ºC	650ºC	100ºC	650ºC	100ºC	650ºC
GK100	43	39	0.30	0.30	2.60	2.63	1.41	1.45
GKM85	52	51	0.40	0.40	2.54	2.57	1.30	1.20
GKM75	52	51	0.34	0.36	2.49	2.55	1.30	1.27
*GKM50	70	64	0.38	0.32	2.46	2.47	1.20	1.23
GKS85	48	48	0.07	0.08	2.48	2.60	1.30	1.40
GKS75	44	43	0.08	0.09	2.47	2.53	1.28	1.43
GKS50	43	43	0.08	0.10	2.46	2.44	1.26	1.30

* Blend chosen for TGA, FTIR, XRD and thermal conductivity tests.

As described earlier, in Procedure II, silicon powder was used in one set of samples as a foaming agent to create highly porous matrices with very small continuous pores that could be used for specific applications such as in water filtration. For such applications, the porous material should have enough porosity and small but continuous pores to trap the contaminants. The pore sizes should be conductive to filter either all or some of: (a) parasites (size around 6 μm), (b) bacteria (size in the range of 0.7 μm to 1.0 μm), and (c) viruses (size range from 25 nm to 28 nm). Figure 3-4 shows the porosity (obtained from MIP) and critical sizes for the blends proportioned using Procedure II (Table 3-3). The foamed samples have, in general, higher cumulative porosities and critical pore sizes than the non-foamed ones, as would be expected. Table 3-5 shows the total porosity of the foamed samples, in addition to the MIP-derived pore structure features, specific gravities, and bulk densities. The foamed samples showed larger pores because of the expansion, but the MIP test cannot account for large pores where mercury intrudes under little to no pressure. Hence, Equation 3-6 that employs the bulk density and specific gravity was used to calculate the total porosity in addition to the MIP-derived pore structure parameters. A comparison of the porosity values determined using both the methods are reported in Table

3-5. It can be noticed from the table that the MIP-derived porosity and the differential pore sizes of all the samples decreased with increasing NP content. The porosity and critical pore sizes of foamed sample (F series) were much higher than that of geopolymerized samples (G series), attributable to addition of foaming agent. Sample (F3) containing 35% of NP showed lower critical pore size compared to other foamed samples, alluding to the fact that NP has played an important role in pore size reduction. The foamed samples were chosen for further tests.

$$Total\ porosity\ (\%) = \left(1 - \frac{Bulk\ density}{Specific\ gravity}\right) X100 \qquad (3\text{-}6)$$

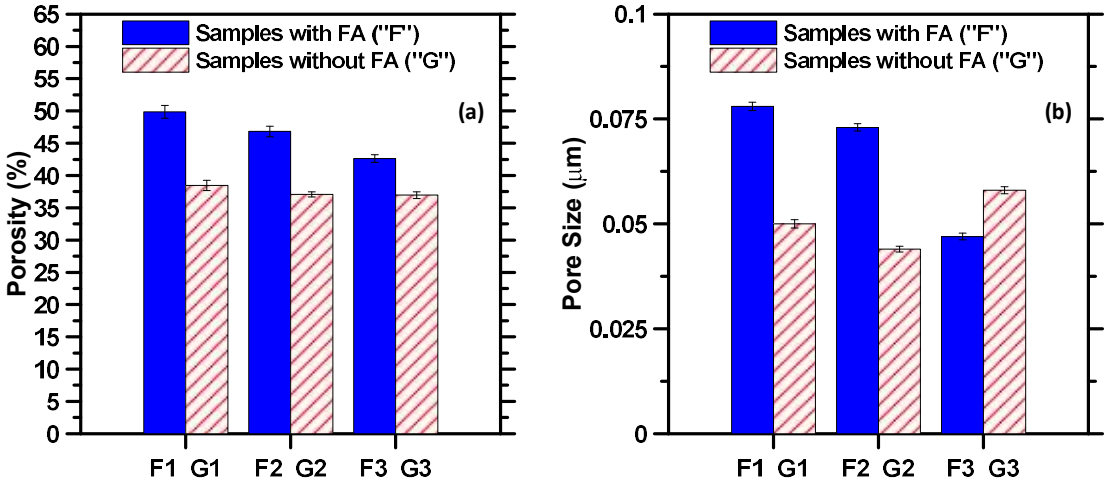

Figure 3-4: (a) Porosity, and (b) critical pore size of samples proportioned using Procedure II.

Table 3-5: Specific gravity, bulk density, total porosity, and MIP-derived pore structure features of samples prepared using Procedure II with the foaming agent.

Foam Samples	Specific Gravity** (g/cm^3)	Bulk Density** (g/cm^3)	Total Porosity (%)	Porosity (%) determined by MIP	Differential Pore Size (μm)
F1*	2.529±0.0005	1.01 ±0.002	≅60	≅50	0.078
F2*	2.577 ±0.0002	1.01±0.003	≅60	≅47	0.073
F3*	2.648 ±0.0003	1.05±0.003	≅60	≅41	0.047

* Samples chosen for TGA, FTIR, XRD, thermal conductivity and percolation tests.
** Standard deviation was calculated on three samples.

3.3.3. Comparison of Pore Structure and Microstructure Features of the Selected Highly Porous Mixtures

Figure 3-5 shows a comparison of pore structure features of the selected highly porous samples synthesized using Procedures I and II. Figure 3-5(a) depicts the porosity determined using MIP as a function of pore diameter for highly porous samples while Figure 3-5(b) shows the fraction of representative size ranges detected using MIP. As per IUPAC guidelines, the pore sizes were divided into the following ranges: 0.0036 to 0.028 μm, 0.028 to 1 μm, and greater than 1 μm. It is observed that the GKM50 samples cured at 100^{o}C and 650^{o}C had almost the same fraction of pores in the size range of 0.028 to 1 μm and 0.0036 to 0.028 μm. However, the fraction of pores greater than 1 μm decreased from approximately 12% in the sample treated at 100^{o}C to 2% for the same sample treated at 650^{o}C. On the other hand, the fraction of pores greater than 1 μm were about 2% in all the foamed samples. Moreover, the F3 sample containing 35% of NP showed the highest fraction of pores (~11%) in the range of 0.0036 to 0.028 μm, whereas the F1 and F2 samples had around 6.5% of pores in this size range. In fact, the fractions of pores of size range 0.028 to 1 μm and 0.0036 to 0.028 μm are the most important ranges in the porous ceramic matrices particularly in separation (filtration) applications in order to trap all the contaminants including viruses.

Figure 3-6 depicts the SEM micrographs of the fracture surfaces of the selected highly porous samples. Only two magnifications are shown here – the first to provide a low-resolution image of the sample to show the relative pore size to the specimen surface, and the second to provide an understanding of the microstructure. For the specimens prepared using Procedure I (GKM50 samples at two temperatures), the surface porosity appears to

be quite low, but the microstructure at the higher resolution show a denser structure in the sample synthesized at 650°C, which is also reflected in the compressive strength and porosity results shown earlier. The higher degree of polymerization owing to the higher temperature is responsible for the denser structure. The low magnification image also shows that the matrix synthesized at the higher temperature has a smoother surface, which made this specimen resist surface abrasion and powdering when scratched. For the samples proportioned using Procedure II with the addition of a foaming agent, all the samples exhibit macropores (large pores) with irregular shapes because of expansion due to foaming agent addition, as can be easily noticed from Figure 3-6. Additionally, samples F2 and F3 sample show denser geopolymeric microstructures as compared to sample F1, which was also reflected in their compressive strengths (see Figure 3-2).

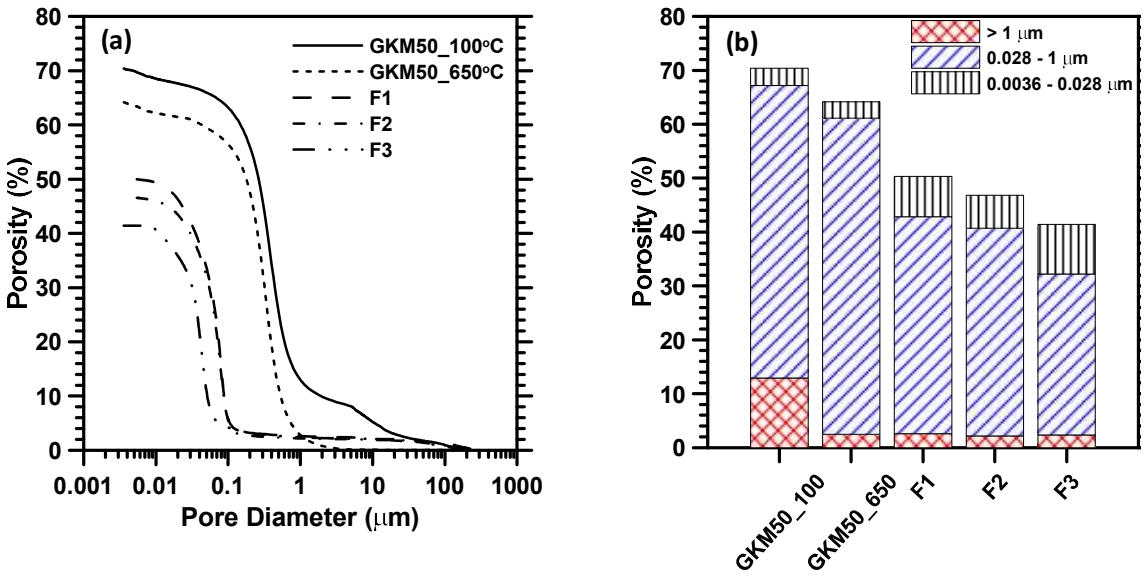

Figure 3-5: Comparison of the pore structure features of the highly porous samples. (a) porosity as functions of pore diameter, (b) pore size ranges of the highly porous samples.

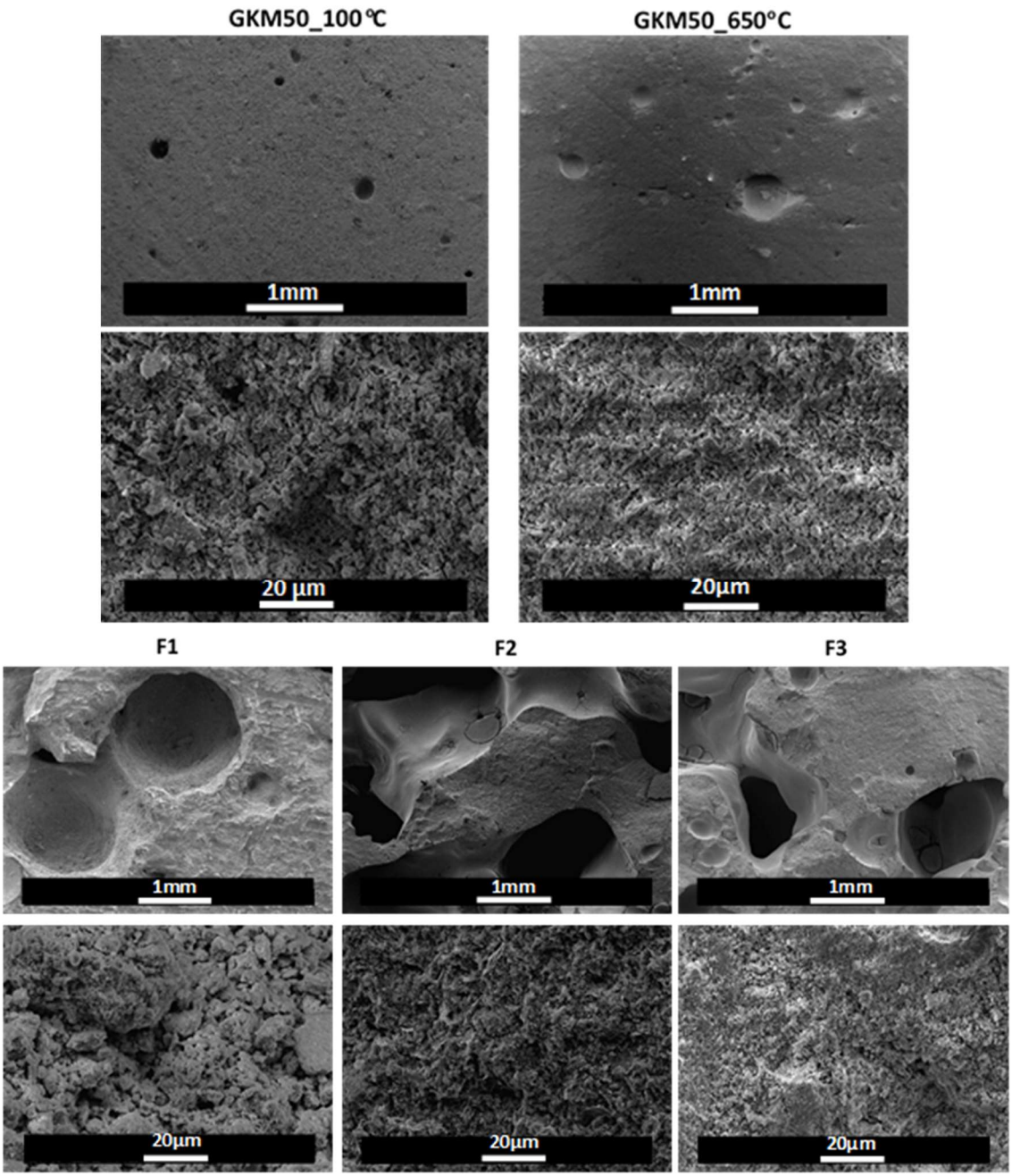

Figure 3-6: SEM micrographs of fracture surfaces of the selected porous matrices at two different magnifications. The matrix with NP and MK processed at 100°C and 650°C are shown as a representative sample for Procedure I, and the three foamed samples (F1, F2, and F3) for Procedure II.

3.3.4. Thermal Analysis

Thermogravimetric (TG) and differential thermogravimetric (DTG) curves of the selected samples are depicted in Figure 3-7. For the GKM50 specimen treated at two different temperatures, the peak in DTG curve in the 100-150ºC range is associated with the mass loss attributed to the major reaction product (K-A-S-H) gel. The mass loss up to 100ºC was 0.64% and 0.11% respectively for the samples treated at 100ºC and 650ºC respectively. The lower mass loss for the sample treated at the higher temperature shows the stability of the reaction products. The remaining loss was attributed to the adsorbed water in the small pores and to the water bound to the K-A-S-H gel [16]. On the other hand, Figures 3-7 (b, c, and d) show the TG and DTG curves of foamed samples F1, F2, and F3. Most of the mass loss for these samples occur below 300ºC. The mass loss until 100ºC was 2.3%, 2.5%, and 7.0% for samples F1, F2, and F3 respectively. The F3 sample containing 35% of NP and 15% of alumina shows the highest mass loss.

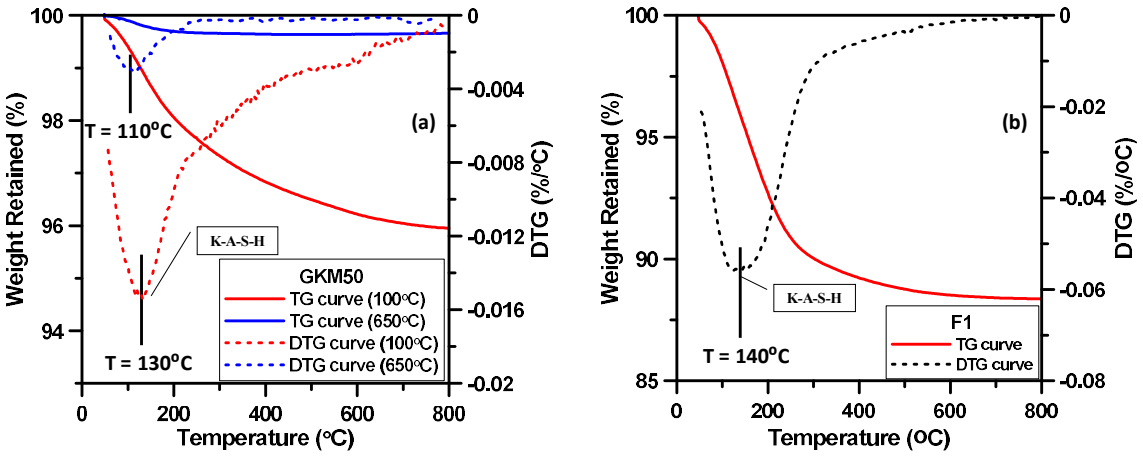

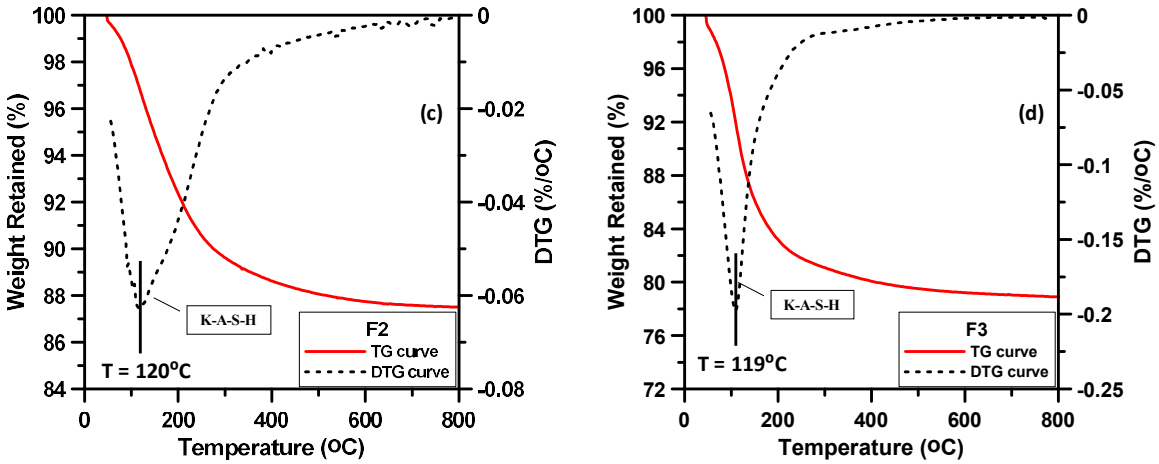

Figure 3-7: TG and DTG curves of (a) GKM50_100ºC and GKM50_650ºC, (b) F1 sample, (c) F2 sample, and (d) F3 sample.

3.3.5. Analysis of XRD and FTIR Spectra of the Porous Ceramic Samples

Figure 3-8 shows the X-ray diffraction patterns for all the highly porous samples. The XRD patterns of GKM50 samples containing equal amounts of NP and MK at both the treatment temperatures (100ºC and 650ºC) show the presence of amorphous phases attributable to the NP and MK phases. In addition, it is seen that the amorphous halo attributable to raw MK at 2Θ = 15-30º (see Fig. 1) is shifted to 2Θ = 20-40º, indicating the formation of alkaline aluminosilicate gel [113]. Also, the crystalline peaks corresponding to the Feldspar group observed in the GKM50 samples at both the treatment temperatures are lower in intensity as compared to the corresponding peaks in the XRD pattern of raw NP (see Fig. 1), which is a dilution effect. The intensity of crystalline peaks was lower in specimens treated at 650ºC than that at 100ºC, attributable to the presence of increased amounts of amorphous gel when treated at the higher temperature. All the diffractograms of ceramic foamed samples F1, F2, and F3 showed the presence of amorphous phases and weak crystalline phases as opposed to the GKM series samples. Some of the Feldspar group

peaks disappeared completely after strong activation in the samples F2 and F3 containing 25 and 35% of NP respectively.

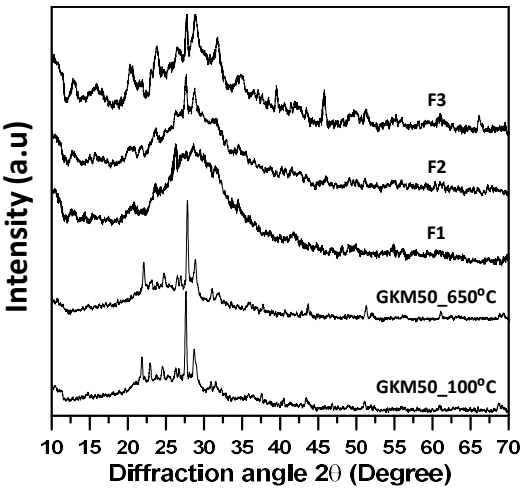

Figure 3-8: XRD patterns of GKM50 samples and foamed ceramic samples.

Figure 3-9 shows the FTIR spectra for the selected samples. The band with peaks centered at 1026 cm^{-1} and 1030 cm^{-1} for GKM50 samples treated at both the temperatures (100°C and 650°C) respectively are attributed to the alkali aluminosilicate gel [114,115]. Also, these bands correspond to asymmetric stretching Si-O-T bonds (where T represents Al or Si) [116]. The crystalline quartz and feldspar phases that were observed in the XRD pattern (see Fig. 8) were confirmed by the weak bands centered at 789 cm^{-1} for the sample treated at 100°C, and 780 cm^{-1} for the sample treated at 650°C, indicating residual crystalline phases. The FTIR spectral peak of highest intensity centered at 998 cm^{-1} for F1, 990 cm^{-1} for F2, and 987 cm^{-1} for F3 can be attributed to the asymmetric stretching (Si-O-T) bonds [114,115] formed as a result of the polymerization process. Also, it was observed that, for the foamed samples, the primary peaks occurred at a lower wavelength as compared to GKM50 samples, denoting the substitution of SiO_4 tetrahedrons by AlO_4 tetrahedrons in the geopolymeric gel [117]. The reason for the T-O-T stretching bonds shifting to lower

wavenumber is due to the lower Al-O bond force compared that of the Si-O bond [118]. Moreover, the peaks at 720 cm^{-1}, 715 cm^{-1}, and 709 cm^{-1} that correspond to Si-O-Si(Al) bonds are sharper in the foamed samples indicating a higher degree of Al substitution in the gel [119]. The F3 sample shows more intense and sharp peaks than the F1 and F2 samples, confirming better polymerization and increased crystallinity as can also be noticed from the XRD patterns shown in Figure 3-8. The wavenumbers in the 3400 cm^{-1} and ~1650 cm^{-1} region is the contribution of water in the reaction products.

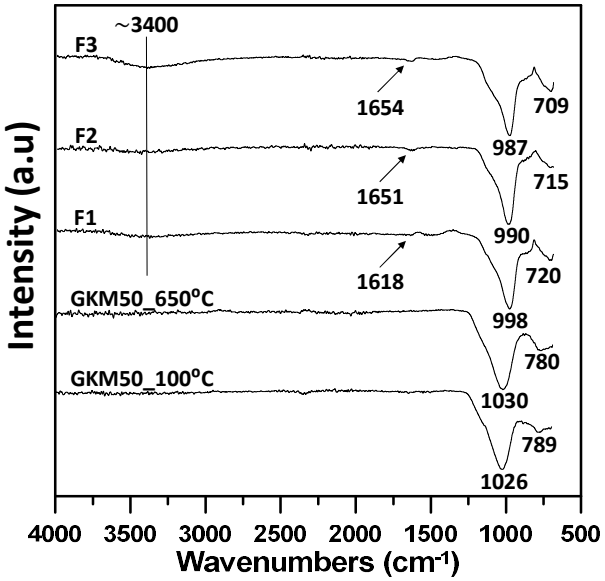

Figure 3-9: FTIR spectra of GKM50 samples and ceramic foam samples.

3.3.6. Pore Structure and Transport Performance of the Foamed Samples

This section evaluates the transport characteristics of foamed samples, which is important towards their performance as filtration media. In this section, the moisture permeability is predicted from the pore structure features obtained through MIP and electrical impedance spectroscopy and evaluated directly using percolation tests.

3.3.6.1. Moisture Permeability Extracted from MIP Data

Previous studies have used mercury intrusion porosimetry (MIP) data to obtain the absolute permeability of porous materials [111,120,121]. The most common model used to predict the absolute permeability (k) is Katz-Thompson equation, given as:

$$k = \frac{1}{226}\left(\frac{\sigma_{eff}}{\sigma}\right)(L_c)^2 \quad (3\text{-}7)$$

$\left(\frac{1}{226}\right)$ is an empirical constant which was developed by Katz-Thompson based on fitting the experimental data for variety of rock specimens, $\left(\frac{\sigma_{eff}}{\sigma}\right)$ is the normalized electrical conductivity, and L_c is the characteristic length of the pore structure that is obtained from the MIP data. Equation 3-7 was simplified by Katz-Thompson to include only the characteristic length terms that could be easily extracted from MIP data to evaluate and predict the permeability [120]. The simplified equation is given as:

$$k = \frac{1}{89}(L_{max})^2 \left(\frac{L_{max}}{L_c}\right) \emptyset S(L_{max}) \quad (3\text{-}8)$$

Here, L_c is the characteristic length (pore diameter corresponding to the threshold pressure) [111,121,122]. L_{max} is the pore size at which the hydraulic conductance is maximum, Ø is the porosity, and $S(L_{max})$ is fractional volume of connected pore space composed of pore of size L_{max} and larger [111].

$$S(L_{max}) = \left(\frac{V_{L_{max}}}{V_t}\right) \quad (3\text{-}9)$$

Here, V_t is the cumulative intrusion volume at threshold pressure (the pressure corresponding to the point of inflection in the rapidly rising range of the cumulative mercury intrusion curve), and V_c is the intrusion volume at each pressure from the threshold pressure to the maximum pressure. A plot of $(V_c\text{-}V_t)$ times d^3 (where d is the pore diameter

at the corresponding pressure) as a function of the pore diameter provides a characteristic peak, the pore size corresponding to which can be taken as L_{max}. Figure 3-10 (a) shows the plot to determine L_{max} for the sample F1.

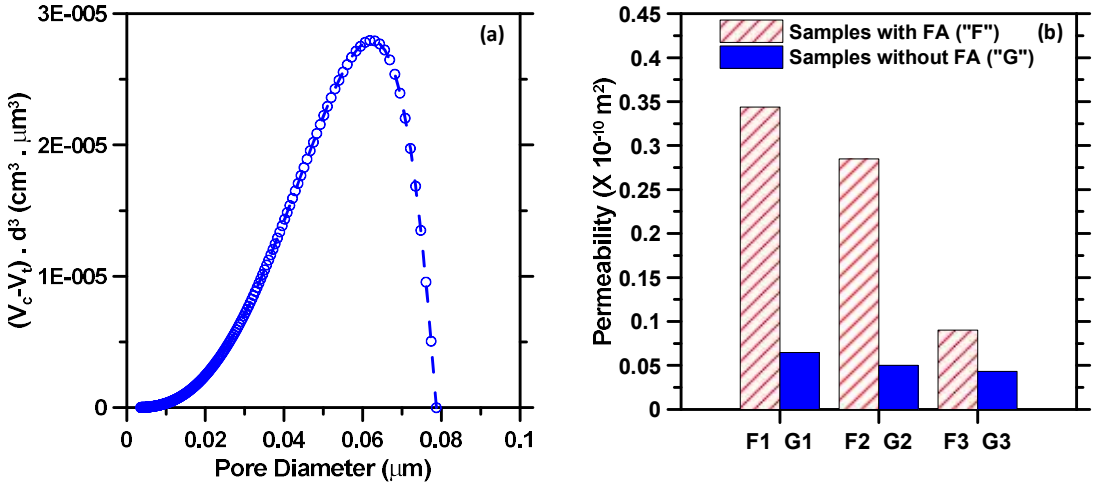

Figure 3-10: (a) Determination of characteristic length from MIP data, and (b) permeability of foamed (F) samples and the comparison with the G-series samples.

Figure 3-10 (b) depicts the moisture permeability of all samples proportioned using Procedure II. The G-series samples have reasonable porosities with small differential pore size but the F-series samples have higher porosities with slightly increased pore sizes. As expected, the permeability is higher for the foamed samples. The extracted permeability of sample F1 and F2 were higher than that of the F3 sample, attributable to the higher porosity and pore size in F1 and F2 samples.

3.3.6.2. Pore Connectivity Factor and Percolation

The percolation test was carried out on 10 mm thick samples as described in an earlier section. The pore connectivity factors were extracted from electrical conductivity tests. The flow rates and the pore connectivity factors are reported in Table 3-6. It is noted that the pore connectivity factors and the flow rates for all samples are similar. The F3 sample which had the smallest differential pore size shows lower flow rate than the F1 and F2

samples. The percolation and permeability is influenced largely by the connectivity of finer pore sizes, which explains the lower permeability for the F3 sample, which has a larger proportion of smaller sizes.

Table 3-6: Pore connectivity and flow rate of the foamed samples.

Ceramic Foam Samples	Pore connectivity factor (β)	Flow Rate (ml/min)
F1	0.34 ± 0.009	0.080 ± 0.02
F2	0.33 ± 0.003	0.075 ± 0.01
F3	0.34 ± 0.003	0.07± 0.01

(Standard deviation is calculated based on three replicate measurements).

3.3.6.3. Thermal Conductivity of Highly Porous Samples

Figure 3-11 shows the thermal conductivity of the highly porous samples determined using the guarded hot plate apparatus. The thermal conductivity of plain OPC paste proportioned using a water-to-cement ratio of 0.40, obtained as 0.75 W/m-K [72] was used as the reference. All samples yielded lower thermal conductivity than the reference sample. Among the porous samples, the GKM50 samples subjected to both the thermal treatments (100 ^{o}C and 650^{o}C) showed the highest thermal conductivity (0.66 and 0.69 W/m-K) which are lower than that of the OPC paste. This reduction in thermal conductivity is attributed to the higher porosity of the GKM50 samples. The foamed samples F1, F2, and F3 show very low thermal conductivity values (around 0.20 W/m-K). These materials can be used as thermally insulating media, as noted from their very low thermal conductivities.

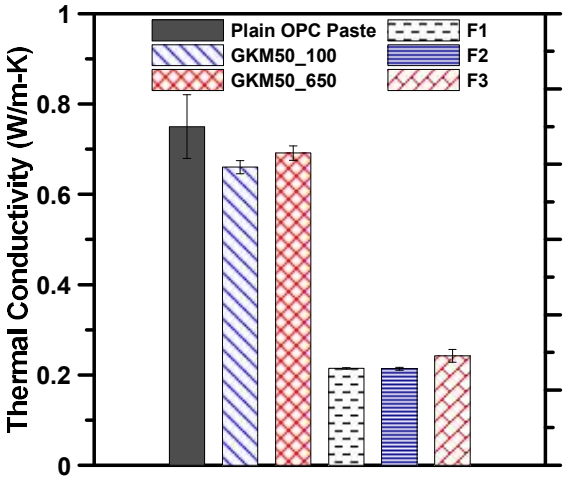

Figure 3-11: Thermal conductivity of the porous ceramic samples and their comparison to the reference OPC paste.

3.4. CONCLUSIONS

This study has reported the synthesis and characterization of a porous ceramic matrix using a volcanic tuff natural pozzolan as the primary source material. Other siliceous and/or aluminous sources such as metakaolin and silica fume were used to supplement the natural pozzolan in the development of geopolymerized ceramic matrices, primarily to provide the reactive species for geopolymerization and a strong network formation. Potassium hydroxide and silicate were used as the alkaline activators, and the sintering and burnout steps required in conventional ceramic fabrication were limited by moderate temperature treatment to provide functional properties of interest. Thus, economy and energy-efficiency were achieved. Two procedures were adopted for synthesis – in the first, geopolymerization and subsequent heat treatment at 100ºC or 650ºC was employed whereas in the second procedure, compositional changes resulted in reducing the treatment temperature to 85ºC. In the second procedure, a silica pore-forming agent was also used. Both the procedures resulted in stable matrices with high porosities (in the 50-70% range).

The synthesized matrices were extensively characterized for a variety of physical properties and evaluated for the desired performance features. Mercury intrusion porosimetry was used to determine the porosity and characteristic pore sizes of the matrices and ascertain the efficiency of the geopolymerization and foaming processes. Electrical impedance spectroscopy was used to determine the connectivity of the pore network in the matrices, while guarded hot-plate method was used to determine the thermal conductivity of the porous ceramics. A significant fraction of the porosity in the synthesized geopolymer matrices belong to the 0.028 to 1 μm and 0.0036 to 0.028 μm ranges, which are effective in filtration applications to trap contaminants including viruses. The thermal conductivity of the porous matrices were about 4 times lower than that of traditional Portland cement systems, rendering their use in thermal insulation of buildings. In summary, the porous ceramic matrices developed in this study using abundant aluminosilicate materials as the major components can be used for multifunctional applications and can be processed at a fraction of the cost of commercially available porous matrices with similar features. The synthesis routes are also more energy efficient than many available technologies. It has been shown that the synthesis parameters including the composition and treatment regimes can be tailored to achieve the desired thermal and fluid transport, and contaminant capture characteristics. Moreover, the abundance of the source materials in nature, the ease with which these systems can be manufactured, and the range of tunable microstructure and properties, enables them to considered for large volume applications such as building insulation, as well as low volume applications such as water filtration.

CHAPTER 4[2]

NOVEL SYNTHESIS OF LIGHTWEIGHT GEOPOLYMER MATRICES FROM FLY ASH THROUGH CARBONATE-BASED ACTIVATION

4.1. INTRODUCTION

Porous materials belong to a broad family of multi-functional materials, with extensive applications in building insulation, separation through filtration, adsorbents, catalysts etc. [64,75,77,123]. In the quest for efficient, sustainable, and economical porous materials, porous geopolymers have emerged as an important class of materials. Geopolymers are binders with a three-dimensional structural network, formulated by reacting aluminosilicates such as industrial wastes (e.g., fly ash), calcined clays (e.g., metakaolin), or natural pozzolans (e.g., volcanic tuff) with highly alkaline activators [64,124,125]. Sodium or potassium hydroxides or silicates are commonly used as the alkaline activators [126,127]. The Si-O-Si and Al-O-Al covalent bonds are broken down by the high pH alkaline activator, and an amorphous/semi-crystalline gel network is precipitated during the geopolymerization process [8,9]. The mechanisms and reactions in geopolymerization are reported in detail in [14,16]. The replacement of ordinary portland cement (OPC), the production of which is CO_2-emitting and energy-intensive, with waste/by-product materials such as fly ash, in the formation of a binding material, is attractive both from environmental and economical perspectives. The use of fly ash as a source material for geopolymerization, to create value-added binding materials has been extensively studied [128–131]. Geopolymers have been reported to deliver comparable or better performance

[2] This chapter is derived from publication: H. Alghamdi, N. Neithalath, Novel synthesis of lightweight geopolymer matrices from fly ash through carbonate-based activation, Materials Today Communications. 17 (2018) 266–277.

including strength, high-temperature resistance, and chemical resistance as compared to OPC-based binders [5,7,132,133].

Recently, a large number of studies have been reported on synergizing the fly ash geopolymerization process with a foaming method to enhance the range of applicability of these materials. Such porous materials can be designed with adequate mechanical strength along with other beneficial properties like thermal insulation, akin to aerated or foamed concretes. The foaming process can be classified as a physical or chemical process – in the former, foaming agents such as surfactants used as physical foaming agents by creating bubbles during mixing [61–63], while in the latter, a chemical reaction is employed to produce gas. Metallic free silicon [11,64], alumina powder [61,65], and hydrogen peroxide [61,63] are generally used as chemical foaming agents to synthesize geopolymeric foams. Geopolymeric foams thus synthesized exhibit high strength-to-weight ratio, low thermal conductivity, and good thermal and chemical stability [5,7,132,133] . The use of fly ash-based geopolymeric foams as inorganic support materials [76], catalysts [123], adsorbents and filters [75], and building insulation (thermal and acoustic) [77,78] have also been reported.

In this study, we employ a novel and economical pore forming process for class F fly ash-based systems, using a low pH activating agent. The chemical agent responsible for activation (to a certain extent) and pore formation is an alkali carbonate (sodium carbonate). It is a common chemical used in a wide array of applications including, but not limited to water softening, manufacture of glass, soaps and detergents, as a food additive, in toothpastes, and as a wetting agent in clay extrusion in brick production. The hydrolysis of sodium carbonate proceeds according to Equations 4-1 and 4-2.

$$Na_2CO_3 + H_2O \rightarrow NaHCO_3 + NaOH \quad (4\text{-}1)$$

$$2NaHCO_3 \xrightarrow{\Delta} Na_2CO_3 + H_2O + CO_2 \uparrow \quad (4\text{-}2)$$

Thus, the alkalinity required for dissolution of fly ash and the precipitation reactions are provided by the NaOH formed in the system. The first reaction is similar to carbonate activation of slags where the $Ca(OH)_2$ from slag also results in the formation of NaOH along with the precipitation of calcium carbonate [134,135]. The reaction sequence can be further accelerated through addition of sodium hydroxide or sodium silicate (waterglass) to increase the alkalinity required for dissolution/precipitation reactions and thus obtain requisite early strengths. Geopolymerization reaction is accelerated by temperature, and this acceleration mechanism enables the decomposition of sodium bicarbonate into H_2O and CO_2. In this study, two treatment temperatures are employed for porous matrix synthesis: 85°C and 100°C – the latter facilitating increased release of CO_2, and thus facilitating the production of a "foamed" material. The pore forming process is controlled in such a manner that the resulting matrices have adequate mechanical strengths along with reduced thermal conductivity, enabling them to serve as structural-thermal materials in building applications. The mechanical and thermal properties of these matrices, reaction products formed, and the microstructural features are evaluated in detail to establish the effectiveness of this novel synthesis route in the production of multi-functional materials.

4.2. SYNTHESIS AND TEST METHODS

4.2.1. Materials

The source material utilized in this study is a Class F fly ash conforming to ASTM C 618. The chemical composition of the fly ash is shown in Table 4-1, and its particle size

distribution in Figure 4-1(a). The median particle size of fly ash is 17.9 μm. The fly ash has a specific gravity of 2.34 g/cm^3.

Table 4-1: Chemical composition of Class F fly ash.

Oxide	SiO_2	Al_2O_3	Fe_2O_3	CaO	MgO	SO_3	LOI
% by mass	58.40	23.80	4.19	7.32	1.11	3.04	2.13

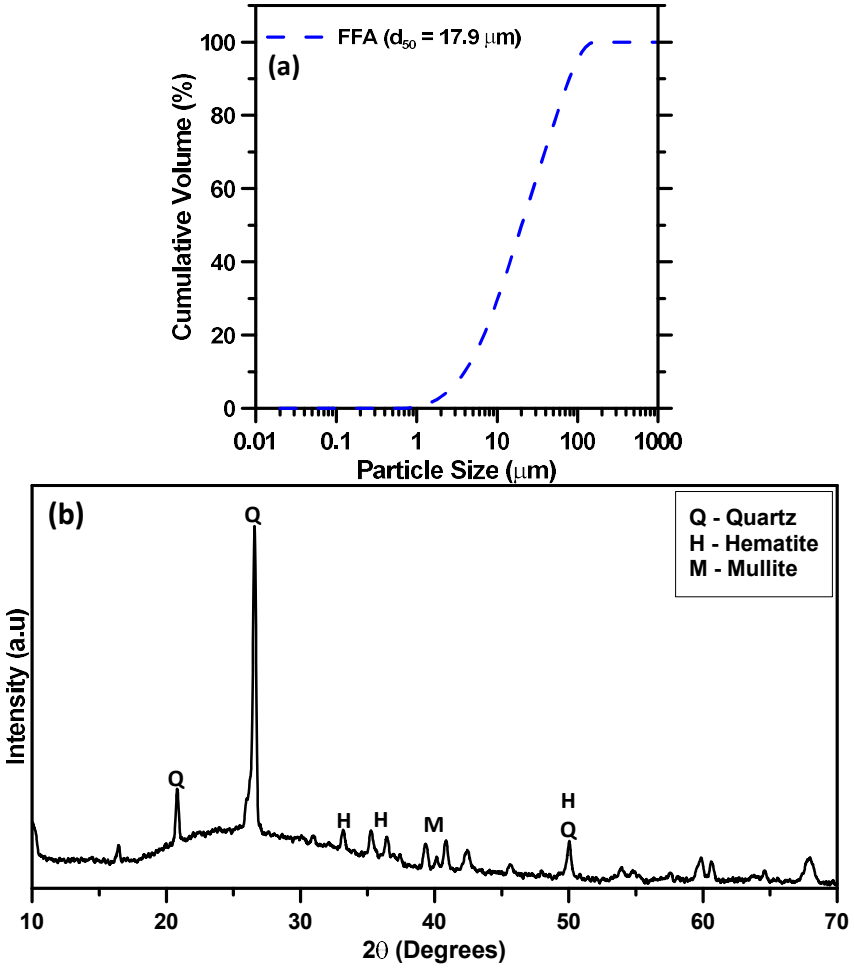

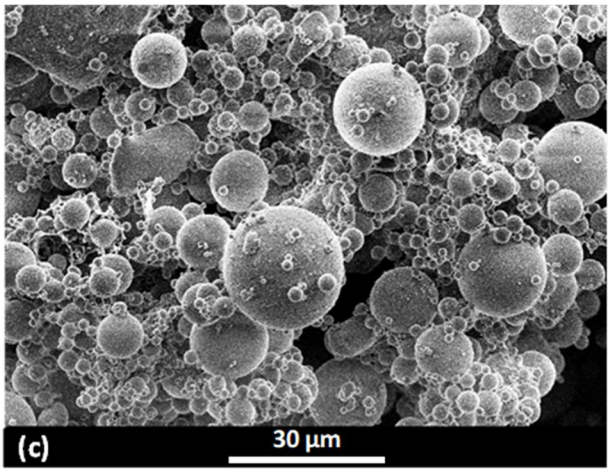

Figure 4-1: (a) Particle size distribution, (b) X-ray diffraction pattern, and (c) scanning electron image of the class F fly ash.

The X-ray diffraction (XRD) pattern of the fly ash is shown in Figure 4-1(b). The halo in the 2θ range of 20° to 40° is indicative of the amorphous nature of the fly ash, which enables better reactivity during the geopolymerization process. Quartz, hematite, and mullite are the major crystalline species as determined from the XRD pattern of the fly ash. Figure 4-1(c) shows the scanning electron image of fly ash, showing the spherical particles.

4.2.2. Synthesis Methods for Lightweight Matrices

The lightweight geopolymer matrices were synthesized by mixing Class F fly ash with an activating solution. The activating agents used in this study were Na_2CO_3 (a basic salt) and sodium silicate (waterglass). Reagent grade sodium carbonate powder of 99.98% purity and a specific gravity of 2.54 g/cm^3 was used. The sodium silicate solution, supplied by PQ Corporation, has a solids content of 36%, a silica modulus (molar ratio of SiO_2-to-Na_2O), M_s, of 3.3, and specific gravity of 1.38 g/cm^3. The activator contained either sodium carbonate alone (for the first two mixtures shown in Table 4-2, where sodium carbonate powder was added as a fraction of the mass of fly ash), or an aqueous solution of sodium carbonate and sodium silicate (for the last four mixtures shown in Table 4-2). In the latter

case, the Na_2O contents in the sodium carbonate and sodium silicate, and the SiO_2 content in the sodium silicate solution were used to arrive at the molar ratio of Na_2O-to-SiO_2 (M_s), and the mass ratio of Na_2O to fly ash (n), which are used as the activator parameters. The pH of the activator solutions are also shown in Table 4-2. The solution-to-fly ash ratio (or water-to-powder ratio for the first two mixtures) was maintained at 0.30 for all the mixtures. The activator solution was added to the powder and mixed for at least 2 minutes until a homogenous mixture was obtained. The mixture was then placed in open polystyrene molds and immediately placed in a laboratory oven for heat curing. All the samples were exposed to two different time-temperature combinations to complete the geopolymerization process. In the first curing procedure, the specimens were subjected to a temperature of 85°C for 24 or 48 h. In the second procedure, the specimens were exposed to 100°C for 24 or 48 h in order to accelerate the polymerization reaction and the formation of reaction products. However, it was also noticed that processing at 100°C created a visible increase in specimen volume (as shown in Figure 4-2), akin to the synthesis of aerated or foamed concrete [136]. Hence the samples treated at 85°C are referred to as non-foamed (NF-series), and those treated at 100°C as foamed (F-series) in this study. While it is known that hydrolysis of sodium carbonate and subsequent heat treatment at greater than 50°C releases CO_2, the formation of CO_2 is rather slow at temperatures less than 100°C. The smaller amounts of CO_2 formed likely diffuses out through the pore paths without creating large enough pores. At higher temperatures, the faster conversion of sodium bicarbonate to CO_2 and H_2O (Equation 4-2) results in faster mass transport of CO_2 to the external atmosphere, leaving larger pores in the structure. It is also likely that the early-age gel strength of the samples treated at 85°C is not enough to withstand the formation of pores

resulting from CO_2 release, and thus could lead to the collapse of the pore structure when the pores are larger than the critical size. The enhanced geopolymerization reaction at higher temperatures could have led to a gel that is strong enough to structurally withstand the presence of larger pores. After heat treatment, the samples were exposed to ambient temperature for 24 h before subjecting them to the relevant tests. For compressive strength tests, mortars with a sand volume of 50% were prepared.

Figure 4-2: Illustration of the volume increase due to CO_2 release when the carbonate activated fly ash samples are heat cured at 100°C.

Table 4-2: Proportions of activators, and the curing conditions.

Sample #	Activator characteristics		Sample identifier		
			cured at 85°C (NF-series)	cured at 100°C (F-series)	pH
Activated using Na_2CO_3					
1	8%		NF1	F1	12.41
2	10%		NF2	F2	12.55
Activated using Na_2CO_3 + waterglass (aqueous solution)					
	Na_2O/binder (mass-based); (n)	SiO_2/ Na_2O (mole- based); (M_s)	cured at 85°C (NF-series)	cured at 100°C (F-series)	pH
3	0.08	1.0	NF3	F3	12.03
4	0.08	1.5	NF4	F4	12.10
5	0.1	1.0	NF5	F5	12.07
6	0.1	1.5	NF6	F6	12.14

(NF stands for non-foamed samples, F for foamed samples)

4.2.3. Test Methods

4.2.3.1. Physical and Mechanical Properties

The mechanical and physical properties of samples such as compressive strength, density, and thermal conductivity were determined to ensure the applicability of the synthesized lightweight geopolymers for different applications. The compressive strengths of the mortar were determined in accordance with ASTM C 109 [137]. Three replicate 50 mm cubes were tested under a load-controlled test procedure to determine the failure strengths. A gas pycnometer (Ultrapyc 1200e, Quantachrome Instruments) was used to determine the specific gravity of the samples. Thermal conductivity of the paste samples was determined in accordance with ASTM C 177 using a guarded hot plate apparatus. Two identical specimens (200 mm x 200 mm x 25 mm) were tested for each mixture. The applied power was measured in a centralized metered section, surrounded by thermally isolated guards to ensure 1D uniform heat flow. Heat sinks located on the top and bottom of the apparatus dissipate the heat to ensure uniform temperatures at the outer surfaces of the specimen [72]. The duration of testing was between 6-to-12 h, as needed to establish a steady-state temperature gradient over the thickness of the specimen. Thermal conductivity (λ) was obtained using Fourier's equation as:

$$\lambda = \frac{q\ L}{2\ A\ (T_{hot} - T_{cold})} \tag{4-3}$$

where q is the power input to the heater, L is the thickness of the plate specimen, A is the surface area of the specimen, T_{hot} is the temperature of the hot surface, and T_{cold} is the temperature of the cold surface.

4.2.3.2. Chemical Signature of The Reaction Products

Thermogravimetric analysis (TGA) and Fourier transform Infrared (FTIR) spectroscopy were carried out on the porous paste samples after the corresponding heat curing regime. Fourier transform Infrared (FTIR) spectra of the samples were acquired using an ATR Mattson Genesis FTIR spectroscope with an attenuated total reflectance (ATR) diamond crystal attachment. The spectra of the powdered samples were obtained in the wavenumber range of 4000 to 700 cm^{-1} at a resolution of 1 cm^{-1}. Thermogravimetric analysis (TGA) was carried out using a Perkin Elmer simultaneous thermal analyzer (STA 6000). The thermal exposure regime was as follows: the sample was heated from room temperature to 50°C and then held for 1 min, and then heated to 850°C at a constant rate of 15°C/min in an inert (N_2) environment. The mass loss during the thermal treatment was recorded as a function of the temperature.

4.2.3.3. Pore Structure and Microstructure

Mercury Intrusion Porosimetry (MIP) and Scanning Electron Microscopy (SEM) were carried out to understand the pore- and micro-structural features of the porous materials synthesized. For MIP, the heat-treated porous samples were crushed to a size of approximately 2 mm. The porosimeter (Quantachrome Instruments Pore Master) is capable of exerting a maximum pressure of 414 MPa. To determine the porosity and critical pore sizes, the samples were weighed and placed into the sample holder. The sample holder was carefully placed into the low-pressure chamber of the porosimeter, where the sample is pressurized with mercury from ambient to 345 KPa (60 psi). The sample was then removed from the low-pressure chamber and placed in the high-pressure chamber, where the pressure was increased to 414 MPa (60,000 psi) to enable mercury to completely penetrate

the pores in the specimen. The pore diameter (d) as a function of the intrusion pressure can be obtained from the Washburn equation (Equation 4- 4) as:

$$d = \frac{-4\,\sigma\,cos\theta}{\Delta P} \quad (4\text{-}4)$$

where ΔP is the difference in the pressure between successive steps (MPa), θ is the contact angle between mercury and the cylindrical pore which was taken as 130° in this study [108], and (σ) is the surface tension of mercury (485 mN/m).

The microstructure and reaction product morphology of the porous samples were evaluated using a Nanoimages SNE-4500 Plus Table top SEM operating in the secondary mode. Small pieces of specimens, cut from larger samples were polished to obtain a smooth surface for electron microscopy. After polishing, the samples were ultrasonically cleaned and rinsed with alcohol to remove the debris from sectioning and handling. The sputter-coated specimens were imaged under an operating voltage of 30 kV. Elemental analysis was carried out using a Bruker XFlash 630 Energy dispersive X-ray spectroscope (EDS) built in the electron microscope.

4.3. RESULTS AND DISCUSSIONS

4.3.1. Bulk Densities and Compressive Strengths

The bulk densities of the non-foamed (NF) and foamed (F) geopolymer matrices are shown in Table 4-3. The numbers in parenthesis represent the standard deviation in measured bulk densities based on three replicate samples. As explained in the previous section, the chemical compositions are the same in the corresponding NF and F series samples, and the only difference is in the curing temperature. The foamed samples are found to be 20-35% lighter than the non-foamed samples because of the increased CO_2 release under a higher treatment temperature.

Table 4-3: Bulk densities (and standard deviation based on three replicates) of non-foamed and foamed geopolymer matrices.

Sample #	Bulk density (g/cm^3)	
	Non-foamed (NF)	Foamed (F)
1	1.69 (0.007)	1.37 (0.009)
2	1.79 (0.06)	1.38 (0.007)
3	1.61 (0.10)	1.21 (0.01)
4	1.79 (0.01)	1.18 (0.004)
5	1.70 (0.02)	1.15 (0.02)
6	1.72 (0.05)	1.23 (0.04)

Compressive strength is an important property of geopolymer systems, especially when they are used in building elements. Figure 4-3(a) and (b) show the compressive strengths of the non-foamed (NF) and foamed (F) samples after the respective treatment durations. From both the figures, it can be noticed that the strength of the matrices prepared using sodium carbonate alone as the activating agent is rather low, attributable to the fact that the fly ash dissolution and precipitation reactions would not have progressed far enough. However, it can be noticed that the F1 and F2 samples (100ºC curing) activated using sodium carbonate alone show higher strengths than their non-foamed (cured at 85ºC) counterparts, which is an indication of better geopolymerization at a higher temperature. These matrices are noted to achieve a compressive strength of 5 MPa, which is similar to or higher than those of foamed matrices synthesized using Al powder or H_2O_2 reported in [61,65], for comparable bulk densities (~1.35-1.4 g/cc). Such strengths are suitable for applications such as masonry blocks and insulation panels.

The sample sets 3 to 6 (both NF and F series) demonstrate increased compressive strengths, attributable to the increased alkalinity and the presence of silicates to better polymerize the reaction product. The compressive strengths of the NF-series samples are found to be higher than those of the F-series samples because of the reduced porosity in the former

(which can be confirmed from the 20-35% higher bulk densities for the NF-series samples as compared to their F-series counterparts). For the NF-series samples (cured at 85°C), increase in curing time from 24 h to 48 h is shown to triple the compressive strength whereas for the F-series samples (cured at 100°C), an increase in curing duration does not significantly alter the strength. This is indicative of the combined influence of time and temperature on the geopolymerization process of fly ash-based binders. Based on the desired properties (strength, bulk density, or an optimized combination of both), the curing temperature and duration can be tuned.

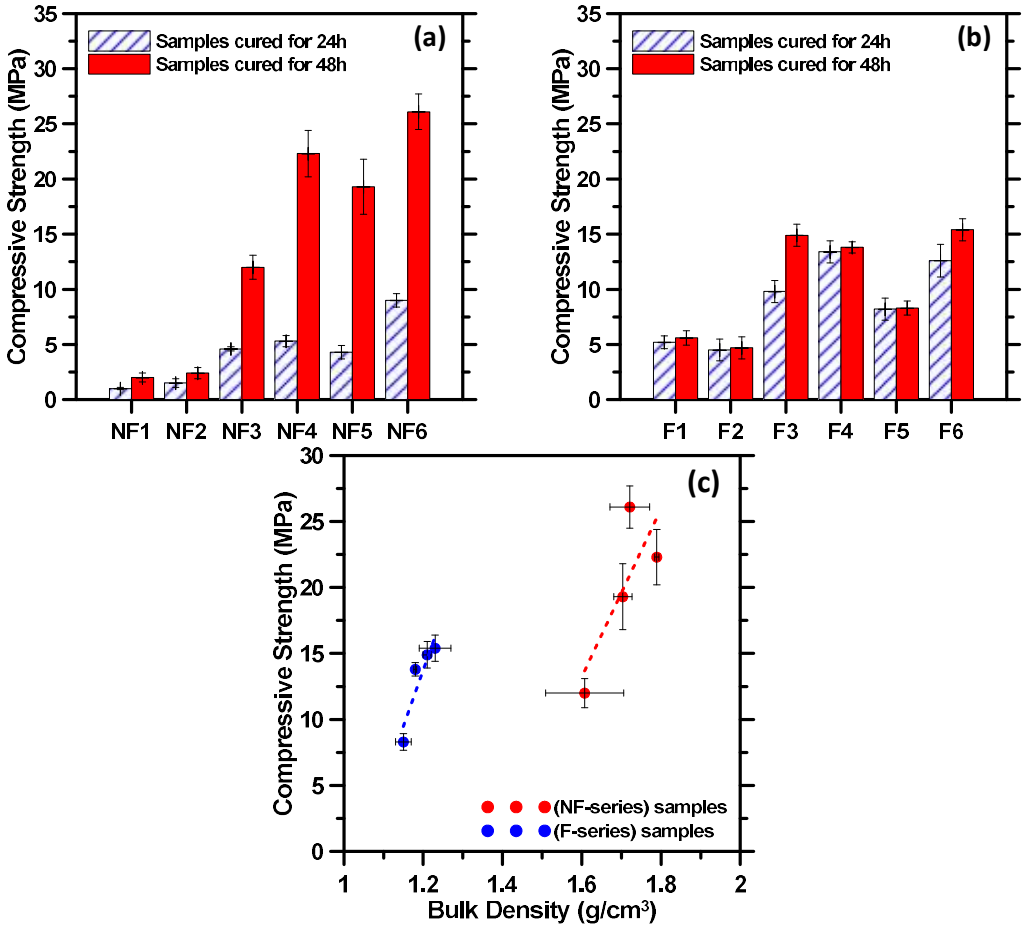

Figure 4-3: (a) Compressive strength of NF-series samples, (b) compressive strength of F-series samples, and (c) relationship between bulk density and compressive strength for the NF and F series samples activated using sodium carbonate and waterglass (samples 3 to 6).

Figure 4-3(c) shows the relationship between bulk density and compressive strength for the NF and F series samples activated using sodium silicate and waterglass and cured at 100ºC for 48 h. Strengths as high as 25 MPa were attained for the NF-series matrices and 15 MPa for the F-series matrices. For several applications including load-bearing masonry blocks and panels, pre-cast wall/roof panels, lightweight thermal insulating and fire-resistant media, a 15 MPa compressive strength is more than adequate. This is higher than the typical reported strengths for many foamed geopolymer matrices [138,139]. While several past studies have attempted to develop foamed geopolymer matrices for insulation purposes [63,77,140–142], this study attempts a compromise between adequate structural and functional performance for such matrices. Also, since the F-series mixtures are about a third lighter than the NF-series mixtures, most of the remaining studies in the study focuses on the foamed matrices.

4.3.2. Thermal Properties of Foamed Geopolymer Matrices

The thermal conductivities of the foamed samples (F-series) were determined in accordance with ASTM C 177, and are shown in Figure 4-4(a) along with the thermal conductivity of an ordinary portland cement paste (water-to-cement ratio of 0.40) [72] for comparison. The foamed geopolymer matrices demonstrate thermal conductivity in the range of 0.29 to 0.37 W/m-K, which is about half as that of the reference OPC paste, owing to their higher porosity. The relationship between the measured conductivity and sample porosity is shown in Figure 4-4(b). The total porosity is determined based on the measured bulk density and specific gravity as shown in Equation 4-5 [62,63]. A 10% increase in porosity (from 45 to 55%) is seen to reduce the thermal conductivity by as much as 20%. Previous studies have shown that lightweight geopolymer matrices (through a variety of

foaming methods) with a bulk density of ~0.8 g/cm^3 or ~0.4 g/cm^3 results in a thermal conductivity of 0.2 W/m-K or 0.1 W/m-K respectively [63,78,143,144]. The results obtained in this study, i.e., 0.29 to 0.37 W/m-K for bulk densities of 1.1-1.3 g/cm^3 (Table 4-3), follows the same trend. In addition to the low thermal conductivity of these porous geopolymeric binders, their reduced flammability and high temperature stability are significant advantages over traditional low thermal conductivity materials used for insulation [145].

$$Total\ porosity\ (\%) = \left(1 - \frac{Bulk\ density}{Specific\ gravity}\right) X100 \quad (4\text{-}5)$$

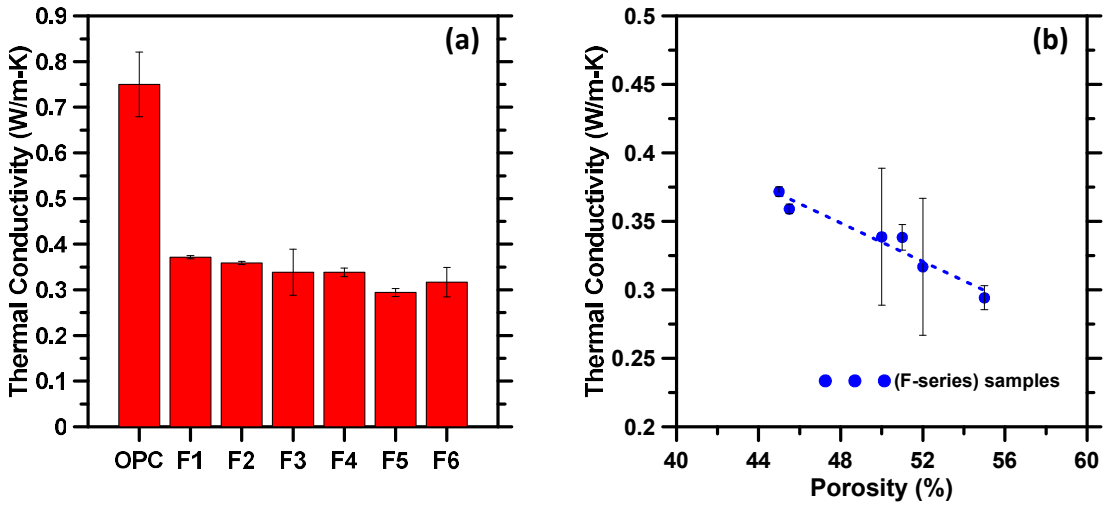

Figure 4-4: (a) Thermal conductivity of the F-series samples, and (b) relationship between porosity and thermal conductivity of the F-series samples.

4.3.3. Pore Structure

Porous materials are generally used for applications such as thermal insulation, fluid transport, and acoustic isolation, all of which critically depend on the pore structure (i.e., volume fraction, size, distribution, connectivity etc.) of the material. The cumulative volume of mercury intruded as a function of the intruding pore sizes, and the differential pore volume-size curve to determine the critical pore sizes are shown in Figure 4-5(a) and

(b) for the F-series geopolymeric matrices synthesized in this study. Mercury intrusion porosimetry can detect pore sizes from 3 nm to 200 μm, even though it has several deficiencies when it comes to size estimation, such as those related to ink-bottle effects [146–148]. It is noticed from Figure 4-5(a) that the F1 and F2 mixtures (those activated with sodium carbonate alone) have the highest cumulative intruded volume, which agrees well with the compressive strength results shown in Figure 4-3(b). However, optical microscopy images shown in Figure 4-6(a) reveal that mixtures F3 to F6 (activated using a combination of sodium carbonate and sodium silicate) have higher porosities, contrary to the MIP results. This is also confirmed through the use of Equation 4-5 to determine the total porosity. Equation 4-5 employs the bulk density and specific gravity in the determination of total porosity. A comparison of MIP-derived porosities and those obtained using Equation 4-5 is shown in Figure 4-6(b). Since very little pressure is needed to intrude the larger pores, they are not recorded in the MIP measurements for samples F3-F6, resulting in lower cumulative volumes of mercury intruded, and thus lower total porosities. Optical microscopy images (Figure 4-6(a)) show that there are indeed more of larger pores in samples F3-F6. Hence, the use of Equation 4-5, which is simpler and faster to perform than MIP, is preferred in the determination of total pore volume of porous samples.

The critical pore size determined using MIP (corresponding to the peak in the differential volume curve, which is indicative of the percolating pore size in the material [111]), denoted by the location of the major peak in the derivative of the pore size-volume intruded curve shown in Figure 4-5(b), is higher for the F1 and F2 mixtures (~3 μm) than those for the F3-F6 mixtures (~1-1.8 μm). Note that the pore sizes captured by MIP does not account for the larger pores formed by the release of CO_2, and is representative of the pores present

within the reaction product phases. The fact that activation by sodium carbonate alone does not lead to a refined reaction product as described earlier, leads to a larger pore size, while the presence of waterglass leads to better polymerization and reduced pore sizes.

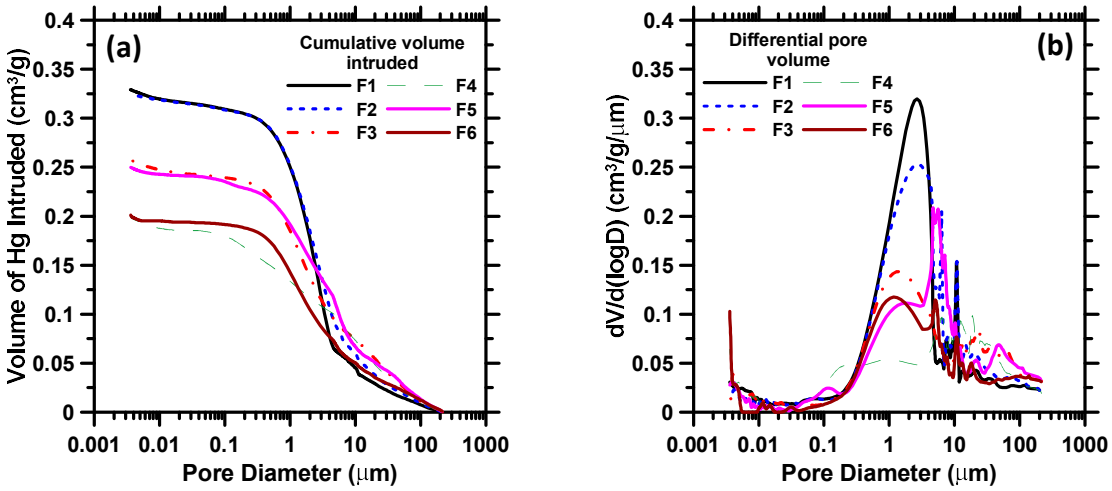

Figure 4-5: (a) Cumulative volume of mercury intruded, and (b) derivative of the pore size-volume intruded curve, for the F-series mixtures.

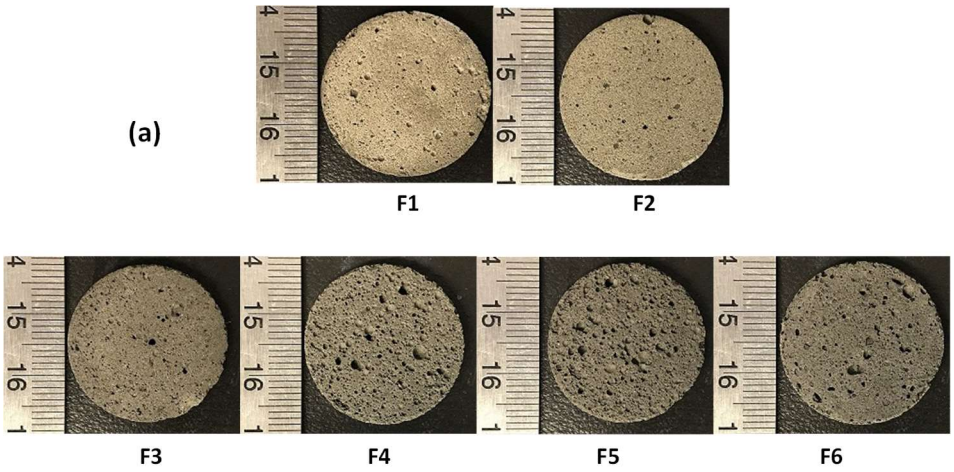

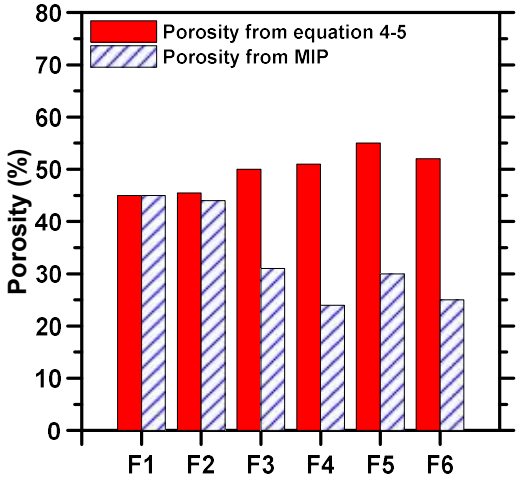

Figure 4-6: (a) Optical microscopy images, and (b) a comparison of total porosity obtained from MIP and using Equation 4-5, for the F-series mixtures.

4.3.4. Characterization of Reaction Products

The reaction products of carbonate-based fly ash activation are identified and quantified in this section through different techniques including TG/DTG analysis, FTIR, and SEM/EDS.

4.3.4.1. Thermal Analysis

Thermogravimetric (TG) and differential thermogravimetric (DTG) curves of sample series 1 (activated by carbonates alone) and series 6 (activated by carbonates and silicates) are shown in Figure 4-7. Figure 4-7(a) and (c) show the TG/DTG curves of NF1 and NF6 samples while Figure 4-7(b) and (d) show the TG/DTG curves of F1 and F6 samples. The overall mass loss is much lower for the series 1 samples than for the series 6 samples, once again showing the beneficial effects of activation using carbonates and silicates rather than carbonates alone.

A rapid reduction in mass loss is observed until about 150°C for all the samples, after which the mass loss is more gradual. The rapid mass loss is attributed to the loss of evaporable water in the sodium aluminosilicate (N-A-S-H) gel [149]. The mass loss in this range is

also higher for the samples 3 to 6 (activated with carbonates and silicates), for reasons described earlier. In the DTG curves of all the samples, a shoulder is observed in the 100-125ºC range, which is likely due to the residual sodium bicarbonate present in the samples. As explained earlier, sodium carbonate in aqueous solution results in the formation of sodium bicarbonate and NaOH. The optimum decomposition temperature of sodium bicarbonate is around 120-150ºC [150]. All the samples also show a mass loss in the 500-850ºC range, which is attributable to the decomposition of sodium carbonate to Na_2O and CO_2. The decomposition of anhydrous sodium carbonate proceeds to completion at 851ºC [151]. Between the non-foamed (NF) and foamed (F) series samples, the overall mass loss and the mass loss up to 150ºC is higher for the NF series samples since they were heat cured only at 85ºC, and it is likely that much more evaporable water is present in those mixtures. Thus, a higher mass loss until 150ºC for the NF series samples does not necessarily mean that there is more N-A-S-H gel formation in those samples than in the F series samples. When the mass loss corresponding to the initial evaporable water content up to 100ºC, and bicarbonate and carbonate decompositions are accounted for, the F series samples showed higher amounts of N-A-S-H gel as expected, attributable to the higher treatment temperature that they were subjected to. The mass loss in the 500-850ºC due to sodium carbonate decomposition was higher in the non-foamed samples than in foamed samples as shown in Figure 4-8, because the higher treatment temperature in the latter case would have already resulted in a higher CO_2 release through the conversion of sodium bicarbonate to sodium carbonate.

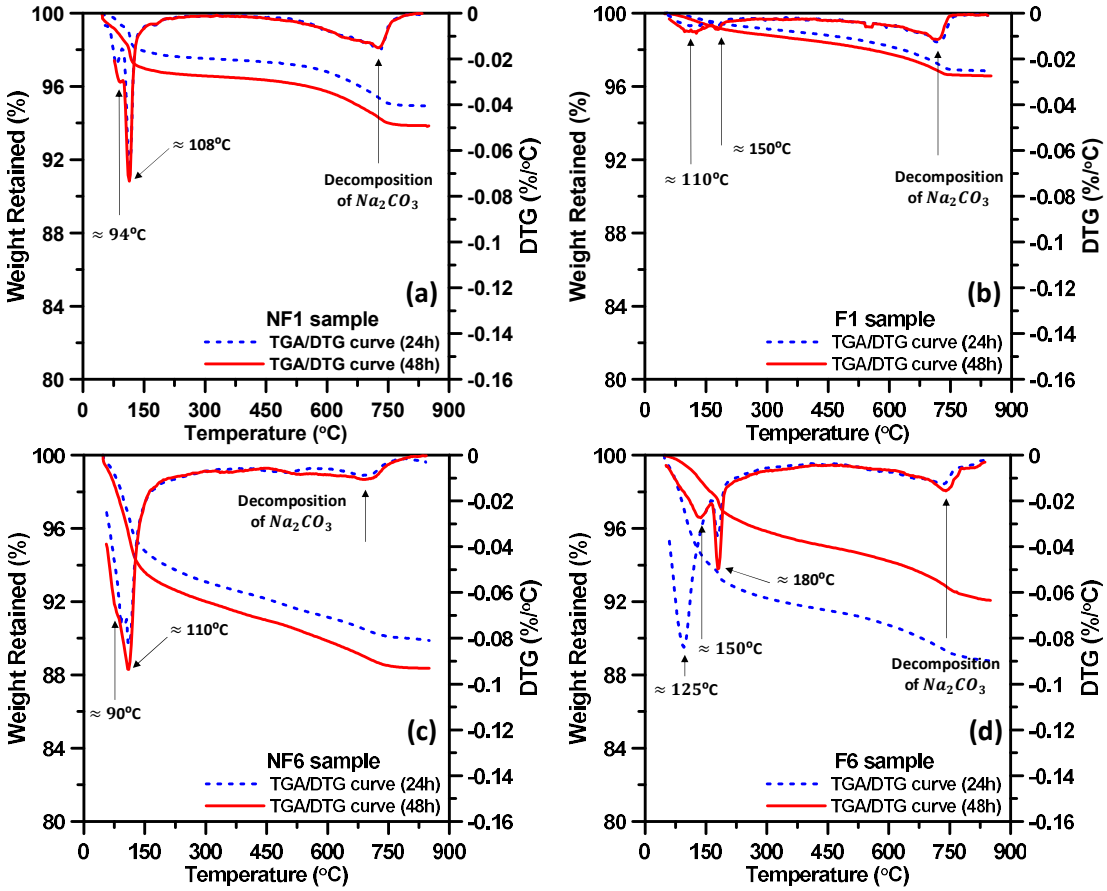

Figure 4-7: Thermogravimetric (TG) curves (a and c), and differential thermogravimetric (DTG) curves (b and d) of sample series 1 (activated by carbonate alone) and sample series 6 (activated by a combination of carbonate and silicate).

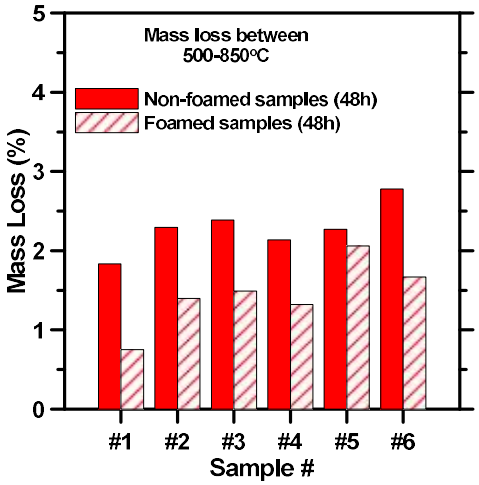

Figure 4-8: Mass loss in the 500-850°C range for the non-foamed (NF) and foamed (F) samples treated for 48 h.

4.3.4.2. FTIR Spectra

FTIR spectra is extremely useful in the structural characterization of geopolymers, since it provides information on short-range and medium-range structural ordering. Figure 4-9(a) and (b) show the FTIR spectra for the non-foamed and foamed geopolymer samples belonging to series 1 and 6 respectively, along with the spectra for raw fly ash. The spectra after heat treatment for 24 and 48 h are shown in the Figure 4-9. Raw fly ash shows the asymmetric Si-O-T (T=Si, Al) stretching band around 1000 cm^{-1} and a band corresponding to quartz at around 775 cm^{-1}. The FTIR spectra of the geopolymers evaluated in this study reveal several bands that are commonly observed in fly ash-based geopolymers, summarized in Table 4-4 [152]. The bands due to Si-O-T bonds, which comprise the reaction product in geopolymers are located in the broad range of wavenumbers from 1200 to 800 cm^{-1}, and their particular position depend on the bond length and bending of the Si-O-T bonds [153]. Whether the system is activated by carbonates alone (Figure 4-9(a)) or by carbonates and silicates (Figure 4-9(b)), the major spectral peaks of highest intensity attributed to the asymmetric stretching (Si-O-T) bonds [114,153], are centered at a narrow wavenumber range between 990 to 1010 cm^{-1}, indicating not much of difference in short- and medium range structural ordering. A slight increase in the wavenumber corresponding to the major peak can be noticed for the 48h cured samples as compared to the 24h cured samples, indicating a slightly higher degree of polymerization. In the non-foamed samples (treated at 85^{o}C), the signature for water (at ~3250 and ~1650 cm^{-1}) [153] are more prominent. The bands in the 1400-1450 cm^{-1} range and at 850 cm^{-1} (as a shoulder band) indicate the C-O stretching vibration in the carbonate group [153,154], the presence of which is explained in the TGA/DTG results shown earlier. The carbonate bands are more

intense in the non-foamed samples, since the higher temperature used in the synthesis of the foamed samples could have resulted in the release of more CO_2 (which causes the foaming), and thus reduced amounts of residual carbonates.

Table 4-4: Characteristic FTIR bands.

Wavenumber	Interpretation
3430 and 1660 cm^{-1}	OH (stretching vibration) and H-O-H (bending vibration
1450 cm^{-1}	C-O stretching vibration
1085 – 1050 cm^{-1}	Asymmetrical Si-O-Si stretching vibration
1010 – 960 cm^{-1}	Si-O-Al stretching vibration

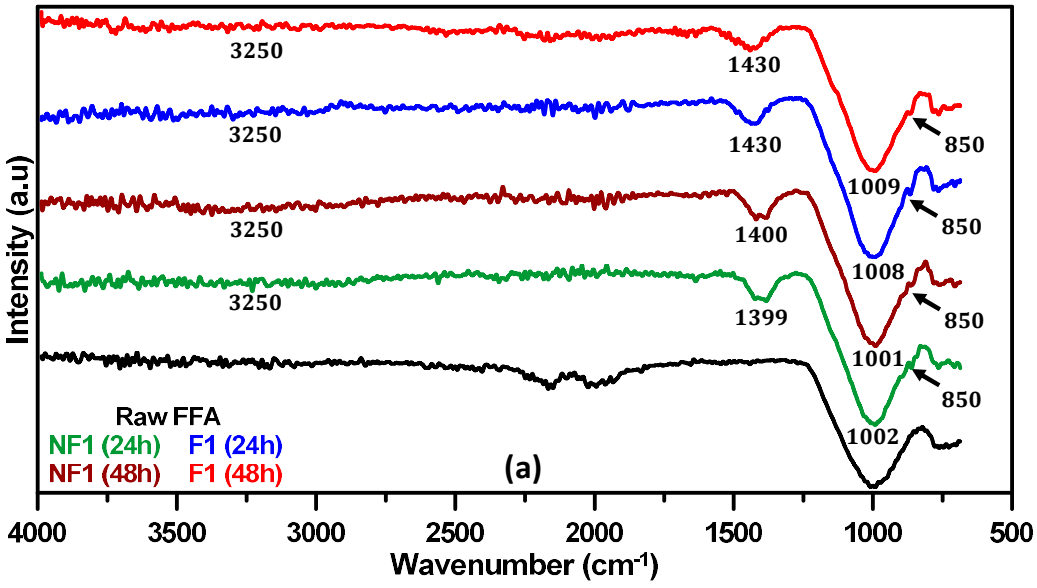

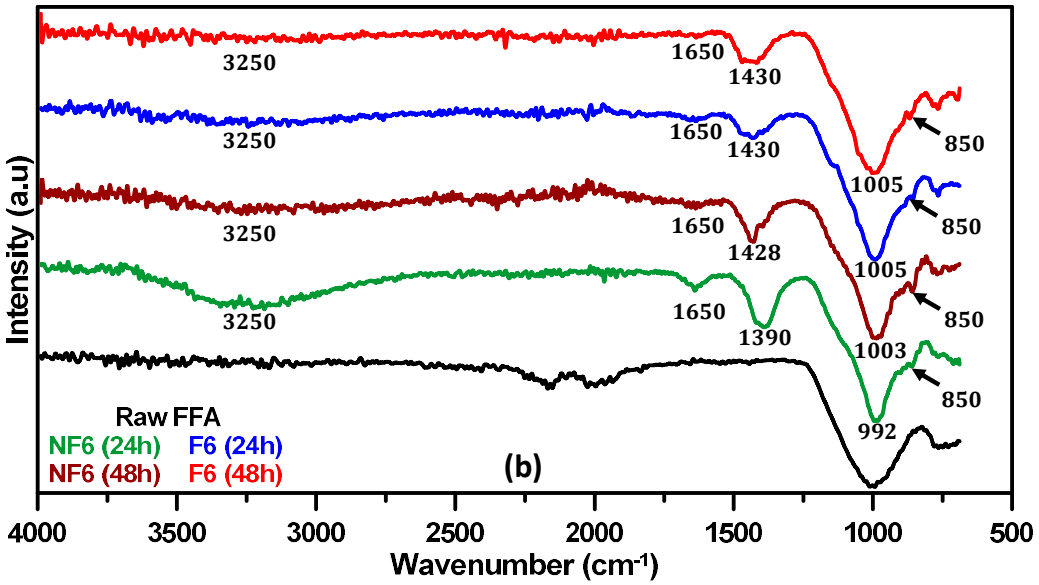

Figure 4-9: FTIR spectra of non-foamed and foamed samples belonging to: (a) series 1 (activated by carbonates alone), and (b) series 6 (activated by carbonate and silicate).

4.3.4.3. Microstructural Analysis

Figure 4-10 shows scanning electron micrographs at different magnifications of the fracture surface of a representative foamed geopolymer sample (F6, here). Large pores 100-500 μm in size, formed due to the release of CO_2 can be observed in this figure. Unreacted/partly reacted fly ash particles and space-filling reaction products are also observed. Closer observation reveals reaction products of different morphologies, which are evaluated in detail as follows.

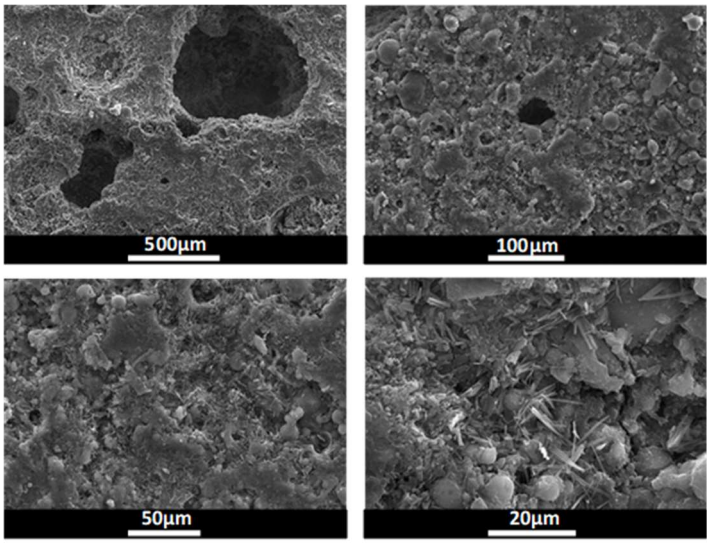

Figure 4-10: Scanning electron micrographs of a representative foamed geopolymer (F6 sample) at different magnifications.

Figure 4-11 depicts the SEM images of the F6 sample along with representative EDX spectra. Figure 4-11(a) shows fly ash particles, a fly ash plerosphere (spherical particle filled with sub-particles), and the N-A-S-H gel which is the reaction product of the geopolymerization reaction. The x-ray spectra for the entire composite material is also shown, with predominant peaks of Na, Al, and Si. Figure 4-11(b) and (c) shows a region in the microstructure with a high density of crystalline whisker (needle) like particles. The EDX spectra of the reaction product around the fly ash particle is also shown in Figure 4-11(b), which confirms the existence of N-A-S-H gel when Class F fly ash is activated using a combination of alkali carbonate and silicate. The average Si/Al and Na/Si ratios of the gel were 2.2 and 0.3 respectively, which are typical for N-A-S-H gels [155,156]. Figure 4-11(c) shows the EDX spectra of the zone with an abundance of needle-like crystals, which identifies it as sodium carbonate crystals, which was also identified in the TGA and FTIR analysis reported in the previous sections. As described earlier in the study, sodium carbonate added to the aqueous medium as an activator converts into sodium bicarbonate

and NaOH, which converts back to sodium carbonate and releases CO_2 when heated. Figure 4-12 shows the elemental map of the needle-like products. Si and Al are completely absent in this reaction product, and contains only Na, C, and O, confirming that it indeed is sodium carbonate which is recrystallized from the starting activator.

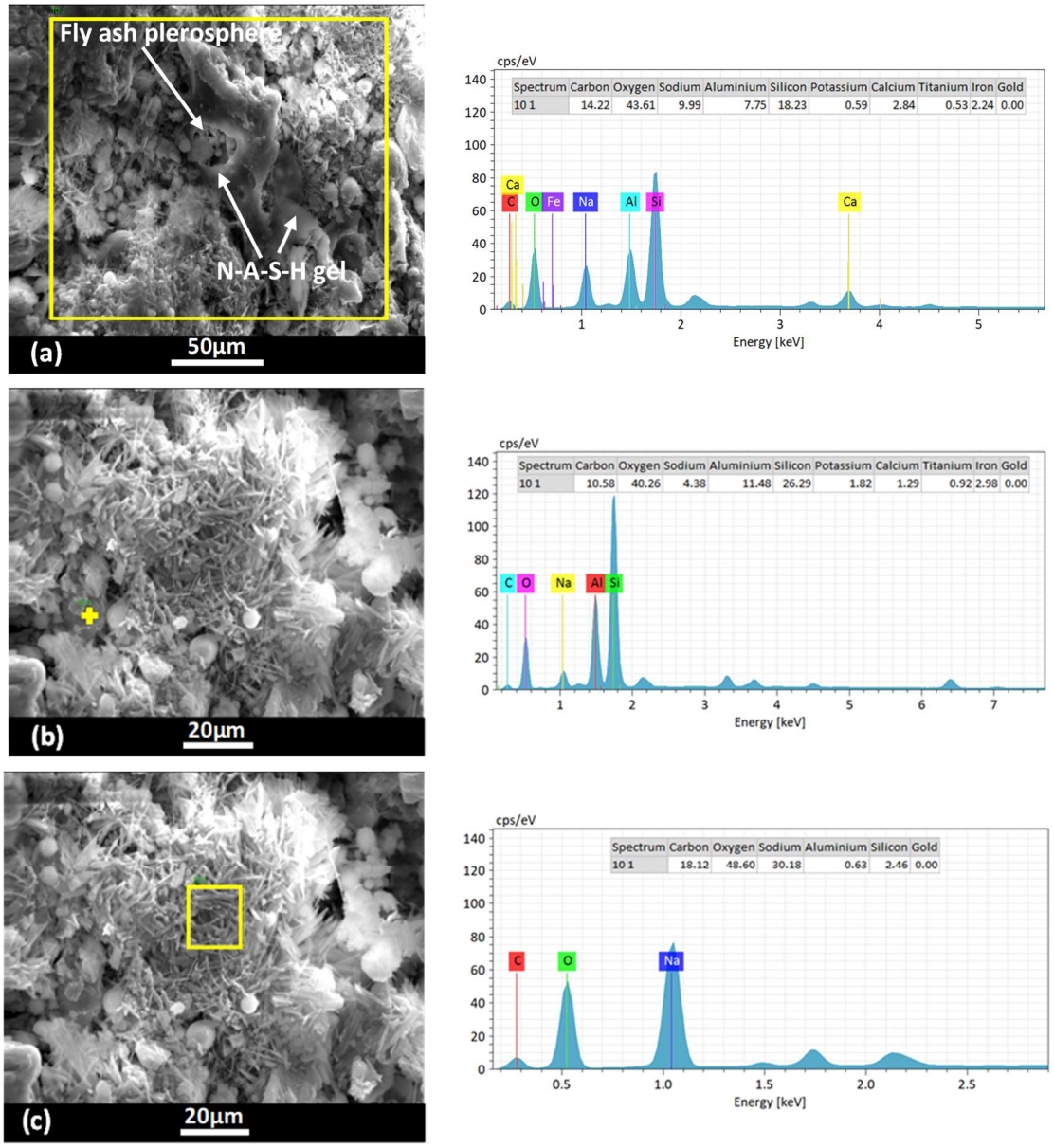

Figure 4-11: (a) SEM image showing fly ash particle and the reaction products under activation using alkali carbonate and silicate, (b) and (c) SEM images along with EDX spectra locations for N-A-S-H gel and sodium carbonate respectively.

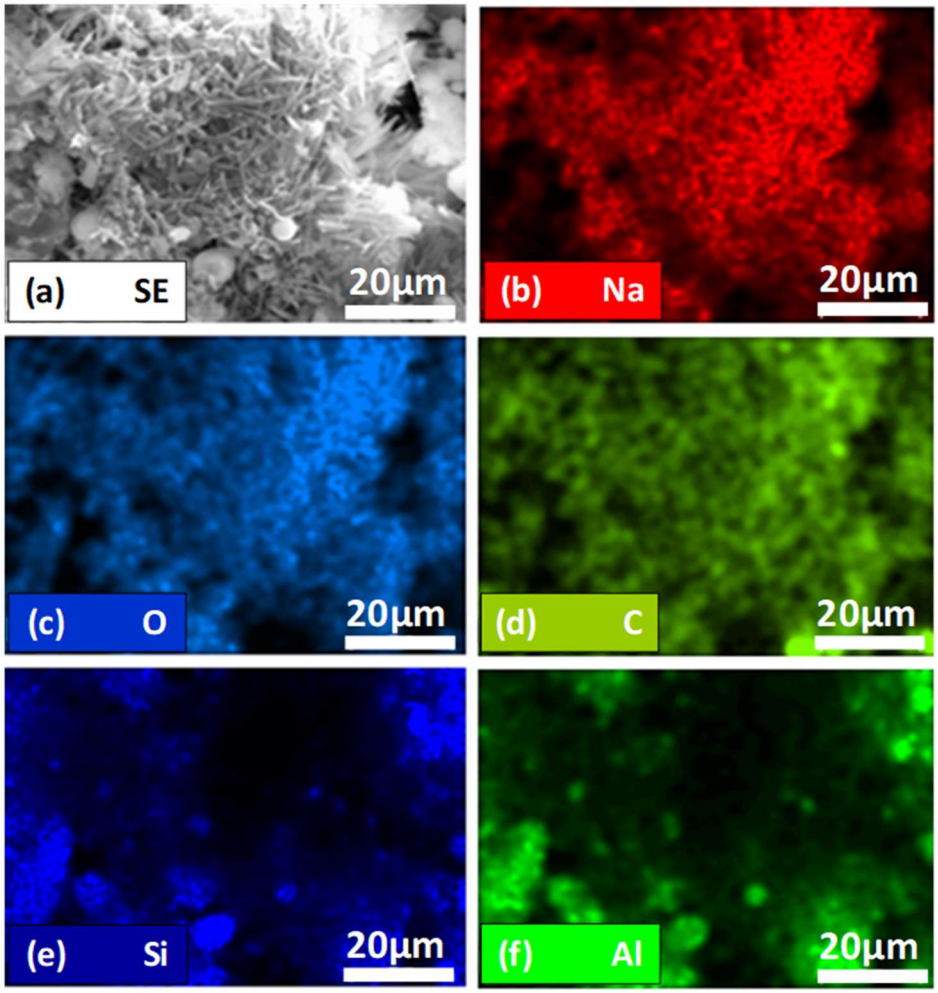

Figure 4-12: Elemental maps of the needle-like reaction product, confirming that it is sodium carbonate. (The brighter the color, the higher the concentration of the element).

4.3.5. Carbon Dioxide Equivalent (CO_2-eq) Emission

An evaluation of CO_2 equivalent (CO_2-eq) emissions of the porous geopolymers formed through carbonate-based activation is provided here. Since some amount of CO_2 is released during foamed geopolymer synthesis, such an exercise establishes the sustainability aspects of this material. The functional unit used in this work is the CO_2-eq emitted due to the materials and processes required to produce 1 m^3 of foamed geopolymer. Determination of CO_2-eq is generally based on the collective contributions of CO_2, NO_2, CH_4, and other gases evolved during the stages in the production of the raw materials, along with the

energy content of the fuel, the greenhouse gas types produced, and the global warming potential when the fuel is fully combusted, in conjunction with [157,158].

A majority of the CO_2-eq values of source materials and processes used in this study has been sourced from [159]. Class F fly ash can be considered to have a zero CO_2-eq emission since it is a waste material. However, collection and transport cannot be ignored, and thus a low value of 0.02 kg of CO_2-eq/kg of fly ash can be used. Sodium carbonate is typically manufactured using the Solway process, and has a CO_2-eq emission of 0.59 kg/kg of Na_2CO_3 [160]. Sodium silicate is considered to have a CO_2-eq estimate of 1.0 to 1.5 kg CO_2-eq per kg of solid (based on the solids content in the sodium silicate solution, e.g., 36%, this value can be adjusted), while NaOH has a corresponding value of 1.9 kg CO_2-eq per kg [159,161]. It is difficult to obtain actual data on elevated temperature curing for geopolymer synthesis, but a conservative value of 70 kg of CO_2-eq/m^3 of foamed geopolymer is used based on guidelines reported in [159]. In this study, we evaluate the CO_2-eq/m^3 of the F1 and F6 mixtures (activated using sodium carbonate alone or sodium carbonate and sodium silicate). Figure 4-8 shows the mass loss corresponding to sodium carbonate in the foamed geopolymers, from which the amount of CO_2 released during the foaming process was calculated. This ranged between 5% to 7% of the mass of the foamed solid, and can be quantified as CO_2-eq/m^3 by multiplying this with the density. Table 4-5 shows a comparison of the CO_2-eq of F1 and F6 mixtures, along with a fly ash based foamed geopolymer (using H_2O_2) as the foaming agent [139], and plain cement-based, non-autoclaved aerated concrete [136] that employs Al powder as the gas-forming agent. It can be noticed that the F1 and F6 matrices have lower CO_2-eq/m^3 of geopolymer even after considering the CO_2 release due to sodium carbonate decomposition under heat curing. For

the companion matrices considered, heat curing/autoclaving are not accounted for, which will further inflate their CO_2-eq values.

Table 4-5: CO_2-eq calculation for different porous matrices.

Porous matrix	**Components, amounts, and CO_2-eq**			**CO_2-eq/m^3**
	Type	**CO_2-eq/kg**	**Content (kg/m^3)**	
F1	Fly ash	0.027	1365.00	36.86
	Na_2CO_3	1.00	109.00	109.00
	Water	0.00	442.00	0.00
	Heat curing			70.00
	CO_2 release (~6% by mass)			82.20
	Total			**298.06**
F6	Fly ash	0.027	1271.00	34.32
	Sodium silicate solution (36% solids)	0.55	356.00	195.80
	Na_2CO_3	1.00	122.00	122.00
	Additional water	0.00	215.00	0.00
	Heat curing			70.00
	CO_2 release (~6% by mass)			72.60
	Total			**494.72**
Fly ash based foamed geopolymer	Fly ash	0.027	1276.00	34.45
	Sodium silicate solution (54.2% solids)	0.82	180.00	147.60
	NaOH	1.90	196.00	372.40
	H_2O_2 (30% in water)	0.68	29.00	19.72
	Additional water	0.00	276.00	0.00
	Total			**574.17**
OPC-based non-autoclaved aerated concrete	OPC	0.82	750	615.00
	Fly ash	0.027	750	20.25
	Water	0	600	0.00
	Al powder	1.5	15	22.50
	Total			**657.75**

4.4. CONCLUSIONS

This study has presented a novel method of synthesis of porous lightweight matrices based on fly ash geopolymers. Sodium carbonate, a less caustic, cheap, and abundant material, was used as the activating/pore forming agent, along with waterglass in some cases to provide additional alkalinity to ensure better geopolymerization. The formation of NaOH in the hydrolysis of sodium carbonate provided the alkalinity for the reactions, while the dissociation of formed sodium bicarbonate into CO_2 under heat accounted for the porosity in the matrix. It was noticed that a heat treatment temperature of 100°C resulted in a porous material with approximately 25% increase in volume, and bulk densities in the 1.1 to 1.4 g/cm^3 range, while treatment at 85°C resulted in a less porous material with bulk densities around 1.7 g/cm^3. Thermal conductivities in the range of 0.29 to 0.37 W/m-K were obtained for the foamed matrices having a porosity of 45-55%. The pore-forming process was tuned in such a way that the resulting matrices have adequate mechanical and insulation properties, but it is possible to tailor the composition and processing to obtain requisite properties, enabling microstructural design of materials for performance. The critical pore sizes were found to be lower (albeit at similar porosities) when the matrices were synthesized using a combination of carbonates and silicates rather than carbonates alone, indicating the influence of silicates and their polymerization on refining the pore structure. The presence of sodium bicarbonate and sodium carbonate in the matrices, along with the alkali aluminosilicate gel was confirmed.

It has been shown that, while carbonates alone can perform the dual function of activation (through alkali hydroxides produced in solution) and pore-forming, slight modification of the activator through the use of silicates enhances the geopolymerization reaction, and thus

the mechanical properties. The calculation of CO_2-equivalent emissions per m^3 of the foamed geopolymeric systems implemented in this study, and their comparison to similar materials shows that these materials have a lower CO_2 footprint, despite some CO_2 emissions in the foaming process. Development of such tunable porous materials from waste/by-product starting materials and less caustic/cheaper chemical agents that can perform activation and pore-forming functions can contribute significantly to the cause of sustainability in the built environment.

CHAPTER 5[3]

INSIGHTS INTO MATERIAL DESIGN, EXTRUSION RHEOLOGY, AND PROPERTIES OF 3D-PRINTABLE ALKALI-ACTIVATED FLY ASH-BASED BINDERS

5.1. INTRODUCTION

3D printing (or additive manufacturing) enables fabrication of complex and multi-scale structures through computer-aided design [43,44]. This technology has been successfully applied in aerospace, automotive, and biomedical fields [38,162,163]. 3D printing of cementitious materials where structures are created by layer-wise construction enables acceleration of the construction process, helps build complex architectural shapes that otherwise are difficult to realize, and facilitates labor and energy reductions [41,84–87]. 3D printing also enables special components to be fabricated. As an example, low cost syntactic foams (hollow particles filled composite materials) were recently created by 3D printing technique as reported in [48,49]. The commonly used 3D printing technique for concrete is material extrusion and layered printing [85,90,164,165], even though direct ink writing and powder-based printing have also been attempted [166–169]. These mixes are designed to flow through a barrel-die system and have enough structural stability when stacked in layers to print a stable structure. In extrusion-based printing, the rheological characteristics of the mixtures play a crucial role, and thus several studies have explored the influence of paste rheology in 3D printing of cementitious materials [37,169–172]. In

[3] This chapter is derived from publication: H. Alghamdi, S.A.O. Nair, N. Neithalath, Insights into material design, extrusion rheology, and properties of 3D-printable alkali-activated fly ash-based binders, Materials & Design. 167 (2019) 107634.

addition to rheological properties, setting time and mechanical properties of the printed elements are also of interest [173,174], as is the case with any construction material.

A large number of ongoing studies on 3D printing of cementitious materials focus on the use of binders based on ordinary portland cement (OPC), as expected [86,90,175]. Significant advances in the field of mineral and chemical admixtures have aided in the production of OPC-based 3D printed materials whose rheology and early-age response can be tailored. The use of geopolymer binders, which has been widely recognized as a sustainable option to reduce the carbon footprint of concrete, for 3D printing has also been reported [17,18,53,54,176]. It is conceivable that such sustainable binders can be utilized in mass construction, especially in areas where waste/by-product materials like fly ash are abundant. 3D printing of low strength geopolymer binders can also be employed in disaster rehabilitation where temporary structures are needed. This study examines the aspects that are relevant in the material design of fly ash-based alkali activated binders for 3D printing. Special focus is given to: (i) the use of minor ingredients including fine limestone powder that contributes to improved microstructural packing that provides the network strength in the fresh state to be extruded and layered in a shape-stable manner, and (ii) the influence of alkaline activators on the rotational, extensional, and extrusion rheology of pastes. These studies elucidate the relevant characteristics of the fresh pastes that are influential in printability. Extrusion rheology experiments combined with phenomenological modeling is used to obtain the linkage between the material design and process-related parameters, thereby enabling better strategies to produce sustainable, alkali-activated 3D printable binder systems.

5.2. EXPERIMENTAL PROGRAM

5.2.1. Source Materials and Activators

The primary source material utilized in this study was class F fly ash conforming to ASTM C 618. Based on our previous work [170] and several trial mixtures, it was observed that other minor ingredients are required to ensure extrudability and buildability (together termed as printability). Moreover, materials such as slag and ordinary portland cement (OPC), when incorporated into alkali activated fly ash-based systems, improves the setting time and the mechanical properties of the binder. Table 5-1 lists the binder components utilized in this study, along with their chemical composition. Figure 5-1 shows the particle size distributions (PSDs) of the source materials used. Sodium hydroxide (NaOH), sodium silicate solution (waterglass), or sodium sulfate (Na_2SO_4) were used as the activating agents in this study. NaOH was used as the sole activator, or in combination with sodium silicate or sodium sulfate to provide requisite alkalinity to enable aluminosilicate dissolution and precipitation. Waterglass supplied by PQ Corporation has a solids content of 36%, a silica modulus (molar ratio of SiO_2-to-Na_2O) (M_s) of 3.3, and specific gravity of 1.38 g/cm^3. The sodium hydroxide and sodium sulfate powders were determined to have specific gravities of 2.13 and 2.66 g/cm^3 respectively.

Table 5-1: Chemical composition of the source materials.

Components of the binders	Chemical composition (% by mass)						
	SiO_2	Al_2O_3	Fe_2O_3	CaO	MgO	SO_3	LOI
Fly ash (F)	58.40	23.80	4.19	7.32	1.11	3.04	2.13
Slag (S)	36.0	10.5	0.67	39.8	7.93	2.10	3.01
OPC (C)	19.60	4.09	3.39	63.21	3.37	3.17	2.54
Limestone (L)	$CaCO_3$ > 99%						
Alumina powder (A)	AL_2O_3> 99%						

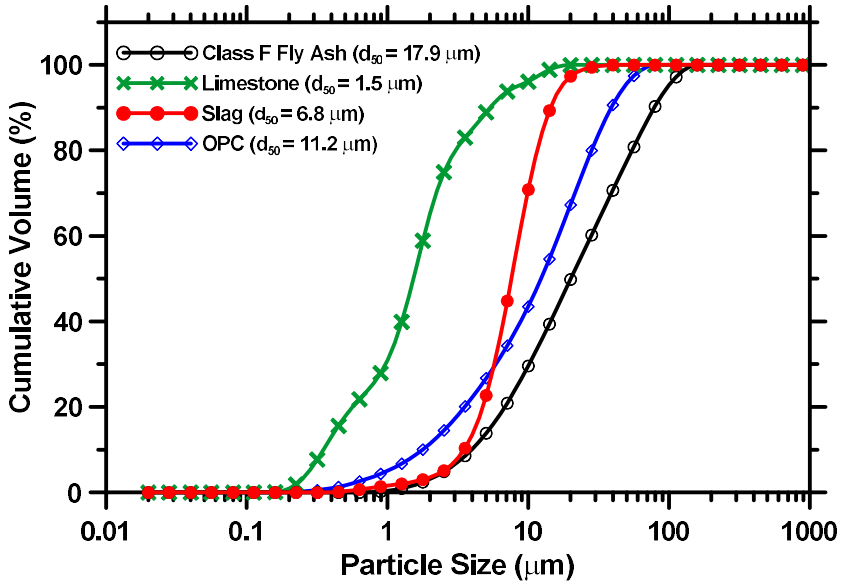

Figure 5-1: Particle size distributions (PSD) of the paste constituents.

5.2.2. Printer and Print Geometries

A desktop printer based on Cartesian configuration [91] was customized with a 100 cm^3 barrel to print the alkali activated paste mixtures. The diameter of the barrel (D_b) used for paste printing was 35 mm. Two different die exit diameters were adopted in this study (4 mm and 6 mm) with lengths of 35 mm and 20 mm respectively to maintain the die length-to-diameter ratios (L_d/D_d) of 9 and 3.33. The die entry diameter was 10 mm. The inner surface of barrel was lubricated to reduce the wall friction and ensure smooth and easy motion of the piston. Several shapes were printed to investigate and visually inspect the printability of mixtures. Slic3r software [92] was used to adjust the printing parameters including printing speed, layer width and height, and infill volume and pattern. The printing parameters used in this study are: layer height of 3mm, layer width of 6 mm, and printing speed of 20 mm/s.

5.2.3. Material Design for Printability: Multi-Component Binders and Activators

The printability criteria employed in this study were: (i) the ease of extrusion through a tapered nozzle (extrudability), and (ii) the stability of the layered printed shape (buildability). These criteria, together termed as printability, were visually ascertained in the preliminary phase of the study to select a matrix of alkali-activated fly ash-based mixtures for 3D printing. The extrudability and buildability of the selected mixtures are quantified later. Note that these are also dependent on printing parameters including nozzle shape and printing speed. The material design procedure started with class F fly ash as the sole binder, activated by a 5% NaOH solution. Mixtures were prepared using a mass-based liquid-to-binder ratio (l/b) starting from 0.20, at 0.01 increments. Mixtures developed using the lower end of this l/b range were very stiff and difficult to extrude. A l/b of 0.25 was found to result in a cohesive, extrudable paste (control mixture); however, this mixture was not buildable, as shown in Figure 5-2(a). This response is similar to that observed for plain OPC and OPC-fly ash pastes reported in [170], which were also not buildable. The buildability of the cement pastes, for a given set of printing parameters, is a strong function of the initial yield stress of the paste, which depends on the number and quality of interparticle contacts. This in turn, is a function of the particle sizes, arrangement of the particles (including effects of flocculation), and the type of interparticle forces [177]. However, flocculation and its effects are not discussed in this study. The use of fly ash (d_{50} of ~18 μm) alone as the binder is likely to result in an insufficient number of interparticle contacts to provide sufficient yield stress to the paste. Thus, fine limestone (d_{50} of 1.5 μm) was used as a filler material [71], replacing 15% of fly ash by mass, to enhance the number of interparticle contacts in a given volume and give better fresh state rigidity to the system

to resist the overburden pressure without instability. The printability was substantially improved through this minor compositional change, as shown in Figure 5-2(b). The l/b was increased to 0.27 to ensure extrudability, attributable to the presence of fine limestone particles.

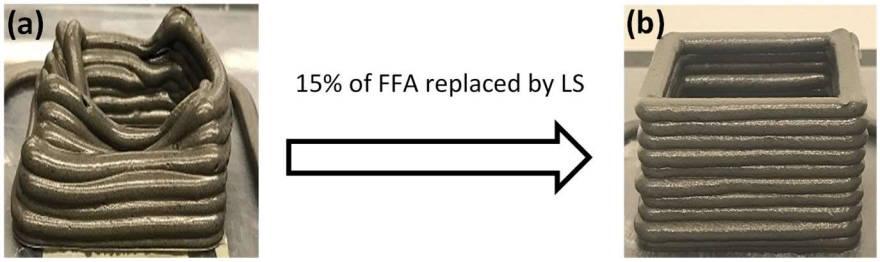

Figure 5-2: Hollow cube geometry printed using fly ash-based binders activated using 5% NaOH: (a) 100% class F fly ash paste (l/b=0.25), showing shape instability, and (b) improvement in printability and buildability when 15% fine limestone is incorporated into the paste (l/b=0.27).

Next, the activator concentration was increased from 5% to 10% NaOH. With a 10% NaOH content in the activator solution, an extrudable mixture containing fly ash alone was obtained with a l/b of 0.20 (as compared to a l/b of 0.25 for 5% NaOH activation). The increase in activator viscosity with increase in NaOH concentration enhances the cohesiveness of the mixture [178]. The combined effects of: (i) reduced interparticle spacing at a lower l/b, (ii) increased activator viscosity, and (iii) greater negative surface charges on fly ash particles at higher NaOH concentrations that result in increased interparticle repulsion [178] enable the production of an extrudable mixture as shown in Figure 5-3(a) and (b), at a l/b of 0.20. However, the mixture was too cohesive, to the extent of being very “sticky”, that resulted in layer deformation at corners during the printing process (as the print head drags already laid material), as can be noticed in these figures. To compensate for this effect, the l/b was increased to 0.24, along with the replacement of 15% of fly ash with fine limestone powder. Figure 5-3(c) shows that, while the mixture

consistency and water retention was improved (note the shine in Figure 5-3(a) and (b), which is due to water draining from the paste, while Figure 5-3(c) shows improved water retention due to limestone addition), the print quality was still inconsistent. Minor compositional changes could account for these effects, but in order to create a more diverse composition, the limestone content was increased to 30%, and the l/b to 0.27, to result in a satisfactorily extrudable and buildable mixture as shown in Figure 5-3(d). Note that the l/b is same for the selected mixtures with 15% and 30% limestone powder (Figure 5-2(b) and 3(d)). It has been suggested that higher hydroxide contents in particulate suspensions might have an effect similar to that of superplasticizers [178].

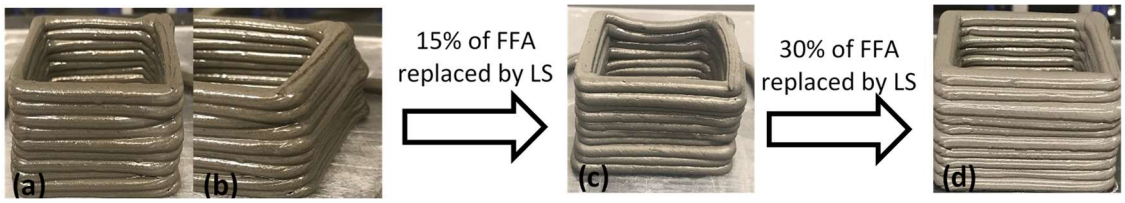

Figure 5-3: Hollow cube geometry printed using fly ash-based binders activated using 10% NaOH: (a and b) 100% Class F fly ash paste (l/b=0.20) showing layer deformation, (c) binder with 15% limestone (l/b=0.24), showing shape instability, and (d) binder with 30% limestone (l/b=0.27) showing satisfactory printability and buildability.

In addition to the binary fly ash – limestone systems discussed earlier, slag or OPC were also used as components of the activated binders to develop ternary blend systems. In such cases, the fly ash content was fixed at 50% (mass-based). The fly ash – OPC – limestone system was activated by a combination of sodium sulfate and NaOH so as to reduce the overall alkalinity of the activator and ensure easier handling. It has been shown that Na_2SO_4 (a neutral salt) activation of high volume fly ash mixtures result in 28-day compressive strengths of ~30 MPa when cured at ambient temperatures [179]. The addition of 1% NaOH enhanced the cohesiveness of this system. The fly ash – slag – limestone system

was activated using NaOH or a combination of NaOH and sodium silicate to provide a Na_2O-to-powder ratio (n) of 0.05 and SiO_2-to-Na_2O ratio of the activator (M_s) of 0.50. In the latter system, 1% Al powder was used to delay the setting time of the mixture. The chosen mixtures were mixed at 200 rpm for 30 seconds, followed by 1200 rpm for 90 seconds to obtain a homogenous mixture. Table 5-2 lists the selected binders used for further studies. Note that the letter (F, L etc.) corresponds to the ingredients (see Table 5-1), and the number in the subscript refers to the mass fraction of the ingredient in the starting binder blend. The median particle sizes of blends are also listed in the table to indicate how the use of minor ingredients change d_{50} of the composite mixture. This is significant since yield stress is known to be well related to the square of d_{50} [170,177].

Table 5-2: Binder proportions and the median particle sizes (d_{50}) for the final printable mixtures.

Mixture ID	FFA (%)	Slag (%)	OPC (%)	LS (%)	Al powder (%)	Alkali activator (%)		Liquid/ powder ratio	d_{50} (µm)
						NaOH (%)	Na_2SO_4 (%)		
$F_{85}L_{15}$	85			15		5		0.27	15.20
$F_{70}L_{30}$	70			30		10		0.27	10.37
$F_{50}C_{30}L_{20}$	50		30	20		1	2	0.30	11.32
$F_{50}S_{30}L_{20}$	50	30		20		5		0.35	8.79
$F_{50}S_{30}L_{19}A_1$	50	30		19	1	n=0.05*, M_s=0.5**		0.30	8.71

* n= Na_2O/total powder (mass based); NaOH is the source of Na_2O.
** M_s= SiO_2/Na_2O (molar based), Sodium silicate solution is the source of SiO_2.

5.2.4. Test Methods

5.2.4.1. Rheological Characterization

A mini slump cone with a bottom diameter of 38 mm, top diameter of 19 mm, and a height of 57 mm was used to determine the shape stability of the printable binders. The paste was loaded in the mini-slump cone and then slowly lifted to determine the slump value. A

dynamic shear rheometer (TA Instruments AR 2000EX) was used to carry out the rheological studies using a parallel plate geometry to determine the shear stress (τ) of the printable pastes as a function of shear rate ($\dot{\gamma}$). The upper and lower plates were serrated at depths of 1 mm and 0.15 mm respectively to prevent paste slip on the shearing surface. The bottom plate contained Peltier elements, and was conditioned to a temperature of 25 ± 0.1 °C. The volume of paste sample was calculated for a plate gap of 2 mm and evenly put on the bottom plate to avoid an overfilled state while testing. The sequence of steps employed in rotational parallel plate rheology includes: (i) a stepped ramp up pre-shear phase for approximately 80 s to homogenize the paste, (ii) a stepped ramp-up, and (iii) a stepped ramp-down, as shown in Figure 5-4(a) [70,71]. The data was collected from only the down-ramp phase. Shear stress and shear rate data were extracted using TA Instruments' TRIOS software package. The range of the shear rate used in this test were from 5-to-100 s^{-1}, and the Bingham model was used to extract the apparent yield stress from the relationship between shear stress and shear strain rate. In addition to shear rheology, the parallel plate test set up was also used for the tack test. The tack test indicates the adhesive properties and cohesion of the paste mixtures. These properties are important to ensure that the pastes adhere well to surfaces, which influences the interface properties [180]. The paste was placed on the bottom plate and a gap of 2 mm was set between the plates. A pre-shear phase similar to the one shown in Figure 5-4(a) was used to homogenize the paste. The top plate was set to rise at a constant velocity of 10 μm/s until the sample was completely separated from the plates. The normal force experienced by the top plate was recorded as a function of plate separation.

A 4.45 kN servo-controlled MTS machine was used to carry out the extrusion rheology studies of alkali activated printable pastes. The paste sample was filled in the extruder immediately after mixing, ensuring that no air voids are entrapped in the paste. The plunger was placed inside the barrel in direct contact with the compacted paste. The assembly was placed in a specially fabricated holder to allow the upper platen of the test machine to axially compress the plunger. A multi-speed extrusion test with ram velocities ranging from 150 mm/min to 10 mm/min was used. Figure 5-4(b) shows the experimental procedure used for the extrusion rheology tests. The nozzle (die) diameters used for the extrusion test were 4 mm and 6 mm, and the corresponding nozzle lengths were 35 mm and 20 mm respectively. The extrusion velocity is calculated from the ram velocity using flow equivalence, given as:

$$D_b^2 V_{ram} = D_d^2 V_{ext} \tag{5-1}$$

where V_{ram} is the ram velocity and V_{ext} is the extrusion velocity, and D_b and D_d are the barrel and die diameters respectively.

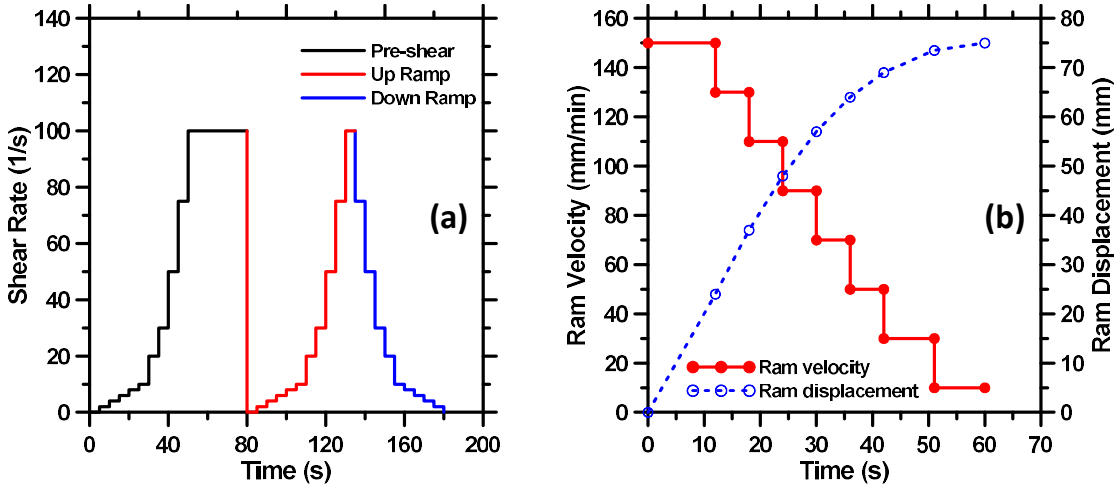

Figure 5-4: Experimental procedure used for: (a) parallel plate rheology, (b) extrusion test.

5.2.4.2. Pore Structure and Mechanical Properties

The setting times of the selected mixtures were determined in accordance with ASTM C 191-18a [181], with a time gap between each penetration reading of 15 minutes. Mercury intrusion porosimetry (MIP) was used to investigate the porosity and critical pore sizes of the different layers of the printed pastes. Small samples carefully obtained from different printed layers were placed in the low-pressure chamber of the porosimeter (Quantachrome Instruments Pore Master). The sample was pressurized with mercury from an ambient pressure to 345 KPa (60 psi). This is followed by intrusion of mercury in a high-pressure chamber where the pressure was increased to 414 MPa (60,000 psi). The pore diameter (d) as a function of the intrusion pressure can be obtained from the Washburn equation as:

$$d = \frac{-4\,\sigma\,cos\theta}{\Delta P} \tag{5-2}$$

where ΔP is the difference in the pressure between successive steps (MPa), θ is the contact angle between mercury and the cylindrical pore (130° in this study) [27,108,109], and (σ) is the surface tension between mercury and the pore walls (485 mN/m).

The specific gravities of the paste samples were determined using a gas pycnometer (Ultrapyc 1200e, Quantachrome Instruments). The compressive strengths of the printed pastes were determined on printed cubes of 40 mm side length. The flexural strength of the printed pastes was determined using a three-point-bending test. A displacement rate of 0.5 mm/min was used for the tests [73]. Three replicate specimens 21 mm x 21 mm x 120 mm in size were tested for each mixture listed in Table 5-2.

5.3. RESULTS AND DISCUSSIONS

5.3.1. Mini-Slump Flow and Initial Setting Times

The workability of the pastes and their setting times are important parameters in the qualification of 3D printable binders. Sufficiently long initial setting time is necessary to avoid premature stiffening while the mixture is being extruded and printed. Figure 5-5(a) shows the mini slump values and Figure 5-5(b) shows the needle penetration as a function of time for the selected paste mixtures. It is desirable to have a cohesive mixture demonstrating minimal slump to obtain a stable print with little or no deformation while maintaining extrudability. The maximum mini-slump value recorded was less than 9 mm which allowed consistent extrusion while being able to retain the shape during and after printing. The initial setting time ranged between 1.5 to 6.0 hours, which is generally attributed to the low reactivity of fly ash at ambient temperatures. For the mixtures ($F_{85}L_{15}$) and ($F_{70}L_{30}$), the setting time of ($F_{70}L_{30}$) was apparently delayed, attributable to increased alkaline activator (10% of NaOH) used in this mixture compared to (5% of NaOH) used in ($F_{85}L_{15}$). The increased NaOH decreased silica polymerization resulting in delayed setting time as reported in [178]. For the slag or OPC containing mixtures ($F_{50}S_{30}L_{20}$, and $F_{50}C_{30}L_{20}$), the rapid setting was attributed to the presence of slag [182] and OPC which helped accelerate the setting time at ambient temperature. However, the mixture containing slag along with alumina ($F_{50}S_{30}L_{19}A_1$) showed the longest setting time of approximately 6 hours due to the presence of alumina that delayed the setting time as proved in literature [183]. The cohesiveness of the mixtures, attained through improved packing of particles [173,184] (Section 5.2.3), ensured that the printed shapes were stable.

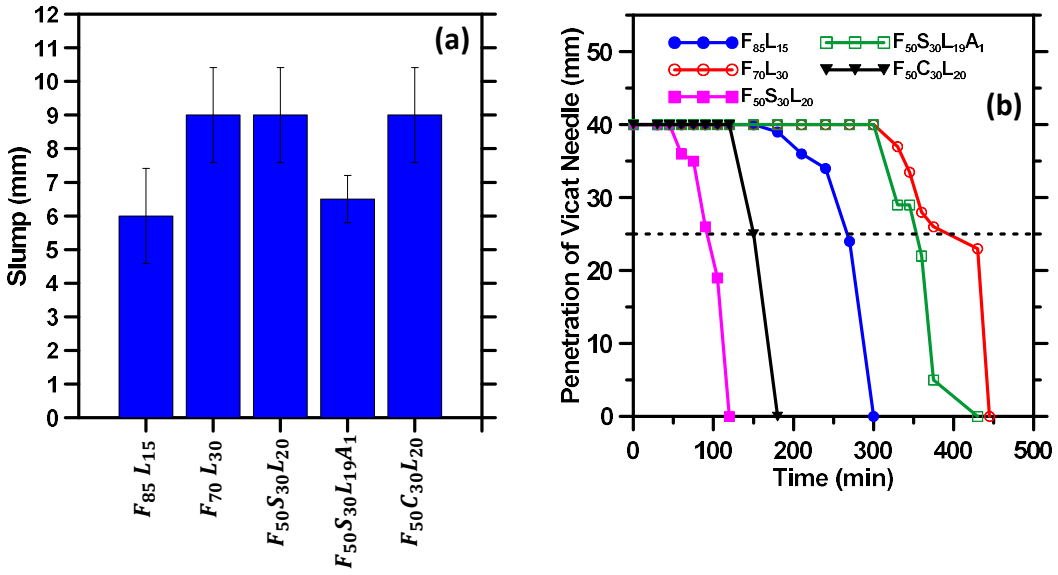

Figure 5-5: (a) Slump values and (b) initial setting times of the printable pastes.

5.3.2. Rheological Characterization of Fresh Pastes

5.3.2.1. Yield Stress from Parallel Plate Rheology and Its Relation to Printability

The yield stress of the pastes is influenced by the composition of the binders, and the type and amount of activators. Figure 5-6(a) shows the effect of mixture composition on the yield stress and plastic viscosity of the selected binders. The $F_{70}L_{30}$ mixture shows the lowest yield stress due to the higher amount of NaOH (10%) which acts like a superplasticizing admixture [178]. The yield stress of the $F_{85}L_{15}$ mixture is higher because of the lower water content in this mixture and the lower amount of NaOH. For mixtures containing 50% of fly ash, the yield stress and plastic viscosity are higher when OPC is present in the mixture than when slag is present. From the particle size distributions shown in Figure 5-1, it appears that OPC has a higher fraction of finer particles (0.5 to 5 μm) than slag, which could explain this behavior from a particle packing point of view. This is consistent with the inverse size dependence on yield stress shown in several studies (e.g. [185]). It is also conceivable that the surface charges in OPC that influence flocculation,

and the effects of particle shapes might also play a role in this behavior. The yield stresses vary between 150 Pa and 500 Pa for all the mixtures evaluated, which is very similar to the extrudable and printable OPC-based binders evaluated in a companion study [170]. As suggested earlier, this range depends on the printing parameters also.

It is instructive to understand the influence of the activating agents on the yield stress of suspensions. Hence the yield stress of the printable binders shown in Figure 5-6(a) are compared to those obtained when water is used as the dispersing medium instead of the alkaline solution. The results are shown in Figure 5-6(b). The decrease in yield stress when alkaline activators are used as dispersing media can be attributed to the fact that alkaline solutions act in a manner similar to that of superplasticizers [178]. The higher the alkalinity of the activator, the larger the decrease in yield stress.

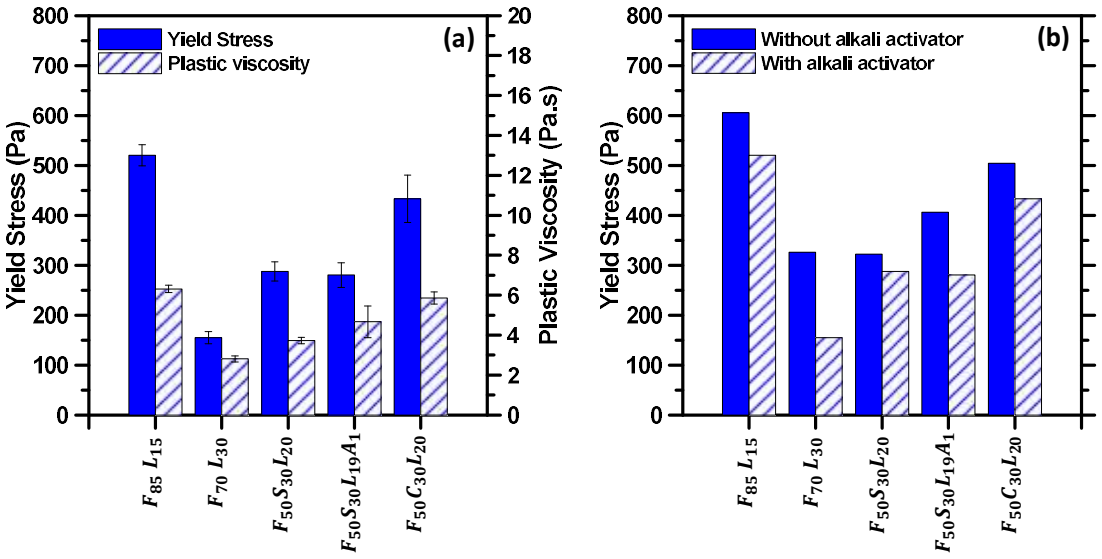

Figure 5-6: (a) Yield stress and plastic viscosity of the printable binders, and (b) effect of alkali activators on yield stress of design printable fresh pastes.

Figure 5-7(a) shows the mini slump test on an extrudable fly ash-water paste at an l/b of 0.25, while Figure 5-7(b) shows an extrudable fly ash-water-NaOH paste at an l/b of 0.20. It can be seen that, in addition to decreasing the yield stress (even at a lower l/b ratio),

alkaline solutions also resulted in enhanced cohesiveness of the pastes and better shape retention.

Printability is defined as the ability of a mixture to extrude (extrudability) and maintain the structural integrity when built in layers (buildability) [172], as explained earlier. Yield stress is an important rheological parameter that influences printability. It is also well known that slump of a cementitious mixture is related to its yield stress [186,187]. Thus, the use of mini slump values and the yield stress obtained from rotational rheology are synergistically considered to arrive at bounds for printability of the paste mixtures. Here, in addition to the alkali-activated binders considered in this study, data from a companion work on OPC-based binders [170] are also used. Figure 5-8 depicts the yield stress and slump of a range of mixtures considered, both printable and non-printable. All the considered mixtures were extrudable. A lower mini slump value and a higher yield stress are generally found to be the requirements for a printable mixture.

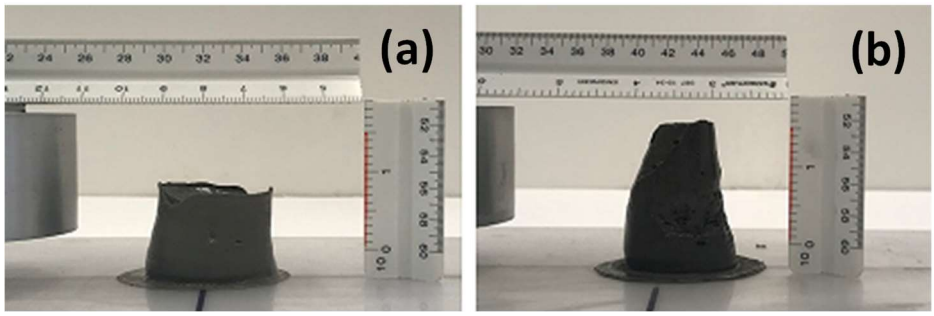

Figure 5-7: Mini slump of 100% fly ash paste mixed with: (a) only water, and (b) water with 10% of NaOH showing the effect of alkaline activator on paste slump and its cohesiveness.

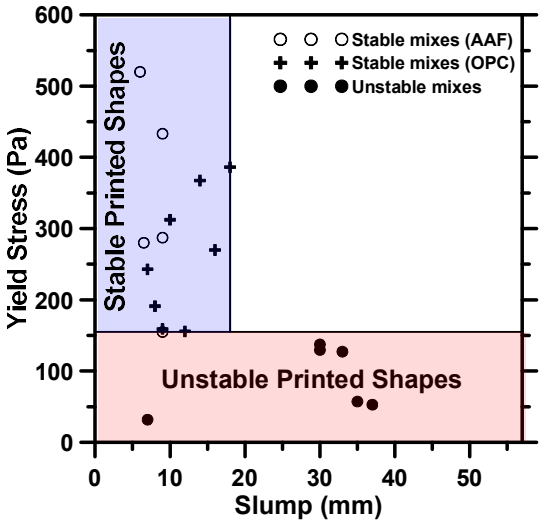

Figure 5-8: Yield stress vs. slump value of printable and non-printable mixtures (Data for stable mixes (OPC) labelled in the graph was obtained from our previous study [170].

The evolution of yield stress with time provides useful indications on the window of printability. For all the selected mixtures, yield stress was determined using the parallel plate geometry after maintaining the paste at rest different periods of time, as shown in Figure 5-9(a). The time interval between two measurements were determined based on the setting time of the pastes (Figure 5-9(b)). For the pastes that set faster (i.e., the 50% fly ash mixtures containing slag or OPC), the yield stress was measured after a rest period of 30 minutes, while for the other mixtures, the first rest period was 60 minutes. Corresponding to every time interval of yield stress measurement, a single filament was extruded and printed at different times after initial mixing. An example is shown in Figure 5-9(b) for the $F_{85}L_{15}$ mixture. The yield stress of the mixture corresponding to the final time beyond which it cannot be extruded and printed is designated as the upper bound of yield stress. For all the mixtures evaluated here, the yield stress limit of extrudability and printability was around 700 Pa (limited by the printer's capacity used in this study). In Figure 5-9(b), it is shown that, at 60 minutes (the time of first yield stress measurement for the $F_{85}L_{15}$

paste), remixing was done for 30 s before printing the filament again. This is to simulate the homogenization that happens during the pre-shear phase in the yield stress measurement method. The time from initial mixing to the time when the yield stress reaches approximately 700 Pa is termed as the printability window. Based on the above analysis, the $F_{70}L_{30}$ and $F_{50}S_{30}L_{19}A_1$ mixtures showed the longest printability window (3h) while the $F_{50}S_{30}L_{20}$ mixture showed the shortest window (1h). The printability window is found to scale relatively well with the initial setting time of the pastes, indicating that the setting time could be used as a surrogate parameter to estimate the printability window. This finding assumes significance since it shows that a simple test such as the setting time can be a useful indicator of an important process parameter, i.e., printability window, relating to 3D printing. It is also important to note that this result has been arrived at based on the few selected mixtures from this study and extensive investigations are needed to ensure that the relationship is valid over a wide range of mixture compositions.

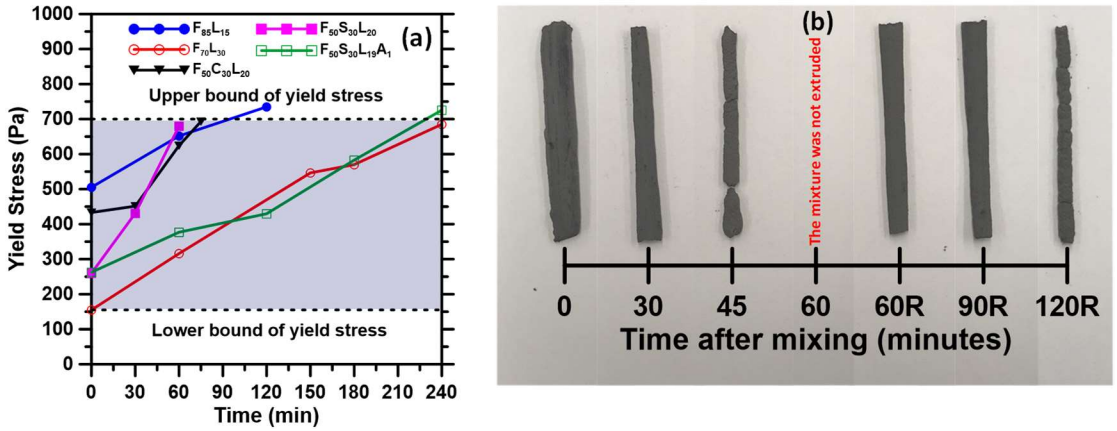

Figure 5-9: (a) Yield stress of printable mixtures with time showing the printability zone, and (b) extruded filaments of $F_{85}L_{15}$ mixture as a function of time after mixing. (R: remixing for 30 s after 60 min from initial mixing time).

5.3.2.2. Tack Test (Extensional Rheology)

Extensional rheology can be used to quantify the adhesive and cohesive nature of the pastes, which are influential in 3D printing. Cohesion is defined as the internal strength of the material at rest while adherence is defined as the tendency of the material to stick to a surface [188]. These properties influence the interlayer bonding in layered manufacturing, which plays an important role in the mechanical properties of the printed components.

Figure 5-10(a) shows the normal force as a function of plate displacement for the printable alkali-activated fly ash-based pastes, and Figure 5-10(b) shows the peak force and the gap displacement corresponding to the peak load. The adhesive and cohesive properties of the paste can be evaluated by the absolute value of the peak force and resistance of the paste to elastic failure [189]. An elastic increase in the normal force until the peak is demonstrated by all the mixtures. The peak load (corresponding to critical gap displacement) corresponds to the cohesion of the mixture beyond which rupture occurs and force starts to decay under a combination of viscous effects in adhesion and intrinsic cohesion. A higher peak force is reported to correspond to a higher adhesive capacity [189]. Figure 5-10(c) depicts the adhesion energy of the selected pastes, defined as the area under the force-displacement curve. The energy required to separate the paste under a normal tensile force is indicative of the influence of material composition on the bonding capacity, which influences interface properties of the 3D-printed structure.

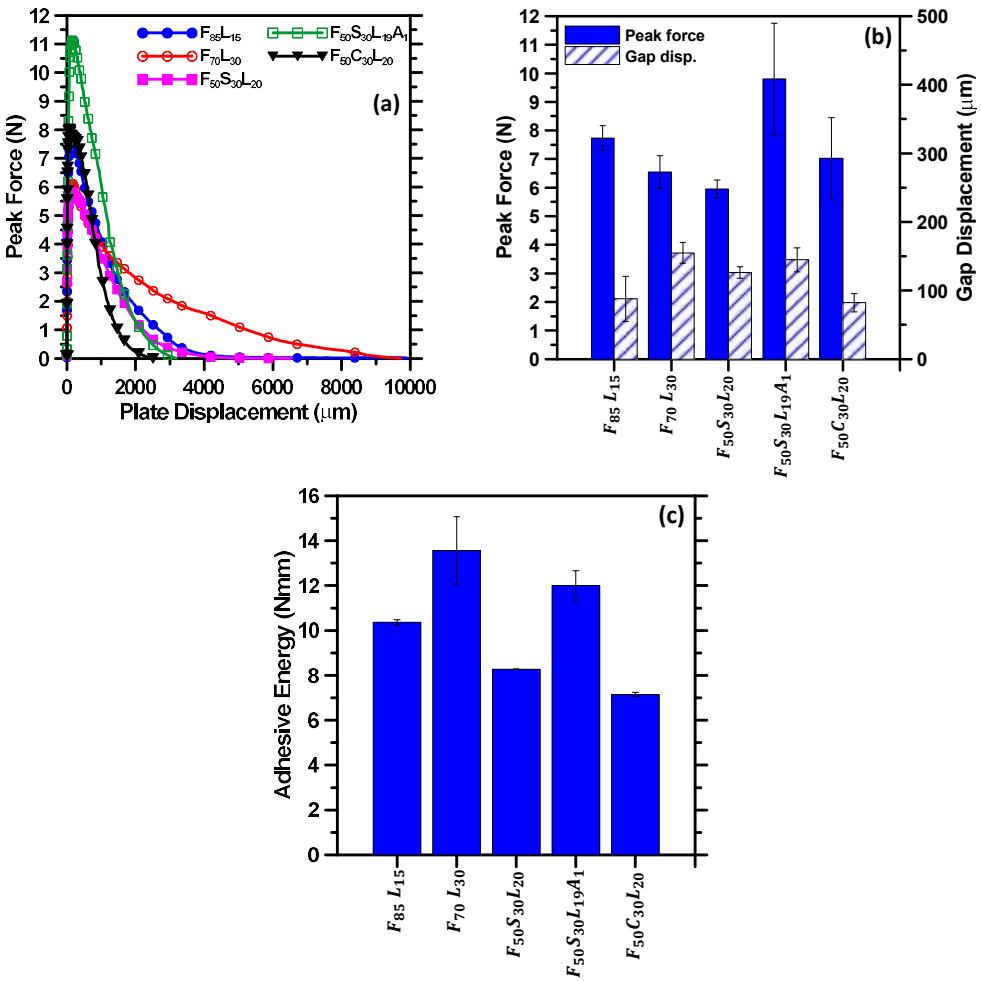

Figure 5-10: Tack test results showing: (a) absolute normal force as a function of plate displacement, (b) peak force and corresponding gap displacement for the selected pastes, and (c) adhesion energy of the design printable pastes.

The average peak forces of the selected pastes were between 6 N and 10 N whereas the total displacement (at complete separation) ranged between 2 to 9 mm (excluding the initial gap of 2 mm). The peak forces and the corresponding gap displacements shown in Figure 5-10(b) indicate that the paste containing OPC demonstrate the lowest gap displacement at peak force. This is corroborated by the lowest adhesive energy showed by this paste as shown in Figure 5-10(c). The lower gap displacement and the faster force decay after rupture indicates lower cohesive forces in the system containing OPC as compared to other mixtures evaluated. This can also be attributed to the lower alkalinity of the paste

containing OPC – the higher viscosity of NaOH combined with its higher concentration in the other systems contributing to increased cohesive stresses in the fresh state. Further, the paste containing the highest amount of NaOH ($F_{70}L_{30}$) showed the highest adhesive energy among the mixture studied, once again emphasizing the influence of the activating agent characteristics on early age adhesive and cohesive forces. The adhesion energy of the alkali-activated fly ash-based pastes reported here are 1.2 to 2 times higher than that of the OPC-based pastes reported in our previous work [170]. While much of this is attributed to the activator characteristics as mentioned earlier, this has implications in interlayer properties when a wet-on-wet layer construction scheme is implemented, as is the case with 3D-printed cementitious structural elements. Also, higher modulus can result in a reduction of inter-layer bond strength [190] which is related to lower adhesive energy of the mixes.

5.3.3. Influence of the Extrusion Process on The Rheology of The Printed Material

The rheological response of fresh binder mixtures was reported in the preceding sections, and criteria that could be used to infer important characteristics such as printability window, yield stress bounds, and adhesive characteristics discussed. However, extrusion involves application of pressure on the fluid paste at a certain velocity, and the rheological characteristics are highly sensitive to pressure and speed of extrusion. Analytical models and numerical models to evaluate the behavior of a yield stress fluid under pressure have been reported [191–195]. However, for ease of analysis and interpretation, we carry out extrusion rheology and implement a phenomenological Benbow-Bridgwater model [195] to analyze paste extrusion and infer the rheological characteristics of the extruded and printed material. The Benbow-Bridgewater model employs a plasticity approach to analyze the extrusion rheology of dense ceramic suspensions [196].

Figure 5-11 shows the extrusion force-displacement relationship for a selected alkali-activated fly ash-based paste ($F_{70}L_{30}$) subjected to different ram velocities, for different L_d/D_d ratios (9 and 3.33). An instantaneous increase in force is experienced because of the upsetting of the paste before its exits through the die. The pressure drops correspond to the changes in ram velocity, and the force plateau for each ram velocity is considered to be the corresponding extrusion force. The significant influence of L_d/D_d ratio on the extrusion force is shown in Figure 5-11, which can be used to glean the importance of the extruder geometry for desirable extrusion-related parameters.

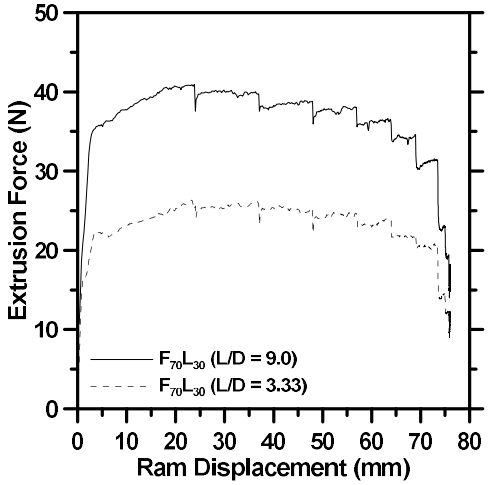

Figure 5-11: Force vs. ram displacement for a printable paste in a syringe extruder subjected to different ram velocities.

The Benbow-Bridgewater model can be expressed as:

$$P_{ext} = P_1 + P_2 = (\sigma_0 + \alpha V_{ext}^m)\, ln\left(\frac{A_b}{A_d}\right) + \frac{ML}{A_d}(\tau_0 + \beta V_{ext}^n) = \sigma_Y\, ln\left(\frac{A_b}{A_d}\right) + \frac{ML}{A_d}\tau_w \quad (5\text{-}3)$$

where P_{ext} is the total extrusion pressure, P_1 is the die entry pressure (the pressure required to extrude the paste from the barrel through the die entry), and P_2 is the die land pressure (which allows the paste to flow through the die under pure shear conditions). V_{ext} is the extrusion velocity, α and β are velocity multipliers, and m and n are velocity exponents.

σ_0 is the extrusion yield stress (as opposed to pure shear yield stress, since the confinement effects of the barrel and the compressional effects of the ram influence yielding) at the die entry, σ_Y is the apparent velocity-dependent extrusion yield stress of the plastic material, τ_0 is the slip yield stress, and τ_w is the velocity-dependent shear stress experienced by the paste due to its interaction with the die wall. The geometrical parameters include M, L, A_b and A_d which are the perimeter of the die, length of the die, barrel area, and die area respectively. The exponents m and n are taken as 1 (i.e., the extrusion pressure-velocity relationship is taken as linear, which was observed here, as well as in [170]), and thus the equation is reduced to a four-parameter model.

The Benbow-Bridgewater equation was derived based on a uniform die diameter. However, the die geometry used in this study is the frustum of a cone ($D_{entry} \neq D_d$). In this case, the area of die is a function of length of the die and the second term corresponding to the die in Equation 5-3 is modified suitably [170] as:

$$P_2 = P_{ext} - P_1 = \frac{ML}{A_d}(\tau_0 + \beta V_{ext}^n) = \sum_{i=0}^{n} \frac{M_i}{A_i} L_i \, (\tau_w) \quad (5\text{-}4)$$

M_iL_i is the surface area of the individual cylinder that forms part of the frustum, and A_i is the cross-sectional area of the cylinder. L_i is taken as 1 mm.

To determine the Benbow-Bridgewater parameters, the extrusion force is plotted as a function of L_d/D_d ratios for different ram velocities. The linear relationship between L_d/D_d and the extrusion force for different velocities is extrapolated back to the Y-axis to give the force at $L_d/D_d = 0$, from which the die entry pressure P_1 for different velocities are calculated. P_1, along with the barrel and die areas, is used to calculate the velocity-dependent yield stress σ_Y. The wall shear stress τ_w is determined from Equation 5-4.

Figure 5-12 depicts the extrusion yield stress (σ_Y) and the wall shear stress (τ_w) predicted by Benbow-Bridgewater model, which can be considered as the extrusion process-related parameters since they are dependent on extrusion velocity. The size of the error bars in this figure show the stresses corresponding to the highest and lowest extrusion velocities (which are deduced from ram velocities) used. The extrusion yield stresses predicted from the model range from 75-to-162 KPa while the shear yield stresses extracted through parallel plate rheology ranged from 155-to-520 Pa. Shear yield stress of 50-to-200 Pa measured through rotational rheology has been correlated to yield stress in the 3-to-40 KPa range from extrusion experiments [197]. The influence of the extrusion process on rheological response of pastes are thus evident. To achieve shape stability, it has been reported that the yield stress of extruded paste should be greater than 20 kPa [198]. All the alkali-activated fly ash-based pastes satisfy this criterion.

Wall slip shear stress is an important parameter in 3D printing of binders since this stress must be surmounted to ensure flow out of the nozzle. The wall shear stress, which is also pressure dependent as is known for other concentrated suspensions [199–201], depends on the L_d/D_d ratio as can be noticed from Figure 5-12, showing that it is. It is seen from this figure that the $F_{70}L_{30}$ mixture shows a higher wall shear stress not withstanding a smaller extrusion yield stress. This could potentially be due significant changes in the paste during the extrusion process (e.g., liquid phase migration) leading to inhomogeneous particle distribution in the die. The consequence is a higher energy need for extrusion and printing, likely resulting in further phase separation and inhomogeneous print quality. Extensional and wall stresses predicted through models thus serve as important tools in the apriori

determination of the effectiveness of chosen mixture compositions and extruder geometry in ensuring efficient extrudability and printability.

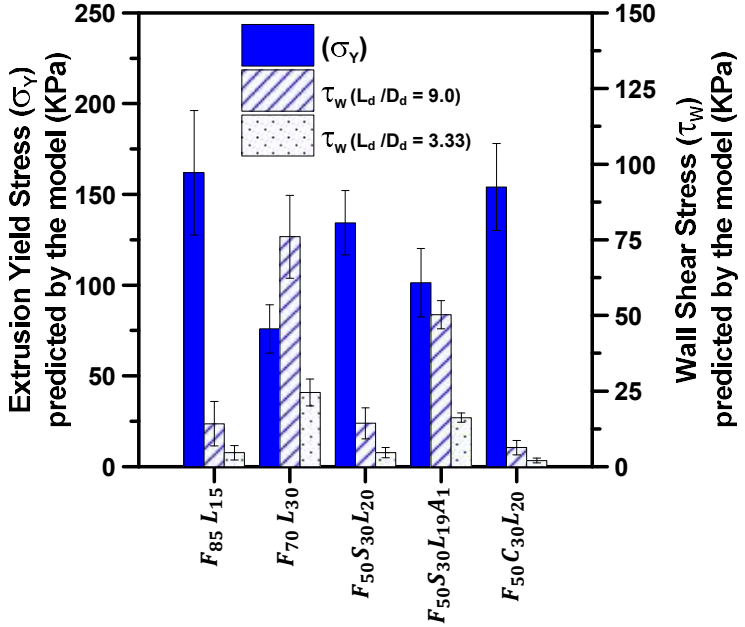

Figure 5-12: Velocity-dependent extrusion yield stress and wall shear stress (at two L_d/D_d ratios) for the printable pastes. The error bars relate to the range of stresses corresponding to the range of extrusion velocities.

Figure 5-13(a) depicts the relationship between the extrusion yield stress and the shear yield stress determined from parallel plate rheology and the peak force from tack test. For the selected mixtures, the extrusion yield stress from extrusion rheology and the shear yield stress from parallel plate rheology are well correlated, indicating that the determination of simple shear yield stress indeed can be used to infer the behavior of the paste under extrusion. The tack force and the extrusion yield stress are also well correlated. It can be postulated that the adhesive forces because of the viscous nature of the mixture in the presence of activators (as explained earlier) keeps the particles closer together, which consequently results in an increased extrusion yield stress for the mixtures exhibiting higher tack force. Figure 5-13(b) depicts the relationship between the shear yield stress

from parallel plate rheology and the extrusion force required. The extrusion force is taken as the force corresponding to the highest point in the force-displacement relationship shown in Figure 5-11. These relationships can be useful in understanding the extrusion response of these binder systems from straightforward laboratory tests.

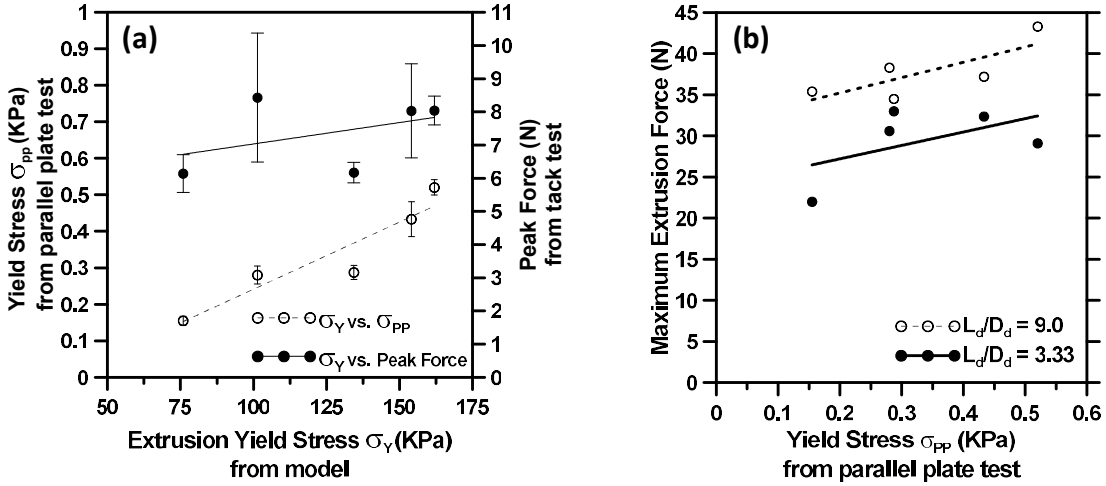

Figure 5-13: Correlation of: (a) extrusion yield stress with shear yield stress from parallel plate and peak force from tack test, and (b) shear yield stress from parallel plate with force of extrusion.

5.3.4. Compressive and Flexural Strengths of 3D-Printed Binders

The compressive and flexural strengths of the alkali-activated fly ash-based 3D printed cubes and beams were evaluated after the respective curing regimes. In the first curing regime, all the samples were cured in a moist chamber (23 ± 1°C, > 98% RH) until 28 days. In the second regime, all the samples except the mixture containing OPC ($F_{50}C_{30}L_{20}$) were exposed to heat curing (at 70°C) for two different durations (24 h and 48 h). Figure 5-14 shows the test directions. Three companion specimens were used for compressive and flexural strength testing.

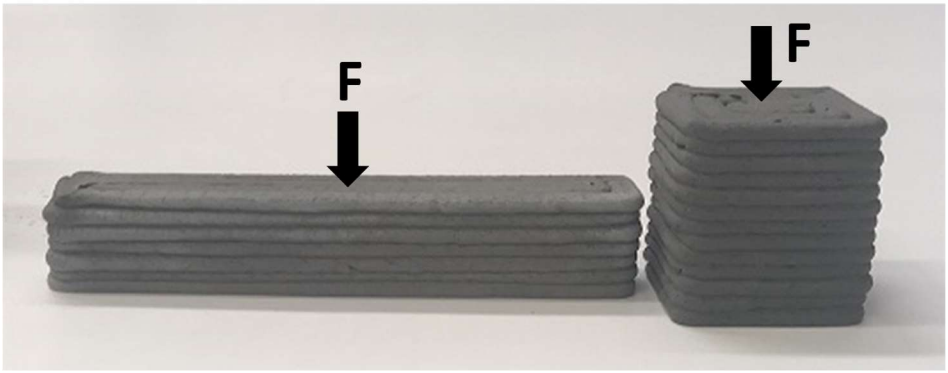

Figure 5-14: The test direction for mechanical strengths.

Figure 5-15 depicts the compressive and flexural strengths of the selected binders. When moist cured, the compressive strength increases with reducing amount of fly ash in the binder, as expected. The compressive strength of the paste containing OPC is the highest. Similar strengths have been attained for mixtures containing high volumes of fly ash, activated using alkali sulfates [179]. The 28-day compressive strength the $F_{50}S_{30}L_{20}$ mixture activated using NaOH was lower than that of $F_{50}S_{30}L_{19}A_1$ mixture activated using sodium silicate, owing to the presence of reactive silica from the sodium silicate leading to enhancement in the reaction product volume and constitution. The fly ash-limestone specimens ($F_{85}L_{15}$ and $F_{70}L_{30}$) cured at (23 ± 1ºC, > 98% RH) and tested at 28-day showed the lowest compressive strength among the test specimens. The compressive strengths of the $F_{85}L_{15}$ and $F_{70}L_{30}$ mixtures activated using NaOH improved when cured at 70ºC, with a longer curing duration providing better strengths. The compressive strength results of 3D printed binders shown here suggest that the trends are similar to the compressive strengths of binders cast in a conventional manner [128,179].

Figure 5-15(b) depicts the flexural strength of the 3D printed alkali activated fly ash-based binders. For the $F_{85}L_{15}$ and $F_{70}L_{30}$ mixtures, the heat treatment improved the flexural strength when compared to the moist curing regime. However, the heat treatment was

found to cause extensive microcracking in the $F_{50}S_{30}L_{20}$ and $F_{50}S_{30}L_{19}A_1$ mixtures due to the high shrinkage of slag-containing alkali activated binders [202,203], thereby leading to poor flexural strength (microcracking influences flexural strength more than the compressive strength). The slag-containing specimens moist-cured at ambient temperatures showed the highest flexural strengths. When shrinkage is countered through moist curing, and the reaction of slag is facilitated, better strengths are obtained. The flexural strength of the OPC-containing mixture was also found to be lower since the interfacial strength of this mixture (as evidenced from tack test results) likely is lower, resulting in interlayer failure at relatively lower flexural stresses. Also, $F_{85}L_{15}$ and $F_{50}C_{30}L_{20}$ showed a higher modulus (peak force to displacement ratio) from the tack test and relatively lower flexural strengths. This complements previous observations where higher modulus resulted in lower inter-layer bond strength [190]. More studies on this aspect is ongoing.

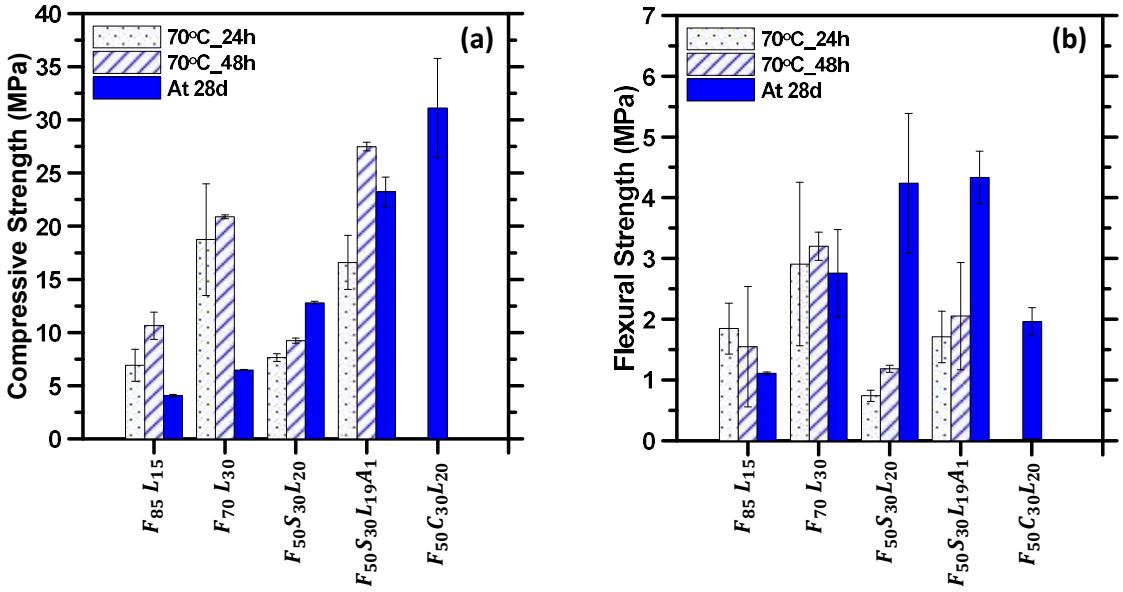

Figure 5-15: (a) Compressive strengths, and (b) flexural strengths of selected binders after subjecting to different curing regimes.

5.3.5. Effect of Extrusion and Overburden Pressure on Pore Structure

Layer-wise printing of cementitious composites can impact the pore structure (and thus the mechanical and durability properties) in multiple ways. The effect of extrusion (consolidation) is not uniform during the time the paste makes its way out of the extruder, resulting in differing particle concentrations and fluid contents (due to potential liquid phase migration). When printed in layers, the bottom layer is subjected to increased overburden pressure from the subsequently printed layers. The specific gravity, porosity, and critical pore size of the top and bottom layers of the printed cubes (layer dimensions of 6 mm x 3 mm; width x height) are compared in this section. Figure 5-16 depicts these pore structure parameters for the pastes studied. The variation in specific gravities between the top and bottom layers was less than 3% for all the pastes. It is observed that no significant difference exists in the porosity and critical pore size between the top and bottom layers for all the specimens. The bottom layer, which is printed first, is generally less influenced by the squeeze and consolidation effects because the material flows only a small distance before being extruded; however, the overburden pressure in this layer is higher. For the top layer, there is no overburden pressure, but the paste that constitutes this layer is subjected to higher confinement effects in the barrel and gets subjected to pressure for a longer time while being extruded. It is thus likely that the net effect on the pastes is rather similar for the extruder geometry and mixture compositions evaluated here, resulting in insignificant changes in porosity between the top and bottom layers.

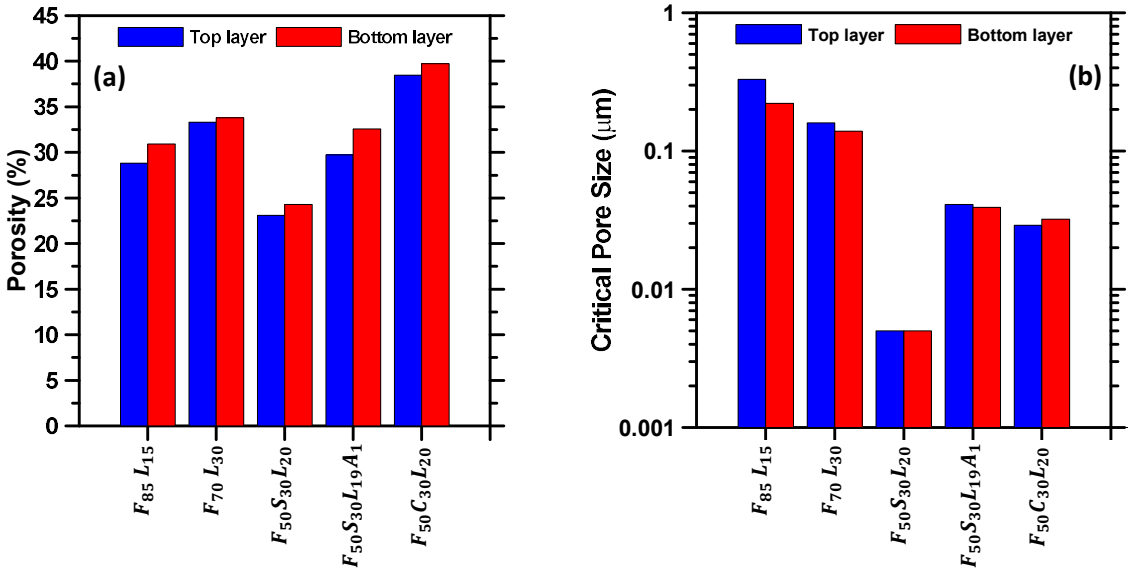

Figure 5-16: (a) Porosity and (b) critical pore sizes of top and bottom layers of the printed cubes.

5.4. CONCLUSIONS

The focus of this study was on the material design and evaluation of 3D-printable binders based on alkali activation of fly ash-based blends. Using fly ash as the major ingredient, and limestone, slag, or OPC as minor ingredients, mixtures were proportioned so as to be extrudable and buildable (printable). When alkaline activators were used in lieu of water, the shear yield stress of the fresh pastes decreased, and the cohesiveness increased, similar to the use of a superplasticizer in conventional OPC systems. The yield stress was also found to depend on the particle sizes (and in turn particle packing in the suspension) of the constituents. The mini slump values and shear yield stresses determined on extrudable mixtures were synergistically used to arrive at bounds for printability of the paste mixtures. This study also defined a printability window based on concurrent measurement of time-dependent yield stress and extrusion printing of a filament of the paste. For the mixtures evaluated, a shear yield stress of 700 Pa (in parallel plate rheometry) indicated an upper limit of printability. This window was found to scale relatively well with the setting time

of the pastes. The presence of alkaline activator also resulted in increased tack force and adhesive energy for these binders as compared to conventional cement-based binders.

The extrusion rheology experiments coupled with the Benbow-Bridgwater model facilitated the extraction of extrusion yield stress and die wall slip shear stress of alkali-activated fly ash-based binders, which are important process-related parameters in extrusion-based 3D printing. These parameters were shown to be related to shear yield stress and extensional (tack) properties of the virgin paste, thereby providing a means to understand the response of the extruded mixture from simple rheological experiments, and therefore could be used to link material design to the extrusion-based printing process. The compressive and flexural strength tests on the pastes showed that, in general, comparable mechanical properties as that of conventionally cast specimens can be obtained through layered printing. However, strength reduction likely due to microcracking (for mixtures containing slag, especially when heat cured) and weak inter-layer bonding (in mixtures containing portland cement) were observed, which requires careful material design and curing conditions to ensure long-term performance and durability. The study has shown that alkali activated fly ash-based binders can be successfully designed for beneficial properties.

CHAPTER 6[4]

SYNTHESIS AND CHARACTERIZATION OF 3D-PRINTABLE GEOPOLYMERIC FOAMS FOR THERMALLY EFFICIENT BUILDING ENVELOPE MATERIALS

6.1. INTRODUCTION

3D-printing or additive manufacturing (AM) is gaining prominence in the construction industry. One of the unique attributes of 3D-printing is the capability to implement complex architectural shapes [84–87]. Furthermore, 3D-printing technology has been shown to result in a reduction in construction cost and time due to the avoidance of formwork and reduced on-site labor [40,41]. Among the many 3D-printing techniques for cementitious materials, material extrusion followed by layered printing is the most commonly used technique [85,90,164,165,170,204,205]. The importance of rheological characteristics of cementitious binders in ensuring smooth flow through the extrusion system without material inhomogeneities and the requirements in terms of yield stress for buildability have been detailed in several recent publications [85,171,206–208].

The use of concrete 3D-printing for architectural and structural elements have been widely discussed in recent literature [17,84–87,209–211]. Building envelopes printed using concrete have appeared as demonstration structures in different parts of the world. This study synergizes the use of 3D-printing and material design of porous cementitious foam for specific building functions – in this case, thermal insulation. Thermal insulation materials reduce the heat gain/loss through building envelopes and it is one of the best

[4] This chapter is derived from the following publication under review: H. Alghamdi, N. Neithalath. Synthesis and characterization of 3D-printable geopolymeric foams for thermal efficient building envelope materials. (2019)

approaches to enhance building energy efficiency. Porous materials find extensive applications in building insulation. This study envisages 3D-printed cementitious foams in lieu of conventional building insulation materials such as extruded polystyrene, mineral wool etc. that can be placed in between the concrete layers of a typical insulated precast concrete wall panel (sandwich wall panel). The fire resistance and environmental sustainability of many of the commonly used insulation materials are questionable [50–52], which can be overcome by the proposed approach. The concrete wall panels can also be 3D-printed if desired, resulting in a co-printed envelope system consisting of the structural and insulating components. While cementitious foams are significantly more insulating than solid concrete, they still exhibit thermal conductivity values that are higher than commercial insulating materials mentioned above. This drawback can be overcome by designing specific architectures using the 3D-printed cementitious foams. A conceptual representation of such a design idea and laboratory prototypes are shown in Figure 1. The porous foams can be printed in such a way that the composite structure has an overall void volume fraction (excluding the voids in the foam) of 40-80% depending on the desired thermal conductivity of the envelope. Thus, the composite structure becomes a dual-porosity medium, with smaller pores in the foam and larger pores in between the printed paths. By proper design of the insulating layer architecture and numerical simulations of heat transfer, issues such as thermal bridges which affect the dynamic thermal performance of sandwich wall panels can also be eliminated. The desired layer architecture (examples of which are shown in Figure 6-1) can only be created using 3D printing, which is an important advantage over conventionally cast cementitious foams. The layer geometry can also be optimized for enhanced structural-thermal performance, which also cannot be

accomplished using conventional casting of foams. Thus, this study lays the foundation for material and geometric design of 3D printable cementitious foams. The emphasis of this paper, however, is the material design of 3D-printable, sustainable cementitious foams and its microstructural/thermal characterization.

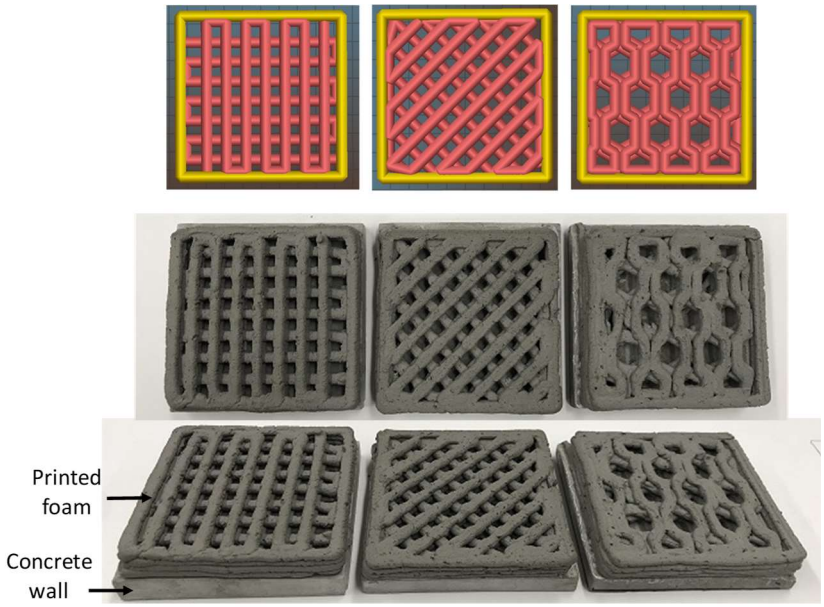

Figure 6-1: Different architectures using 3D-printed foams to develop energy efficient composite envelope systems. The 3D-printed insulation here has a void volume fraction of 0.50 (excluding the voids in the geopolymeric foam itself).

Past studies have reported the use of 3D-printing to fabricate porous materials from different starting materials for many applications such as water filtration, catalysis, biomedical scaffolds, and lightweight structural elements [23,32,34,45–49]. In this study, the foamed matrix is designed using alkali activated fly ash to ensure economical, sustainable, and lightweight matrices. While several chemical foaming agents including hydrogen peroxide, alumina powder, metallic silicon, and recently sodium carbonate [61,64,68] have been used as foaming agents, this study employs a physical foaming process using surfactants [61–63] that introduce homogeneous bubbles in the geopolymer matrix. The choice of a surfactant-based foaming process was based on the evaluation of

bubble stability under extrusion-based 3D-printing. While the surfactant also stabilizes the air bubbles [212–215], unjammed (wet) foams are sometimes formed because of the reduction in water-air surface tension [216]. Wet foams[5] where the foam volume fraction is lower than the jamming transition are flowable and hence not amenable to 3D-printing. The jamming transition for 3D disordered foams is ~0.64 [217,218]. To ensure adequate skeletal density and cohesiveness of the mixtures to enable 3D-printing, and at the same time maintaining a higher porosity, the particle packing in the suspension is modified through the use of fine powders such as limestone. Moreover, a modified mixing procedure is employed to facilitate the formation of stable dry foams.

6.2. EXPERIMENTAL PROGRAM

6.2.1. Materials and Printing Parameters

A Class F fly ash conforming to ASTM C 618 was the major source material used in this study. To improve the printability (which includes extrudability, shape retention, and buildability) of the foamed suspension, additional materials such as ordinary portland cement (OPC), silica fume, and fine limestone powder were used based on our previous published work [170,204]. The chemical composition of all the source materials are listed in Table 6-1. Figure 6-2 shows the particle size distributions (PSD) of the source materials. The median particle sizes are 17.9 μm for the fly ash, 1.5 μm for limestone, and 11.2 μm for OPC, as determined from laser particle size analysis. The activation agents utilized in this study were sodium silicate solution (waterglass), sodium hydroxide (NaOH), or sodium sulfate (Na_2SO_4). Waterglass, supplied by PQ Corporation, has a solids content of

[5] The terms “wet” and “dry” foams do not reflect the literal meaning of the terms; in fact, these terms are used to denote volume fraction of foams below and above the foam jamming transition, respectively.

36%, a silica modulus (molar ratio of SiO_2-to-Na_2O) (M_s) of 3.3, and specific gravity of 1.38 g/cm^3. NaOH was added to waterglass to lower the M_s and obtain the desired Na_2O-to-total powder (n) values. Sodium sulfate, which is a non-caustic activator, was used when a small amount of OPC was used in addition to fly ash as the binding material. More details of such mixture designs are available in [179]. Lightcrete 02™ surfactant liquid was used as a foaming agent and foam stabilizer.

A BCN3D Cartesian printer [170,204] was used in this study to print the foamed suspensions. All printing parameters including printing speed, layer width and height, and infill volume and pattern were adjusted using Slic3r software [92]. The printing parameters used in this study were: layer height of 3mm, layer width of 6 mm, and printing speed of 20 mm/s. The diameters of the barrel, die entry, and die exit were 35 mm, 10 mm, and 4 mm respectively.

Table 6-1: Chemical composition of the source materials.

Components of the binders	Chemical composition (% by mass)						
	SiO_2	Al_2O_3	Fe_2O_3	CaO	MgO	SO_3	LOI
Fly Ash (F)	58.40	23.80	4.19	7.32	1.11	3.04	2.13
Silica fume (S)	> 90.0	-	-	< 1.0	-	-	-
OPC (C)	19.60	4.09	3.39	63.21	3.37	3.17	2.54
Limestone (L), 1.5 μm	$CaCO_3$ > 99%						

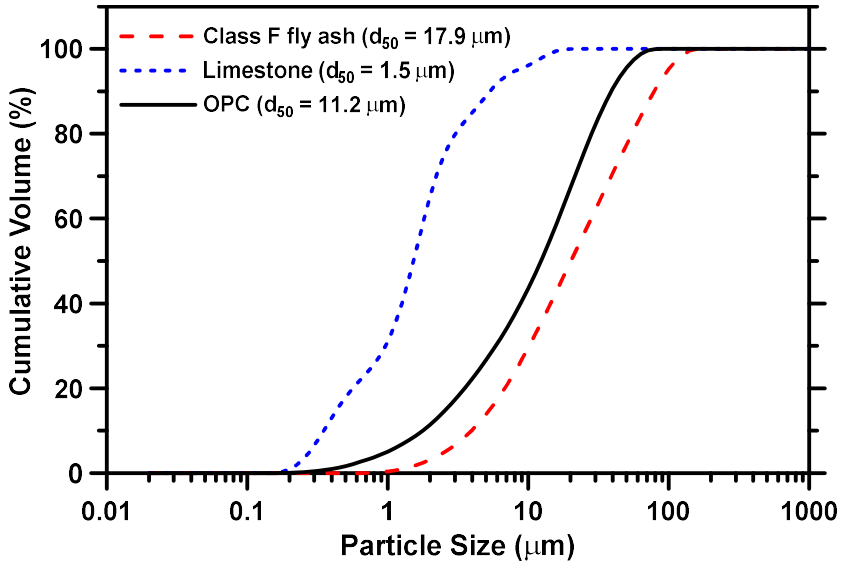

Figure 6-2: Particle size distributions (PSD) of the suspension constituents.

6.2.2. Preparation of the Printable Foamed Suspensions: Importance of the Mixing Procedure

The smooth extrusion of foamed suspensions through the nozzle and retention of the printed shape are the printability criteria adopted in this study towards material design. Since the mini-slump test can be used to indicate shape stability [170,204], it was utilized in the initial development of a family of alkali-activated fly ash-based printable foamed suspensions.

A binder combination that contained 70% fly ash and 30% limestone powder (by mass) was chosen from a series of printable alkali-activated fly ash-based binders reported earlier [204], as a starting point. The amounts of sodium silicate and NaOH were adjusted to provide an activator with an M_s of 1.0. The ratio of Na_2O-to-total powder (n) was maintained at 0.07. Three different surfactant (S) dosages were used: 1, 2, and 3% by mass of the binder. A mass-based liquid-to-binder (l/b) ratio of 0.60 (including the liquid surfactant and the water content in the activator) was chosen. This was needed to avoid the stickiness of suspension due to the highly viscous alkali activator that reduces foam

expansion and consequently the porosity [62]. This l/b also helped maintain appropriate workability and flowability of the foamed suspension, at the same time ensuring buildability (which is quantified using viscosity recovery as described later). The activator solution and requisite amount of water were added to the binder and mixed at 200 rpm for 30 sec and then at 1200 rpm for 4.5 min until a homogeneous mixture was obtained. The surfactant was then added and mixed until a uniform mixture resulted. The resultant mixture was observed to be very soft (wet foam), resulting in a non-printable suspension (Figure 6-3(a)). It is likely that large and isolated bubbles were created, and the mixture had a foam volume fraction lower than the jamming transition of 0.64 [217,218] which resulted in instability. To obtain a stable, dry foam with a foam volume fraction at or near the jamming transition, this study developed a modified mixing procedure where water was added in a stepwise manner. In this procedure, the activator solution with a quarter of the total water requirement was added to the powder mixture and mixed at 200 rpm for 30 sec and then at 1200 rpm for 4.5 min until a homogenous mixture was obtained. Then the total amount of surfactant was added and mixed for further 10 min. This mixture has a high surfactant concentration. Subsequently, the remaining water was gradually added in three equal steps until the total amount of water was fully added and mixed for further approximately 3 mins during each step to disperse the foam. The formation of dry foam (jammed foam) along with a solid skeleton having adequate particle packing to ensure stability, resulted in a foamed suspension which was cohesive enough and demonstrated shape stability as shown in Figure 6-3(b).

Figure 6-3: Shape stability as observed during: (a) the normal mixing procedure when all the water was added to the powder in a single step, and (b) the modified mixing procedure when the water was added to the powder in multiple steps.

Along with the binary suspension prepared from fly ash and limestone, silica fume and OPC were also used as minor ingredients to improve the particle packing and mechanical properties of the foamed matrices. The fly ash – silica fume – limestone system was activated using a combination of NaOH and sodium silicate to provide a Na_2O-to-powder ratio (n) of 0.07 and an M_s of 1.0. The fly ash – OPC – limestone system was activated using only Na_2SO_4 as reported in [179]. In the latter case, a cohesive and printable foamed suspension (dry foam) was obtained directly during mixing with a reduced amount of water (there was no need for adding more water to avoid the stickiness issue experienced in suspensions activated by highly alkaline activators). The fly ash – limestone (FL) and fly ash – limestone – silica fume (FLS) systems, were synthesized using the modified mixing procedure where the water was added in steps, while for the fly ash – limestone-cement (FLC) system, the activator and the requisite amount of water were added to the binder in a single step, followed by the surfactant and mixed for only 5 min. The final printable foamed suspensions are listed in Table 6-2. The third system is not strictly a geopolymer

since OPC is used, but is compared to the two geopolymeric systems described above. All the printed shapes were cured for 24h at 70°C to enhance the polymerization reaction and the formation of products. After the curing duration, the compressive strengths tested on 50 mm side cubes ranged from 1.0 MPa to 6.5 MPa depending on the mixture proportion and surfactant content. The highest strengths were recorded for the FLC mixture.

Table 6-2: Binder proportions for the final printable suspensions.

Suspension ID	Binders (% by mass)				Sodium sulfate (%)	NaOH + waterglass		Liquid/binder Ratio (by mass)	Surfactant (S) (% by mass of binder)
	FFA (F)	LS (L)	SF (S)	OPC (C)		n	M_s		
FL	70	30	-	-	-	0.07	1.0	0.60	1, 2, 3
FLS	60	20	20	-	-	0.07	1.0	0.65	1, 2, 3
FLC	50	20	-	30	3	-	-	0.25	1, 2, 3

6.2.3. Test Methods

6.2.3.1. Foam Expansion and Shape Retention

Foam expansion (F_E) was determined as the increase in the suspension volume after mixing according to:

$$F_E\ (\%) = \left(\frac{V_F - V_I}{V_I} \times 100\right) \quad (6\text{-}1)$$

where, V_F is the final volume of the suspension after addition of the surfactant and V_I is the initial volume of the suspension that does not contain the surfactant.

Shape retention factor of printed filament (SRF) was determined to evaluate the layer stability of foamed suspensions in accordance with the procedure described in [54]. This factor is quantified as:

$$SRF = \left(\frac{Designed\ layer\ width\ of\ filament}{Actual\ printed\ layer\ width\ of\ filament}\right) \quad (6\text{-}2)$$

6.2.3.2. Rheological Characterization

Mini-slump test was used to estimate the shape stability of the foamed suspensions. A mini slump cone with a bottom diameter of 38 mm, top diameter of 19 mm, and a height of 57 mm was used. A TA Instruments AR 2000EX dynamic shear rheometer was used to carry out parallel plate rheology tests. The rheometer was setup with Peltier elements for the bottom plate and conditioned to 25±0.1 °C. The upper and lower plates were serrated with a notch depth of 1 mm and 0.15 mm respectively to prevent slip on the shearing surface. The sample volume for a 2 mm plate gap was calculated and placed on the bottom plate to avoid an overfilled state while testing. The plate gap was chosen so as to ensure that it is at least 10 times larger than the largest bubble size. The following steps were employed in the rheology testing, as shown in Figure 6-4(a): (i) a stepped ramp-up pre-shear phase for approximately 80 s to homogenize the suspension, (ii) a stepped ramp-up phase for about 40 s, and (iii) a stepped ramp-down phase [70,71]. The data collected from the ramp-down phase was used in the analysis. Rheological parameters of the suspensions (apparent yield stress and plastic viscosity) were extracted from the relationship between shear stress and shear rate. The range of the shear rate used in this test was from 5-to-100 s^{-1}. The Y-intercept of this relationship was recorded as the Bingham yield stress and the slope as the plastic viscosity. The use of a Bingham model for foamed suspensions has been reported [219].

In addition, the parallel plate test was also carried out to measure viscosity recovery (suspension buildability). The buildability test was done in a sequence of steps that mimic extrusion-based 3D printing [53,54]. The steps employed include: (i) a stepped ramp-up pre-shear phase for approximately 80 s to homogenize the suspension, (ii) constant low

shear rate of 0.01 s^{-1} for 60 s to determine the initial viscosity of fresh suspensions before printing, (iii) constant high shear rate of 100 s^{-1} for 30s which mimics the extrusion process, and (iv) constant low shear rate of 0.01 s^{-1} for 60 s to determine the final viscosity of suspensions after extrusion printing. The experimental scheme is shown in Figure 6-4(b).

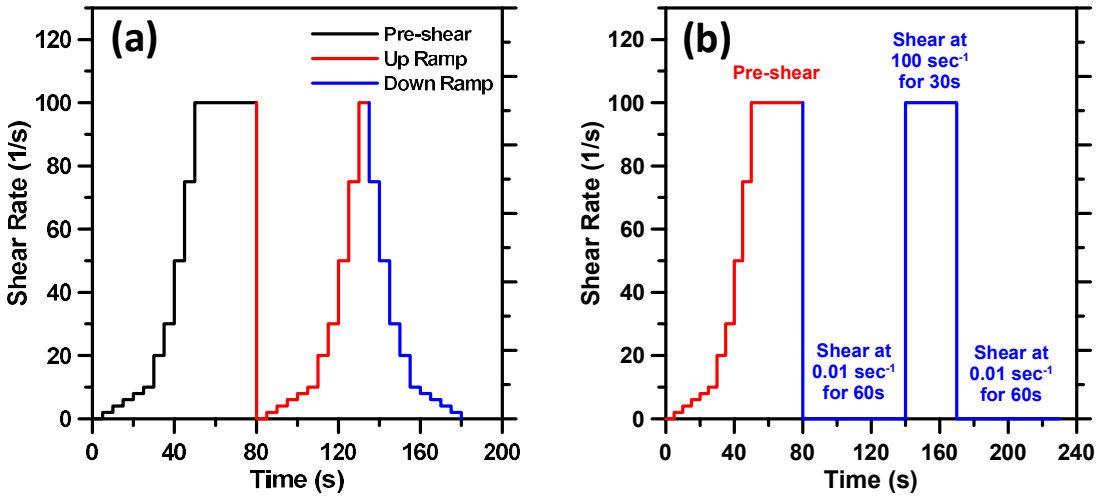

Figure 6-4: Parallel plate rheology test procedure to determine: (a) yield stress and plastic viscosity, and (b) plastic viscosity recovery of the suspensions for buildability.

6.2.3.3. Pore Structure and Microstructure of Foamed Matrices

The pore structure and the microstructure of the hardened foamed matrices were evaluated using Mercury Intrusion Porosimetry (MIP) and Scanning Electron Microscopy (SEM). For MIP experiments, small chunks of the foamed matrix were weighed and placed in the low-pressure chamber of the porosimeter (Quantachrome Instrument Pore Master). The sample was filled with mercury starting from ambient pressure to 345 kPa (60 psi) in this step. The sample was then placed in the high-pressure chamber and the applied pressure increased to 414 MPa (60,000 psi). The pore diameter (d) as a function of the intrusion pressure was obtained from the Washburn equation as:

$$d = \frac{-4\,\sigma\,cos\theta}{\Delta P} \qquad (6\text{-}3)$$

where ΔP is the difference in the pressure between successive steps (MPa), θ is the contact angle between mercury and the cylindrical pore (taken as 130^{o} in this study) [27,108,109], and (σ) is the surface tension between mercury and the pore walls (0.485 N/m). To understand the effect of extrusion printing on the porosity and pore sizes of the foamed suspensions, two sets of samples were used. First, samples were obtained from the printed filaments to represent the influence of extrusion. Second, samples not influenced by extrusion effects were obtained from specimens that were conventionally poured and cast in a 25 mm x 50 mm cylinder mold.

A Nanoimages SNE-4500 Plus Table top scanning electron microscope operating in the secondary mode was used to image the microstructure. All the samples prepared for SEM imaging were gold sputtered before imaging under an operating voltage of 30 kV.

6.2.3.4. Physical and Thermal Properties of Foamed Matrices

The specific gravities of the foamed samples were determined using a gas pycnometer (Ultrapyc 1200e, Quantachrome Instruments). The thermal conductivity of the foamed samples was determined using the guarded hot plate method in accordance with ASTM C 177. Plain OPC paste plate samples (100 mm x 100 mm x 15 mm) were prepared at a w/c of 0.40 to be used as a reference. One layer of foamed suspension, 3 mm in thickness was printed on the aforementioned OPC plate to form a composite, and the thermal conductivity of the foam was determined from the composite thermal conductivity using a series rule of mixtures. 1D uniform heat flow is ensured by using thermally isolated guards surrounding the central metered section where the applied power is measured. Heat sinks located on the top and bottom of the apparatus dissipate the heat to ensure uniform temperatures at the

outer surfaces of the specimen [72]. Thermal conductivity (k) was calculated using Fourier's equation as:

$$k = \frac{q\ L}{2\ A\ (T_{hot} - T_{cold})} \quad (6\text{-}4)$$

where q is the power input to the heater, L is the thickness of the plate specimen, A is the surface area of the specimen, T_{hot} is the temperature of the hot surface, and T_{cold} is the temperature of the cold surface.

6.3. RESULTS AND DISCUSSION

6.3.1. Foam Expansion and Rheological Characterization

Foam expansion and slump flow are important characteristics that define the early age properties of 3D-printable foamed suspensions. Figure 6-5(a) shows the foam expansion and Figure 6-5(b) shows the mini slump values of the foamed suspensions. Foam expansion increases with increasing surfactant content as expected. All three mixtures (FL, FLS, and FLC) expanded to ~100% (or doubled their volume) when 3% of surfactant powder (by mass) was used. Even with a significantly reduced water content, the FLC mixture shows comparable expansion to those of the other mixtures. The high viscosity of the activator solution necessitated a higher liquid content in FL and FLS mixtures for desirable expansion. The slump values shown in Figure 6-5(b) also demonstrate a similar trend as that of expansion. The higher the surfactant content, the higher the slump value, attributable to a lower suspension yield stress with increasing surfactant concentration [216,220], which is also shown in a forthcoming section of this study. These mixtures demonstrated excellent consistency and smooth flow during extrusion. Generally, a higher slump is beneficial in extrusion but not in shape stability, which is an important criterion for 3D

printed elements. However, the foamed suspensions with relatively higher slump values were also successful in retaining their shapes because of their low densities.

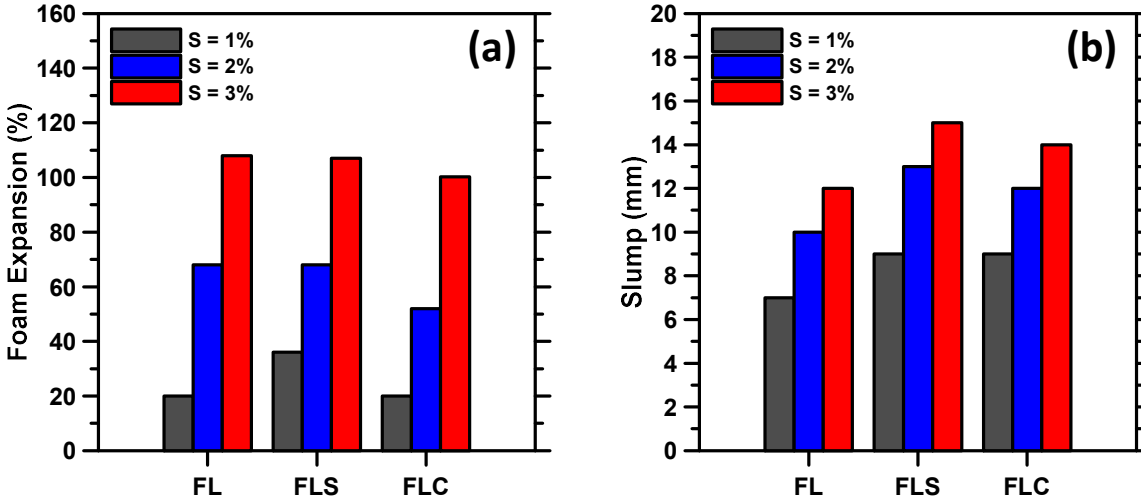

Figure 6-5: (a) Foam expansion and (b) slump values of the printable foamed suspensions.

Yield stress and plastic viscosity are important rheological parameters that have been used to evaluate the influence of starting materials and proportions on 3D printed binders [53,54,170,204]. Foams with void volume fractions greater than the jamming transition are known to be yield stress fluids, just as conventional cement pastes, and hence rheological techniques used for cement pastes can be safely used for dry foams. Thus, below the yield stress the foams behave as viscoelastic solids and above the yield stress as non-Newtonian fluids. Figure 6-6 shows the yield stress and plastic viscosity of printable foamed suspensions evaluated in this study using parallel plate rheometry, which is reported as the most appropriate tool to study bulk foam rheology [221]. The yield stress of FL, FLS, and FLC suspensions are similar at a given surfactant dosage, while plastic viscosity is found to be generally invariant with the suspension type and the surfactant dosage within the scope of materials and dosages used in this study. Foam viscosity is known to increase with decreasing bubble size and foam density. With an increase in surfactant dosage, bubble

size increases (shown later through pore size distributions) and overall density decreases, plausibly negating their effects on changes in viscosity.

The yield stress of the foamed suspensions with low surfactant dosage (S = 1%) vary between 120 Pa and 130 Pa, while it is around 60 Pa for higher surfactant dosages (S = 2, and 3%). For foam volume fractions up to around 50% (for e.g., the 1% surfactant mixture with a porosity of 55%[6] – see a later section for porosity values), the yield stress of the foamed suspension has been reported to be similar to that of the paste that forms the skeleton [222]. The rheological response of the foamed sample can be considered to be a result of competition between the skeleton yield stress that tends to deform the bubbles and the capillary stress acting on the bubble surface that resists this deformation. The net effect can be expressed in terms of a plastic capillary number [222,223], C_p, expressed as:

$$C_p = \frac{\tau_y}{(2T/R)} \tag{6-5}$$

Here, τ_y is the yield stress of the foamed suspension, T is the surface tension and R is the bubble radius. Assuming that the surface tension scales between 0.06 N/m and 0.03 N/m between 1% and 3% surfactant dosage, and the bubble size ranges between 25 μm and 100 μm (see a later section on pore structure), the C_p value for the 1% surfactant dosage case is around 0.02 for all the three mixtures. For C_p values $\sim\leq 0.10$ (i.e., surface tension is dominant), it has been shown that τ_y is invariant of foam volume fraction ϕ when $\phi \leq 0.50$ [222]. Thus, the yield stress of foamed samples is unaffected by the bubbles since the bubbles behave as rigid inclusions in the paste. However, for $\phi \geq 0.64$ (2% and 3%

[6] It is assumed for the sake of simplicity that the total pore volume and the pore size in fresh samples are equal to those measured in hardened samples. While mechanisms such as ripening and drainage are likely to influence the pore structure features between fresh and hardened samples, it is ignored in the discussions here.

surfactant dosages), C_p increases to >0.10 and the bubbles behave as softer, deformable inclusions in the paste. This reduces the yield stress as shown in Figure 6-6. The calculation of capillary number as a function of time thus enables an understanding of the rheology of foamed suspensions from those of their skeletal pastes. Even when the yield stress is reduced with increasing surfactant dosage, the printability of the foamed suspensions is not influenced because of their lower density which enables shape retention even at lower yield stresses. The significant drop in the yield stress between a surfactant dosage of 1% and 2% can also be attributed to steric repulsion between the particles in the suspension and the surfactant molecules [220].

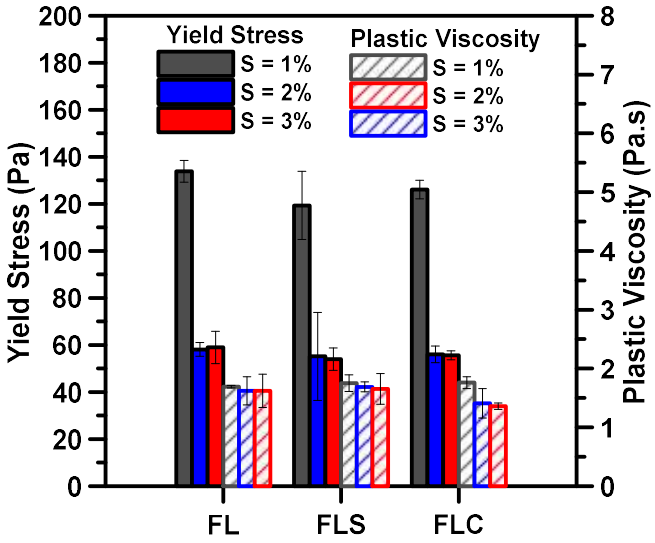

Figure 6-6: Yield stress and plastic viscosity of the printable foamed suspensions.

6.3.2. Buildability of Foamed Suspensions

The fresh foamed suspensions must have ability to resist the overburden pressure due to the superimposed printed layers and remain shape stable after printing. This requires the mixtures to be able to recover most of its initial viscosity after the extrusion effect is simulated. Figure 6-7 depicts the viscosity recovery response of the FL, FLS, and FLC mixtures. These figures indicate three stages of viscosity evolution: the initial viscosity of

the suspensions at rest or before extrusion (before printing; from 0 to 60 s), the viscosity of the suspensions during the simulated extrusion process (during printing; 60 s to 90 s), and the viscosity of the simulated extruded suspensions (after printing; 90s to 150 s) as defined in [53,54]. All the foamed suspensions (FL, FLS, and FLC) show a high viscosity at rest and the values dropped significantly when the shear rate was increased to simulate extrusion, as expected. The smooth material flow during extrusion was ensured by the low viscosity. On further lowering of the shear rate, significant recovery of the initial viscosity is noticed, indicating better buildability of the suspensions. Previous work [170,204] have shown that the addition of finer particles like limestone improve the cohesiveness, packing and colloidal interaction thereby providing high initial viscosity and yield stress [177]. For all the three mixtures, the viscosity recovery was in the range of 80% to 95%. The effect of high shear rate that simulates extrusion would have resulted in changes in the fresh state microstructure, that impedes total viscosity recovery. Among the three foamed mixtures, the FLS mixture showed slightly lower retention than the FL mixture. Even at a much lower w/b, the OPC-containing mixture showed similar viscosity recovery, because of the difference in the activating solution characteristics as explained earlier. However, it can be seen that the viscosity recovery for all the mixtures considered here are similar to or higher than those of conventional and geopolymeric 3D-printed pastes reported in literature [53,54], attesting to the buildability of these foamed suspensions.

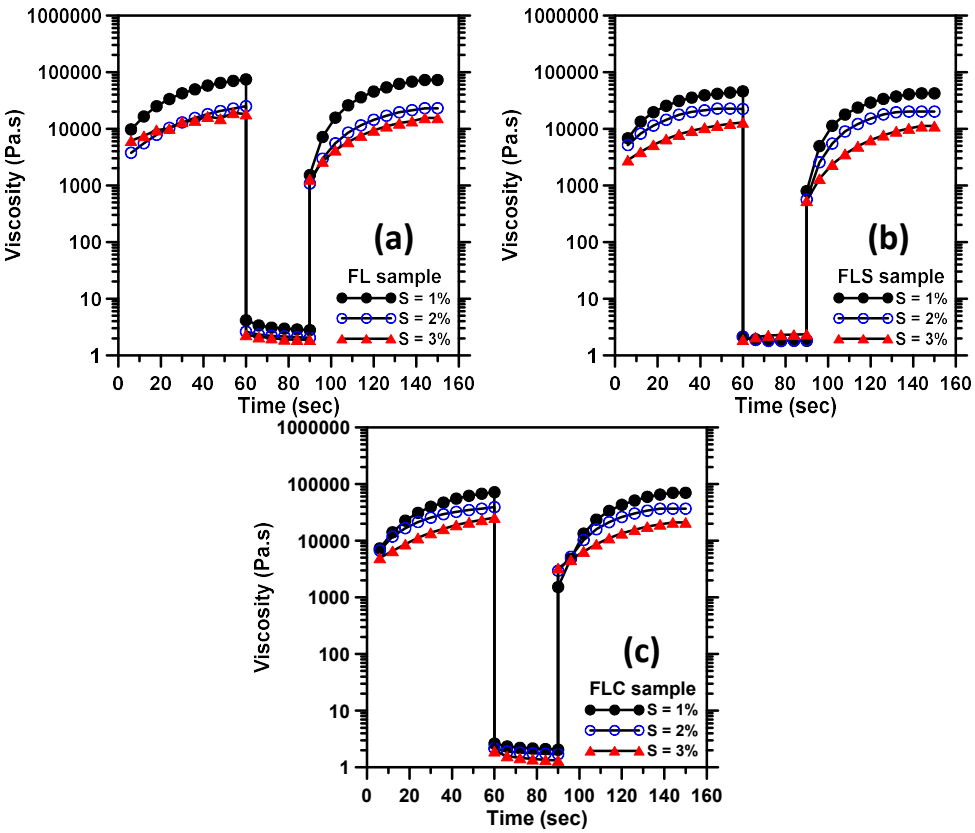

Figure 6-7: Viscosity recovery (buildability) of printable suspensions: (a) FL, (b) FLS, and (c) FLC mixtures.

A single filament (layer) of each suspension at different surfactant dosages were printed and the shape retention factor of printed filament (SRF) was determined using Equation 6-2. Figure 6-8 shows the single printed filaments showing actual layer width after printing (FLS suspension used as an example). The SRF values are reported in Table 6-3, which roughly scale with the viscosity recovery values described earlier – higher the viscosity retention, higher the SRF. The SRF values are found to decrease with increasing surfactant dosage due to the increased wettability when higher amounts of surfactant are used, which was also evident from the mini-slump values (see Figure 6-5). Also, the mixtures with 1% surfactant dosage was stiffer than mixtures with 2% and 3% surfactant dosages which explains its better SRF value, as reported in [224].

In addition to a single layer, a single perimeter shape with multiple layers was also printed to represent the buildability of the printable foams as shown in Figure 6-9. The aspect ratio (overall height to layer width) was found to be 12.5 (25 layers for a total height of ~75 mm) for the mixtures with 1% surfactant dosage, and 8.5 (17 layers for a total height of ~51 mm) for the mixtures with 2%, and 3% surfactant dosages. For the suspensions with 1% surfactant dosage, particularly with FL and FLC mixtures, the aspect ratio could have been higher but for the printed shape reaching the z-axis limit of the printer used in this study. The layer stability was generally preserved under overburden pressures due to the combined effect of cohesive and uniform suspensions and the fact that the suspensions have very low densities - similar to or lower than that of water (see Table 6-4), which enabled the layers to withstand the stress from the superimposed layers. The 3% surfactant mixture shown in Figure 6-9 has the lowest bulk density (Table 6-4), which has slightly compromised the geometry of the printed shape.

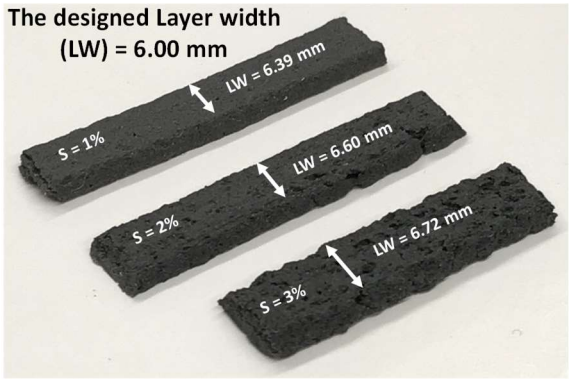

Figure 6-8: Single printed filaments (FLS suspension used as an example) showing actual layers width after printing.

Table 6-3: Shape retention factor (SRF) of the foamed suspensions.

Mixture ID	Shape retention factor of printed filament (SRF)		
	S = 1%	S = 2%	S = 3%
FL	0.96	0.94	0.92
FLS	0.94	0.91	0.89
FLC	0.95	0.92	0.90

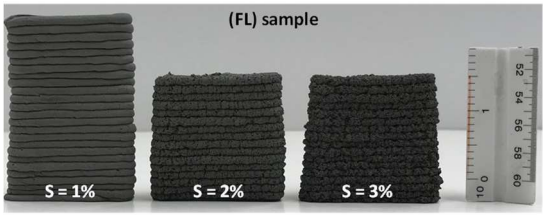

Figure 6-9: Number of stacked printed layers to evaluate the stability and buildability of foamed suspensions.

6.3.3. Bulk Densities, Pore Structure, and Microstructure of Foamed Matrices

This section investigates the bulk densities, pore structure, and microstructural features of the 3D-printable foamed matrices developed in this study. Two types of samples were prepared and studied in this section: (i) samples subjected to extrusion during printing, and (ii) samples cast directly in the molds. The influence of the processing method on the physical and microstructural of the foamed matrices are evaluated.

Table 6-4 shows the specific gravity and bulk densities of extruded and normally cast foamed matrices, measured based on three replicate samples. It can be noticed from the table that the specific gravity of the FLC mixture is the highest while that of FLS, the lowest. The higher specific gravity of the FLC mixture can be attributed to the presence of OPC in this mixture that has the highest specific gravity among the constituents used. The foamed samples showed bulk densities ranging from 0.63 to 1.15 g/cm^3 based on the surfactant dosage. The bulk densities are observed to reduce with increasing surfactant

dosage, as expected. Here also, the FLC samples show the highest bulk densities. There is virtually no difference in the bulk densities between the extruded and cast samples, implying that the applied extrusion pressure, rate and extruder geometry does not significantly influence the pore structure.

Table 6-4: Specific gravity and bulk densities of foamed matrices (standard deviation in parentheses based on three replicates).

Samples ID	Specific gravity (g/cm^3)	Bulk density (g/cm^3)					
		Extruded and printed*			Cast in molds**		
		S =1%	S =2%	S =3%	S =1%	S =2%	S =3%
FL	2.43 (0.04)	0.92 (0.007)	0.72 (0.002)	0.63 (0.038)	0.93 (0.010)	0.71 (0.004)	0.64 (0.020)
FLS	2.37 (0.074)	1.03 (0.099)	0.81 (0.035)	0.67 (0.082)	1.04 (0.100)	0.84 (0.050)	0.68 (0.094)
FLC	2.58 (0.078)	1.15 (0.055)	1.08 (0.099)	0.94 (0.086)	1.16 (0.070)	1.10 (0.097)	0.95 (0.074)

*Samples were exposed to extrusion effect during printing.
**Samples normally poured and cast into molds (not exposed to extrusion effect).

The pore structure (total pore volume and critical pore size) of the foamed samples are important in ensuring adequate functional performance, including thermal insulation. Figure 10 depicts the cumulative volume of mercury intruded and the differential mercury intrusion curves for all the printed (extruded) and cast foamed samples. It can be noticed that the cumulative volume intruded and the critical pore size (corresponding to the peak in the differential volume curve, which is indicative of the percolating pore size in the material [111]) increases when the surfactant dosage is increased. It is also observed that the cumulative volume intruded shows only minor differences between the printed (extruded) and cast samples, but the critical pore sizes showed an increase (shifted to right) in printed samples as compared to the cast samples. It is important to note that mercury intrusion does not accurately capture pores that are generally greater than ~100 μm in size, and thus even if such pores collapse under extrusion pressure, it would not be captured

using MIP. However, in the range of pore sizes measured by MIP, it is possible that smaller pores coalesce under extrusion pressure, and form larger pores, which is captured through the rightward shift of the differential volume curves corresponding to the extruded samples as shown in Figures 10(d-f). In general, a bimodal pore size distribution with smaller pores in the 0.08-to-0.5 μm range and larger pores in the 12-to-80 μm range is observed for the cast samples, while this changes to 0.3-to-0.8 μm range and 20-to-100 μm range for the extruded samples. The pore size distribution and the similarity in the cumulative intrusion curves show that the extrusion process does not significantly influence the stability of the pore network.

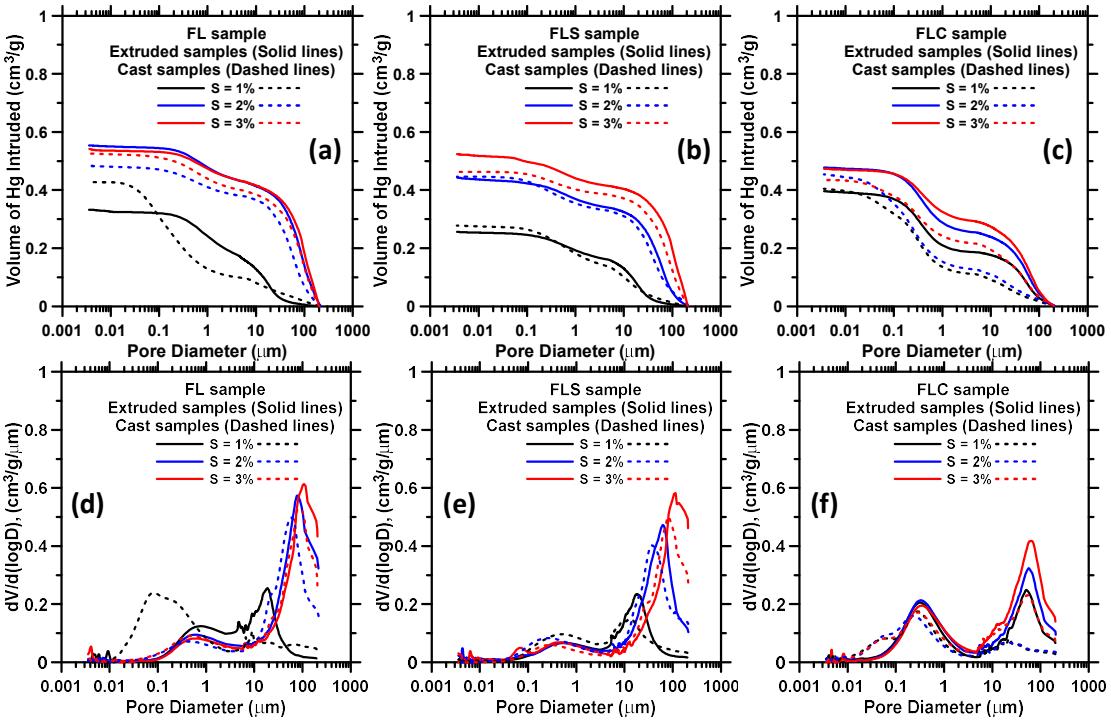

Figure 6-10: Cumulative pore volume and differential pore volume of all foamed samples (a and d) FL, (b and e) FLS, and (c and f) FLC samples. (Extruded samples represented by solid lines and cast samples represented by dashed lines).

Scanning electron micrographs of the extruded FL mixture is shown in Figure 6-11, for all the three surfactant dosages. The micrographs clearly show the distribution of macropores.

The increase in pore volumes and the pore morphology as a function of surfactant dosage are clearly depicted in this figure. The jamming transition (~0.64) in 3D foams corresponds to random close packed density for hard spheres [225,226]. However, for the soft spheres, foam volume fraction above the jamming transition indicates that the voids have to deform or interpenetrate (see the associated rheological discussion earlier). Careful observation of Figure 6-11 for mixtures with higher surfactant content reveals this aspect. Since larger pores that cannot be detected using MIP will be present in these mixtures, the total porosities of the samples were determined using Equation 6-6, while the MIP porosities were determined using the cumulative volume intruded and the bulk densities of the samples. Figure 6-12(a) depicts the total porosity and the porosity extracted from MIP for the extruded samples, showing that MIP accounts for only about 50-60% of the total pore volume in these samples for the FL and FLS mixtures. For the FLC mixtures, the presence of OPC and the much lower w/b results in generally lower pore sizes, and thus the MIP porosity and that determined using Equation 6-6 are quite similar. Figure 6-12(b) shows the relationship between the bulk densities and porosities. The FL and FLS mixtures show similar trends while the FLC mixture shows a slightly different trend, because of reasons described above.

$$Total\ porosity\ (\%) = \left(1 - \frac{Bulk\ density}{Specific\ gravity}\right) X100 \qquad (6\text{-}6)$$

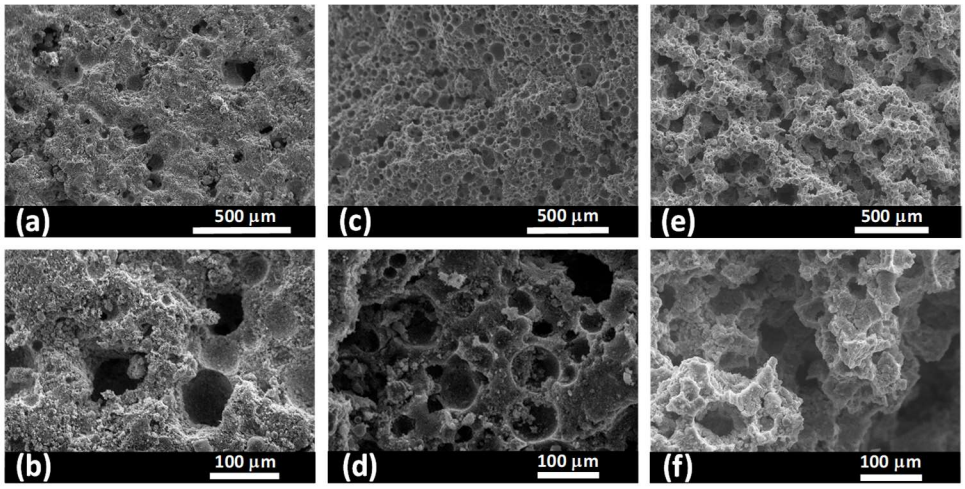

Figure 6-11: SEM micrographs at two different magnifications of microstructure of the extruded FL sample at different surfactant dosages (a and b) S = 1%, (c and d) S = 2%, and (e and f) S = 3%.

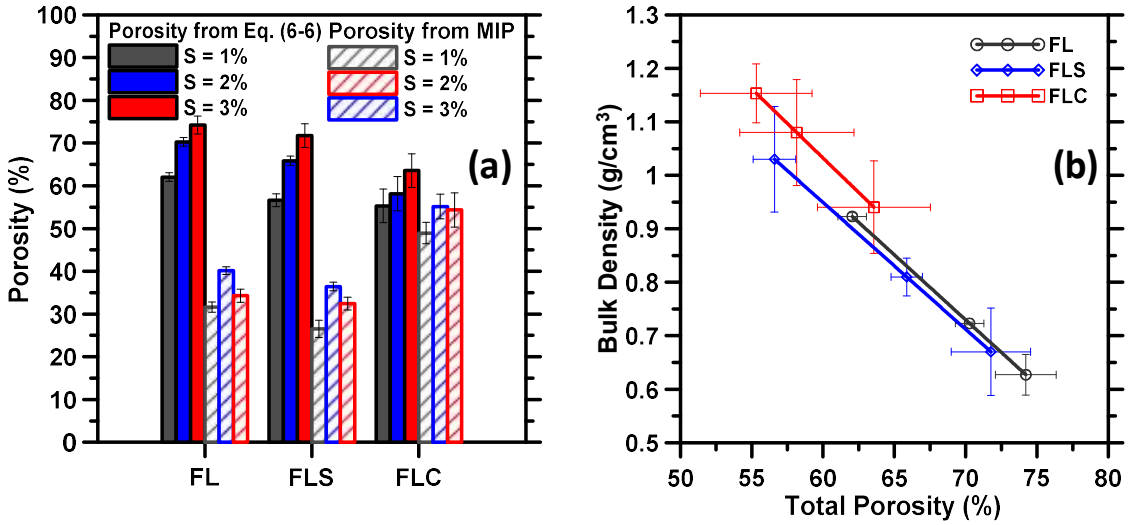

Figure 6-12: (a) Total theoretical porosity calculated from Equation 6-6 and the porosity obtained from MIP, and (b) relationship between the total porosity and bulk densities of printed foamed samples.

6.3.4. Thermal Properties of Foamed Matrices and Design of Energy-Efficient Envelope Materials

The thermal conductivities of the printed foamed matrices were determined from the OPC plate-foam composite specimens using a series rule of mixtures approach. Figure 6-13(a) depicts the thermal conductivity of the printed foamed samples along with the thermal

conductivity of an OPC paste (w/c of 0.40) while Figure 6-13(b) shows the relationship between the thermal conductivities and bulk densities of the printed foamed matrices. Samples with higher content of surfactant yielded lower thermal conductivities because of their higher porosities. The relationship between porosity and thermal conductivity is shown in Figure 6-13(b). The thermal conductivity of the printed foamed matrices are similar to other insulating materials including aerated/foamed concrete, expanded clay, cork boards etc. as well as porous fly ash based geopolymers reported in [68,78,140].

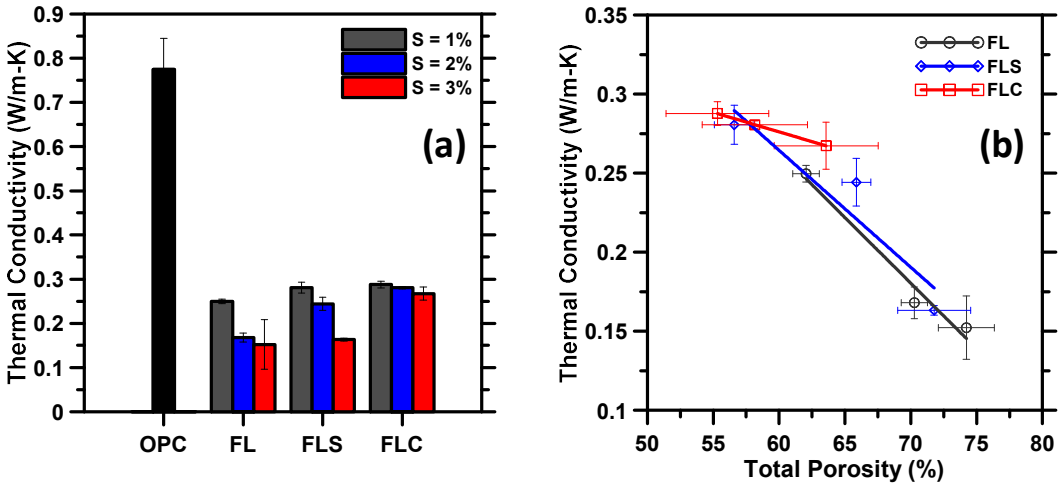

Figure 6-13: (a) Thermal conductivity of all printed foamed matrices and the OPC plain paste, and (b) relationship between porosity and thermal conductivity of all printed foamed samples.

As noticed from Figure 6-13, the printed geopolymer foams exhibit low thermal conductivities, but these values are higher than those of commonly used building insulation materials such as mineral wool, expanded or extruded polystyrene (EPS/XPS), or polyisocyanurate which are generally lower than 0.05 W/m-K. However, it is possible to reduce the thermal conductivity of the entire insulation layer in insulated sandwich concrete wall panels by careful architecture of the geopolymeric foam, which is enabled by 3D printing (see Figure 6-1). 3D-printed precast concrete insulated wall panels can thus

be produced with two layers of concrete separated by printed geopolymeric foam of suitable architecture, examples of which were shown in Figure 6-1. The properties and geometry of the concrete wythes (external layers of concrete that provides structural resistance) and the foam layer can be designed based on the structural and functional requirements of the building.

To demonstrate the effectiveness of 3D-printed geopolymer foam layers for insulated wall panels, the FL mixture with 3% surfactant dosage is considered, which has a thermal conductivity of 0.15 W/m-K. As shown in Figure 6-1, this mixture can be printed on a concrete backing as a prototype for an insulated sandwich wall panel. The printed material in Figure 6-1 occupies only 50% of the volume with the remaining being air of low thermal conductivity (0.0257 W/m-K). Using several analytical models for effective thermal conductivity including the simple series and parallel models, Maxwell model, and effective media theory (EMT) [72,227,228], the effective thermal conductivities determined as a function of volume fraction of air (this does not include the voids in the foams themselves since they are accounted for in the measured thermal conductivity of the foam) are shown in Figure 6-14. The horizontal line corresponds to the desired thermal conductivity of the foam layer, to match that of commercially available insulation materials. It can be seen that, with an air volume fraction of ~60-70% (i.e., printed solid volume fraction of 30-40%), EMT predicts that the geopolymeric foam layer will have a thermal conductivity similar to that of commercial insulation materials. This analysis does not consider the system to be a dual-porosity media composed of smaller pores within the foam and larger spaces between the foam layers. The interface effects that hinder heat conduction are not considered, rendering the determined values to be more conservative. Moreover, the

printing architecture can also be tailored to change the interface areas or lengths of heat transport path to induce more losses, and thus enhance insulation.

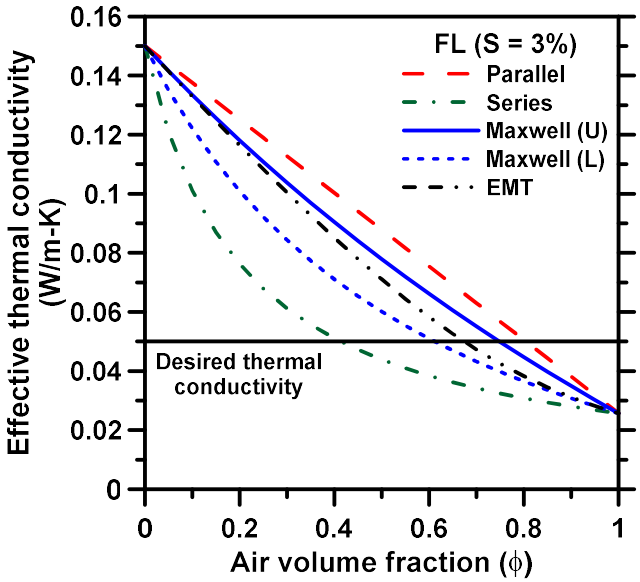

Figure 6-14: Model-based determinations of effective thermal conductivity of geopolymeric foam layers printed with air gaps.

6.4. SUMMARY AND CONCLUSIONS

This study has presented an extrusion-based 3D-printing technique to create geopolymeric foams for thermal insulation applications. A novel synthesis method using different surfactant contents where foam jamming transition is achieved through multiple mixing steps has been detailed. Improvements in microstructural packing that reinforces the solid skeleton also contributed to ensuring the stability of the foamed matrices when subjected to extrusion. The final ingredients of the foamed suspensions included fly ash, limestone and silica fume or OPC. The activators used were sodium silicate and NaOH or sodium sulfate. All the foamed matrices were designed to have bulk densities lower than that of water, and unsurprisingly, increase in surfactant dosage resulted in significantly reduced bulk densities of the printed foams.

Mini-slump test was used to obtain preliminary indications of shape stability, and single printed filaments were used to determine the shape retention factor. The shear yield stress of the chosen suspensions ranged from 60 to 130 Pa; the higher the surfactant dosage, the lower the yield stress. Below the foam jamming transition, the bubbles acted as hard spheres that enhance the yield stress while below the jamming transition, they were able to deform, which was shown through the capillary number. The lower yield stress of the foamed suspensions did not influence their buildability because of their lower density. The buildability was explicitly determined using viscosity response of the suspensions after subjecting them to simulated extrusion through changes in the shear rate. The low viscosity under extrusion (high shear rates) enabled smooth and continuous printing without any defects. The viscosity recovery of the chosen foamed matrices were high, demonstrating excellent buildability, which was verified through printing multiple layers and determining the aspect ratio (ratio of overall height to later width) of the printed structure. It was noted that the layer stability was preserved under the weight of the superimposed layers due to the combined effect of cohesive mixtures with high skeletal densities due to microstructural packing and low overall densities due to the stable bubbles. The differences in bulk densities between the extruded samples and normally cast samples were minimal, alluding to the fact that the extrusion process did not significantly change the overall pore volume in the foamed mixtures. However, mercury intrusion porosimetry identified slight increase in the critical pore sizes of extruded samples as compared to normally cast samples, indicating some coalescence of smaller pores under extrusion.

The thermal conductivities of the foamed matrices ranged between 0.15 and 0.25 W/m-K, for porosities ranging from 55-75%. These values are significantly lower than those of

conventional cement pastes (~0.8 W/m-K), but higher than those of commonly used insulation materials including polystyrene and mineral wool (~0.05 W/m-K). To enable substitution of conventional insulation materials with 3D-printed geopolymeric foam in sandwich wall panels, this study has proposed the use of 3D-printed foam layer architecture in such a way that dual-porosity systems - with smaller pores in the foam and larger pores in between the printed paths - can be achieved. Using effective medium theory, it has been shown that if the printed structure has an overall volume fraction of 60-70% (excluding the voids in the foam matrix itself), the effective thermal conductivity of the system approaches that of a commercial insulation material. Thus, 3D-printing of geopolymeric foams can be used in conjunction with precast wall manufacturing (which could also be 3D printed) to develop economical and sustainable structural systems that compare with existing systems with respect to thermal insulation capacity.

CHAPTER 7

NOVEL MIXING PROCEDURE TO EXTEND THE SETTING TIME OF ALKALI-ACTIVATED SLAG FOR 3D-PRINTING OF CONCRETE

7.1. INTRODUCTION

Alkali-activation of ground granulated blast furnace slag (AAS) dates back to 1950s and the interest in AAS has grown distinctly during 1970s [229]. Recently, many studies have reported the use of slag as a main binder for alkali activated systems which are comparable with OPC based concrete due to the higher environmental impacts associated with OPC production [69,230–232]. Alkali activated slag concrete compared with equivalent OPC based concrete has added advantages in terms of high initial mechanical properties, low thermal conductivity, and excellent resistance to fire, acid, sea water, sulfates, and alkali aggregate reaction [233–239]. Most common activation agents used in AAS are sodium hydroxide (NaOH) in combination with sodium silicate solution (waterglass). These high alkaline activators help to initiate the activation of slag particles and break down the silica and alumina covalent bonds to form durable gel network during the geopolymerization process (C-A-S-H) [12]. More details about geopolymerization mechanism can be found in the literature [14–16].

Recently, digital fabrication or three-dimensional printing (3D-printing) technology has been attracting many researchers' attention and has also been employed in the construction industry [18,35–41]. 3D-printing technology does not require formwork to build structural elements leading to reduction in labor and energy (economically efficient technique) [40,41]. Apart from the economical advantage, constructing complicated architectural shapes become easier with 3D-printing technique. Many studies have focused on

developing 3D-printable mixes based on OPC concrete [86,170,175,240]. In addition, geopolymer mixes as a sustainable alternative for extrusion-based 3D-printing technology was reported in [17,18,53,54,176,204]. Although, alkali-activated slag has many advantages in terms of high strength and durability, previous studies have not tried using slag as a sole binder to develop 3D-printable geopolymer mixture owing to its short setting time, leading to unfavorable effects in 3D-printing applications. Some studies have used a combination of slag and fly ash along with silica fume to prepare 3D-printable binders with longer setting time aided by the presence of fly ash [53–55]. Other studies reported that the initial setting time of AAS can be extended to about 3 hours by increasing the mixing time up to 30 min, but this mixture was not printable [56,57].

The current study mainly focuses on solving this challenge and developing alkali-activated slag mixture as an alternative sustainable binder that satisfies 3D-printing requirements. Consequently, a novel processing technique was established to significantly extend the setting time of slags activated using highly alkaline activator (NaOH + sodium silicate). In addition to the setting time, viscosity and cohesion which are essential fresh parameters of the mixture are also considered to develop a 3D printable mixture with slag as a sole binder. This study did not use any admixtures to overcome the uncontrolled setting time of slag. Also, fine ingredients or thixotropic modifiers were not added to improve the rheological characteristics of the mixture. A simple mixing method which depends on deflocculation and dispersion of early formed C-S-H is adopted to delay the initial setting time and obtain a cohesive mixture at the same time. Fresh and hardened properties of the printable mixture are investigated and evaluated in this study.

7.2. EXPERIMENTAL PROGRAM

7.2.1. Materials, Printer and Printing Parameters

Ground granulated blast furnace slag (GGBFS) Type 100 conforming to ASTM C 989 was used as the source material in this study. Table 7-1 shows the chemical composition of slag. The median particle size of slag is 8.9 μm as determined using laser particle size analysis. Figure 7-1 shows the particle size distribution (PSD) of slag. For mortar preparation, commercially available fine sand with a median size of 0.2 mm was used.

Sodium silicate solution (waterglass) and sodium hydroxide (NaOH) are used as the alkaline activation agents. Waterglass, supplied by PQ Corporation, has a solids content of 36%, a silica modulus (molar ratio of SiO_2-to-Na_2O) (M_s) of 3.3, and specific gravity of 1.38 g/cm^3. NaOH was added to waterglass to lower the M_s and obtain the desired Na_2O-to-total powder (n) values.

Alkali activated slag mixtures were printed by a desktop cartesian printer which was customized with a 100 cm^3 barrel with tapered nozzle. The barrel diameter was 35 mm. The entry and outer diameter of tapered nozzle (die) were 10 and 4 mm respectively. All printing parameters including printing speed and layer width and height were adjusted by Slic3r software [92]. Printing speed of 20 mm/s, layer width of 6 mm and layer height of 3 mm as printing parameters were used in this study.

Table 7-1: Chemical composition and physical properties of slag.

SiO_2	Al_2O_3	Fe_2O_3	CaO	MgO	SO_3	Na_2O	K_2O	LOI	Density
36.0	10.5	0.67	39.8	7.93	2.10	0.27	0.80	3.01	2.90

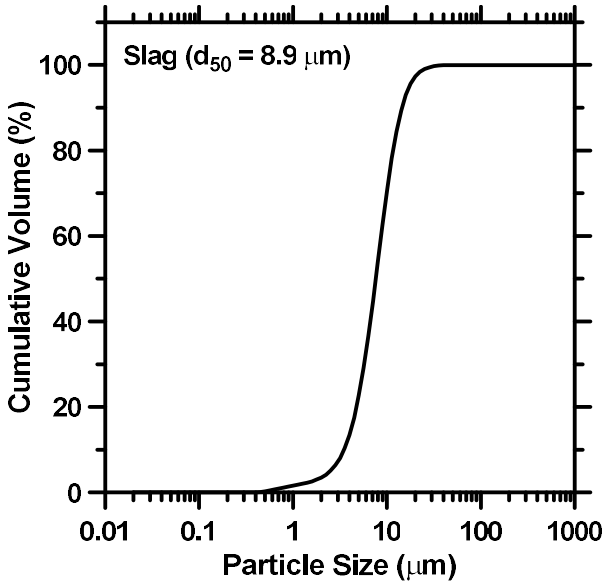

Figure 7-1: Particle size distributions (PSD) of slag.

7.2.2. Preparation of 3D-printable Mixture

Extrudability and shape stability are the major printability parameters for any 3D-printable mixture. The printable mixture should have enough flowability to ensure smooth extrusion out of nozzle and print continuous filaments. Besides flowability, the mixture should possess adequate yield stress and plastic viscosity to enable shape retention after printing. Hence, these essential properties have been quantified in detail later. In the early stages of the study, visual qualification of printability was followed by printing one single perimeter hollow shape (50 x 50 x 30 mm) as shown in Figure 7-2.

According to a previous study, and based on the compressive strength, the optimum ratio of Na_2O-to-total powder (n) was found to 0.05 to limit carbonation and leaching due to excess alkalis [69]. Also, NaOH was added to waterglass to lower the activator M_s to 1.5 which was shown to demonstrate better strength development [69]. Hence, these activator ratios were used in this study. The mass-based liquid-to-slag powder ratio (l/p) of 0.50 was

used in this study after many trials to ensure suitable workability, extrudability, and enough initial setting time.

A previous study reported that increasing the mixing time up to 30 min can extend the initial setting time of AAS to about 3 h [56]. Thus, a paste mixture with an l/p ratio of 0.40 was initially prepared which set and hardened while mixing (approximately after 7 min of mixing time). It can be probably attributed to the large size of early C-S-H flocs that need high shear forces to disperse and break down. However, the mixing procedure used in this study was not able to disintegrate the formed C-S-H gel (flocs). Consequently, the l/p ratio was increased to 0.50 (including the water from waterglass) and the mixture was mixed continuously for 30 min as reported in [56]. The formation of C-S-H gel (flocs) was observed during mixing and deflocculation was attained compared to the mixture with an l/p of 0.40. Subsequently, a hollow shape (50 x 50 x 30 mm) was printed to check the printability of the mixture. The mixture was extrudable and cohesive due to flocculation effects but was not cohesive enough to retain its shape and also not buildable as shown in Figure 7-2. In addition to the shape instability, the water draining from the paste was obvious after extrusion. In this procedure, it is deduced that the lengthy total mixing time was able to disperse and disintegrate most of the C-S-H leading to a more fluidic mixture, but failed to meet the printability requirements.

Figure 7-2: Hollow shape geometry (50 x 50 x 30 mm) printed after mixing the paste continuously for 30 min, showing shape instability.

Modified mixing procedure was established in this study to obtain printable mixtures (cohesive) with initial setting delayed enough to avoid the premature stiffening while mixture can be extruded and printed. Alkali activator solution with an l/p of 0.40 was added to the slag powder first and mixed at a low speed of 200 rpm for 30s and then at a high-speed of 1200 rpm for 150s until a homogeneous mixture was obtained. The mixture was rested for 1-2 min to allow the Ca^{2+} ions from surfaces of small slags particles (< 2µm) react with the silicate ions $[SiO4]^{4-}$ from waterglass solution resulting in formation of a thin layer of early C-S-H around the slag particles (flocs) [241]. Flocculation is the process when the particles in the mixture are alternately attracted by van der Waals and electrostatic forces and stick with one another to produce agglomerates [242]. Hence, the remnant mixing water was added to the mixture to attain the designed l/p of 0.50 and remixed for 2 min at a high speed of 1200 rpm to enable break-up and disintegration of flocs that are formed because of the thin layer of C-S-H around the slag particles. The disintegration of C-S-H and adding the remaining water delayed the setting time (as quantified later using vicat needle penetration test) and creates a cohesive and thixotropic (printable) mixture (see Figure 7-3(a)). Also, the remixing was able to break down and disperse the initial gel

product before remixing, leading to formation of new products on slag surfaces and creating additional bonds between slag particles [243,244]. In other words, remixing helps to make the mixture more cohesive than the mixture mixed continuously for 30 min. Eventually, it was observed that the mixture hardens quickly (~7 min) when mixed continuously and increasing mixing time and remixing did not help in terms of setting time. Therefore, adding water after a resting time, up to a l/p of 0.50 was found to be ideal in this study to enable disintegration of the formed C-S-H and delaying the activation. This also enables adequate flowability and extrudability of the mixture and helps shape retention after extrusion. The excess water covers the slag particle surfaces and thus leads to easy remixing. A hollow shape (50 x 50 x 30 mm) was printed to check the printability and it was observed that the paste mixture was extrudable and cohesive, and able to retain its shape after printing as shown in Figure 7-3(b). In addition, a printable mortar mixture with 30 % volume fraction of fine sand (0.2 mm median particle size) was prepared and checked for printability (see Figure 7-3(c)). Additional water (~3% by mass of fine sand) was used for preparation of the mortar so as to compensate the water absorbed by fine sand. For n value of 0.05 and M_s of 1.5, the activator proportions are summarized in Table 7-2.

Table 7-2: Amounts of alkali silicate activators solution for 1000 g of slag.

Type of mixture	Fine sand (g)	Sodium silicate solution (g)	NaOH (g)	Water (g)
Paste	---	262.5	35.4	386.2
Mortar	999	262.5	35.4	419.8

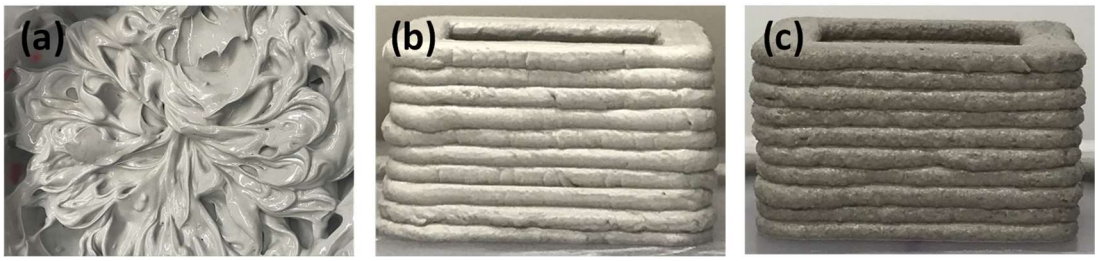

Figure 7-3: (a) Cohesive and thixotropic mixture prepared by dispersing the formed flocs by remixing for 2 min, (b) 50 x 50 x 30 mm printed paste, and (c) mortar respectively.

7.2.3. Test Methods

7.2.3.1. Setting Time of Alkali-activated Slag Pastes

The setting times of the printable paste mixtures were determined in accordance with ASTM C 191-18a [181]. The penetration reading was recorded every 15 minutes. Three samples were subjected for the vicat needle penetration test to understand the effect of remixing (deflocculation) on the setting time. The control sample (S0.5_5_R0) was prepared by mixing the slag powder with alkali activator solution (l/p of 0.5) for 5 min (continuously without remixing). The other two samples were remixed samples (mixed based on the modified mixing procedure) with a remixing time of 1 min (S0.5_3_R1) and 2 min (S0.5_3_R2). Two different remixing times were chosen to compare the effect of remixing time on the setting response as well.

7.2.3.2. Thermal Analysis

A TAM Air micro calorimeter 2700 Series was used to carry out isothermal calorimetry experiments in accordance with ASTM C 1702 for a duration of 72 h on pastes. Thermo-gravimetric analysis (TGA) was performed by using a Perkin Elmer simultaneous thermal analyzer (STA 6000). The procedure of TGA involves a temperature sweep between 50 ^{o}C

and 800 ºC at a rate of 15 ºC/min in an inert nitrogen purged environment. The mass loss as a function of the temperature was recorded.

Three samples were prepared for this test to understand the effect of remixing (deflocculation) on the reaction and hydration of paste. These samples were extracted at three different stages of the mixing. First sample was extracted after mixing the slag powder and alkaline activator (l/p = 0.4) for 3 mins followed by 1-2 mins for rest which allow the flocs to be formed. The extracted sample (S0.4_3_R0) was immediately placed in the instrument. Following the rest time, the sample was remixed for 2 min after adding the remaining water. The second sample was extracted at 1 min (S0.5_3_R1) of remixing time and the third sample was extracted at the end of 2 min (S0.5_3_R2) of remixing.

7.2.3.3. Rheological Characterization

To estimate the shape stability of paste and mortar, mini-slump cone test with a bottom diameter of 38 mm, top diameter of 19 mm, and a height of 57 mm was used. TA Instruments AR 2000EX dynamic shear rheometer was used to carry out vane shear and parallel plate rheology tests to determine the rheological characteristics of the printable pastes and mortars. Approximately 40 ml of the mixture was used. The temperature was maintained at 25±0.1°C for all experiments. Figure 7-4(a) depicts the steps employed in the rheological procedure. This procedure consists of (i) a stepped ramp-up pre-shear lasting approximately 80 s to homogenize the mixture, (ii) a stepped ramp-up lasting about 40 s, and (iii) a stepped ramp-down [70,71]. TA Instruments' TRIOS software package was used to extract the shear stress and shear rate data. The data used in analysis is collected only from the down-ramp phase. The range of the shear rate used in this test was from 5-to-100 s^{-1}.

In addition, the vane shear set up was also carried out to evaluate the buildability of printable paste and mortar (viscosity recovery). A sequence of steps that mimic extrusion-based 3D-printing was done in this test as reported in [53,54]. The steps consist of a stepped ramp-up pre-shear phase lasting approximately 80 s to homogenize the mixture, followed immediately by constant low shear rate of 0.01 s^{-1} lasting 60 s to determine the initial viscosity of fresh mixtures before printing. Then, it is followed by a constant high shear rate of 100 s^{-1} lasting 30 s to determine the viscosity of the mixture under extrusion process. Finally, a constant low shear rate of 0.01 s^{-1} lasting 60 s is applied to determine the final viscosity of mixture after extrusion printing. The experimental scheme is shown in Figure 7-4(b).

The parallel plate geometry was used to determine the extensional rheological response of the paste and mortar (tack test) which indicates the adhesive and cohesive nature of the mixtures These properties are very important to ensure that the successive printed layer adheres well on the surface of the previous printed layer [180]. The upper and lower plates in this geometry were serrated with a notch depth of 1 mm and 0.15 mm respectively to prevent slip on the shearing surface. The sample was placed on the bottom plate and a 2 mm gap was set between the upper and lower plates (10 times of fine sand size). A pre-shear phase similar to the one shown in Figure 7-4(a) was used to homogenize the mixture. Then, the upper plate is moved up with a constant velocity of 10 μm/s until the sample completely separates from the plates. The normal force experienced by the top plate was recorded as a function of plate separation.

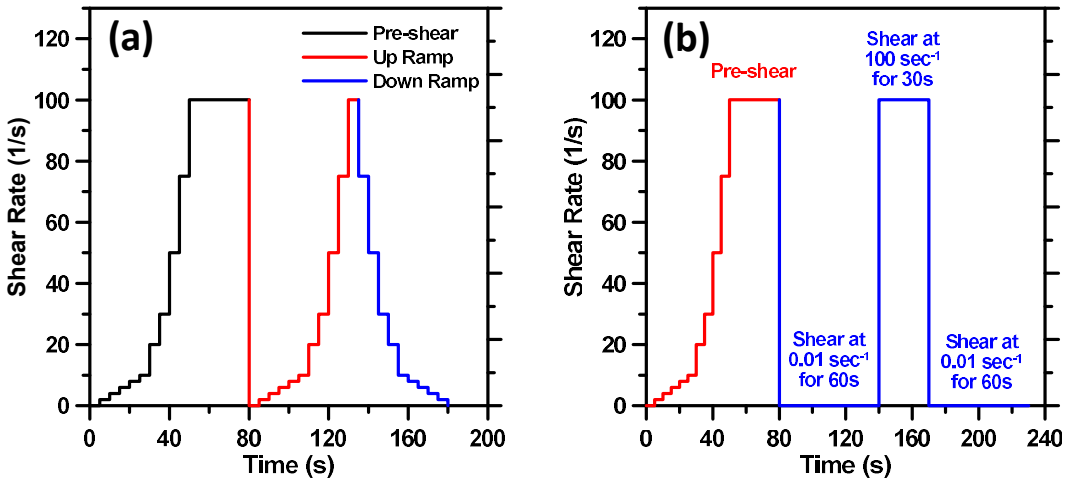

Figure 7-4: Vane shear rheology test procedure to determine: (a) yield stress and plastic viscosity, and (b) plastic viscosity recovery of the mixtures for buildability.

7.2.3.4. Shape Retention Factor of Printable Mixtures

Shape retention factor of single printed filaments of paste and mortar mixtures was calculated using Equation 7-1 in accordance with the procedure described in [54]. This factor helps to evaluate the printable mixtures stability.

$$SRF = \left(\frac{Designed\ layer\ width\ of\ filament}{Actual\ printed\ layer\ width\ of\ filament}\right) \quad (7\text{-}1)$$

7.2.3.5. Mechanical Properties of Alkali-activated Slag Samples

The compressive strengths of the printed mortar cubes 30 mm side length were determined in accordance with ASTM C 109. In addition, the flexural strength of the printed mortar beams (21 x 21 x 120 mm) was determine using a three-point-bending test. A displacement rate of 0.5 mm/min was used for the tests [73].

7.3. RESULTS AND DISCUSSIONS

7.3.1. Comparison of Setting Time

Initial setting time of the printable mixtures are very important to avoid the rapid stiffening of alkali-activated slag (uncontrolled setting time) while the mixture is being extruded and

printed. The novel mixing procedure was established to increase the initial setting time of alkali-activated slag to suit 3D-printing as described in Section 7.2.2. Figure 7-5 shows the needle penetration as a function of time for the control paste and two pastes with two different remixing time duration. The control sample shows very short initial setting time around 30 min which makes it not suitable for 3D-printing. This short initial setting time explains the major issue associated with alkali-activated slag when conventionally mixed. However, the other two samples which formed C-S-H (flocs) were disintegrated and dispersed due to mechanical remixing, showed long enough initial setting time (~8 h). The lengthened initial setting time of the mixtures prepared in this study make them suitable for 3D-printing in terms of sufficient open time and ease of handling these printable mixtures.

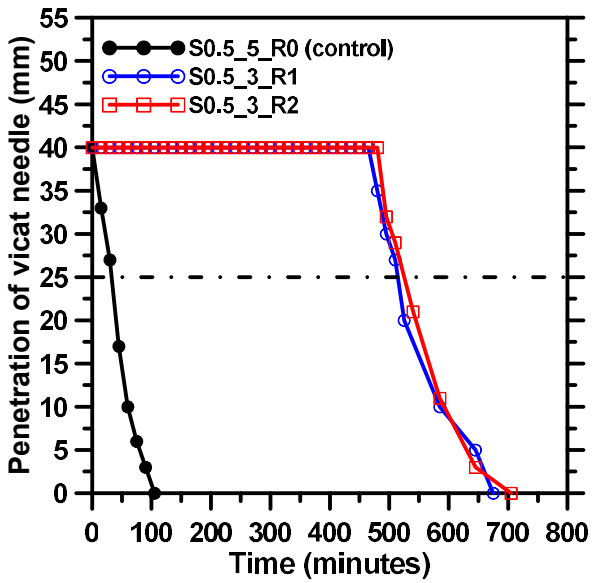

Figure 7-5: Initial setting times of the control sample and two pastes remixed for two different remixing duration.

7.3.2. Thermal Analysis of Fresh Printable Paste

Samples collected at different stages of the mixing procedure (as stated in section 7.2.3.2) have been subjected to the thermal analysis. As seen in Figure 7-6(a), two major thermal

peaks appear as a result of slag reaction with alkali activators. The first peak represents the initial stage of dissolution and reaction of calcium ions Ca^{2+} dissolved from small slag particles (< 2μm) in alkaline solution with silicate ions $[SiO4]^{4-}$ from waterglass solution producing a thin layer of early C-S-H around the slag particles [241]. The first peak followed by induction period which represents the hydration inhibition due to the coated slag particles by C-S-H layer (barrier) which inhibit or slower the diffusion leading to slow formation of new products. The second peak corresponds to the acceleration stage of the hydration occurred because of incorporation of aluminate ions in reaction products and forming secondary calcium aluminate silicate hydrate (C-(A)-S-H) [245]. For sample S0.4_3_R0, the initial dissolution peak occurred in the first few minutes (around 3 min) and had the highest peak magnitude. This is attributable to fast dissolution of calcium ions in the high pH activator and subsequent reaction with silica ions producing primary C-S-H (floc) which explains the rapid setting time in this sample. In this short time (3 min), the flocs started forming and that ensured the importance of resting time of the mixture (~2 min) before remixing as established in this study. Moreover, the second peak occurred after 6 h with a short dormant period, similar to AAS as documented in literature [69,241]. This peak indicates the reaction and precipitation to form more C-(A)-S-H. For the samples S0.5_3_R1 and S0.5_3_R2, the initial peak magnitude of former was higher than the latter, and both were lower than the peak magnitude of S0.4_3_R0. This lower magnitude values are attributed to the deflocculation of C-S-H due to the mechanical remixing. In addition, the increased remixing time decreases the magnitude of the first peak (see Figure 7-6(a)). The initial peak of both samples extracted after remixing followed by longer induction period (dormant period) explains the delayed setting time in these samples (see Figure 7-

5). This long induction period obviously explains the workability retention of these samples that favors the requisite printability criteria (as quantified and discussed in section 7.3.3). In the samples extracted after remixing, the heat flow started increasing again after long induction period. The incorporation of aluminates in later hydration products, and the larger slag particles control this peak (the acceleration peak) [245]. The remixed samples showed invariant peak magnitude. The total heat flow of all three different samples were 176, 168, and 163 (J/g) for S0.4_3_R0, S0.5_3R1, and S0.5_3_R2 respectively (see Figure 7-6(b)).

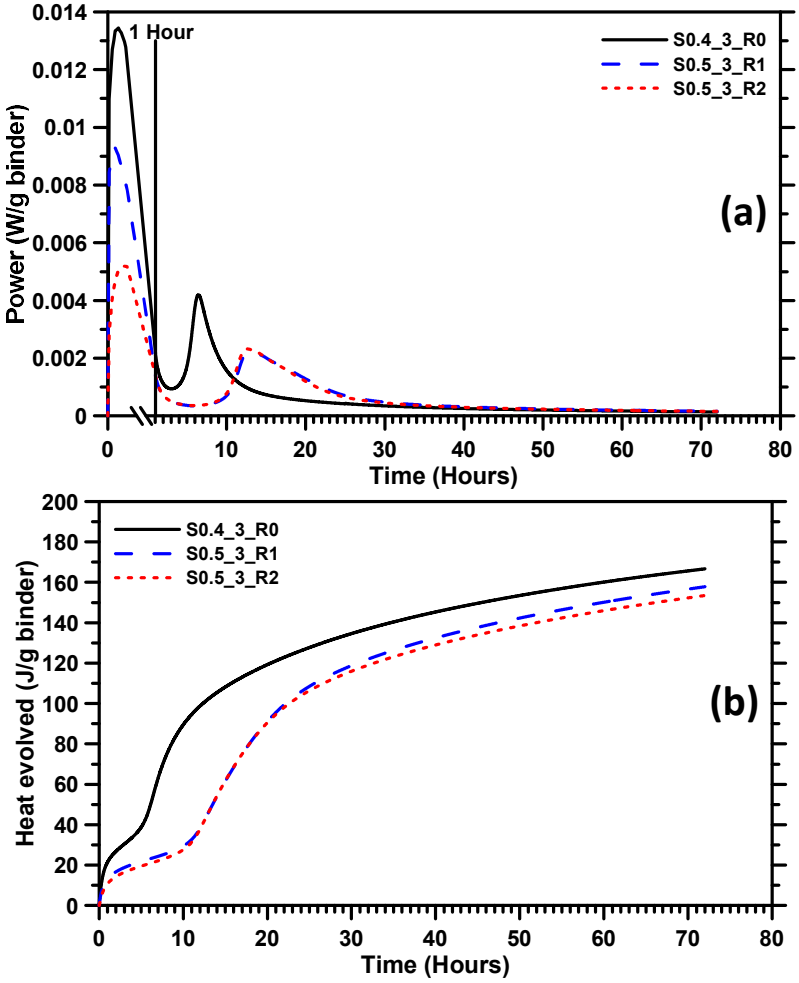

Figure 7-6: Comparison between three fresh past samples taken at different stages of mixing in (a) heat release, and (b) cumulative heat evolution of alkali-activated slag pastes.

Figure 7-7(a) depicts the thermogravimetric (TG) and differential thermogravimetric (DTG) curves, while Figure 7-7(b) shows the evaporable and non-evaporable water content of the three fresh paste samples taken at different stages of mixing. A difference in the behavior is noticeable between the samples extracted after remixing (S0.5_3_R1 and S0.5_3_R2) and the sample extracted before remixing (S0.4_3_R0). All three samples showed the major peak in the 105-200^{o}C range which represents the primary C-S-H gel. The evaporable water content which occurs between 50-105^{o}C were 4.8, 6.8, and 8.3% for S0.4_3_R0, S0.5_3_R1, and S0.5_3_R2 respectively. The increase in the evaporable water in the remixed samples could be attributed to the water added during remixing. The non-evaporable water contents which indicate the water bound to the primary C-S-H were 19.8, 23.2, and 21.4% for S0.4_3_R0, S0.5_3_R1, and S0.5_3_R2 respectively. It can be seen that the remixed samples showed slight increase in non-evaporable water content compared to the sample taken before remixing . This increase might be because of water addition during remixing which improved the dissolution of slag particles [233]. In addition to the better dissolution of slag particles, new products start to form by dissolving some smaller slag particles into alkali activator solution after the high shear mixing and subsequent C-S-H rim removal [243]. The remixed samples showed almost similar TG and DTG curves. These similarities in mass loss curve behavior was shown before in the calorimetry curve between the remixed samples (see Figure 7-6) and also in initial setting time (see Figure 7-5) which obviously explains that the remixing time (either 1 min or 2 min) does not show any significant change in early hydration and initial setting time of the mixture.

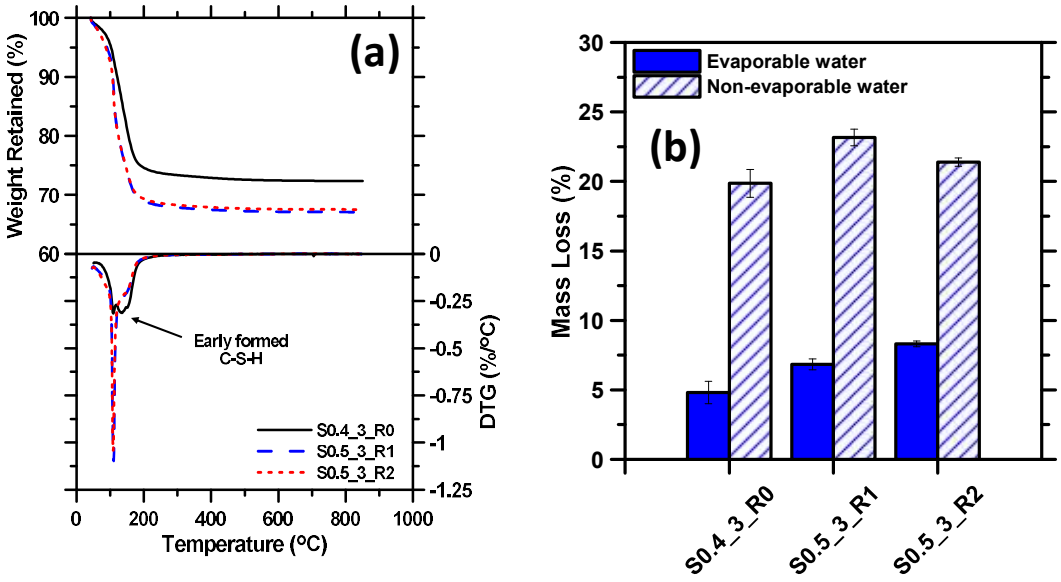

Figure 7-7: Comparison between the three fresh paste samples taken at different stages of mixing (a) TGA and DTG curves, and (b) the evaporable and non-evaporable content of the three fresh paste samples.

7.3.3. Rheological Characterization of Fresh Printable Mixtures

7.3.3.1. Mini-Slump, and Yield Stress from Vane Shear Rheology

Rheological characteristics of the mixtures are essential to understand the mixture consistency and cohesion, which are important in developing 3D-printable mixtures. Pastes and mortars (see Table 7-2) were subjected to rheological studies. Mini-slump test, rotational rheology (yield stress and plastic viscosity), open time of printability, and extensional rheology (tack test) are discussed in this section.

There is a strong relationship between mini-slump value and the yield stress as reported in [186,187]. The mini-slump is more indicative to shape retention of the printable mixtures. The yield stress is the resistance to initiate the flow and the plastic viscosity is the resistance to flow with increasing shear rate. For 3D-printing applications, it is required to have a cohesive mixture showing minimal slump (high yield stress) to ensure a stable print with little or no deformation while maintaining extrudability. Figure 7-8 (a) depicts the mini-

slump values, while Figure 7-8(b) shows the yield stress and plastic viscosity of the printable paste and mortar. The recorded mini-slump values were 9 mm and 5 mm for printable paste and mortar samples respectively. The mortars showed lower slump value as expected, attributable to the presence of fine aggregates. Both printable mixtures (paste and mortar) showed slump values in the same range of other family of printable mixtures on our previous published work [204]. Moreover, these slump values demonstrated consistent extrusion while printing and was shape stable after printing as described earlier (section 7.2.2). The yield stress and plastic viscosity were 69 Pa and 0.8 Pa.s for the printable paste whereas 90 Pa and 1.5 Pa.s for mortar respectively. The mortar also showed higher yield stress and plastic viscosity by approximately ~30% and ~79% respectively. The increase in yield stress and plastic viscosity is mostly attributed to the presence of fine sand particles which makes the mixture resist the applied stress with less deformation [246]. Flocculation is the attraction between particles due to van der Waals and electrostatic forces producing agglomerates and forming flocs [242]. Therefore, the flocculation effect plays a major role in rheological parameters of these printable paste mixtures. The yield stress measures the attraction forces (colloidal forces) between slag particles resulting from the formation of C-S-H around slag particles (flocs), while the number and size of the flocs which are broken under applied shear force reflects the plastic viscosity [177,246]. In other words, the dissolution of slag particles in the alkali activator, along with the size of particles that improve the mixture packing and inter-particle forces, result in better rheological parameters [244]. The values of yield stresses and plastic viscosities ensure easy and smooth extrusion and shape stability after printing as reported earlier (see Figure 7-3).

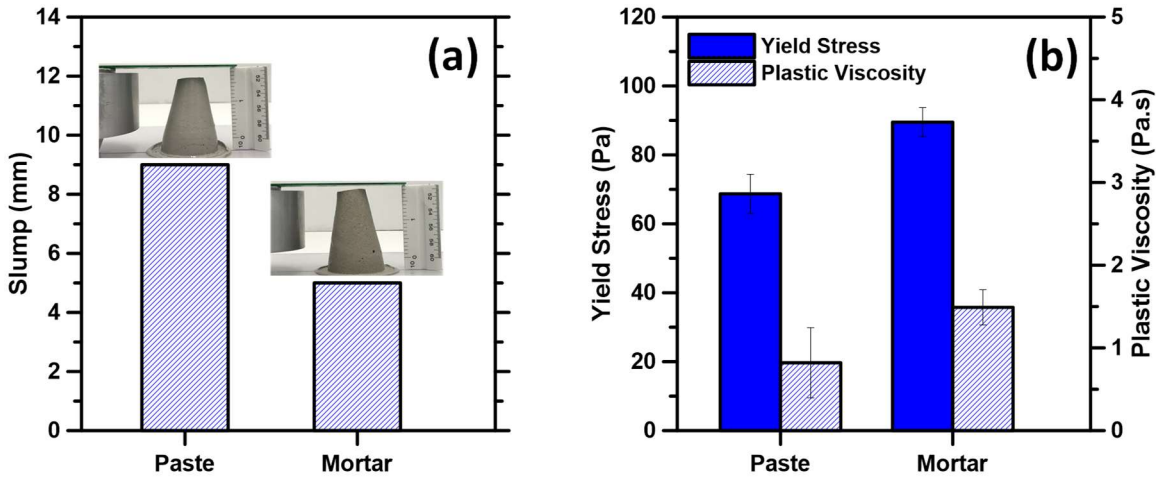

Figure 7-8: (a) Slump values and (b) yield stress and plastic viscosity of the printable paste and mortar.

7.3.3.2. Open Time of Printability

Open time of printability (extrudability zone) is the duration at the end of which the mixture loses its workability (and hence its extrudability) leading to difficulties in mixture extrusion [54,85]. This property is significant in 3D-printing since the mixture is not poured at once as in a conventional technique, but it should have enough time to deposit the material without setting (or stiffening of the mixture).

The evolution of yield stress with respect to time is a useful indicator to determine open time of printability. For both printable paste and mortar, yield stress was determined using vane shear geometry. The first reading was taken after maintaining the mixtures at an initial rest period of 2 h and then the subsequent measurements were taken after every 1 h as shown in Figure 7-9. To check if the mixture was printable, a single filament was printed at every yield stress measurement step to evaluate the open time of these mixtures. The limit of lower yield stress shown in Figure 7-9 corresponds to the initial yield stress measured immediately after mixing, while the upper yield stress limit corresponds to the yield stress measured when the mixture became no longer printable. The extrudability zone

of printable alkali-activated slag paste and mortar designed in this study was found to be between 69 Pa and 380 Pa (limited by printer's capacity used in this study). The paste and mortar mixtures were extrudable and printable till around 7 h and 6 h respectively, which can be considered to be the respective open time for 3D-printing applications. Usually, the mixtures lose their workability earlier than their initial setting time. However, the open time of printable alkali activated slag mixtures were found to scale relatively well with their initial setting time. Therefore, a simple test such as setting time can be used as an initial indicator for extrudability of these printable slag mixtures.

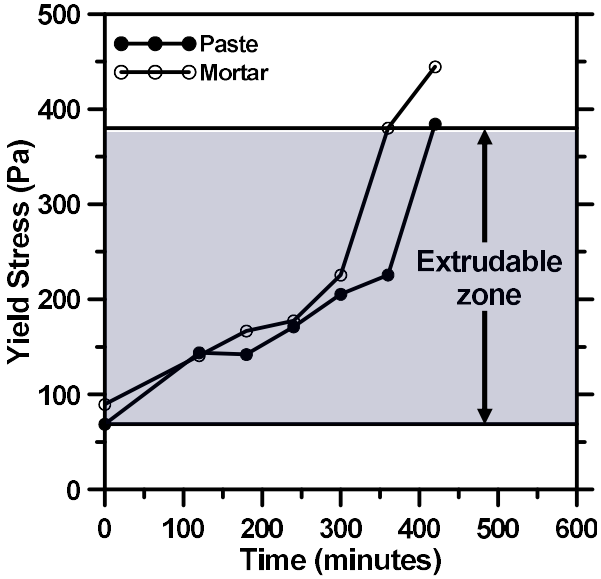

Figure 7-9: Yield stress of printable paste and mortar mixtures with time showing the extrudable zone.

7.3.3.3. Extensional Rheology (Tack Test)

The adhesive and cohesive nature of the mixtures are very important in 3D printing and can be quantified by using extensional rheology (tack test). Cohesion is defined as internal attraction forces between particles at rest while adhesion is defined as the attraction forces between different surfaces which determines the tendency of the mixtures to stick to another surface [188]. These properties are very influential in layered 3D-printing. Figures

7-10(a) show the evolution of the normal force as a function of plate separation for printable paste and mortar, Figure 7-10(b) shows the peak force and the plate separation corresponding to the peak load, and Figure 7-10(c) shows the adhesion energy of the printable paste and mortar. The absolute value of the peak force indicates the adhesive characteristics of the mixture while the cohesion characteristics can be evaluated by the resistance of the mixture to elastic failure [189]. The gap at the peak force is associated with the critical strain of the mixture, describing its deformation before the onset of failure. Initially, the mixtures show an elastic behavior where the normal force linearly increases until the peak load (corresponding to critical gap separation) where rupture occurs, and then the force starts to decay denoting the failure process.

It is observed that the mortar has a higher peak force than paste, attributable to the presence of fine sand aggregates which increases the stiffness of the mixture. The average peak forces were between 5.5 N and 8.2 N while the plate gap at complete separation were between 2.0 and 2.3 mm for the paste and mortar respectively. Both mixtures showed comparable peak force to our previous family of printable mixture prepared from OPC and fly ash along with fine powders to improve their rheology [170,204]. In alkali-activated printable slag mixtures prepared in this study, the flocculation effect (colloidal forces) plays a major role in improving rheological characteristics without any admixtures. Moreover, the bonding capacity and tendency of mixtures to stick on other surfaces can be inferred by the energy required to detach the mixture under tensile force and is very important to evaluate the interlayer properties when a wet-on-wet filament is implemented. As shown in Figure 7-10(c), the adhesion/cohesion energy (represented by the area under the force-displacement curves) is the highest for the mortar. The adhesion energy of the

paste was 4.2 N-mm, while was 6.5 N-mm for mortar. These adhesion values were relatively similar to that of the OPC-based pastes and alkali-activated fly ash-based pastes reported in our previous published work [170,204].

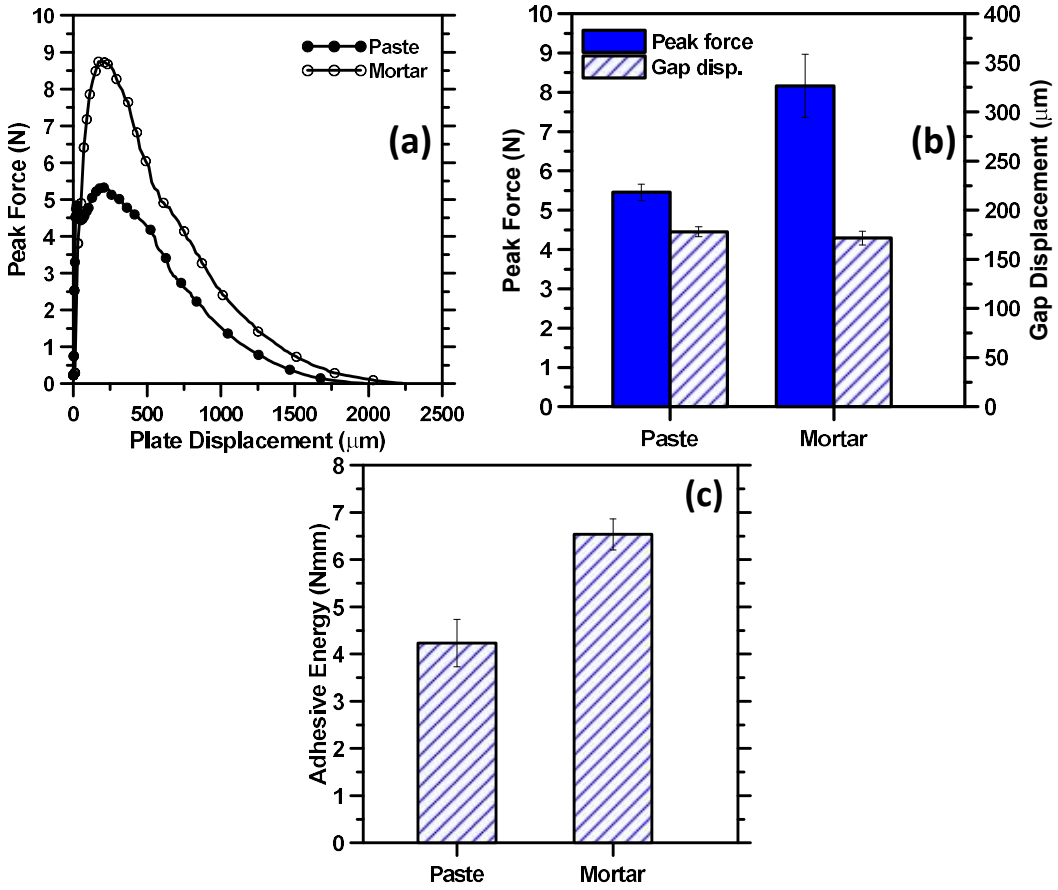

Figure 7-10: Tack test results showing (a) absolute normal force as a function of plate displacement, (b) peak force and corresponding gap displacement , and (c) adhesion energy for printable paste and mortar.

7.3.4. Buildability of Printable Mixtures

The 3D printable mixtures must have ability to build up, resist the overburden pressure due to the overlaid layers and eventually sustain their shapes after printing. Therefore, the mixture must recover most of the its initial viscosity after printing so that the printed layer is able to load the subsequent layers leading to stable shape. Figure 7-11 depicts the behavior of viscosity recovery of printable paste and mortar. Three stages of viscosity

evolution were adopted in this figure which are the initial viscosity of the mixtures at rest that reflects the initial viscosity of the mixtures before extrusion (before printing; from 0 to 60 s), the viscosity of the mixtures during extrusion (during printing; from 60 to 90 s) and the viscosity of the extruded mixtures (after printing; from 90 s to 150 s) as defined in [53,54]. It was observed that both paste and mortar showed a high viscosity at rest and significantly dropped to very low viscosity at high shear rate explaining the smooth and continuous material flow during printing (under extrusion effect) and then most of the viscosity was recovered to its initial viscosity leading to better buildability of the mixtures. The colloidal interaction forces between particles provide high initial viscosity [177]. The high shear rate which simulates the extrusion results in deflocculation and changes in fresh state microstructure leading to lower viscosity. The recovered viscosity of these mixtures (~61% for both paste and mortar) is attributed to the reflocculation effect after the material comes to rest. However, the viscosity recovery of these mixtures are higher than the viscosity recovery of geopolymeric 3D-printed pastes reported in literature [53,54], demonstrating better buildability of these mixtures.

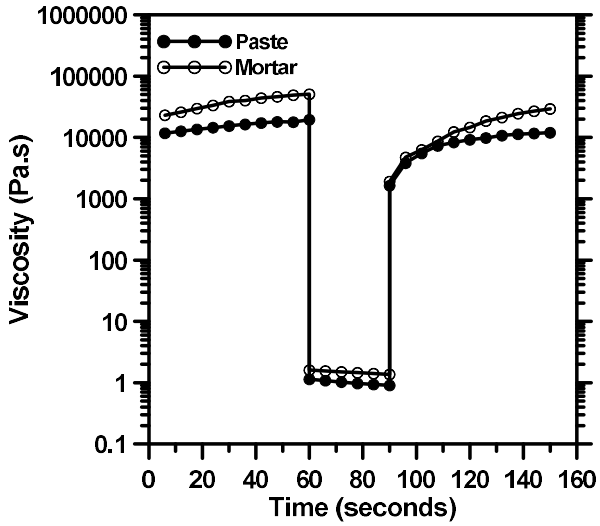

Figure 7-11: Viscosity recovery (buildability) of printable paste and mortar.

The layer stability refers to the stability of a single filament (layer) when extruded and laid and extent of its ability to load and hold the subsequent layers without shape instability. Consequently, a single filament (layer) of the paste and mortar were printed and then shape retention factor of printed filament (SRF) was calculated using equation 7-1. Figure 7-12 (a and b) shows the printed filaments for paste and mortar showing actual layer width (spread of layer) after printing. The SRF values were 93% for the paste and 98% for the mortar. These SRF values scale with the viscosity recovery discussed earlier. The SRF value of mortar was higher than the paste as expected because of the presence of fine sand resulting in a stiffer mixture with higher yield stress (see Figure 7-8). In addition, a single perimeter shape was printed as a practical and straightforward test to check the buildability of the printable paste (worst case based on the SRF value). Figure 7-12(c) shows the number of stacked printed layers of the paste. The aspect ratio was calculated based on the total height-to-layer width ratio. The aspect ratio of the paste was 15.5 (31 layers which means 93 mm of total height). It was observed that the aspect ratio can go higher than 15.5, but the total height of printed shape reached the z-axis height limit of the printer used in this study. In addition to buildability, overburden pressure effect was not observed on the bottom layers of the paste explaining that the viscosity recovery (described earlier) was enough to hold and withstand the own weight of the overlaid layers.

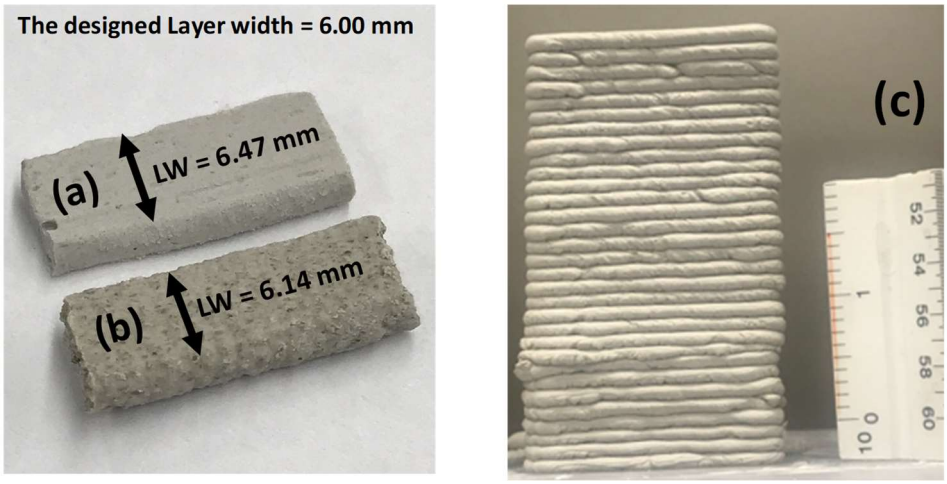

Figure 7-12: (a and b) Single printed filaments of paste and mortar respectively showing the actual layer width after printing, and (c) number of stacked printed layers of paste to investigate the buildability and aspect ratio.

7.3.5. Mechanical Properties of Hardened components

After evaluating the fresh properties of alkali-activated printable slag mixtures favoring 3D-printing, the mechanical properties (i.e. compressive and flexural strength) are very crucial to be sufficient for structural applications. Three replicate specimens of mortars (cubes and beams) were printed and kept for curing in a moist chamber (23 ± 1ºC, > 98% RH) until the respective testing duration (see Figure 7-13). The compressive and flexural strength of alkali-activated printable slag mortars were tested for printed specimens and compared with specimens prepared from the same mixture but in cast form (not printed).

Figure 7-13: The printed mortar cubes and beam prepared for mechanical tests.

Figure 7-14 depicts the compressive and flexural strengths of mortars. No significant differences are observed in compressive strength between the printed and cast cubes attributable to good bonding between the printed layers . The average compressive strength was 75.3 MPa for cast cubes, while it was 74.2 MPa for the printed cubes at 28 days. Also, both specimens showed sufficient early age average strengths (higher than 30 MPa at 3 days). Hence this printable mixture is an appropriate one to deliver high early mechanical strength when compared to conventional OPC-based mixtures. The average compressive strengths of cast and printed samples (prepared by remixing mixtures for 2 min as described in section 7.2.2) are similar to the compressive strengths of alkali-activated slag mixed conventionally [69]. This proves that the modified mixing procedure established in this study did not negatively impact the mechanical properties of the mixtures. The flexural strengths also showed similar trends as shown in Figure 7-14(b). The printed beams showed improved flexural strength when compared with cast beams. The flexural strength was 10.4 MPa and 12.2 MPa for cast and printed beams respectively at 28 days. The bottom layers are the crucial for beams because the flexural strength determination depends on the maximum tensile stress at the bottom layer. The bottom layers of the printed beams are denser and well-compacted than upper layers (superimposed layers). This might explain the higher flexural strength of printed beams. These high flexural strengths of printed beams also is a reflection of good bonding between layers.

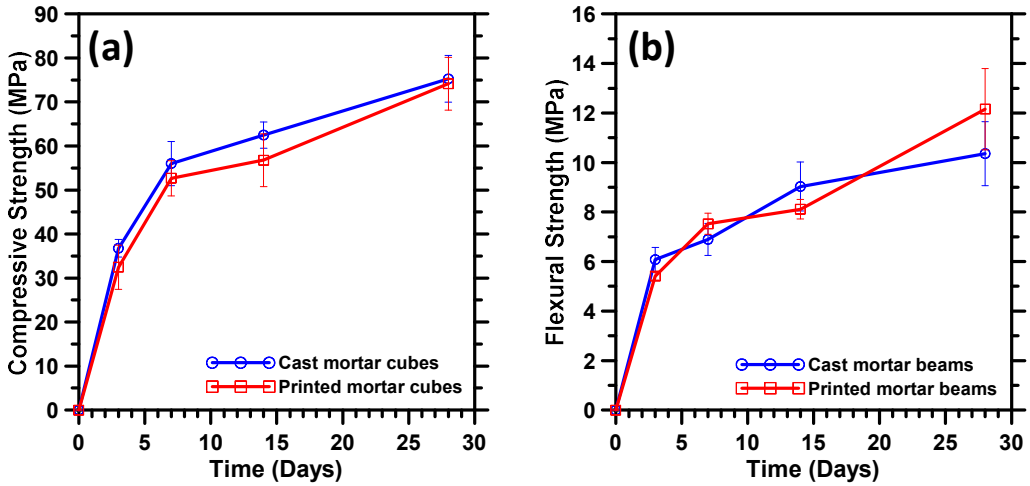

Figure 7-14: (a) Compressive strengths, and (b) flexural strengths of cast and printed mortar specimens.

7.4. CONCLUSIONS

This study has presented a novel mixing procedure to produce alkali activated slag mixtures suitable for 3D-printing with delayed setting time and improved rheological properties without adding admixtures. This procedure depended on deflocculating the alkali-activated slag mixture so as to prolong the initial setting time and create cohesive mixtures.

The initial setting time was approximately around 8 hours. This long initial setting time was evident on the calorimetric curves showing lower value of initial peak and long induction period lasting approximately 10 h for these mixtures. In addition, these mixtures showed more reaction products (more non-evaporable water) after deflocculation due to dissolution of more calcium ions into activator solution which helps to produce more reaction products which results in cohesive mixtures. The printability of these mixtures was qualified based on the extrudability and shape stability. The yield stresses of these mixtures were 68 Pa and 90 Pa for paste and mortar respectively. The extrudable zone of the paste and mortar was established based on the evolution of yield stress with time which was found to scale relatively well with the initial setting time of the mixtures. The

extrudable zone was established to be between 68 to 380 Pa with ~6 h of open time of printability. The tack force and adhesive energy of printable slag mixtures were similar to several printable binders investigated earlier. The buildability of these mixtures was evaluated using the viscosity response with different shear rates which mimics extrusion-based 3D-printing. The low viscosity during extrusion (high shear rate) allowed easy and smooth printing without discontinuity. The ability of these mixture to sufficiently recover their viscosity demonstrated desirable buildability which was confirmed by printing a single perimeter shape with many stacked layers. The aspect ratio of printed shape was 15.5 and the layer stability had higher shape retention factor. Moreover, the compressive and flexural strengths of the layered printed samples were comparable to that of conventionally cast samples. The flexural strength results were observed to be slightly higher in printed specimens than conventionally cast ones. Finally, this study has provided a simple solution to mitigate the uncontrolled setting time of alkali-activated slag mixtures. No admixtures are used, The mechanical properties of the printed shapes are also found to be better.

CHAPTER 8

CONCLUSIONS

8.1. Characteristics of Multi-functional Porous Ceramic Matrices

- Silica fume and metakaolin as siliceous and aluminous sources along with the natural pozzolan developed the geopolymerization resulting in strong and stable formed gel network. Potassium hydroxide in combination with potassium silicate solution as an activation agent promoted and stimulated the condensation reactions due to the large cation (K^+). The steps of sintering and burnout needed in conventional ceramic fabrication were limited by moderate temperature treatment to provide functional properties of interest. Thus, economy and energy-efficiency were achieved.
- Porous ceramic matrices were synthesized by two different procedures – in the first, low concentration of alkaline activator solution (n = 0.05, and M_s = 1.5) with heat treatment at 100ºC or 650ºC was employed whereas in the second procedure, high concentration of alkaline activator solution with maintained molar composition (K_2O. $2SiO_2$. $18H_2O$) along with pore forming agent resulted in reducing the treatment temperature to 85ºC.
- 50-70% of porosity was achieved with a significant porosity fraction in the range of 0.028 to 1 μm and 0.0036 to 0.028 which are effective in filtration applications to trap contaminants including viruses.
- The synthesized porous ceramics had low thermal conductivities, rendering their use in thermal insulation of buildings.

- The plenty amount of the source materials in nature, the ease of manufacturing these systems, and the range of tunable microstructure and properties enables them to be considered for many applications such as building insulation, and also filtration.

8.2. Sodium Carbonate Activated Fly Ash Lightweight Matrices

- Sodium carbonate which is cheap, less caustic, and plentiful material succeeded to be activating/pore forming agents. The produced NaOH after dissolving sodium carbonate in water or water glass solution provided enough alkalinity for the reaction and complete polycondensation. Also, the hydrolysis of sodium carbonate produced sodium bicarbonate that released CO_2 due to decomposition at low temperatures (85ºC and 100ºC).
- The samples treated at 100ºC resulted in porous materials with 25% increase in volume with 1.1 to 1.4 g/cm^3 range of bulk densities whereas the ones treated at 85ºC resulted in a less porous material with bulk densities around 1.7 g/cm^3.
- The porous samples had low thermal conductivities in the range of 0.29 to 0.37 W/m-K and porosities of 45-55%.
- The use of sodium silicate solution (waterglass) along with sodium carbonate produced foamed matrices with smaller critical pore sizes indicating the effect of silicate on refining the pore structure.
- The presence of sodium silicate along with sodium carbonate improved the geopolymerization reactions resulting in foamed matrices with adequate mechanical properties.

- The CO_2-equivalent emissions per m^3 was calculated and showed that the foamed geopolymeric systems synthesized in this study emitted lower CO_2 than other similar materials synthesized by using many different foaming agents.

8.3. Rheological Characterization and Hardened Properties of 3D-printable Alkali-activated Fly Ash

- Family of alkali-activated fly ash along with minor ingredient (limestone, slag, or OPC) were prepared for 3D-printing.
- The finer powder such as limestone improved the rheological properties (improved particle packing) of binders whereas the slag and OPC improved the hardened properties.
- The use of alkaline activators increased the cohesiveness of pastes favoring buildability and simultaneously decreased the shear yield stresses favoring extrudability.
- The bounds for extrudability and printability of the pastes were determined based on their mini-slump values and shear yield stresses. Also, the printability window was established based on the time-dependent shear yield stresses measurements. The upper limit of shear yield stress for smooth extrudability was found to be 700Pa (in parallel plate rheometry). The printability window was found to scale relatively with pastes setting time results.
- The tack force and adhesion of pastes increased due to presence of alkaline activators as compared to conventional cement-based binders.
- The parameters extracted from extrusion test were shown to be related to shear yield stress and extensional (tack) properties determined by using simple

rheological experiments. Thus, simple rheological experiments were able to evaluate the response of extruded mixtures and then used to link material design to the extrusion-based printing process.

- The mechanical properties of printed components showed comparable results to those of conventionally cast ones. The reduction in strength observed in mixtures containing slag likely due to the microcracking due to heat curing and high shrinkage of slag while the poor interlayer bonding in mixtures containing OPC caused reduction in flexural strength.

8.4. 3D-printable Alkali-activated Fly Ash Foamed Suspensions

- A novel method with different contents of surfactant succeeded to synthesize 3D-printable foamed suspensions (dry foam) for thermal insulation applications. The improved particle packing of suspensions created stable mixtures after extrusion as well as reinforcing the solid skeleton.
- Unsurprisingly, the increase in surfactant contents resulted in very low bulk density of printed foamed matrices which were lower than that of water.
- The shear yield stresses of synthesized foamed suspensions ranged from 60 to 130 Pa. The bubbles acted as hard spheres in mixtures below the jamming transition (low surfactant dosage) resulting in increased yield stress while the mixtures below the jamming transition showed lower yield stress.
- The foamed suspensions showed low viscosity under extrusion and most of their viscosity recovered indicating better buildability. Moreover, the shape retention factor of the synthesized foamed matrices was high.
- No significant difference between the extruded and conventional cast samples.

- The porosity and thermal of foamed matrices were in the range of 55-75% and 0.15 and 0.25 W/m-K. Thus, 3D-printing of geopolymeric foams can be used in conjunction with precast wall manufacturing by replacing the conventional foam insulation (mineral wool) by printing these suspensions with 50-70% of air voids (gaps).

8.5. 3D-printable Alkali-activated Slag Paste and Mortar

- A novel mixing procedure was established to prepare 3D-printable alkali-activated slag mixtures with prolonged initial setting time, without the use of any admixtures. Disintegration of early formed C-S-H (deflocculation) delayed the setting time and increased the cohesiveness of the mixtures due to the colloidal forces between slag particles.
- The initial setting time was found to be around ~8h and was evident on the calorimetric curves. The lower initial peak and long induction period of the prepared mixtures (remixed or deflocculated mixtures) explained the delayed setting time of these mixtures.
- The yield stresses were 68 Pa and 90 Pa (vane in cup rheometry) for paste and mortar respectively. The extrudable zone was established based on the time-dependent shear yield stress measurements. The lower and upper limit of yield stresses were 68 Pa and 380 Pa respectively with around ~6h of printability open time.
- The mortar mixture showed higher tack force and adhesion (more stiffness) than the paste. Both paste and mortar showed low viscosity under extrusion explaining

smooth and continuous printing and also most of the viscosity was recovered after printing, explaining better buildability.

- The mechanical properties (compressive and flexural strength) of the printed mortars were comparable or higher than those of their cast counterparts. Thus, 3D-printing of alkali-activated slags with adequate fresh and hardened properties can be accomplished.

REFERENCES

[1] P. NATH, P.K. SARKER, FLY ASH BASED GEOPOLYMER CONCRETE: A REVIEW, New Developments in Structural Engineering and Construction. (2013) 1091–1096. doi:10.3850/978-981-07-5354-2_M-54-431.

[2] A. Motorwala, V. Shah, R. Kammula, P. Nannapaneni, Prof.D.B. Raijiwala, ALKALI Activated FLY-ASH Based Geopolymer Concrete, International Journal of Emerging Technology and Advanced Engineering. 3 (2013) 159–166.

[3] J.G. Jang, N.K. Lee, H.K. Lee, Fresh and hardened properties of alkali-activated fly ash/slag pastes with superplasticizers, Construction and Building Materials. 50 (2014) 169–176. doi:10.1016/j.conbuildmat.2013.09.048.

[4] P. Hlaváček, V. Šmilauer, F. Škvára, L. Kopecký, R. Šulc, Inorganic foams made from alkali-activated fly ash: Mechanical, chemical and physical properties, Journal of the European Ceramic Society. 35 (2015) 703–709. doi:10.1016/j.jeurceramsoc.2014.08.024.

[5] A. Mehta, R. Siddique, Sulfuric acid resistance of fly ash based geopolymer concrete, Construction and Building Materials. 146 (2017) 136–143. doi:10.1016/j.conbuildmat.2017.04.077.

[6] W.D.A. Rickard, A. van Riessen, Performance of solid and cellular structured fly ash geopolymers exposed to a simulated fire, Cement and Concrete Composites. 48 (2014) 75–82. doi:10.1016/j.cemconcomp.2013.09.002.

[7] G. Roviello, L. Ricciotti, C. Ferone, F. Colangelo, O. Tarallo, Fire resistant melamine based organic-geopolymer hybrid composites, Cement and Concrete Composites. 59 (2015) 89–99. doi:10.1016/j.cemconcomp.2015.03.007.

[8] V.F.F. Barbosa, K.J.D. MacKenzie, C. Thaumaturgo, Synthesis and characterisation of materials based on inorganic polymers of alumina and silica: sodium polysialate polymers, International Journal of Inorganic Materials. 2 (2000) 309–317. doi:10.1016/S1466-6049(00)00041-6.

[9] H. Xu, J.S.J. Van Deventer, The geopolymerisation of alumino-silicate minerals, International Journal of Mineral Processing. 59 (2000) 247–266. doi:10.1016/S0301-7516(99)00074-5.

[10] E. Prud'homme, P. Michaud, E. Joussein, C. Peyratout, A. Smith, S. Arrii-Clacens, J.M. Clacens, S. Rossignol, Silica fume as porogent agent in geo-materials at low temperature, Journal of the European Ceramic Society. 30 (2010) 1641–1648. doi:10.1016/j.jeurceramsoc.2010.01.014.

[11] E. Landi, V. Medri, E. Papa, J. Dedecek, P. Klein, P. Benito, A. Vaccari, Alkali-bonded ceramics with hierarchical tailored porosity, Applied Clay Science. 73 (2013) 56–64. doi:10.1016/j.clay.2012.09.027.

[12] F. Pacheco-Torgal, J. Castro-Gomes, S. Jalali, Alkali-activated binders: A review: Part 1. Historical background, terminology, reaction mechanisms and hydration products, Construction and Building Materials. 22 (2008) 1305–1314. doi:10.1016/j.conbuildmat.2007.10.015.

[13] J. Davidovits, Geopolymer Chemistry and Applications, Geopolymer Institute, 2008.

[14] P. Duxson, G.C. Lukey, F. Separovic, J.S.J. van Deventer, Effect of Alkali Cations on Aluminum Incorporation in Geopolymeric Gels, Ind. Eng. Chem. Res. 44 (2005) 832–839. doi:10.1021/ie0494216.

[15] P. Duxson, A. Fernández-Jiménez, J. Provis, G. Lukey, A. Palomo, J. Deventer, Geopolymer technology: the current state of the art, Journal of Materials Science. 42 (2007) 2917–2933. doi:10.1007/s10853-006-0637-z.

[16] J.S.J. van Deventer, J.L. Provis, P. Duxson, G.C. Lukey, Reaction mechanisms in the geopolymeric conversion of inorganic waste to useful products, Journal of Hazardous Materials. 139 (2007) 506–513. doi:10.1016/j.jhazmat.2006.02.044.

[17] B. Panda, S.C. Paul, L.J. Hui, Y.W.D. Tay, M.J. Tan, Additive manufacturing of geopolymer for sustainable built environment, Journal of Cleaner Production. 167 (2017) 281–288. doi:10.1016/j.jclepro.2017.08.165.

[18] M. Xia, J. Sanjayan, Method of formulating geopolymer for 3D printing for construction applications, Materials & Design. 110 (2016) 382–390. doi:10.1016/j.matdes.2016.07.136.

[19] B. Das, B. Chakrabarty, P. Barkakati, Preparation and characterization of novel ceramic membranes for micro-filtration applications, Ceramics International. 42 (2016) 14326–14333. doi:10.1016/j.ceramint.2016.06.125.

[20] S. Benfer, P. Árki, G. Tomandl, Ceramic Membranes for Filtration Applications — Preparation and Characterization, Adv. Eng. Mater. 6 (2004) 495–500. doi:10.1002/adem.200400577.

[21] F. Frizon, C.J. Dubien, Method of preparing a controlled porosity geopolymer, the resulting geopolymer and the various applications thereof, US20100222204 A1, 2010. http://www.google.com/patents/US20100222204 (accessed December 18, 2017).

[22] C. Yang, G. Zhang, N. Xu, J. Shi, Preparation and application in oil–water separation of ZrO2/α-Al2O3 MF membrane, Journal of Membrane Science. 142 (1998) 235–243. doi:10.1016/S0376-7388(97)00336-0.

[23] A. Vyatskikh, A. Kudo, S. Delalande, J.R. Greer, Additive Manufacturing of Polymer-Derived Titania for One-Step Solar Water Purification, Materials Today Communications. (2018). doi:10.1016/j.mtcomm.2018.02.010.

[24] P. Sazama, O. Bortnovsky, J. Dědeček, Z. Tvarůžková, Z. Sobalík, Geopolymer based catalysts—New group of catalytic materials, Catalysis Today. 164 (2011) 92–99. doi:10.1016/j.cattod.2010.09.008.

[25] J. Sunarso, S. Baumann, J.M. Serra, W.A. Meulenberg, S. Liu, Y.S. Lin, J.C. Diniz da Costa, Mixed ionic–electronic conducting (MIEC) ceramic-based membranes for oxygen separation, Journal of Membrane Science. 320 (2008) 13–41. doi:10.1016/j.memsci.2008.03.074.

[26] E. Kamseu, B. Nait-Ali, M.C. Bignozzi, C. Leonelli, S. Rossignol, D.S. Smith, Bulk composition and microstructure dependence of effective thermal conductivity of porous inorganic polymer cements, Journal of the European Ceramic Society. 32 (2012) 1593–1603. doi:10.1016/j.jeurceramsoc.2011.12.030.

[27] K. Okada, A. Ooyama, T. Isobe, Y. Kameshima, A. Nakajima, K.J.D. MacKenzie, Water retention properties of porous geopolymers for use in cooling applications, Journal of the European Ceramic Society. 29 (2009) 1917–1923. doi:10.1016/j.jeurceramsoc.2008.11.006.

[28] G. Pia, L. Casnedi, U. Sanna, Porous ceramic materials by pore-forming agent method: An intermingled fractal units analysis and procedure to predict thermal conductivity, Ceramics International. 41 (2015) 6350–6357. doi:10.1016/j.ceramint.2015.01.069.

[29] H. Takahara, The sound absorption characteristics of particulate porous ceramic materials, Applied Acoustics. 41 (1994) 265–274. doi:10.1016/0003-682X(94)90076-0.

[30] F.-Z. Zhang, T. Kato, M. Fuji, M. Takahashi, Gelcasting fabrication of porous ceramics using a continuous process, Journal of the European Ceramic Society. 26 (2006) 667–671. doi:10.1016/j.jeurceramsoc.2005.07.021.

[31] Z. Živcová, E. Gregorová, W. Pabst, D.S. Smith, A. Michot, C. Poulier, Thermal conductivity of porous alumina ceramics prepared using starch as a pore-forming agent, Journal of the European Ceramic Society. 29 (2009) 347–353. doi:10.1016/j.jeurceramsoc.2008.06.018.

[32] Y. Chen, H. Yao, L. Wang, Acoustic band gaps of three-dimensional periodic polymer cellular solids with cubic symmetry, Journal of Applied Physics. 114 (2013) 043521. doi:10.1063/1.4817168.

[33] Y. Chen, T. Li, F. Scarpa, L. Wang, Lattice Metamaterials with Mechanically Tunable Poisson's Ratio for Vibration Control, Physical Review Applied. 7 (2017) 024012. doi:10.1103/PhysRevApplied.7.024012.

[34] Y. Chen, F. Qian, L. Zuo, F. Scarpa, L. Wang, Broadband and multiband vibration mitigation in lattice metamaterials with sinusoidally-shaped ligaments, Extreme Mechanics Letters. 17 (2017) 24–32. doi:10.1016/j.eml.2017.09.012.

[35] X. Wang, M. Jiang, Z. Zhou, J. Gou, D. Hui, 3D printing of polymer matrix composites: A review and prospective, Composites Part B: Engineering. 110 (2017) 442–458. doi:10.1016/j.compositesb.2016.11.034.

[36] G.J. Gibbons, R. Williams, P. Purnell, E. Farahi, 3D Printing of cement composites, Advances in Applied Ceramics. 109 (2010) 287–290. doi:10.1179/174367509X12472364600878.

[37] F. Bos, R. Wolfs, Z. Ahmed, T. Salet, Additive manufacturing of concrete in construction: potentials and challenges of 3D concrete printing, Virtual and Physical Prototyping. 11 (2016) 209–225. doi:10.1080/17452759.2016.1209867.

[38] Robert Bogue, 3D printing: the dawn of a new era in manufacturing?, Assembly Automation. 33 (2013) 307–311. doi:10.1108/AA-06-2013-055.

[39] P. Feng, X. Meng, J.-F. Chen, L. Ye, Mechanical properties of structures 3D printed with cementitious powders, Construction and Building Materials. 93 (2015) 486–497. doi:10.1016/j.conbuildmat.2015.05.132.

[40] P. Marks, The many flavours of printing in 3D, New Scientist. 211 (2011) 18. doi:10.1016/S0262-4079(11)61818-6.

[41] P. Wu, J. Wang, X. Wang, A critical review of the use of 3-D printing in the construction industry, Automation in Construction. 68 (2016) 21–31. doi:10.1016/j.autcon.2016.04.005.

[42] H. Lipson, M. Kurman, Fabricated the New World of 3D Printing, Wiley, Hoboken, 2013.

[43] J. Malda, J. Visser, F.P. Melchels, T. Jüngst, W.E. Hennink, W.J.A. Dhert, J. Groll, D.W. Hutmacher, 25th Anniversary Article: Engineering Hydrogels for Biofabrication, Advanced Materials. 25 (2013) 5011–5028. doi:10.1002/adma.201302042.

[44] S.V. Murphy, A. Atala, 3D bioprinting of tissues and organs, Nature Biotechnology. 32 (2014) 773–785. doi:10.1038/nbt.2958.

[45] M.L. Lifson, M.-W. Kim, J.R. Greer, B.-J. Kim, Enabling Simultaneous Extreme Ultra Low-k in Stiff, Resilient, and Thermally Stable Nano-Architected Materials, Nano Lett. 17 (2017) 7737–7743. doi:10.1021/acs.nanolett.7b03941.

[46] C. Minas, D. Carnelli, E. Tervoort, A.R. Studart, 3D Printing of Emulsions and Foams into Hierarchical Porous Ceramics, Advanced Materials. 28 (2016) 9993–9999. doi:10.1002/adma.201603390.

[47] B.G. Compton, J.A. Lewis, 3D-Printing of Lightweight Cellular Composites, Advanced Materials. 26 (2014) 5930–5935. doi:10.1002/adma.201401804.

[48] A.K. Singh, B. Patil, N. Hoffmann, B. Saltonstall, M. Doddamani, N. Gupta, Additive Manufacturing of Syntactic Foams: Part 1: Development, Properties, and Recycling Potential of Filaments, JOM. 70 (2018) 303–309. doi:10.1007/s11837-017-2734-7.

[49] A.K. Singh, B. Saltonstall, B. Patil, N. Hoffmann, M. Doddamani, N. Gupta, Additive Manufacturing of Syntactic Foams: Part 2: Specimen Printing and Mechanical Property Characterization, JOM. 70 (2018) 310–314. doi:10.1007/s11837-017-2731-x.

[50] L. Jiang, H. Xiao, W. An, Y. Zhou, J. Sun, Correlation study between flammability and the width of organic thermal insulation materials for building exterior walls, Energy and Buildings. 82 (2014) 243–249. doi:10.1016/j.enbuild.2014.06.013.

[51] A.A. Stec, T.R. Hull, Assessment of the fire toxicity of building insulation materials, Energy and Buildings. 43 (2011) 498–506. doi:10.1016/j.enbuild.2010.10.015.

[52] Y. Ai-hua, L. Jian-yong, Z. Xia, Y. Zhan, Study of the Combustion Performance of Three Kinds of Organic Heat Insulation Materials, Procedia Engineering. 11 (2011) 614–619. doi:10.1016/j.proeng.2011.04.704.

[53] B. Panda, C. Unluer, M.J. Tan, Investigation of the rheology and strength of geopolymer mixtures for extrusion-based 3D printing, Cement and Concrete Composites. 94 (2018) 307–314. doi:10.1016/j.cemconcomp.2018.10.002.

[54] B. Panda, M.J. Tan, Experimental study on mix proportion and fresh properties of fly ash based geopolymer for 3D concrete printing, Ceramics International. 44 (2018) 10258–10265. doi:10.1016/j.ceramint.2018.03.031.

[55] A. Kashani, T.D. Ngo, Optimisation of mixture properties for 3D printing of geopolymer concrete, in: ISARC. Proceedings of the International Symposium on Automation and Robotics in Construction; Waterloo, IAARC Publications, Waterloo, Canada, Waterloo, 2018: pp. 1–8. https://search.proquest.com/docview/2123611495/abstract/B4336DBA51F34AD4PQ/1 (accessed June 12, 2019).

[56] M. Palacios, P.F. Banfill, F. Puertas, Rheology and setting of alkali-activated slag pastes and mortars: effect of organic admixture., ACI Materials Journal. 105 (2008) 140.

[57] M. Palacios, F. Puertas, Effectiveness of Mixing Time on Hardened Properties of Waterglass-Activated Slag Pastes and Mortars., ACI Materials Journal. 108 (2011).

[58] M.L. Wilson, Design and Control of Concrete Mixtures, 15th (Fifteenth), n.d.

[59] K. Vance, M. Aguayo, T. Oey, G. Sant, N. Neithalath, Hydration and strength development in ternary portland cement blends containing limestone and fly ash or metakaolin, Cement and Concrete Composites. 39 (2013) 93–103. doi:10.1016/j.cemconcomp.2013.03.028.

[60] S.M. Mansour, M.T. Abadlia, K. Bekkour, I. Messaoudene, Improvement of rheological behaviour of cement pastes by incorporating metakaolin., European Journal of Scientific Research. 42 (2010) 442–452.

[61] G. Masi, W.D.A. Rickard, L. Vickers, M.C. Bignozzi, A. van Riessen, A comparison between different foaming methods for the synthesis of light weight geopolymers, Ceramics International. 40 (2014) 13891–13902. doi:10.1016/j.ceramint.2014.05.108.

[62] C. Bai, P. Colombo, High-porosity geopolymer membrane supports by peroxide route with the addition of egg white as surfactant, Ceramics International. 43 (2017) 2267–2273. doi:10.1016/j.ceramint.2016.10.205.

[63] C. Bai, G. Franchin, H. Elsayed, A. Zaggia, L. Conte, H. Li, P. Colombo, High-porosity geopolymer foams with tailored porosity for thermal insulation and wastewater treatment, Journal of Materials Research. 32 (2017) 3251–3259. doi:10.1557/jmr.2017.127.

[64] H. Alghamdi, A. Dakhane, A. Alum, M. Abbaszadegan, B. Mobasher, N. Neithalath, Synthesis and characterization of economical, multi-functional porous ceramics based on abundant aluminosilicates, Materials & Design. 152 (2018) 10–21. doi:10.1016/j.matdes.2018.04.060.

[65] J.G. Sanjayan, A. Nazari, L. Chen, G.H. Nguyen, Physical and mechanical properties of lightweight aerated geopolymer, Construction and Building Materials. 79 (2015) 236–244. doi:10.1016/j.conbuildmat.2015.01.043.

[66] J.L. Bell, W.M. Kriven, Preparation of ceramic foams from metakaolin-based geopolymer gels, in: H.-T. Lin, K. Koumoto, W.M. Kriven, D.P. Norton, E. Garcia, I.E. Reimanis (Eds.), Developments in Strategic Materials, Ceramic Engineering and Science Proceedings, 2009: pp. 97–111.

[67] A. Hajimohammadi, T. Ngo, P. Mendis, How does aluminium foaming agent impact the geopolymer formation mechanism?, Cement and Concrete Composites. 80 (2017) 277–286. doi:10.1016/j.cemconcomp.2017.03.022.

[68] H. Alghamdi, N. Neithalath, Novel synthesis of lightweight geopolymer matrices from fly ash through carbonate-based activation, Materials Today Communications. 17 (2018) 266–277. doi:10.1016/j.mtcomm.2018.09.014.

[69] A. Dakhane, Z. Peng, R. Marzke, N. Neithalath, Comparative Analysis of the Influence of Sodium and Potassium Silicate Solutions on the Kinetics and Products of Slag Activation, ACEM. 3 (2014) 371–387. doi:10.1520/ACEM20140005.

[70] K. Vance, G. Sant, N. Neithalath, The rheology of cementitious suspensions: A closer look at experimental parameters and property determination using common rheological models, Cement and Concrete Composites. 59 (2015) 38–48. doi:10.1016/j.cemconcomp.2015.03.001.

[71] K. Vance, A. Arora, G. Sant, N. Neithalath, Rheological evaluations of interground and blended cement–limestone suspensions, Construction and Building Materials. 79 (2015) 65–72. doi:10.1016/j.conbuildmat.2014.12.054.

[72] M. Aguayo, S. Das, C. Castro, N. Kabay, G. Sant, N. Neithalath, Porous inclusions as hosts for phase change materials in cementitious composites: Characterization, thermal performance, and analytical models, Construction and Building Materials. 134 (2017) 574–584. doi:10.1016/j.conbuildmat.2016.12.185.

[73] T. Lin, D. Jia, P. He, M. Wang, D. Liang, Effects of fiber length on mechanical properties and fracture behavior of short carbon fiber reinforced geopolymer matrix composites, Materials Science and Engineering: A. 497 (2008) 181–185. doi:10.1016/j.msea.2008.06.040.

[74] P. Mangat, P. Lambert, 18 - Sustainability of alkali-activated cementitious materials and geopolymers, in: J.M. Khatib (Ed.), Sustainability of Construction Materials (Second Edition), Woodhead Publishing, 2016: pp. 459–476. doi:10.1016/B978-0-08-100370-1.00018-4.

[75] P. Duan, C. Yan, W. Zhou, D. Ren, Development of fly ash and iron ore tailing based porous geopolymer for removal of Cu(II) from wastewater, Ceramics International. 42 (2016) 13507–13518. doi:10.1016/j.ceramint.2016.05.143.

[76] L. Chen, K. Zheng, Y. Liu, Geopolymer-supported photocatalytic TiO2 film: Preparation and characterization, Construction and Building Materials. 151 (2017) 63–70. doi:10.1016/j.conbuildmat.2017.06.097.

[77] J. Feng, R. Zhang, L. Gong, Y. Li, W. Cao, X. Cheng, Development of porous fly ash-based geopolymer with low thermal conductivity, Materials & Design (1980-2015). 65 (2015) 529–533. doi:10.1016/j.matdes.2014.09.024.

[78] Z. Zhang, J.L. Provis, A. Reid, H. Wang, Mechanical, thermal insulation, thermal resistance and acoustic absorption properties of geopolymer foam concrete, Cement and Concrete Composites. 62 (2015) 97–105. doi:10.1016/j.cemconcomp.2015.03.013.

[79] N.H. Jamil, W.M.A.W. Ibrahim, M.M.A.B. Abdullah, A.V. Sandu, M.F.M. Tahir, Fabrication of Porous Ceramic-Geopolymer Based Material to Improve Water Absorption and Retention in Construction Materials: A Review, IOP Conf. Ser.: Mater. Sci. Eng. 209 (2017) 012004. doi:10.1088/1757-899X/209/1/012004.

[80] T. Luukkonen, A. Heponiemi, H. Runtti, J. Pesonen, J. Yliniemi, U. Lassi, Application of alkali-activated materials for water and wastewater treatment: a review, Rev Environ Sci Biotechnol. 18 (2019) 271–297. doi:10.1007/s11157-019-09494-0.

[81] M.A. Aleem, P.D. Arumairaj, Geopolymer concrete–a review, International Journal of Engineering Sciences & Emerging Technologies. 1 (2012) 118–122.

[82] J. Thaarrini, S. Dhivya, Comparative Study on the Production Cost of Geopolymer and Conventional Concretes, International Journal of Civil Engineering Research. 7 (2016) 117–124.

[83] B.C. McLellan, R.P. Williams, J. Lay, A. van Riessen, G.D. Corder, Costs and carbon emissions for geopolymer pastes in comparison to ordinary portland cement, Journal of Cleaner Production. 19 (2011) 1080–1090. doi:10.1016/j.jclepro.2011.02.010.

[84] G. De Schutter, K. Lesage, V. Mechtcherine, V.N. Nerella, G. Habert, I. Agusti-Juan, Vision of 3D printing with concrete — Technical, economic and environmental potentials, Cement and Concrete Research. 112 (2018) 25–36. doi:10.1016/j.cemconres.2018.06.001.

[85] R.A. Buswell, W.R. Leal de Silva, S.Z. Jones, J. Dirrenberger, 3D printing using concrete extrusion: A roadmap for research, Cement and Concrete Research. 112 (2018) 37–49. doi:10.1016/j.cemconres.2018.05.006.

[86] D. Asprone, F. Auricchio, C. Menna, V. Mercuri, 3D printing of reinforced concrete elements: Technology and design approach, Construction and Building Materials. 165 (2018) 218–231. doi:10.1016/j.conbuildmat.2018.01.018.

[87] I. Hager, A. Golonka, R. Putanowicz, 3D Printing of Buildings and Building Components as the Future of Sustainable Construction?, Procedia Engineering. 151 (2016) 292–299. doi:10.1016/j.proeng.2016.07.357.

[88] D. Falliano, E. Gugliandolo, D. De Domenico, G. Ricciardi, Experimental Investigation on the Mechanical Strength and Thermal Conductivity of Extrudable Foamed Concrete and Preliminary Views on Its Potential Application in 3D Printed Multilayer Insulating Panels, in: T. Wangler, R.J. Flatt (Eds.), First RILEM International Conference on Concrete and Digital Fabrication – Digital Concrete 2018, Springer International Publishing, 2019: pp. 277–286.

[89] M. Hojati, A. Radlinska, S. Nazarian, J. Duarte, A. Memari, N. Meisel, S. Bilén, DESIGN AND 3D PRINTING OF TWO-PART GEOPOLYMER MORTAR, 1st International Conference on Concrete and Digital Fabrication. (2018) 10–12.

[90] C. Gosselin, R. Duballet, Ph. Roux, N. Gaudillière, J. Dirrenberger, Ph. Morel, Large-scale 3D printing of ultra-high performance concrete – a new processing route for architects and builders, Materials & Design. 100 (2016) 102–109. doi:10.1016/j.matdes.2016.03.097.

[91] J. Sun, W. Zhou, L. Yan, D. Huang, L. Lin, Extrusion-based food printing for digitalized food design and nutrition control, Journal of Food Engineering. 220 (2018) 1–11. doi:10.1016/j.jfoodeng.2017.02.028.

[92] Slic3r, (2017). http://slic3r.org/.

[93] J. Ma, X. Wang, W. Cao, C. Han, H. Yang, J. Yuan, M. Cao, A facile fabrication and highly tunable microwave absorption of 3D flower-like Co3O4-rGO hybrid-architectures, Chemical Engineering Journal. 339 (2018) 487–498. doi:10.1016/j.cej.2018.01.152.

[94] W. Cao, W. Wang, H. Shi, J. Wang, M. Cao, Y. Liang, M. Zhu, Hierarchical three-dimensional flower-like Co3O4 architectures with a mesocrystal structure as high capacity anode materials for long-lived lithium-ion batteries, Nano Res. 11 (2018) 1437–1446. doi:10.1007/s12274-017-1759-0.

[95] M.-S. Cao, H. Chen, X.-X. Wang, M. Zhang, Y.-L. Zhang, J. Shu, H. Yang, X. Fang, J. Yuan, Graphene nanohybrid：Excellent electromagnetic properties for electromagnetic wave absorbing and shielding, Journal of Materials Chemistry C. (2018). doi:10.1039/C7TC05869A.

[96] S. Dhara, P. Bhargava, A Simple Direct Casting Route to Ceramic Foams, Journal of the American Ceramic Society. 86 (2003) 1645.

[97] R.K. Nishihora, P.L. Rachadel, M.G.N. Quadri, D. Hotza, Manufacturing porous ceramic materials by tape casting—A review, Journal of the European Ceramic Society. (2017). doi:10.1016/j.jeurceramsoc.2017.11.047.

[98] S.J. Powell, J.R.G. Evans, The Structure of Ceramic Foams Prepared from Polyurethane-Ceramic Suspensions, Materials and Manufacturing Processes. 10 (1995) 757–771. doi:10.1080/10426919508935063.

[99] M.A. Anderson, L. Chu, Method for forming porous ceramic materials, US5439624 A, 1995. http://www.google.com/patents/US5439624 (accessed December 18, 2017).

[100] A.R. Studart, U.T. Gonzenbach, E. Tervoort, L.J. Gauckler, Processing Routes to Macroporous Ceramics: A Review, Journal of the American Ceramic Society. 89 (2006) 1771–1789. doi:10.1111/j.1551-2916.2006.01044.x.

[101] P. Duxson, G.C. Lukey, J.S.J. van Deventer, Thermal Conductivity of Metakaolin Geopolymers Used as a First Approximation for Determining Gel Interconnectivity, Ind. Eng. Chem. Res. 45 (2006) 7781–7788. doi:10.1021/ie060187o.

[102] B. Nair, Q. Zhao, R. Cooper, Geopolymer matrices with improved hydrothermal corrosion resistance for high-temperature applications, Journal of Materials Science. 42 (2007) 3083–3091. doi:10.1007/s10853-006-0526-5.

[103] J.W. Phair, J.S.J. Van Deventer, Effect of the silicate activator pH on the microstructural characteristics of waste-based geopolymers, International Journal of Mineral Processing. 66 (2002) 121–143. doi:10.1016/S0301-7516(02)00013-3.

[104] D.C. Comrie, W.M. Kriven, Composite Cold Ceramic Geopolymer in a Refractory Application, Ceramic Transactions. 153 (2003) 211–225. doi:10.1002/9781118406892.

[105] A. v McCormick, A.T. Bell, The Solution Chemistry of Zeolite Precursors, Catalysis Reviews. 31 (1989) 97–127. doi:10.1080/01614948909351349.

[106] B. Singh, G. Ishwarya, M. Gupta, S.K. Bhattacharyya, Geopolymer concrete: A review of some recent developments, Construction and Building Materials. 85 (2015) 78–90. doi:10.1016/j.conbuildmat.2015.03.036.

[107] Z. Zuhua, Y. Xiao, Z. Huajun, C. Yue, Role of water in the synthesis of calcined kaolin-based geopolymer, Applied Clay Science. 43 (2009) 218–223. doi:10.1016/j.clay.2008.09.003.

[108] T. Bakharev, Thermal behaviour of geopolymers prepared using class F fly ash and elevated temperature curing, Cement and Concrete Research. 36 (2006) 1134–1147. doi:10.1016/j.cemconres.2006.03.022.

[109] P. Rovnaník, Effect of curing temperature on the development of hard structure of metakaolin-based geopolymer, Construction and Building Materials. 24 (2010) 1176–1183. doi:10.1016/j.conbuildmat.2009.12.023.

[110] N. Neithalath, M.S. Sumanasooriya, O. Deo, Characterizing pore volume, sizes, and connectivity in pervious concretes for permeability prediction, Materials Characterization. 61 (2010) 802–813. doi:10.1016/j.matchar.2010.05.004.

[111] P.A. Webb, An Introduction To The Physical Characterization of Materials by Mercury Intrusion Porosimetry with Emphasis On Reduction And Presentation of Experimental Data, Micromeritics Instrument Corp., Norcross, Georgia. (2001).

[112] E. Prud'homme, P. Michaud, E. Joussein, C. Peyratout, A. Smith, S. Rossignol, In situ inorganic foams prepared from various clays at low temperature, Applied Clay Science. 51 (2011) 15–22. doi:10.1016/j.clay.2010.10.016.

[113] M. Criado, A. Fernández-Jiménez, A.G. de la Torre, M.A.G. Aranda, A. Palomo, An XRD study of the effect of the SiO2/Na2O ratio on the alkali activation of fly ash, Cement and Concrete Research. 37 (2007) 671–679. doi:10.1016/j.cemconres.2007.01.013.

[114] M. Criado, A. Fernández-Jiménez, A. Palomo, Alkali activation of fly ash: Effect of the SiO2/Na2O ratio: Part I: FTIR study, Microporous and Mesoporous Materials. 106 (2007) 180–191. doi:10.1016/j.micromeso.2007.02.055.

[115] P. Chindaprasirt, C. Jaturapitakkul, W. Chalee, U. Rattanasak, Comparative study on the characteristics of fly ash and bottom ash geopolymers, Waste Management. 29 (2009) 539–543. doi:10.1016/j.wasman.2008.06.023.

[116] M. Granizo, M. Blanco-Varela, S. Martínez-Ramírez, Alkali activation of metakaolins: parameters affecting mechanical, structural and microstructural properties, Journal of Materials Science. 42 (2007) 2934–2943. doi:10.1007/s10853-006-0565-y.

[117] W.K.W. Lee, J.S.J. van Deventer, Structural reorganisation of class F fly ash in alkaline silicate solutions, Colloids and Surfaces A: Physicochemical and Engineering Aspects. 211 (2002) 49–66. doi:10.1016/S0927-7757(02)00237-6.

[118] P. Duxson, G.C. Lukey, J.S.J. van Deventer, Evolution of Gel Structure during Thermal Processing of Na-Geopolymer Gels, Langmuir. 22 (2006) 8750–8757. doi:10.1021/la0604026.

[119] C.A. Rees, J.L. Provis, G.C. Lukey, J.S.J. van Deventer, Attenuated Total Reflectance Fourier Transform Infrared Analysis of Fly Ash Geopolymer Gel Aging, Langmuir. 23 (2007) 8170–8179. doi:10.1021/la700713g.

[120] A.J. Katz, A.H. Thompson, Quantitative prediction of permeability in porous rock, Phys. Rev. B. 34 (1986) 8179–8181. doi:10.1103/PhysRevB.34.8179.

[121] A.J. Katz, A.H. Thompson, Prediction of rock electrical conductivity from mercury injection measurements, J. Geophys. Res. 92 (1987) 599–607. doi:10.1029/JB092iB01p00599.

[122] M.S. Sumanasooriya, N. Neithalath, Pore structure features of pervious concretes proportioned for desired porosities and their performance prediction, Cement and Concrete Composites. 33 (2011) 778–787. doi:10.1016/j.cemconcomp.2011.06.002.

[123] M.I.M. Alzeer, K.J.D. MacKenzie, R.A. Keyzers, Porous aluminosilicate inorganic polymers (geopolymers): a new class of environmentally benign heterogeneous solid acid catalysts, Applied Catalysis A: General. 524 (2016) 173–181. doi:10.1016/j.apcata.2016.06.024.

[124] P.N. Lemougna, K. Wang, Q. Tang, U.C. Melo, X. Cui, Recent developments on inorganic polymers synthesis and applications, Ceramics International. 42 (2016) 15142–15159. doi:10.1016/j.ceramint.2016.07.027.

[125] Z. Zhang, J.L. Provis, A. Reid, H. Wang, Geopolymer foam concrete: An emerging material for sustainable construction, Construction and Building Materials. 56 (2014) 113–127. doi:10.1016/j.conbuildmat.2014.01.081.

[126] Z. Peng, K. Vance, A. Dakhane, R. Marzke, N. Neithalath, Microstructural and 29Si MAS NMR spectroscopic evaluations of alkali cationic effects on fly ash activation, Cement and Concrete Composites. 57 (2015) 34–43. doi:10.1016/j.cemconcomp.2014.12.005.

[127] A. Wardhono, The Effect of Sodium Hydroxide Molarity on Strength Development of Non-Cement Class C Fly Ash Geopolymer Mortar, J. Phys.: Conf. Ser. 947 (2018) 012001. doi:10.1088/1742-6596/947/1/012001.

[128] D. Ravikumar, S. Peethamparan, N. Neithalath, Structure and strength of NaOH activated concretes containing fly ash or GGBFS as the sole binder, Cement and Concrete Composites. 32 (2010) 399–410. doi:10.1016/j.cemconcomp.2010.03.007.

[129] S. Shi, H. Li, M. Fabian, T. Sun, K.T.V. Grattan, D. Xu, P.A.M. Basheer, Y. Bai, Alkali-activated Fly Ash Manufactured with Multi-stage Microwave Curing, in: 4th International Conference on Sustainable Construction Materials and TechnologY, CreateSpace Independent Publishing Platform, 2017. http://www.claisse.info/Proceedings.htm (accessed May 16, 2018).

[130] A. Cerveira, E. Correia, N. Cristelo, T. Miranda, F. Castro, A. Fernández-Jiménez, Statistical Analysis of the Influence of Several Factors on Compressive Strength of Alkali Activated Fly Ash, Procedia Structural Integrity. 5 (2017) 1116–1122. doi:10.1016/j.prostr.2017.07.099.

[131] M. Kheradmand, Z. Abdollahnejad, F. Pacheco-Torgal, Shrinkage Performance of Fly Ash Alkali-activated Cement Based Binder Mortars, KSCE J Civ Eng. 22 (2018) 1854–1864. doi:10.1007/s12205-017-1714-3.

[132] A. Gharzouni, L. Vidal, N. Essaidi, E. Joussein, S. Rossignol, Recycling of geopolymer waste: Influence on geopolymer formation and mechanical properties, Materials & Design. 94 (2016) 221–229. doi:10.1016/j.matdes.2016.01.043.

[133] A. Sabbatini, L. Vidal, C. Pettinari, I. Sobrados, S. Rossignol, Control of shaping and thermal resistance of metakaolin-based geopolymers, Materials & Design. 116 (2017) 374–385. doi:10.1016/j.matdes.2016.12.039.

[134] B. Yuan, C. Straub, S. Segers, Q.L. Yu, H.J.H. Brouwers, Sodium carbonate activated slag as cement replacement in autoclaved aerated concrete, Ceramics International. 43 (2017) 6039–6047. doi:10.1016/j.ceramint.2017.01.144.

[135] B. Yuan, Q.L. Yu, H.J.H. Brouwers, Reaction kinetics, reaction products and compressive strength of ternary activators activated slag designed by Taguchi method, Materials & Design. 86 (2015) 878–886. doi:10.1016/j.matdes.2015.07.077.

[136] N. Narayanan, K. Ramamurthy, Structure and properties of aerated concrete: a review, Cement and Concrete Composites. 22 (2000) 321–329. doi:10.1016/S0958-9465(00)00016-0.

[137] ASTM C109, Standard Test Method for Compressive Strength of Hydraulic Cement Mortars (Using 2-in. or [50-mm] Cube Specimens), ASTM International. (2016).

[138] H. Cheng-Yong, L. Yun-Ming, M.M.A.B. Abdullah, K. Hussin, Thermal Resistance Variations of Fly Ash Geopolymers: Foaming Responses, Scientific Reports. 7 (2017) 45355. doi:10.1038/srep45355.

[139] V. Ducman, L. Korat, Characterization of geopolymer fly-ash based foams obtained with the addition of Al powder or H2O2 as foaming agents, Materials Characterization. 113 (2016) 207–213. doi:10.1016/j.matchar.2016.01.019.

[140] R.M. Novais, L.H. Buruberri, G. Ascensão, M.P. Seabra, J.A. Labrincha, Porous biomass fly ash-based geopolymers with tailored thermal conductivity, Journal of Cleaner Production. 119 (2016) 99–107. doi:10.1016/j.jclepro.2016.01.083.

[141] M. Łach, K. Korniejenko, J. Mikuła, Thermal Insulation and Thermally Resistant Materials Made of Geopolymer Foams, Procedia Engineering. 151 (2016) 410–416. doi:10.1016/j.proeng.2016.07.350.

[142] V. Vaou, D. Panias, Thermal insulating foamy geopolymers from perlite, Minerals Engineering. 23 (2010) 1146–1151. doi:10.1016/j.mineng.2010.07.015.

[143] G. Roviello, C. Menna, O. Tarallo, L. Ricciotti, F. Messina, C. Ferone, D. Asprone, R. Cioffi, Lightweight geopolymer-based hybrid materials, Composites Part B: Engineering. 128 (2017) 225–237. doi:10.1016/j.compositesb.2017.07.020.

[144] F. Colangelo, G. Roviello, L. Ricciotti, V. Ferrándiz-Mas, F. Messina, C. Ferone, O. Tarallo, R. Cioffi, C.R. Cheeseman, Mechanical and thermal properties of lightweight geopolymer composites, Cement and Concrete Composites. 86 (2018) 266–272. doi:10.1016/j.cemconcomp.2017.11.016.

[145] R.M. Novais, G. Ascensão, N. Ferreira, M.P. Seabra, J.A. Labrincha, Influence of water and aluminium powder content on the properties of waste-containing geopolymer foams, Ceramics International. 44 (2018) 6242–6249. doi:10.1016/j.ceramint.2018.01.009.

[146] S. Diamond, Mercury porosimetry: An inappropriate method for the measurement of pore size distributions in cement-based materials, Cement and Concrete Research. 30 (2000) 1517–1525. doi:10.1016/S0008-8846(00)00370-7.

[147] S. Diamond, M.E. Leeman, Pore Size Distributions in Hardened Cement Paste by Sem Image Analysis, MRS Online Proceedings Library Archive. 370 (1994). doi:10.1557/PROC-370-217.

[148] K. Vance, Early Age Characterization and Microstructural Features of Sustainable Binder Systems for Concrete, Ph.D., Arizona State University, 2014. http://search.proquest.com/docview/1550352973/abstract/D753A20C6E484B18PQ/1 (accessed May 15, 2018).

[149] A. Fernández-Jiménez, A. Palomo, J.Y. Pastor, A. Martín, New Cementitious Materials Based on Alkali-Activated Fly Ash: Performance at High Temperatures, Journal of the American Ceramic Society. 91 (2008) 3308–3314. doi:10.1111/j.1551-2916.2008.02625.x.

[150] T.C. Keener, G.C. Frazier, W.T. Davis, THERMAL DECOMPOSITION OF SODIUM BICARBONATE, Chemical Engineering Communications. 33 (1985) 93–105. doi:10.1080/00986448508911162.

[151] J.-W. Kim, H.-G. Lee, Thermal and carbothermic decomposition of Na2CO3 and Li2CO3, Metall and Materi Trans B. 32 (2001) 17–24. doi:10.1007/s11663-001-0003-0.

[152] P. Rożek, M. Król, W. Mozgawa, Spectroscopic studies of fly ash-based geopolymers, Spectrochimica Acta Part A: Molecular and Biomolecular Spectroscopy. 198 (2018) 283–289. doi:10.1016/j.saa.2018.03.034.

[153] M. Catauro, F. Papale, G. Lamanna, F. Bollino, M. Catauro, F. Papale, G. Lamanna, F. Bollino, Geopolymer/PEG Hybrid Materials Synthesis and Investigation of the Polymer Influence on Microstructure and Mechanical Behavior, Materials Research. 18 (2015) 698–705. doi:10.1590/1516-1439.342814.

[154] J. Liu, J. Song, H. Xiao, L. Zhang, Y. Qin, D. Liu, W. Hou, N. Du, Synthesis and thermal properties of ZnAl layered double hydroxide by urea hydrolysis, Powder Technology. 253 (2014) 41–45. doi:10.1016/j.powtec.2013.11.007.

[155] N.K. Lee, G.H. An, K.T. Koh, G.S. Ryu, Improved Reactivity of Fly Ash-Slag Geopolymer by the Addition of Silica Fume, Advances in Materials Science and Engineering. (2016). doi:10.1155/2016/2192053.

[156] L. Zheng, W. Wang, Y. Shi, The effects of alkaline dosage and Si/Al ratio on the immobilization of heavy metals in municipal solid waste incineration fly ash-based geopolymer, Chemosphere. 79 (2010) 665–671. doi:10.1016/j.chemosphere.2010.02.018.

[157] European Commission. Commission Regulation (EU) No 601/2012 of 21/06/2012 on the monitoring and reporting of greenhouse gas emissions pursuant to Directive 2003/87/EC of the European Parliament and of the Council, OJEC. L181 (2012) 30–104.

[158] US Environmental Protection Agency. Greenhouse gas reporting rule (74 FR 56260), Fed Reg. 74 No 209 (2009) 56260–519.

[159] L.K. Turner, F.G. Collins, Carbon dioxide equivalent (CO2-e) emissions: A comparison between geopolymer and OPC cement concrete, Construction and Building Materials. 43 (2013) 125–130. doi:10.1016/j.conbuildmat.2013.01.023.

[160] WSTP_South_End_Plant_Process_Selection_Report_Appendix7, (2012). http://www.winnipeg.ca/finance/findata/matmgt/documents/2012/682-2012/682-2012_Appendix_H-WSTP_South_End_Plant_Process_Selection_Report/Appendix%207.pdf.

[161] P. Duxson, J.L. Provis, G.C. Lukey, J.S.J. van Deventer, The role of inorganic polymer technology in the development of 'green concrete,' Cement and Concrete Research. 37 (2007) 1590–1597. doi:10.1016/j.cemconres.2007.08.018.

[162] V. Petrovic, J.V.H. Gonzalez, O.J. Ferrando, J.D. Gordillo, J.R.B. Puchades, L.P. Griñan, Additive layered manufacturing: sectors of industrial application shown through case studies, International Journal of Production Research. 49 (2011) 1061–1079. doi:10.1080/00207540903479786.

[163] T.J. Horn, O.L.A. Harrysson, Overview of current additive manufacturing technologies and selected applications, Science Progress; St Albans. 95 (2012) 255. doi:http://dx.doi.org.ezproxy1.lib.asu.edu/10.3184/003685012X13420984463047.

[164] M. Hambach, D. Volkmer, Properties of 3D-printed fiber-reinforced Portland cement paste, Cement and Concrete Composites. 79 (2017) 62–70. doi:10.1016/j.cemconcomp.2017.02.001.

[165] A. Kazemian, X. Yuan, E. Cochran, B. Khoshnevis, Cementitious materials for construction-scale 3D printing: Laboratory testing of fresh printing mixture, Construction and Building Materials. 145 (2017) 639–647. doi:10.1016/j.conbuildmat.2017.04.015.

[166] M. Xia, B. Nematollahi, J. Sanjayan, Compressive Strength and Dimensional Accuracy of Portland Cement Mortar Made Using Powder-Based 3D Printing for Construction Applications, in: First RILEM International Conference on Concrete and Digital Fabrication – Digital Concrete 2018, Springer, Cham, 2018: pp. 245–254. doi:10.1007/978-3-319-99519-9_23.

[167] P. Shakor, J. Sanjayan, A. Nazari, S. Nejadi, Modified 3D printed powder to cement-based material and mechanical properties of cement scaffold used in 3D printing, Construction and Building Materials. 138 (2017) 398–409. doi:10.1016/j.conbuildmat.2017.02.037.

[168] M. Moini, J. Olek, J.P. Youngblood, B. Magee, P.D. Zavattieri, Additive Manufacturing and Performance of Architectured Cement-Based Materials, Advanced Materials. 0 (2018) 1802123. doi:10.1002/adma.201802123.

[169] Y. Zhang, Y. Zhang, G. Liu, Y. Yang, M. Wu, B. Pang, Fresh properties of a novel 3D printing concrete ink, Construction and Building Materials. 174 (2018) 263–271. doi:10.1016/j.conbuildmat.2018.04.115.

[170] S.A.O. Nair, H. Alghamdi, A. Arora, I. Mehdipour, G. Sant, N. Neithalath, Linking fresh paste microstructure, rheology and extrusion characteristics of cementitious binders for 3D printing, Journal of the American Ceramic Society. 0 (2018). doi:10.1111/jace.16305.

[171] N. Roussel, Rheological requirements for printable concretes, Cement and Concrete Research. 112 (2018) 76–85. doi:10.1016/j.cemconres.2018.04.005.

[172] R.J.M. Wolfs, F.P. Bos, T.A.M. Salet, Early age mechanical behaviour of 3D printed concrete: Numerical modelling and experimental testing, Cement and Concrete Research. 106 (2018) 103–116. doi:10.1016/j.cemconres.2018.02.001.

[173] A. Perrot, D. Rangeard, A. Pierre, Structural built-up of cement-based materials used for 3D-printing extrusion techniques, Mater Struct. 49 (2016) 1213–1220. doi:10.1617/s11527-015-0571-0.

[174] T.T. Le, S.A. Austin, S. Lim, R.A. Buswell, A.G.F. Gibb, T. Thorpe, Mix design and fresh properties for high-performance printing concrete, Mater Struct. 45 (2012) 1221–1232. doi:10.1617/s11527-012-9828-z.

[175] A. Pierre, D. Weger, A. Perrot, D. Lowke, Penetration of cement pastes into sand packings during 3D printing: analytical and experimental study, Mater Struct. 51 (2018) 22. doi:10.1617/s11527-018-1148-5.

[176] B. Panda, S.C. Paul, N.A.N. Mohamed, Y.W.D. Tay, M.J. Tan, Measurement of tensile bond strength of 3D printed geopolymer mortar, Measurement. 113 (2018) 108–116. doi:10.1016/j.measurement.2017.08.051.

[177] R.J. Flatt, P. Bowen, Yodel: A Yield Stress Model for Suspensions, Journal of the American Ceramic Society. 89 (2006) 1244–1256. doi:10.1111/j.1551-2916.2005.00888.x.

[178] K. Vance, A. Dakhane, G. Sant, N. Neithalath, Observations on the rheological response of alkali activated fly ash suspensions: the role of activator type and concentration, Rheol Acta. 53 (2014) 843–855. doi:10.1007/s00397-014-0793-z.

[179] A. Dakhane, S. Tweedley, S. Kailas, R. Marzke, N. Neithalath, Mechanical and microstructural characterization of alkali sulfate activated high volume fly ash binders, Materials & Design. 122 (2017) 236–246. doi:10.1016/j.matdes.2017.03.021.

[180] P. Bosscher, R.L. Williams, L.S. Bryson, D. Castro-Lacouture, Cable-suspended robotic contour crafting system, Automation in Construction. 17 (2007) 45–55. doi:10.1016/j.autcon.2007.02.011.

[181] ASTM C 191-13, Standard Test Methods for Time of Setting of Hydraulic Cement by Vicat Needle, ASTM International. (2013).

[182] P. Nath, P.K. Sarker, Effect of GGBFS on setting, workability and early strength properties of fly ash geopolymer concrete cured in ambient condition, Construction and Building Materials. 66 (2014) 163–171. doi:10.1016/j.conbuildmat.2014.05.080.

[183] P. Chindaprasirt, P.D. Silva, K. Sagoe-Crentsil, S. Hanjitsuwan, Effect of SiO2 and Al2O3 on the setting and hardening of high calcium fly ash-based geopolymer systems, J Mater Sci. 47 (2012) 4876–4883. doi:10.1007/s10853-012-6353-y.

[184] T. Lecompte, A. Perrot, Non-linear modeling of yield stress increase due to SCC structural build-up at rest, Cement and Concrete Research. 92 (2017) 92–97. doi:10.1016/j.cemconres.2016.11.020.

[185] Z. Zhou, M.J. Solomon, P.J. Scales, D.V. Boger, The yield stress of concentrated flocculated suspensions of size distributed particles, Journal of Rheology. 43 (1999) 651–671. doi:10.1122/1.551029.

[186] Z. Tan, S.A. Bernal, J.L. Provis, Reproducible mini-slump test procedure for measuring the yield stress of cementitious pastes, Mater Struct. 50 (2017) 235. doi:10.1617/s11527-017-1103-x.

[187] C. Lu, H. Yang, G. Mei, Relationship between slump flow and rheological properties of self compacting concrete with silica fume and its permeability, Construction and Building Materials. 75 (2015) 157–162. doi:10.1016/j.conbuildmat.2014.08.038.

[188] S. Kawashima, M. Chaouche, D.J. Corr, S.P. Shah, Influence of purified attapulgite clays on the adhesive properties of cement pastes as measured by the tack test, Cement and Concrete Composites. 48 (2014) 35–41. doi:10.1016/j.cemconcomp.2014.01.005.

[189] A. Kaci, R. Bouras, V.T. Phan, P.A. Andréani, M. Chaouche, H. Brossas, Adhesive and rheological properties of fresh fibre-reinforced mortars, Cement and Concrete Composites. 33 (2011) 218–224. doi:10.1016/j.cemconcomp.2010.10.009.

[190] Y.W.D. Tay, G.H.A. Ting, Y. Qian, B. Panda, L. He, M.J. Tan, Time gap effect on bond strength of 3D-printed concrete, Virtual and Physical Prototyping. 14 (2019) 104–113. doi:10.1080/17452759.2018.1500420.

[191] A. Perrot, C. Lanos, P. Estellé, Y. Melinge, Ram extrusion force for a frictional plastic material: model prediction and application to cement paste, Rheol Acta. 45 (2006) 457–467. doi:10.1007/s00397-005-0074-y.

[192] C. Ness, J.Y. Ooi, J. Sun, M. Marigo, P. McGuire, H. Xu, H. Stitt, Linking particle properties to dense suspension extrusion flow characteristics using discrete element simulations, AIChE Journal. 63 (2017) 3069–3082. doi:10.1002/aic.15768.

[193] D.J. Horrobin, R.M. Nedderman, Die entry pressure drops in paste extrusion, Chemical Engineering Science. 53 (1998) 3215–3225. doi:10.1016/S0009-2509(98)00105-5.

[194] R.A. Basterfield, C.J. Lawrence, M.J. Adams, On the interpretation of orifice extrusion data for viscoplastic materials, Chemical Engineering Science. 60 (2005) 2599–2607. doi:10.1016/j.ces.2004.12.019.

[195] J. Benbow, J. Bridgwater, Paste flow and extrusion, Clarendon Press, Oxford, UK. (1993).

[196] J. Powell, S. Assabumrungrat, S. Blackburn, Design of ceramic paste formulations for co-extrusion, Powder Technology. 245 (2013) 21–27. doi:10.1016/j.powtec.2013.04.017.

[197] P.F.G. Banfill, Rheology of Fresh Cement and Concrete: Proceedings of an International Conference, Liverpool, 1990, CRC Press, 1990.

[198] D. Konigsberg, T.M. Nicholson, P.J. Halley, T.J. Kealy, P.K. Bhattacharjee, Online process rheometry using oscillatory squeeze flow, Applied Rheology. 23 (2013). doi:10.3933/ApplRheol-23-35688.

[199] M.P. Bryan, S.L. Rough, D.I. Wilson, Measurement of the wall slip behaviour of a solid granular soap in ram extrusion, Powder Technology. 323 (2018) 76–85. doi:10.1016/j.powtec.2017.09.053.

[200] C.W. Stewart, Wall slip in the extrusion of linear polyolefins, Journal of Rheology. 37 (1993) 499–513. doi:10.1122/1.550456.

[201] P. Ballesta, R. Besseling, L. Isa, G. Petekidis, W.C.K. Poon, Slip and Flow of Hard-Sphere Colloidal Glasses, Phys. Rev. Lett. 101 (2008) 258301. doi:10.1103/PhysRevLett.101.258301.

[202] H. Ye, A. Radlińska, Shrinkage mechanisms of alkali-activated slag, Cement and Concrete Research. 88 (2016) 126–135. doi:10.1016/j.cemconres.2016.07.001.

[203] N.K. Lee, J.G. Jang, H.K. Lee, Shrinkage characteristics of alkali-activated fly ash/slag paste and mortar at early ages, Cement and Concrete Composites. 53 (2014) 239–248. doi:10.1016/j.cemconcomp.2014.07.007.

[204] H. Alghamdi, S.A.O. Nair, N. Neithalath, Insights into material design, extrusion rheology, and properties of 3D-printable alkali-activated fly ash-based binders, Materials & Design. 167 (2019) 107634. doi:10.1016/j.matdes.2019.107634.

[205] B. Panda, G.B. Singh, C. Unluer, M.J. Tan, Synthesis and characterization of one-part geopolymers for extrusion based 3D concrete printing, Journal of Cleaner Production. 220 (2019) 610–619. doi:10.1016/j.jclepro.2019.02.185.

[206] D. Marchon, S. Kawashima, H. Bessaies-Bey, S. Mantellato, S. Ng, Hydration and rheology control of concrete for digital fabrication: Potential admixtures and cement chemistry, Cement and Concrete Research. 112 (2018) 96–110. doi:10.1016/j.cemconres.2018.05.014.

[207] L. Reiter, T. Wangler, N. Roussel, R.J. Flatt, The role of early age structural build-up in digital fabrication with concrete, Cement and Concrete Research. 112 (2018) 86–95. doi:10.1016/j.cemconres.2018.05.011.

[208] S.C. Paul, G.P.A.G. van Zijl, M.J. Tan, I. Gibson, A review of 3D concrete printing systems and materials properties: current status and future research prospects, Rapid Prototyping Journal. 24 (2018) 784–798. doi:10.1108/RPJ-09-2016-0154.

[209] M. Ashraf, I. Gibson, M.G. Rashed, CHALLENGES AND PROSPECTS OF 3D PRINTING IN STRUCTURAL ENGINEERING, 13th International Conference on Steel, Space and Composite Structures (Perth, WA). (2018) 11.

[210] Y.W.D. Tay, M.Y. Li, M.J. Tan, Effect of printing parameters in 3D concrete printing: Printing region and support structures, Journal of Materials Processing Technology. 271 (2019) 261–270. doi:10.1016/j.jmatprotec.2019.04.007.

[211] B. Panda, S. Chandra Paul, M. Jen Tan, Anisotropic mechanical performance of 3D printed fiber reinforced sustainable construction material, Materials Letters. 209 (2017) 146–149. doi:10.1016/j.matlet.2017.07.123.

[212] S. Swarup, C.K. Schoff, A survey of surfactants in coatings technology, Progress in Organic Coatings. 23 (1993) 1–22. doi:10.1016/0033-0655(93)80002-R.

[213] M. Strozi Cilla, P. Colombo, M. Raymundo Morelli, Geopolymer foams by gelcasting, Ceramics International. 40 (2014) 5723–5730. doi:10.1016/j.ceramint.2013.11.011.

[214] S. Guignot, S. Faure, M. Vignes-Adler, O. Pitois, Liquid and particles retention in foamed suspensions, Chemical Engineering Science. 65 (2010) 2579–2585. doi:10.1016/j.ces.2009.12.039.

[215] I. Lesov, S. Tcholakova, N. Denkov, Drying of particle-loaded foams for production of porous materials: mechanism and theoretical modeling, RSC Advances. 4 (2014) 811–823. doi:10.1039/C3RA44500C.

[216] L. Du, K.J. Folliard, Mechanisms of air entrainment in concrete, Cement and Concrete Research. 35 (2005) 1463–1471. doi:10.1016/j.cemconres.2004.07.026.

[217] D. Weaire, S. Hutzler, The physics of foams, Clarendon, 1999.

[218] D. Langevin, Aqueous foams and foam films stabilised by surfactants. Gravity-free studies, Comptes Rendus Mécanique. 345 (2017) 47–55. doi:10.1016/j.crme.2016.10.009.

[219] I. Lesov, S. Tcholakova, N. Denkov, Factors controlling the formation and stability of foams used as precursors of porous materials, Journal of Colloid and Interface Science. 426 (2014) 9–21. doi:10.1016/j.jcis.2014.03.067.

[220] B. Feneuil, O. Pitois, N. Roussel, Effect of surfactants on the yield stress of cement paste, Cement and Concrete Research. 100 (2017) 32–39. doi:10.1016/j.cemconres.2017.04.015.

[221] R. Prud'homme, Foams: Theory: Measurements: Applications, Routledge, 2017.

[222] L. Ducloué, O. Pitois, L. Tocquer, J. Goyon, G. Ovarlez, Yielding and flow of foamed metakaolin pastes, Colloids and Surfaces A: Physicochemical and Engineering Aspects. 513 (2017) 87–94. doi:10.1016/j.colsurfa.2016.11.015.

[223] L. Ducloué, O. Pitois, J. Goyon, X. Chateau, G. Ovarlez, Rheological behaviour of suspensions of bubbles in yield stress fluids, Journal of Non-Newtonian Fluid Mechanics. 215 (2015) 31–39.

[224] B. Panda, J.H. Lim, M.J. Tan, Mechanical properties and deformation behaviour of early age concrete in the context of digital construction, Composites Part B: Engineering. 165 (2019) 563–571. doi:10.1016/j.compositesb.2019.02.040.

[225] J.D. Bernal, J. Mason, Packing of spheres: co-ordination of randomly packed spheres, Nature. 4754 (1960) 910.

[226] A. Donev, F.H. Stillinger, S. Torquato, Unexpected density fluctuations in jammed disordered sphere packings, Physical Review Letters. 95 (2005).

[227] B. Troschke, H. Burkhardt, Thermal conductivity models fro two-phase systems, Physics and Chemistry of the Earth. 23 (1998) 351–355. doi:10.1016/S0079-1946(98)00036-6.

[228] M.M. Awad, Y.S. Muzychka, Effective property models for homogeneous two-phase flows, Experimental Thermal and Fluid Science. 33 (2008) 106–113. doi:10.1016/j.expthermflusci.2008.07.006.

[229] V.D. Glukhovsky, G.S. Rostovskaja, G.V. Rumyna, High strength slag-alkaline cements, 7th International Congress on the Chemistry of Cement. 3 (1980) 164–168.

[230] S. Aydın, B. Baradan, Effect of activator type and content on properties of alkali-activated slag mortars, Composites Part B: Engineering. 57 (2014) 166–172. doi:10.1016/j.compositesb.2013.10.001.

[231] D. Bondar, Q. Ma, M. Soutsos, M. Basheer, J.L. Provis, S. Nanukuttan, Alkali activated slag concretes designed for a desired slump, strength and chloride diffusivity, Construction and Building Materials. 190 (2018) 191–199. doi:10.1016/j.conbuildmat.2018.09.124.

[232] C. Shi, J. Qian, High performance cementing materials from industrial slags — a review, Resources, Conservation and Recycling. 29 (2000) 195–207. doi:10.1016/S0921-3449(99)00060-9.

[233] J. Davidovits, J.L. Sawyer, Early high-strength mineral polymer, US4509985A, 1985. https://patents.google.com/patent/US4509985A/en (accessed May 16, 2019).

[234] T. Bakharev, J.G. Sanjayan, Y.-B. Cheng, Resistance of alkali-activated slag concrete to acid attack, Cement and Concrete Research. 33 (2003) 1607–1611. doi:10.1016/S0008-8846(03)00125-X.

[235] T. Bakharev, J.G. Sanjayan, Y.-B. Cheng, Resistance of alkali-activated slag concrete to alkali–aggregate reaction, Cement and Concrete Research. 31 (2001) 331–334. doi:10.1016/S0008-8846(00)00483-X.

[236] M. Komljenović, Z. Baščarević, N. Marjanović, V. Nikolić, External sulfate attack on alkali-activated slag, Construction and Building Materials. 49 (2013) 31–39. doi:10.1016/j.conbuildmat.2013.08.013.

[237] H. El-Didamony, A.A. Amer, H. Abd Ela-ziz, Properties and durability of alkali-activated slag pastes immersed in sea water, Ceramics International. 38 (2012) 3773–3780. doi:10.1016/j.ceramint.2012.01.024.

[238] H.M. Khater, Studying the effect of thermal and acid exposure on alkali activated slag Geopolymer, MATEC Web of Conferences. 11 (2014) 01032. doi:10.1051/matecconf/20141101032.

[239] A. Hajimohammadi, T. Ngo, P. Mendis, A. Kashani, J.S.J. van Deventer, Alkali activated slag foams: The effect of the alkali reaction on foam characteristics, Journal of Cleaner Production. 147 (2017) 330–339. doi:10.1016/j.jclepro.2017.01.134.

[240] T. Marchment, J. Sanjayan, M. Xia, Method of enhancing interlayer bond strength in construction scale 3D printing with mortar by effective bond area amplification, Materials & Design. 169 (2019) 107684. doi:10.1016/j.matdes.2019.107684.

[241] A. Gruskovnjak, B. Lothenbach, L. Holzer, R. Figi, F. Winnefeld, Hydration of alkali-activated slag: comparison with ordinary Portland cement, Advances in Cement Research. 18 (2006) 119–128. doi:10.1680/adcr.2006.18.3.119.

[242] C. Qing-Hua, S.L. Sarkar, A study of rheological and mechanical properties of mixed alkali activated slag pastes, Advanced Cement Based Materials. 1 (1994) 178–184. doi:10.1016/1065-7355(94)90009-4.

[243] F. Puertas, C. Varga, M.M. Alonso, Rheology of alkali-activated slag pastes. Effect of the nature and concentration of the activating solution, Cement and Concrete Composites. 53 (2014) 279–288. doi:10.1016/j.cemconcomp.2014.07.012.

[244] A. Kashani, J.L. Provis, G.G. Qiao, J.S.J. van Deventer, The interrelationship between surface chemistry and rheology in alkali activated slag paste, Construction and Building Materials. 65 (2014) 583–591. doi:10.1016/j.conbuildmat.2014.04.127.

[245] Z. Huanhai, W. Xuequan, X. Zhongzi, T. Mingshu, Kinetic study on hydration of alkali-activated slag, Cement and Concrete Research. 23 (1993) 1253–1258. doi:10.1016/0008-8846(93)90062-E.

[246] P.F. Banfill, The rheology of fresh cement and concrete-a review, Proceedings of the 11th International Cement Chemistry Congress. 1 (2003) 50–62.